

NYO-9657
MITNE-18

SPATIAL DISTRIBUTION OF THE NEUTRON FLUX
ON THE SURFACE OF A GRAPHITE-LINED CAVITY

by

J.T.Madell, T.J.Thompson, A.E.Profio, I. Kaplan

APRIL, 1962

CONTRACT AT(30-1)2344
U. S. ATOMIC ENERGY COMMISSION

Department of Nuclear Engineering
Massachusetts Institute of Technology
Cambridge, Massachusetts



Room 14-0551
77 Massachusetts Avenue
Cambridge, MA 02139
Ph: 617.253.2800
Email: docs@mit.edu
<http://libraries.mit.edu/docs>

DISCLAIMER OF QUALITY

Due to the condition of the original material, there are unavoidable flaws in this reproduction. We have made every effort possible to provide you with the best copy available. If you are dissatisfied with this product and find it unusable, please contact Document Services as soon as possible.

Thank you.

Some pages in the original document contain text that runs off the edge of the page.

MASSACHUSETTS INSTITUTE OF TECHNOLOGY
DEPARTMENT OF NUCLEAR ENGINEERING
Cambridge 39, Massachusetts

SPATIAL DISTRIBUTION OF THE NEUTRON FLUX
ON THE SURFACES OF A GRAPHITE-LINED CAVITY

by

J. T. MADELL, T. J. THOMPSON, A. E. PROFIO AND I. KAPLAN
April, 1962

NYO-9657
AEC Research and Development Report
UC-34 Physics
(TID-4500, 17th Edition)

Contract AT(30-1)2344
U.S. Atomic Energy Commission

DISTRIBUTION

NYO-9657

AEC Research and Development Report

UC-34 Physics

(TID-4500, 17th Edition)

1. USAEC, New York Operations Office (D. Richtmann)
2. USAEC, Division of Reactor Development (P. Hemmig)
3. USAEC, New York Patents Office (H. Potter)
4. USAEC, New York Operations Office (S. Strauch)
5. USAEC, Division of Reactor Development,
Reports and Statistics Branch
6. USAEC, Maritime Reactors Branch
7. USAEC, Civilian Reactors Branch
8. USAEC, Army Reactors Branch
9. USAEC, Naval Reactors Branch
10. Advisory Committee on Reactor Physics (E. R. Cohen)
11. ACRP (G. Dessauer)
12. ACRP (D. de Bloisblanc)
13. ACRP (M. Edlund)
14. ACRP (R. Ehrlich)
15. ACRP (I. Kaplan)
16. ACRP (H. Kouts)
17. ACRP (F. C. Maienschein)
18. ACRP (J. W. Morfitt)
19. ACRP (B. I. Spinrad)
20. ACRP (P. F. Zweifel)

21. ACRP (P. Gast)
22. ACRP (G. Hansen)
23. ACRP (S. Krasik)
24. ACRP (T. Merkle)
25. ACRP (T. M. Snyder)
26. ACRP (J. J. Taylor)
27. - 29. O.T.I.E., Oak Ridge, for Standard Distribution
UC - 34, TID-4500 (17th Edition)
30. - 100 Internal Distribution

ABSTRACT

A graphite-lined cavity was built at the outer end of the thermal column of the MIT Reactor. Seven variations of the material and geometrical arrangement of the cavity were made. The neutron flux was measured on the top surface and in the top wall of each variation and also on all surfaces and in the cavity itself of one of the variations. Absolute flux, cadmium ratio, and albedo measurements were made. The experimental results demonstrated that the cavity suitably modified the magnitude, distribution, and direction of the neutrons emerging from the thermal column.

A theoretical model was developed to calculate the magnitude and distribution of the neutron flux on the surfaces of a cavity. The values of the view factors and the albedos, which were necessary to calculate the flux in the cavities, were obtained from computer programs. The values of the flux were also calculated by using an electronic computer.

The calculated values of the flux are in excellent agreement with the measured values and it is felt that the use of the theoretical model is justified.

ACKNOWLEDGEMENTS

The MIT Heavy Water Lattice Project is a group effort with the success of any part of it being the result of the combined work of a number of individuals and groups. The results of this particular report are primarily due to the work of the principal author, John T. Madell, who has submitted substantially this same report in partial fulfillment for the requirements of the Sc.D. degree at M.I.T. The assistance of other students in the group was most helpful in the lengthy work required to stack the graphite in appropriate configurations and to assist in other ways. Overall guidance and direction of the research is shared by T. J. Thompson, I. Kaplan, and A. E. Profio.

Mrs. Selden and Miss Kelley were responsible for much of the data reduction. Mrs. Corrigan, Miss Ludwig, and Mrs. Madell were responsible for the typing of the project report.

The use of the facilities of the M.I.T. Computation Center and the Argonne National Laboratory computer were invaluable in carrying out the calculations.

The financial assistance of the General Dynamics Fellowship in Nuclear Engineering and the National Science Foundation Fellowship to Mr. John Madell has been greatly appreciated.

ERRATA

Correction to Eq. B1.9, page 248. The following should be added

$$\begin{aligned}
 & + \int_0^L \left\{ [(L+B-y)^2 + C^2]^{1/2} \left\{ \tan^{-1} \frac{[(L+B-y)^2 + C^2]^{1/2}}{(L+A+y)} - \tan^{-1} \frac{[(L+B-y)^2 + C^2]^{1/2}}{A+y} \right\} \right. \\
 & + [(2L+B-y)^2 + C^2]^{1/2} \left\{ \tan^{-1} \frac{[(2L+B-y)^2 + C^2]^{1/2}}{y+A} - \tan^{-1} \frac{[(2L+B-y)^2 + C^2]^{1/2}}{L+A+y} \right\} \\
 & \left. + \frac{(A+y)}{2} \ln \left[\frac{(y+A)^2 + (L+B-y)^2 + C^2}{(y+A)^2 + (2L+B-y)^2 + C^2} \right] + \frac{(L+A+y)}{2} \ln \left[\frac{(L+A+y)^2 + (2L+B-y)^2 + C^2}{(L+A+y)^2 + (L+B-y)^2 + C^2} \right] \right\} dy
 \end{aligned}$$

TABLE OF CONTENTS

| | | |
|----------------------|--|-----|
| INTRODUCTION | | 1 |
| EXPERIMENTAL SECTION | | |
| CHAPTER E1 | DESCRIPTION OF EXPERIMENTAL FACILITY | 7 |
| CHAPTER E2 | DISCUSSION OF EXPERIMENTAL FACILITY | 20 |
| CHAPTER E3 | FLUX DISTRIBUTIONS IN THE CAVITY ASSEMBLY | |
| E3.1 | Tabulation of flux distribution experiments | 22 |
| E3.2 | Selection of the detector | 24 |
| E3.3 | Procedure for the flux distribution measurements | 24 |
| E3.4 | Errors in the flux distribution measurements | 26 |
| E3.5 | Experimental results | 27 |
| CHAPTER E4 | ABSOLUTE FLUX MEASUREMENT | 87 |
| CHAPTER E5 | THE CADMIUM RATIO EXPERIMENTS | |
| E5.1 | Introduction | 91 |
| E5.2 | Selection of the foil material | 91 |
| E5.3 | Foil preparation | 91 |
| E5.4 | Positioning of the foil | 92 |
| E5.5 | Counting equipment | 92 |
| E5.6 | Counting procedure | 94 |
| E5.7 | Data reduction | 94 |
| E5.8 | Discussion of the experimental results | 97 |
| CHAPTER E6 | MEASUREMENT OF THE ALBEDO OF GRAPHITE | |
| E6.1 | Discussion of the experiment | 98 |
| E6.2 | Experimental procedure | 102 |
| E6.3 | Data reduction | 105 |
| E6.4 | Results and discussion | 106 |

THEORETICAL SECTION

| | | |
|------------|--|-----|
| CHAPTER T1 | DERIVATION OF THE THEORETICAL MODEL | 111 |
| CHAPTER T2 | VIEW FACTORS | |
| T2.1 | Derivation of the general equation defining the view factor | 119 |
| T2.2 | Discussion of the view factors | 124 |
| T2.3 | Testing for error in the view factors | 136 |
| CHAPTER T3 | CALCULATION OF THE ALBEDO AND DISCUSSION OF THE NEUTRON SOURCE | |
| T3.1 | Calculation of the albedo | 138 |
| T3.2 | Discussion of the neutron source | 158 |
| CHAPTER T4 | CALCULATION OF THE FLUX DISTRIBUTION | |
| T4.1 | Introduction | 159 |
| T4.2 | Representation of the cavity in the theoretical model | 159 |
| T4.3 | Selection of unit length | 166 |
| T4.4 | Assignment of the average value for the albedo of a sub-area | 177 |
| T4.5 | Calculation of the neutron source terms | 191 |
| T4.6 | Introduction to the discussion of the computer code | 194 |
| T4.7 | Description of the general flow diagram of the computer code | 198 |
| CHAPTER T5 | THEORETICAL RESULTS | |
| T5.1 | Tabulation of the results | 201 |
| T5.2 | Comparison of the results for the 6" and 12" sub-areas | 201 |
| T5.3 | Discussion of the applicability of the theoretical model | 211 |
| T5.4 | Analysis of the theoretical flux distribution | 213 |

| | | |
|-------------|---|-----|
| T5.5 | Comparison of theory and experiment | 222 |
| APPENDIX B1 | DERIVATION OF THE EXPRESSIONS FOR THE THIRTEEN VIEW FACTORS | 232 |
| APPENDIX B2 | COMPUTATION OF THE VIEW FACTORS | 259 |
| APPENDIX B3 | DETAILED FLOW OF THE CODE FOR THE 45° CAVITY | 269 |
| REFERENCES | | |

LIST OF FIGURES

| | | |
|-------|--|----|
| E1.1 | Vertical section of the exponential facility | 8 |
| E1.2 | Vertical section of the basic assembly (Assembly I) | 10 |
| E1.3 | Top view of the basic assembly shown without honeycomb and pedestal in place | 10 |
| E1.4 | Cross-sectional view of the basic assembly looking towards the back wall | 11 |
| E1.5 | Honeycomb with pedestal in place | 11 |
| E1.6 | Detailed view of graphite pedestal | 13 |
| E1.7 | The foil locations in the bottom (lower) and second from bottom (upper) layers of the pedestal | 13 |
| E1.8 | Vertical section of Assembly II | 15 |
| E1.9 | The graphite frame for Assemblies II and VI | 15 |
| E1.10 | Vertical section of Assembly III | 16 |
| E1.11 | Vertical section of Assembly IV | 16 |
| E1.12 | Vertical section of Assembly V | 17 |
| E1.13 | Vertical section of Assembly VI | 17 |
| E1.14 | Vertical section of Assembly VII | 18 |
| E3.1 | Horizontal traverse flux distribution of neutron source | 28 |
| E3.2 | Vertical traverse of flux distribution of neutron source | 30 |
| E3.3 | Symmetrical flux distributions from experiments 10 and 11 | 32 |
| E3.4 | Flux distribution on honeycomb, 6" off center line for Assemblies I through VII | 33 |
| E3.5 | Flux distribution on honeycomb, 7" from front of honeycomb for Assemblies I through VII | 35 |
| E3.6 | Flux distribution on honeycomb 67" from front of honeycomb for Assemblies I through VII | 36 |
| E3.7 | Vertical section of the graphite-filled cavity | 37 |
| E3.8 | Flux distribution for Assembly II, from front to back, 6" off center line | 43 |
| E3.9 | Flux distribution for Assembly III, from front to back, 6" off center line | 44 |

| | | |
|-------|--|-----|
| E3.10 | Fitting the values of ϕ_{abs} to the cosine curve | 45 |
| E5.1 | The locations on the walls of the Assembly at which the cadmium ratio was measured | 93 |
| E6.1 | Arrangement of the foils for the four irradiations of the albedo experiments | 99 |
| E6.2 | The positions on the walls of the Assembly at which the albedo was measured | 104 |
| E6.3 | Vertical section of the cavity assembly | 107 |
| E6.4 | Horizontal section of the cavity assembly | 107 |
| T1.1 | Cubic cavity with a coordinate system for each surface | 115 |
| T2.1 | General representation of the areas A_1 and A_2 for which the view factor F_{12} is derived | 120 |
| T2.2 | General representation of the areas A_1 and A_2 , with the differential areas dA_1 and dA_2 | 120 |
| T2.3 | The geometrical arrangement of A_1 and A_2 , defined by I, J, and K, for $F_1(I,J,K)$ | 123 |
| T2.4 | Arrangement of areas A_1 and A_2 | 123 |
| T2.5 | Arrangement of areas A_1 and A_2 for variable values of J_{out} | 126 |
| T2.6 | Arrangement of areas A_1 and A_2 for variable values of J_{out} | 126 |
| T2.7 | Relative angular distribution vs. $\cos\phi$ for Placzek's distribution, $\cos\phi$, and $\cos^2\phi$ | 129 |
| T2.8 | Probability of a neutron emerging with $\cos\phi$ vs. $\cos\phi$ | 134 |
| T3.1 | The slab with the coordinate system, squares and direction of incident neutrons shown | 142 |
| T3.2 | Flow diagram for the Monte Carlo Code which calculated the reflectivity | 142 |
| T3.3 | Average albedo for surface of a 16" thick, infinite area graphite slab divided into 4" sub-areas | 148 |
| T3.4 | Average albedo for 6" sub-areas on a 16" thick infinite area graphite slab | 149 |
| T3.5 | Average albedo for 6" sub-areas on a 12" thick graphite slab | 150 |

| | | |
|-------|---|-----|
| T3.6 | Average albedo for 4" sub-areas on the graphite frame | 151 |
| T3.7 | Average albedo for 6" sub-areas on graphite frame | 152 |
| T3.8 | Percentage of re-entering neutrons leaving through each 4" square | 154 |
| T3.9 | Surface of 16" thick, large graphite slab, divided into 12" sub-areas | 156 |
| T4.1 | The theoretical representation of Assembly I | 161 |
| T4.2 | The theoretical representation of Assembly II | 162 |
| T4.3 | Theoretical representation of the parallelepiped cavity | 165 |
| T4.4 | Theoretical representation of the 45° cavity | 165 |
| T4.5 | Theoretical representation of Assembly II | 167 |
| T4.6 | The walls of the PARA cavity assembly with 12" sub-areas | 168 |
| T4.7 | Wall of the 45° cavity assembly with 12" sub-areas | 170 |
| T4.8 | Theoretical representation of cavity assemblies I, II, IV, V, and VI | 172 |
| T4.9 | The average value of the albedo for the 6" sub-areas in Assembly I | 175 |
| T4.10 | The average value of the albedo for the 6" sub-areas in Assembly II | 179 |
| T4.11 | The average value of the albedo for 12" sub-areas in Assembly I | 181 |
| T4.12 | The average value of the albedo for 12" sub-areas in Assembly II | 183 |
| T4.13 | The average value of the albedo in the 12" sub-areas in Assembly IV | 185 |
| T4.14 | The average value of the albedo for 12" sub-areas in Assembly V | 187 |
| T4.15 | The average value of the albedo for 12" sub-areas in Assembly VI | 189 |
| T4.16 | The thermal column face and the foil locations superimposed on Surface #1 | 196 |
| T4.17 | Surfaces #1 and #4 with 12" sub-areas | 196 |

| | | |
|-------|--|-----|
| T4.18 | General flow diagram for computer code that calculates the flux distribution | 199 |
| T5.1 | Location of the 6" sub-areas on the honeycomb | 202 |
| T5.2 | Location of the 12" sub-areas on the honeycomb | 202 |
| T5.3 | Location of 6" and 12" sub-areas on the honeycomb | 208 |
| T5.4 | The values of $\phi_3(I,J)$ plotted from the center line to the edge of the honeycomb | 209 |
| T5.5 | Comparison of theoretical values of the flux for 6" and 12" sub-areas on the honeycomb of Assembly II | 210 |
| T5.6 | The values of the total, reflected, and source flux, plotted from front to back for Assemblies I and II | 215 |
| T5.7 | The values of the total, reflected, and source flux, plotted from side to side for Assemblies I and II | 217 |
| T5.8 | The comparison of the values of the flux in Assembly V obtained by using a constant and a variable value of the albedo | 218 |
| T5.9 | Vertical section of the idealized 45° cavity assembly | 220 |
| T5.10 | The values of the flux calculated for the idealized 45° cavity assembly | 221 |
| T5.11 | Experimental and theoretical flux for 6" sub-areas on the honeycomb of Assembly I | 223 |
| T5.12 | Experimental and theoretical flux for 6" sub-areas on the honeycomb of Assembly II | 224 |
| T5.13 | Experimental and theoretical flux for 12" sub-areas on the honeycomb of Assembly I | 226 |
| T5.14 | Experimental and theoretical flux for 12" sub-areas on the honeycomb of Assembly II | 227 |
| T5.15 | Experimental and theoretical flux for 12" sub-areas on the honeycomb of Assembly IV | 228 |
| T5.16 | Experimental and theoretical flux for 12" sub-areas on the honeycomb of Assembly V | 229 |
| T5.17 | Experimental and theoretical flux for 12" sub-areas on the honeycomb of Assembly VI | 230 |
| B1.1 | The geometrical arrangement of A_1 and A_2 for $V_1(I,J,K)$ | 233 |

| | | |
|-------|---|-----|
| B1.2 | The geometrical arrangement of A_1 and A_2 for $V2(I,J,K)$ | 236 |
| B1.3 | Relationship between rectangular and polar coordinates for area A_2 | 239 |
| B1.4 | Surface of the 45° cavity | 239 |
| B1.5 | Arrangement of A_1 and A_2 for $V4(I,J,K)$ | 242 |
| B1.6 | Arrangement of A_1 and A_2 for $V5(I,J,K)$ | 245 |
| B1.7 | Arrangement of A_1 and A_2 for $V12(I,J,K)$ | 247 |
| B1.8 | Arrangement of A_1 and A_2 for $V13(I,J,K)$ | 247 |
| B1.9 | Arrangement of A_1 and A_2 for $V9(A,B)$ | 251 |
| B1.10 | Two triangles, A_1 and A_2 , of unit dimension and two units away | 252 |
| B1.11 | The two triangles in Figure B1.10 divided into sub-areas | 252 |
| B1.12 | Arrangement of A_1 and A_2 for $V11(I,J,K)$ | 255 |
| B1.13 | Arrangement of A_1 and A_2 for $V14(I,J,K)$ | 255 |
| B1.14 | Arrangement of A_1 and A_2 for $V8(I,J,K)$ | 256 |
| B1.15 | Arrangement of A_1 and A_2 for $V10(I,J,K)$ | 256 |
| B1.16 | Arrangement of A_1 and A_2 for $V6(I,J,K)$ | 257 |
| B1.17 | Arrangement of A_1 and A_2 for $V7(I,J,K)$ | 257 |
| B1.18 | Enclosed space used to calculate $V6(3,3,1)$ | 258 |
| B1.19 | Enclosed space used to calculate $V6(3,3,2)$ | 258 |
| B2.1 | Flow diagrams for $V1(I,J,K)$ and $V2(I,J,K)$ | 260 |
| B2.2 | Flow diagrams for $V4, V5, V12, V13$ | 263 |
| B2.3 | Flow diagrams for $V9(A,B)$ | 264 |
| B2.4 | Areas A_1 and A_2 with their respective coordinate systems | 265 |
| B2.5 | Enclosed space used to calculate $V6(I,J,K)$ | 265 |
| B2.6 | Flow diagram for view factor $V6(I,J,K)$ | 267 |
| B3.1 | Flow diagram for MAIN routine | 277 |

| | | |
|-------|--|-----|
| B3.2 | Flow diagram for subroutine SOPNOR | 278 |
| B3.3 | Flow diagram for subroutine ALBEDO | 278 |
| B3.4 | Flow diagram for subroutine TEST 1 | 279 |
| B3.5 | Flow diagram for subroutine NORMAL | 280 |
| B3.6 | Flow diagram for subroutine CURIN | 280 |
| B3.7 | Flow diagram for subroutine RESET | 281 |
| B3.8 | Flow diagram for subroutine FINAL | 281 |
| B3.9 | Flow diagram for code which calculated C(I,J) for 45° cavity | 282 |
| B3.10 | Flow diagram for code which calculated C(I,J) for PARA cavity | 286 |

LIST OF TABLES

| | | |
|-------|--|----|
| E3.1 | List of experiments which measure the flux distribution in the cavity assemblies | 23 |
| E3.2 | The values of the flux measured on the face of the thermal column | 48 |
| E3.3 | The values of the flux measured on the honeycomb in Assembly I | 49 |
| E3.4 | The values of the flux measured on the honeycomb in Assembly II | 50 |
| E3.5 | The values of the flux measured in the lower layer of the pedestal in Assembly II | 51 |
| E3.6 | The values of the flux measured in the upper layer of the pedestal in Assembly II | 52 |
| E3.7 | The values of the flux measured on the honeycomb in Assembly II | 53 |
| E3.8 | The values of the flux measured in the lower layer of the pedestal in Assembly II | 54 |
| E3.9 | The values of the flux measured in the upper layer of the pedestal in Assembly II | 55 |
| E3.10 | The values of the flux measured on the honeycomb in Assembly III | 56 |
| E3.11 | The values of the flux measured in the lower layer of the pedestal in Assembly III | 57 |
| E3.12 | The values of the flux measured in the upper layer of the pedestal in Assembly III | 58 |
| E3.13 | The values of the flux measured on the honeycomb in Assembly III | 59 |
| E3.14 | The values of the flux measured on the honeycomb in Assembly IV | 60 |
| E3.15 | The values of the flux measured in the lower layer of the pedestal in Assembly IV | 61 |
| E3.16 | The values of the flux measured in the upper layer of the pedestal in Assembly IV | 62 |
| E3.17 | The values of the flux measured on the honeycomb in Assembly V | 63 |
| E3.18 | The values of the flux measured in the lower layer of the pedestal in Assembly V | 64 |

| | | |
|-------|--|----|
| E3.19 | The values of the flux measured in the upper layer of the pedestal in Assembly V | 65 |
| E3.20 | The values of the flux measured on the honeycomb in Assembly V | 66 |
| E3.21 | The values of the flux measured in the lower layer of the pedestal in Assembly V | 67 |
| E3.22 | The values of the flux measured in the upper layer of the pedestal in Assembly V | 68 |
| E3.23 | The values of the flux measured on the honeycomb in Assembly VI | 69 |
| E3.24 | The values of the flux measured in the lower layer of the pedestal in Assembly VI | 70 |
| E3.25 | The values of the flux measured in the upper layer of the pedestal in Assembly VI | 71 |
| E3.26 | The values of the flux measured on the honeycomb in Assembly VI | 72 |
| E3.27 | The values of the flux measured in the lower layer of the pedestal in Assembly VI | 73 |
| E3.28 | The values of the flux measured in the upper layer of the pedestal in Assembly VI | 74 |
| E3.29 | The values of the flux measured on the honeycomb in Assembly VII | 75 |
| E3.30 | The values of the flux measured in the lower layer of the pedestal in Assembly VII | 76 |
| E3.31 | The values of the flux measured in the upper layer of the pedestal in Assembly VII | 77 |
| E3.32 | The values of the flux measured on the honeycomb in Assembly VII | 78 |
| E3.33 | The values of the flux measured in the lower layer of the pedestal in Assembly VII | 79 |
| E3.34 | The values of the flux measured in the upper layer of the pedestal in Assembly VII | 80 |
| E3.35 | The values of the flux obtained in Experiment #14 | 81 |
| E3.36 | The values of the flux obtained in Experiment #15 | 85 |

| | | |
|------|---|-----|
| E4.1 | Results from coincidence countings | 88 |
| E5.1 | Results of cadmium ratio measurements | 96 |
| E6.1 | The schedule for the four irradiations of the albedo experiments | 108 |
| E6.2 | The results of the albedo experiments | 108 |
| T2.1 | Corrections to the flux for the 12" sub-areas on the honeycomb | 131 |
| T2.2 | Corrections to the flux for the 6" sub-areas on the honeycomb | 132 |
| T3.1 | Values of the reflectivities for the 21 cases of the Monte Carlo Code | 145 |
| T4.1 | Neutron source terms for 12" sub-areas on Surface #1 | 192 |
| T4.2 | Neutron source terms for 6" sub-areas on Surface #1 | 193 |
| T5.1 | The values of the flux in the 6" sub-areas on the honeycomb of Assembly I | 203 |
| T5.2 | The values of the flux in the 6" sub-areas on the honeycomb of Assembly II | 204 |
| T5.3 | The values of the flux in the 12" sub-areas on the honeycomb of Assemblies I, II, IV, V, and VI | 205 |

Introduction

In 1959, the Nuclear Engineering Department at M.I.T., with the support of the Atomic Energy Commission, undertook an experimental and theoretical study of the nuclear properties of lattices of partially enriched uranium rods in heavy water. The measurements in this study are to include: the buckling, the age and thermal diffusion area, the thermal neutron distribution in the lattice cell, and the various ratios related to the parameters ϵ , f , and p . The M.I.T. Reactor (MITR) provides the neutron source for the experiments.

In planning the experiments, it was decided that the rods should be suspended vertically in the heavy water to avoid bowing of the rods, and to facilitate the changing of both the lattice and the detectors in the lattices. The source neutrons are to enter the tank containing the lattice from the bottom and the exponential decrease of the thermal neutron flux will then be along the direction of the rods, that is, in the vertical direction. The exponential experiments are conveniently interpreted and compared to the experiments of other workers, if the source neutrons are supplied to the lattice in this manner. A problem arose, however, because the neutrons were available as a horizontal beam from the thermal column of the MITR. As a solution to this problem, Dr. T. J. Thompson suggested that a graphite-lined cavity be constructed in front of the outer end of the thermal column. The neutrons from the horizontal thermal column would enter the cavity and undergo many collisions with the graphite walls. Some of the neutrons in the cavity would diffuse upward through the top graphite wall and serve as a vertical neutron beam to the exponential tank placed above the cavity. Besides having a vertical direction, it was necessary that the neutron

source also have a sufficient magnitude and an appropriate distribution to be used in the various lattice experiments. Since the use of a cavity to change the direction of a neutron beam has not been investigated in any detail, it was not known whether the desired magnitude and distribution could be obtained by means of such a cavity. An experimental study was therefore undertaken to measure the magnitude and distribution of the neutrons diffusing upward from the cavity for various arrangements of the cavity. The first purpose of this study was to determine whether a cavity is feasible for the proposed use and, if feasible, to select the arrangement of the cavity best suited for the M.I.T. experiments.

Other workers with research reactors are likely to meet problems similar to the one described above and may be interested in using such a cavity. The particular physical situation, for example, the dimensions, shape, and purpose of the cavity will, in general, be different for each reactor. In order that the results of this work may be applicable to physical situations other than that at the MITR, a theoretical study of the magnitude and distribution of the neutrons on the surface of a cavity was made.

The general purpose of the present study is, therefore, to investigate, both theoretically and experimentally, the use of a cavity as a practical means of extending and modifying a neutron source. The purpose of the experimental study is to measure the magnitude and distribution of the neutron flux on a surface of the cavity. The purpose of the theoretical study is to develop a method of calculating the flux. The shape of the cavity and the materials forming the surfaces of the cavity were varied to determine how these factors influence the extension and modification of the neutron source.

Since it is only in recent years that there has arisen an interest in the use of a cavity to extend and modify a neutron source, the terminology used in this study will be defined, and the behavior of the neutrons in the cavity will be discussed in some detail. The term "cavity" refers to a region through which neutrons may pass with a very small probability of collision. If the region is empty, or is filled with a gas having a long collision mean free path, the region is considered to be a cavity. In this study, air, which has a collision mean free path of about 3700 cm, occupies the cavity. The cavity is completely surrounded by a material with which the neutrons collide; the cavity and its walls are referred to as the cavity assembly.

The neutrons enter the cavity from some source: they may diffuse through a wall into the cavity, in which case, the surface of the wall bounding the cavity may be called the source; or they may enter the cavity through a hole in the wall. The actual source of the neutrons may be a reactor, or a source such as a Pu-Be capsule, placed in the wall or in the cavity itself. In the present study, the neutrons enter the cavity by diffusing through the thermal column of the MITR, which forms one of the walls of the cavity.

After a neutron enters the cavity, it passes through without being absorbed or scattered and impinges on a wall. The neutron may diffuse through the wall, it may be absorbed by the wall material, or it may be scattered back into the cavity. If the neutron does re-enter the cavity, its energy, direction, and location on the surface of the wall are different from what they were when the neutron entered the wall. The neutron, after re-entering the cavity, continues to collide with the walls of the cavity until it is finally absorbed in the wall or leaks out of the cavity

assembly and is lost. The possibility of extending a neutron source arises from the fact that neutrons travel without absorption or scattering in a cavity; and after the neutrons have undergone many collisions in a cavity assembly, the magnitude, distribution, direction, and energy spectrum of the source neutrons may be modified considerably.

Many cases may arise, especially in the use of small research reactors, where the neutron source must be modified for experimental purposes. The change in direction and distribution of the neutrons from the MITR in lattice experiments is one example. As another example, a cavity assembly made of hydrogenous material may be used to provide neutrons of very low energy from an epithermal beam source. As a third example, a neutron beam may be extended from a small core of a reactor to a region outside the biological shield by means of a cavity assembly and used to irradiate a large sample at the outer end of the cavity.

One criterion of the practicality of the use of a cavity is the effectiveness with which the neutron source is used; both the magnitude and spatial distribution of the re-entering neutrons must meet the requirements of the experiments. Thus, if in using a cavity to modify the distribution of a neutron source, only a small fraction of the original neutron source is available in the modified source, the cavity may not be practical. The difficulty and expense of constructing a cavity assembly make it important to be able to predict in advance the performance of the cavity for the use proposed. In this study the practicality of using a cavity has been determined by building several cavity assemblies and by determining experimentally the properties of the resulting neutron flux. The concurrent theoretical studies have shown that it is possible to predict the behavior of such a cavity.

The use of a cavity for various purposes has been suggested by several people independently, including Thompson (1), Völcker (2), Sleeper (3), and others. Thompson suggested its use as a means of changing the direction and the extent of a downward directed beam from the reactor to a horizontal thermal column for irradiation use. Völcker discussed the possibility of using the neutrons from a horizontal thermal column to feed the bottom of a vertical exponential tank. He outlined some possible methods of calculating the flux distribution on the bottom of the tank but did not give any solutions. Sleeper and later Clark (4) measured the flux distribution on the surfaces of a cavity into which neutrons from a Pu-Be source were being fed. These experiments, however, were not extensive, and no attempt was made to interpret the measured distribution theoretically.

From the description of the behavior of neutrons in a cavity and from past experience with black body radiation from a "hohlraum" (5), it is evident that the behavior of the neutrons in a cavity is similar in many respects to that of radiation in an enclosure. Both neutrons and radiation travel through a cavity in a straight line and without collision; both obey the inverse square law; upon striking a wall of the cavity, both are either transmitted, reflected or absorbed. The energy spectrum of either neutrons or radiation emerging from a wall depends on the temperature of the wall.

The similarity between the behavior of neutrons in a cavity and of radiation in a "hohlraum" will also be seen in the theoretical model developed in this paper for calculating the magnitude and distribution of the neutron flux on the surface of a cavity. View factors, which are used in problems of radiant heat transfer, are used in this paper to calculate the number of neutrons incident on a surface from all of the other surfaces.

Lambert's Law can be used to describe the angular distribution both of neutrons and of radiation leaving a surface. The albedo, defined in this paper as the ratio of the number of neutrons leaving a wall to the number entering the wall, is analogous to the emissivity of a wall. The term, albedo, was first used by astrophysicists for the ratio of reflected to incident light at the surface of a planet. The term "neutron current" is the analogue of the term "intensity" used in studies of radiation transfer. Because of this analogy, the theoretical model developed for the behavior of neutrons in a cavity may be used for problems of radiation in a cavity. Radiant heat transfer in a furnace and the transmission of gamma rays through a duct in a shield are two examples of problems to which this model may be applied.

The black body radiation from a hohlraum has been extremely useful in understanding some of the basic principles of radiation. In explaining the energy spectrum for black body radiation, Planck proposed that atoms are excited by discrete quantities of energy. This, of course, is the basic idea in quantum mechanics. Since these systems are analogous, it is conceivable that a cavity could also be used to study the factors which influence the energy spectrum of neutrons.

Saha and Srivastava (5) point out the analogy between black body radiation and an ideal gas. An analogy also exists between neutrons and the molecules of an ideal gas in an enclosure. Because of the similarity in some of the aspects of the behavior of neutrons, radiation, and an ideal gas in an enclosure, the information obtained from the study of one of these systems may possibly be applied to one or both of the other systems.

Thompson, Clark, Sleeper and Völcker all referred to the cavity as a "hohlraum" because of the analogy between the two systems. In this paper, the two terms, "cavity" and "hohlraum", are used interchangeably, without any difference in meaning.

Chapter E1

Description of Experimental Facility

Before discussing the experiments, the cavity assembly will be described in detail. A cross-sectional view of the MITR core, the thermal column, the cavity assembly, and the exponential tank is shown in Figure E1.1. Descriptions of the MITR and of the lattice assembly have been given by Thompson (6) and Profio, et al. (7), respectively.

The neutrons originate in the reactor core and diffuse through the heavy water reflector in the core tank, then through a 52" long, 63" x 63" graphite thermal column and into the cavity. The cavity contains air at room temperature and pressure. Most of the neutrons and gamma rays can be prevented from entering the cavity by lowering the cadmium and lead shutters. Before the cavity assembly was built, a 32"-thick movable thermal column door was in place at the outer end of the thermal column. This door was rolled back and a shielded room was constructed at the outer end of the thermal column with the door forming part of the shielding. The room is lined with boral to prevent neutron activation of the shield. A new set of 14"-thick, movable shielding doors is suspended from an I-beam attached to the side of the biological shield. When these doors are closed, they are in front of the opening left by the thermal column door and serve to lower the level of the neutron and gamma radiation entering the cavity. When the doors are closed and the lead and cadmium shutters are lowered, the radiation level in the region of the exponential tank is below tolerance at full power operation of the reactor. Both the shutters and shielding doors are operated by remote control. The shielding doors are wrapped with cadmium to prevent neutron activation. A cadmium sheet is also placed above the shielding doors in the area between the reactor shield face and the 72" tank to prevent neutrons from streaming into the exponential tank or the reactor building. Starting at the thermal column

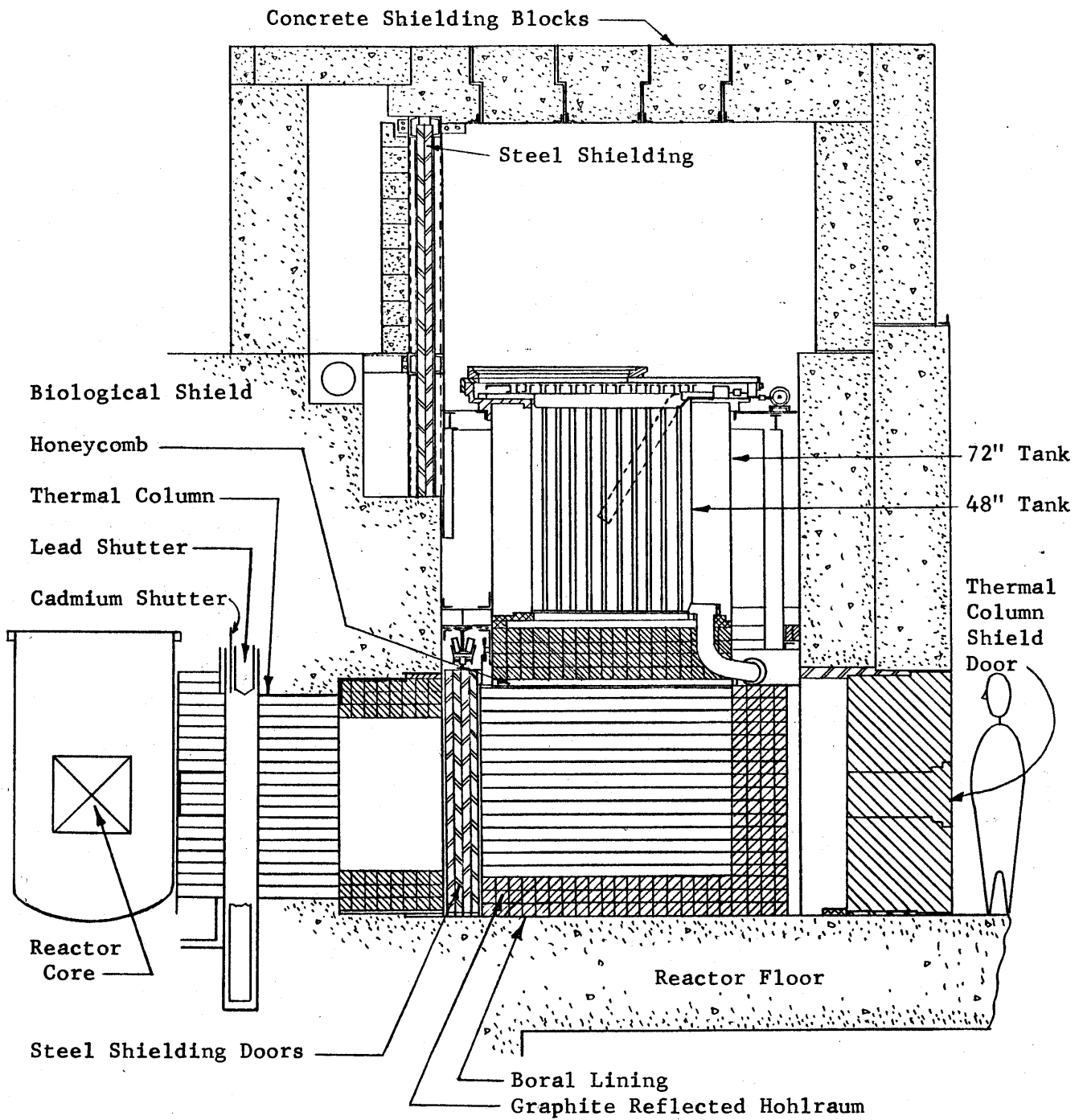


Figure E1.1 Vertical Section of the Exponential Facility.

face, the first 32" of the walls of the cavity are covered with boral. When the shielding doors are open, the next 16" are covered with boral on the bottom surface (floor of the reactor building) and with cadmium on the top and side surfaces (the ends of the cadmium-covered shield door).

The geometrical arrangement and the wall material of the cavity assembly were changed as part of the experimental program, but all of these changes may be described as variations on a basic cavity assembly. This basic assembly, which was not changed, is described first and then the variations are described.

Figures E1.2, E1.3, and E1.4 give three views of this basic assembly. The thermal column door space and shielding doors, shown in the open position in Figure E1.3, have already been discussed. The floor, side walls, back wall, and top of the cavity indicated in the figures are made up of 4" by 4" stringers of reactor grade graphite. The top of the cavity is normally referred to as the "pedestal". The stringers meet close tolerances and no gaps exist between the stringers when they are stacked in the form of a wall or floor. Graphite pins, one-half inch in diameter, are used to stabilize the layers of graphite stringers in the side and back walls. The floor is 12" thick and the side and back walls are 16" thick. The pedestal, with dimensions 16" by 72" by 72", is supported over the cavity by a 2" by 74" by 90" honeycomb structure.

The honeycomb structure consists of very thin aluminum foil in a form similar to that of the walls of a honeycomb, held together by resin and sandwiched between two 0.064" sheets of aluminum. Most of the space between the aluminum sheets is occupied by air, so that the honeycomb structure is quite transparent to neutrons while still able to support the graphite pedestal. The honeycomb is supported in turn by a system of I-beams and angle irons. A 4" angle iron runs across the top of each side wall and

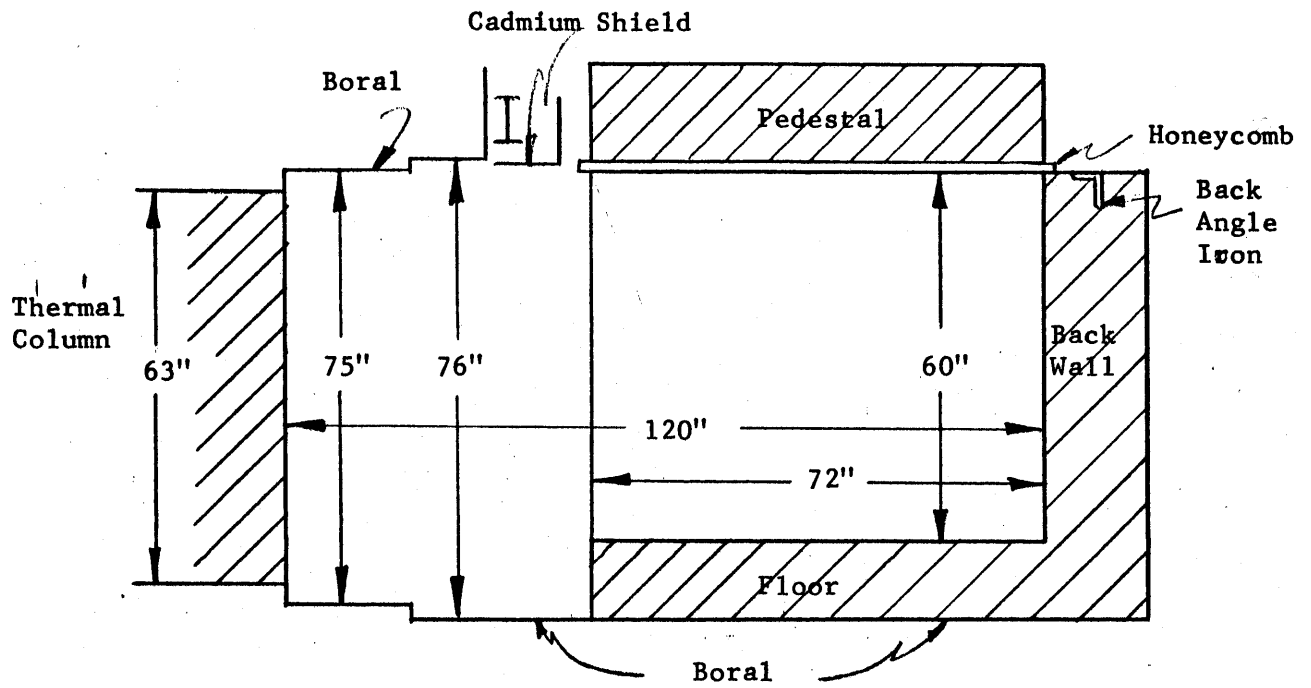


Figure E1.2 Vertical Section of the Basic Assembly (Assembly I).

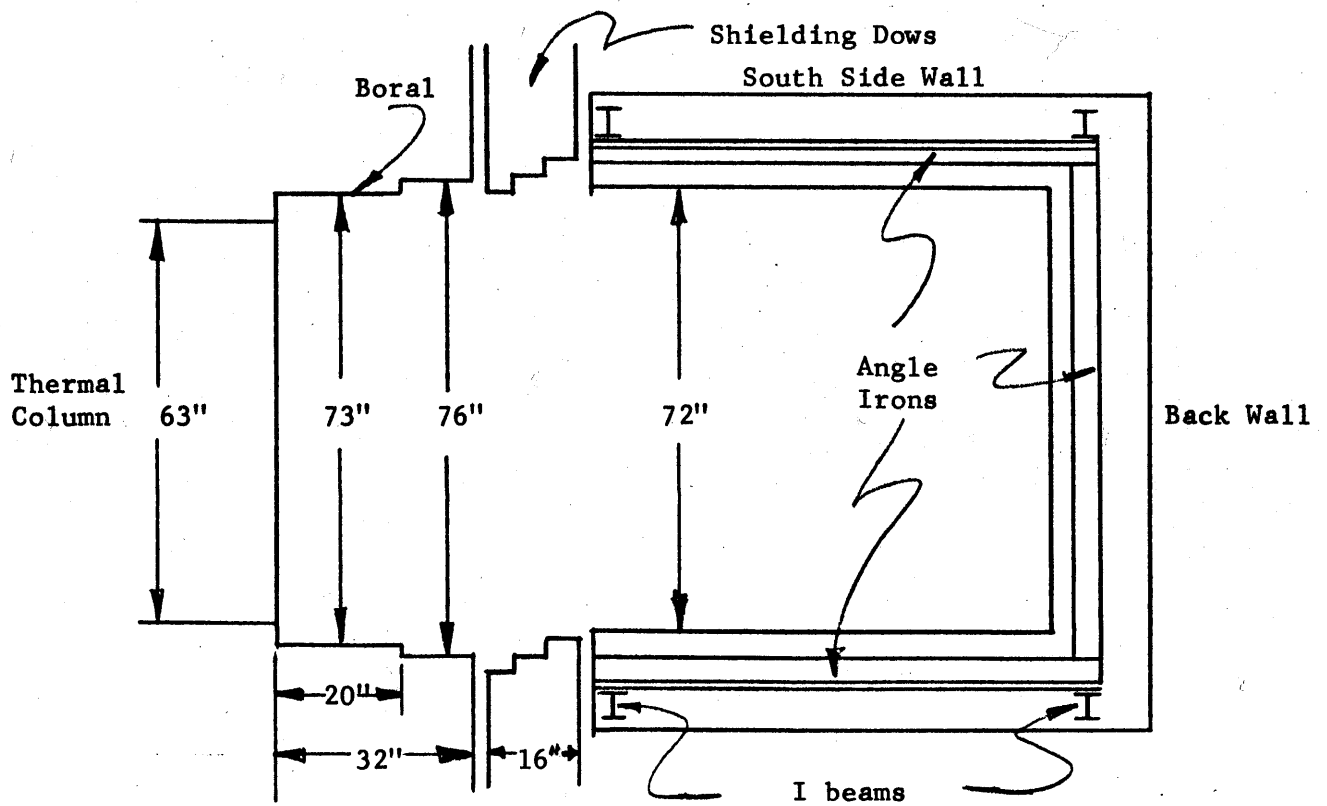


Figure E1.3 Top View of the Basic Assembly Shown Without the Honeycomb and Pedestal in place.

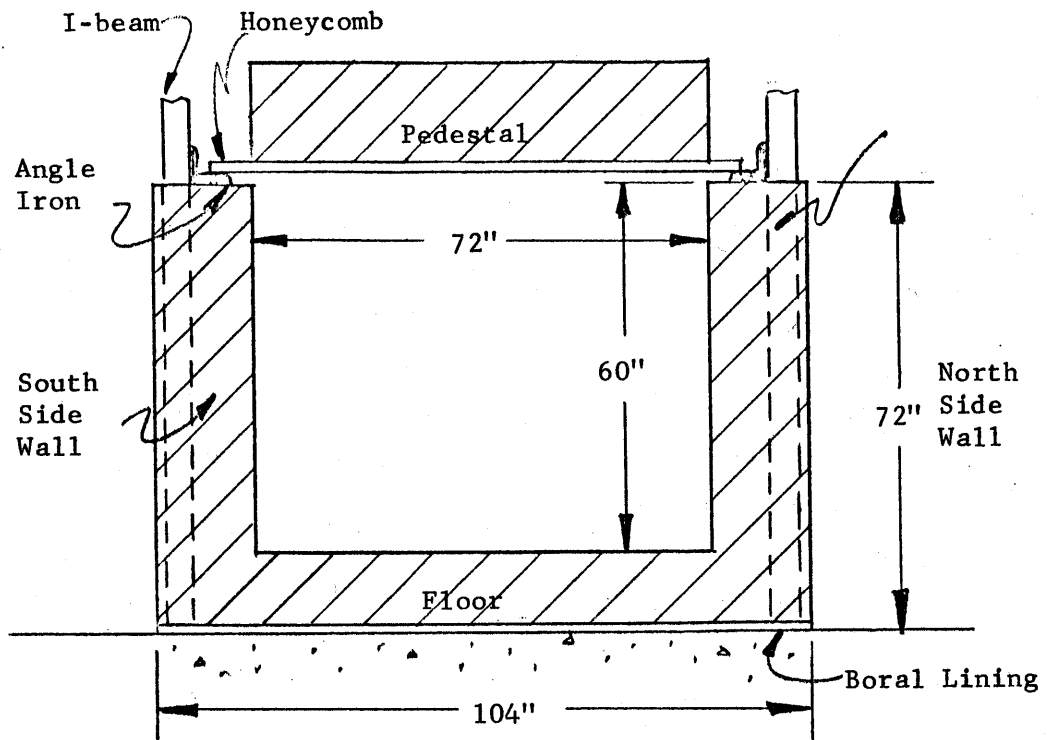


Figure E1.4 Cross Sectional View of the Basic Assembly Looking Towards the Back Wall.

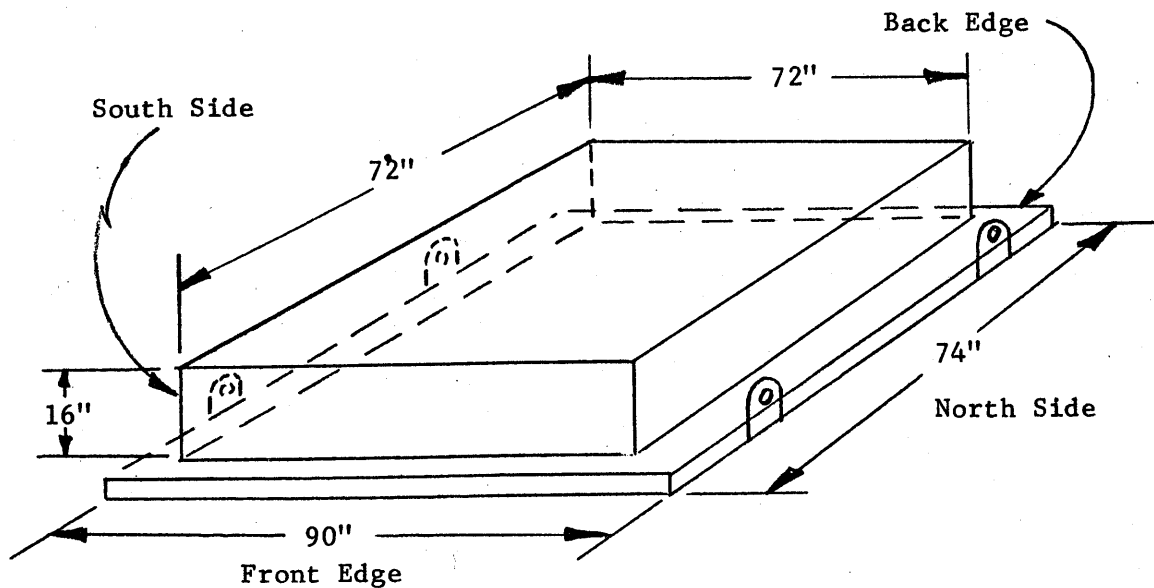


Figure E1.5 Honeycomb with Pedestal in place. Note Designation on Front and Back Edges, and North and South Sides.

is fastened to the vertical I-beams at both ends. (See Figure E1.3) Another 4" angle iron, which runs along the top of the back wall, stabilizes the I-beam structure. The flanges of the angle irons, which are on the side walls, are 92" apart. The pedestal and honeycomb structure are shown in Figures E1.5 and E1.6. Note the designation of a front and back edge; the front edge is the one closest to the face of the thermal column, and the back edge is the one farthest away. The sides of the pedestal and honeycomb are labeled "north" and "south" to differentiate between them. A 1/4" plywood frame is placed around the pedestal, and cadmium is wrapped around the sides and top of the framed pedestal. The plywood frame prevents the graphite stringers on the top of the pedestal from sliding off while the pedestal is being moved. The cadmium absorbs any slow neutrons incident on the sides or top of the pedestal. Steel plates with holes cut in them are bolted to the side of the honeycomb; turn-buckles are attached to these plates, and the whole assembly is moved about with the overhead crane.

Indentations, 1/16" in diameter and about 1/16" deep, were drilled in the bottom row (lower layer) and the second from the bottom row (upper layer) of graphite stringers in the pedestal. The location of the stringers and of the indentations is shown in Figure E1.7. The indentations are used to hold foils during the irradiations, the details of which will be discussed later. The foil locations in the upper layer are 8" directly above those in the lower layer. As will be seen later, the foil locations on the honeycomb are directly below those in the pedestal so that a vertical flux transverse may be measured.

Heavy concrete shielding blocks, the first two layers of which were in place during these experiments, surround the cavity assembly on all sides. The honeycomb and pedestal must be lifted over the shielding block

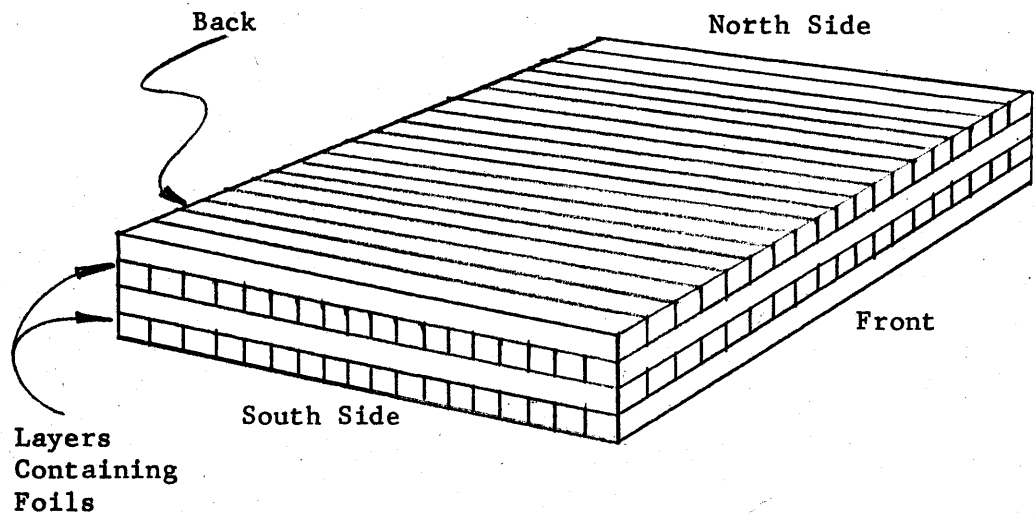


Figure E1.6 Detailed View of Graphite Pedestal. The Layers which Contain Foils are Indicated on the Drawing.

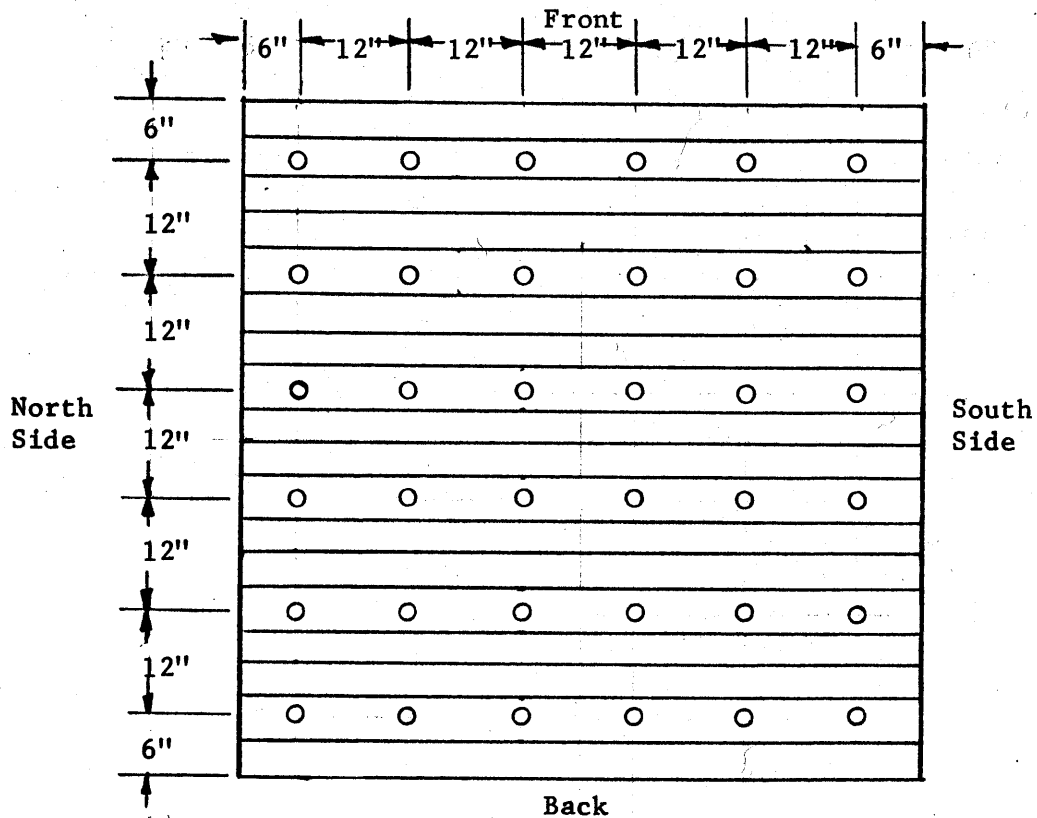


Figure E1.7 The Foil Locations in the Bottom (Lower) and Second from the Bottom (Upper) Layers of the Pedestal.

wall which forms the sides of the room, and then lowered into place. During the cavity experiments the exponential tank was not in place; this did not effect the results of the experiments, while making it easier to change the geometrical arrangements of the walls.

Assembly I is the basic cavity assembly (Figure E1.2) which has boral and cadmium in the thermal column and shielding door spaces. Assembly II is obtained by adding an eight inch thick, graphite "frame" in the thermal column door space (Figures E1.8 and E1.9). Graphite replaces boral as the wall material in this variation. In Assembly III, the graphite "frame" is changed into a "tooth" arrangement as shown in Figure E1.10. The purpose of this variation will be discussed together with the results of the measurements. A graphite floor, eight inches thick, is extended into the shielding and thermal column door spaces, and 4" of graphite are added to the sides and back of the pedestal to form Assembly IV (Figure E1.11). These four assemblies (I, II, III, IV) are referred to as PARA assemblies because of the general parallelepiped shape of the cavity.

The next set of variations (Assemblies V, VI, and VII) are all characterized by a rearrangement of the floor. Graphite is added to the floor of the basic cavity so as to create a stepped inclined surface. This geometrical variation results in Assembly V (Figure E1.12). By smoothing this stepped arrangement, a 45° inclined plane is obtained and is indicated by the dotted line in Figure E1.12. A cavity with this stepped arrangement is referred to as a 45° cavity. Variations to Assembly V are made by adding the graphite "frame" (Assembly VI, Figure E1.13) and graphite "tooth" (Assembly VII, Figure E1.14) to Assembly V. If the inclined plane is removed from Assembly V, VI, and VII, the resulting assemblies are identical with Assemblies I, II, and III, respectively. With these seven cavity assemblies, it is possible to study the effect of different geometrical

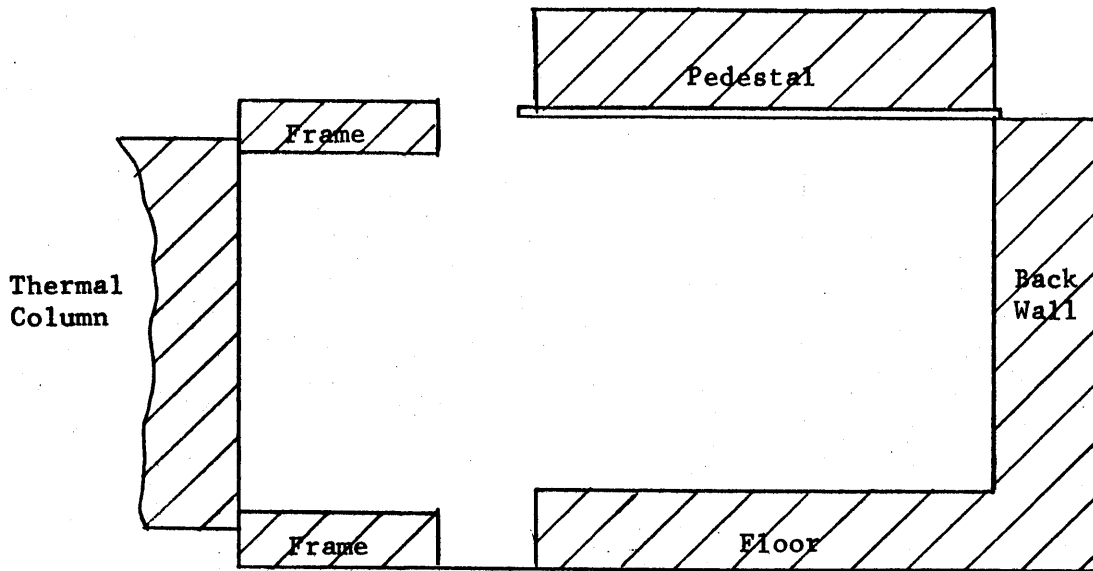


Figure E1.8 Vertical Section of Assembly II.

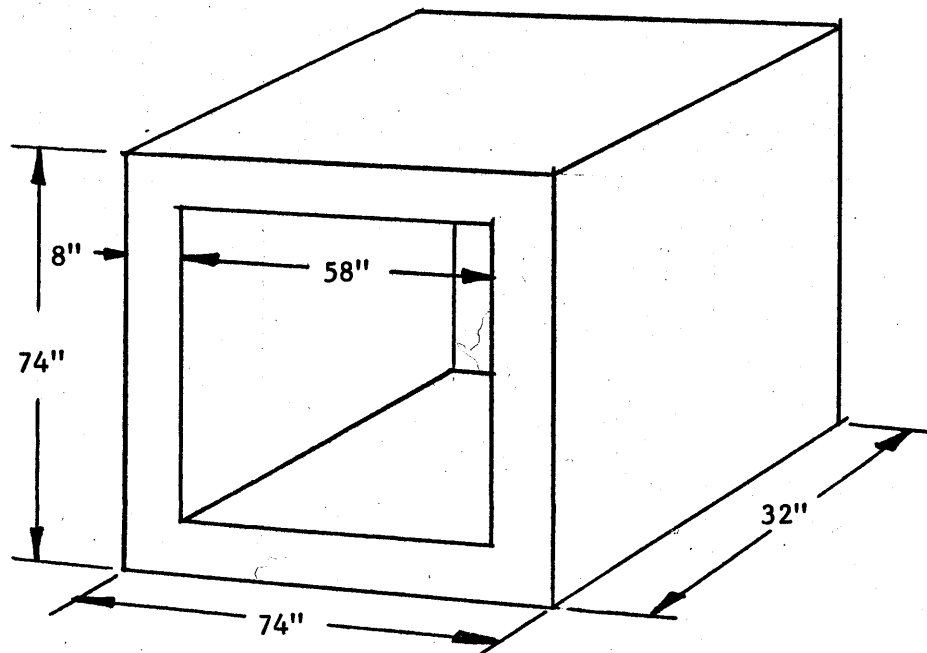


Figure E1.9 The Graphite Frame for Assemblies II and VI.

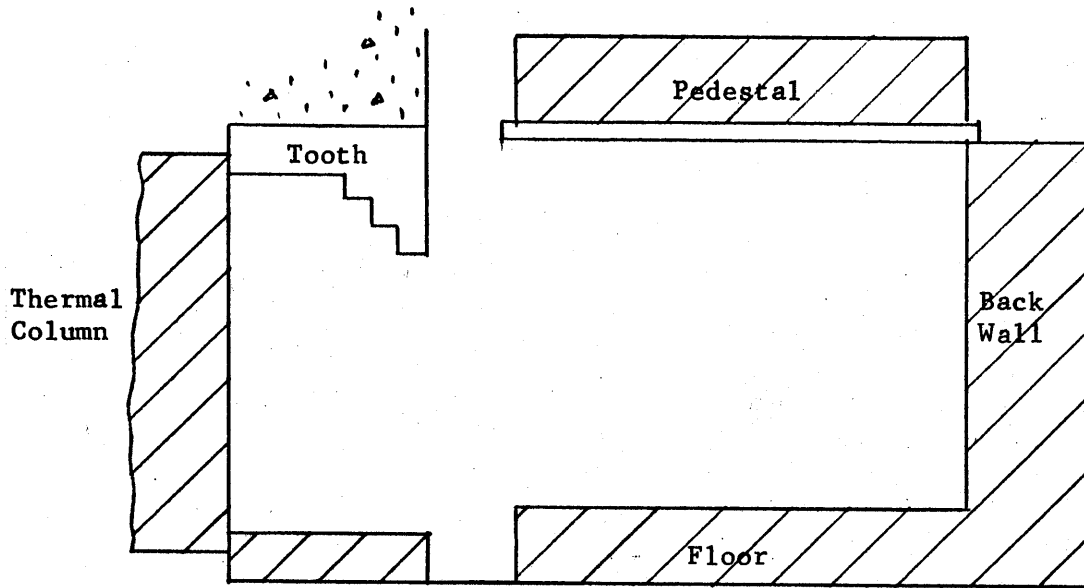


Figure E1.10 Vertical Section of Assembly III.

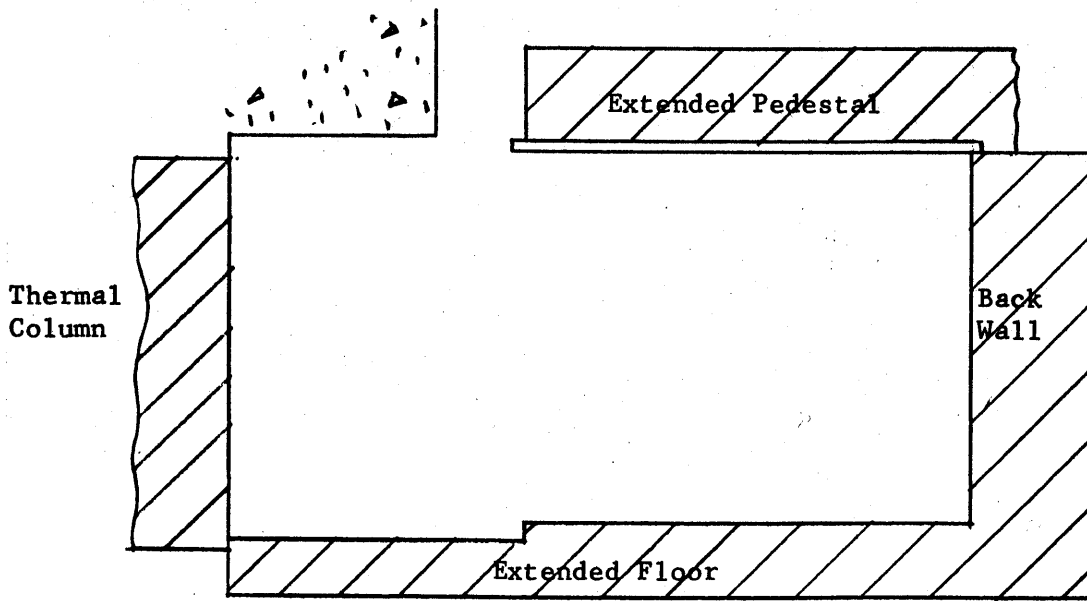


Figure E1.11 Vertical Section of Assembly IV.

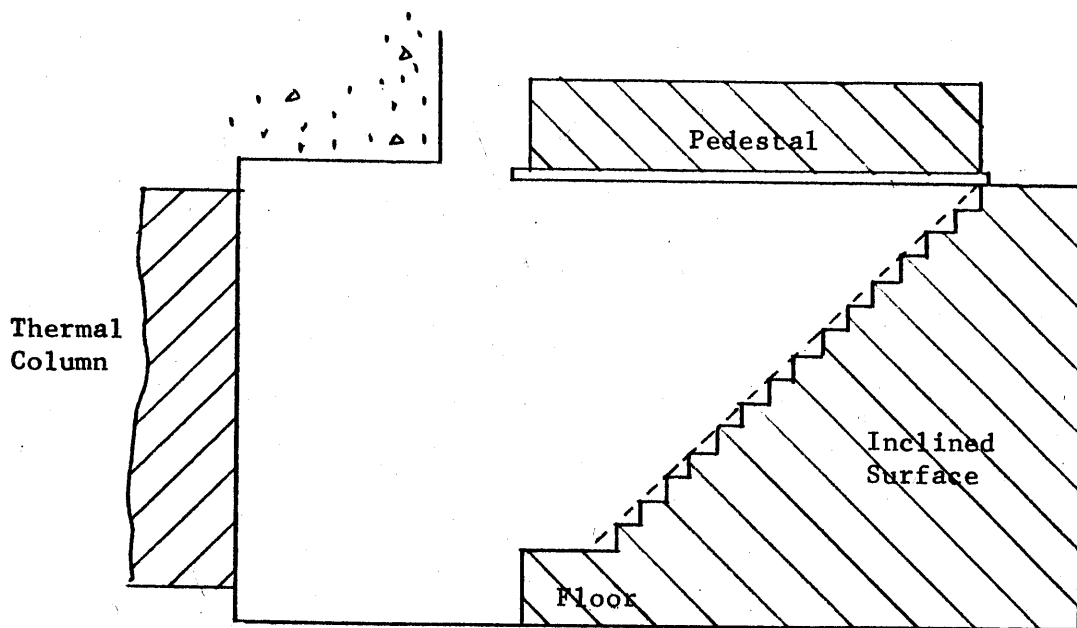


Figure E1.12 Vertical Section of Assembly V

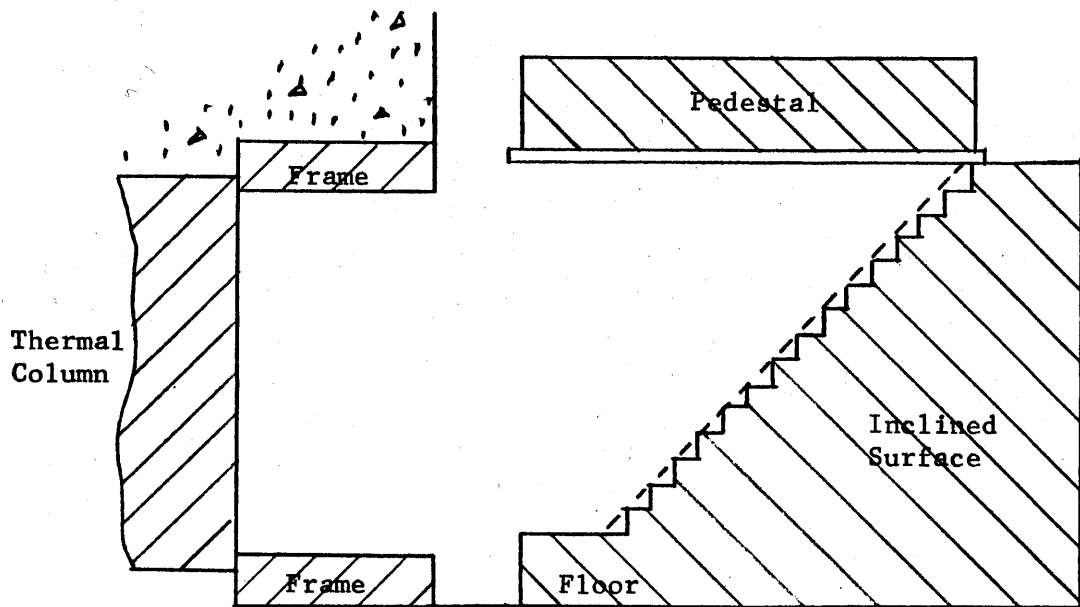


Figure E1.13 Vertical Section of Assembly VI.

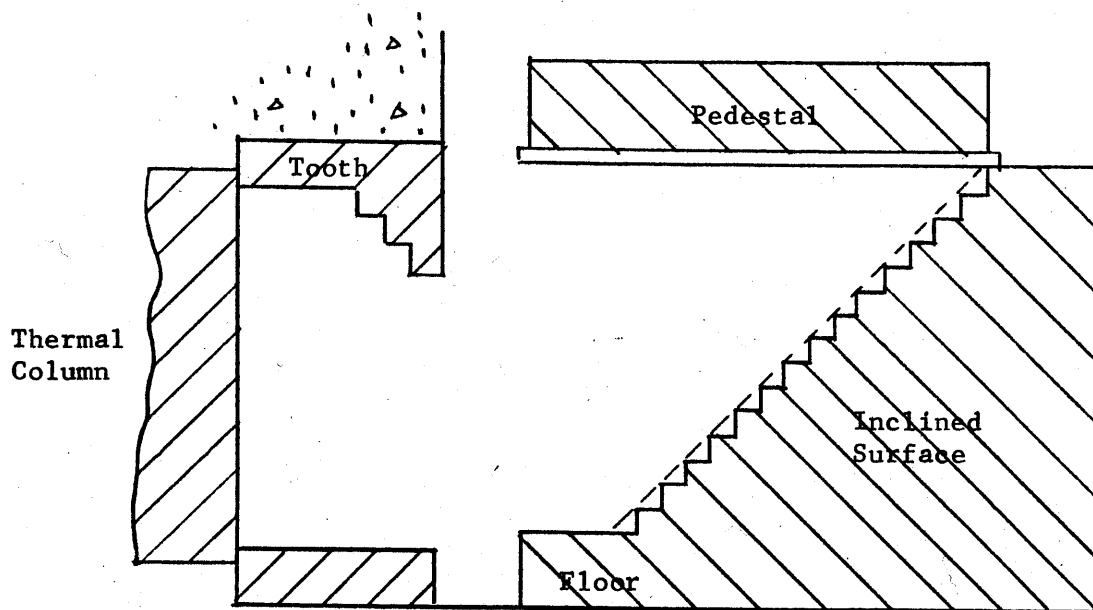


Figure E1.14 Vertical Section of Assembly VII.

arrangements of walls for the same wall material, and the effect of different wall materials for the same geometrical arrangement.

The cavity has another effect beside that of modifying the neutron source. The exponential tank has been moved out of the direct line of the gamma rays emitted from the thermal column, (see Figure E1.1) with the result that there is a reduction in the number of photoneutrons produced in the heavy water in the tank and a corresponding reduction in the correction for these photoneutrons.

Chapter E2

Discussion of Experimental Program

One purpose of the experimental program was to obtain the data leading to a selection of the cavity assembly best suited for the M.I.T. lattice measurements. Measurements were also made to investigate the general problem of extending and modifying a neutron source by means of a cavity.

The absolute magnitude and distribution of the flux was measured in the seven cavity assemblies described in Chapter E1. Experiments were also performed to obtain values of the cadmium ratio and the albedo of the graphite forming the walls of the cavity. It is evident from Figure E1.1 that the neutrons which enter the tank have first passed through the honeycomb and pedestal. The magnitude and distribution of the flux in the pedestal, therefore, provide a basis for selecting the most suitable cavity arrangement. Each of the seven assemblies modified the magnitude and distribution of the neutron source differently. Since the material and the shape of the honeycomb and pedestal were the same for all of the assemblies, the flux on the honeycomb was used to study the modification of the source produced by each assembly. The influence of the inclined plane, the frame, and the tooth were determined by comparing the flux on the honeycomb for the different assemblies.

The magnitude and distribution of the neutron source was also measured; these measurements were needed to determine the effectiveness of the cavity assembly, and in the calculation of the flux. The magnitude and distribution of the flux on all of the surfaces of a cavity and in the cavity itself were measured to investigate the features of a cavity assembly.

The cadmium ratio measurements indicate the ratio of the thermal to the fast flux in the assembly. A high value of the cadmium ratio means that most of the neutrons are thermal, and that the theoretical model can

treat the neutrons as being thermal. The values of the albedo of the cavity were useful in understanding the behavior of the neutrons in the cavity assembly. The albedo was used in the theoretical model and the values of the albedo for the walls were needed for the calculation of the flux.

The flux distribution measurements are discussed in Chapter E3, the absolute flux measurements in Chapter E4, the cadmium ratio measurements in Chapter E5, and the albedo measurements in Chapter E6.

Chapter E3

Flux Distributions in the Cavity Assembly

Flux distributions in the cavity assembly were obtained from activation measurements. An array of foils was placed in the assembly and was irradiated for a specified time at a known power level of the reactor. The activity of the foils was then measured and a flux distribution was obtained by plotting the counting rates due to the activity.

E3.1 Tabulation of Flux Distribution Experiments

Fifteen experiments were performed to measure the flux distribution on the surfaces of the cavity, in the pedestal, and in the cavity itself. The fifteen experiments are listed in Table E3.1, which gives the location of the foils, the geometrical arrangement of the cavity assembly, and the total number of foils used in each experiment.

The purpose of Experiment #1 was to measure the distribution of source neutrons on the face of the thermal column. Source neutrons are those which enter the cavity for the first time; they have not undergone collisions in the cavity assembly and then returned to the thermal column face. In measuring the distribution of the source neutrons, it is important to insure that no neutrons return to the thermal column face. When this experiment was performed, the graphite was removed from the thermal column door space and the cadmium-covered shielding doors were closed. The source neutrons struck the cadmium covered shielding door or the boral-lined walls and thus would have had only a very small probability of returning to the thermal column face.

All of the other Experiments (#2 through #15) were performed with the shielding doors opened. In Experiments #2 through #13, the flux distribution was measured on the honeycomb and in the pedestal for all of the geometrical arrangements of the cavity assembly. The flux distribution

Table E3.1

List of Experiments which Measure the Flux
Distribution in the Cavity Assemblies

| <u>#</u> | <u>Geometrical Arrangement</u> | <u>Location of Foils</u> | <u>Total Number of Foils</u> |
|----------|---|--------------------------------------|------------------------------|
| 1 | - | Face of Thermal Column | 36 + 2 monitors |
| 2 | Assembly I | Honeycomb, | 36 + 2 monitors |
| 3 | Assembly II | Honeycomb, two layers of pedestal | 108 + 2 monitors |
| 4 | Assembly II (with pedestal extended in the back) | " | " |
| 5 | Assembly III | " | " |
| 6 | Assembly III | " | " |
| 7 | Assembly IV | " | " |
| 8 | Assembly V | " | " |
| 9 | Assembly V | " | " |
| 10 | Assembly VI | " | " |
| 11 | Assembly VI | " | " |
| 12 | Assembly VII | " | " |
| 13 | Assembly VII | " | " |
| 14 | Assembly II | All surfaces of hohlraum | 150 + 2 monitors |
| 15 | Assembly II | In hohlraum itself | 75 + 2 monitors |

was measured for Assembly II on all surfaces and in the cavity itself in Experiments #14 and #15, respectively.

E3.2 Selection of the Detector

Activation measurements were used to obtain the neutron density. A movable neutron counter, such as a BF_3 tube or fission chamber, would produce a continuous neutron distribution by scanning the desired surface. However, the inside surfaces of the cavity assembly are inaccessible when the honeycomb and pedestal are in place. The 40" concrete shielding on all sides further complicates the problem of designing a positioning device to scan the inside surfaces, so a movable counter was not used. Wires, which could also measure a continuous distribution, were not used because they would not become sufficiently active in the available flux to give accurate results.

E3.3 Procedure for the Flux Distribution Measurements

A set of procedures was devised and used in all of the 15 experiments which measure the flux distribution. The selection of the foil material and the procedure for preparing and irradiating the foils are given in Appendix A1 of the thesis (8) on which this report is based. The description of the equipment, the procedure used for counting the foils and the procedure for reducing the data are given in Appendix A2 of the thesis. The results of the experiments are expressed in terms of the absolute flux, ϕ_{abs} , incident on the foils at LMW operation of the MITR.

The following relationships are used in deducting the data for the flux distribution measurements:

$$\text{CR(SAT)} = \frac{\text{PC-BGD}}{T_C} \left(\frac{\lambda T_C}{1 - e^{-\lambda T_C}} \right) \left(\frac{e^{+\lambda T_D}}{1 - e^{-\lambda T_R}} \right), \quad (\text{E3.1})$$

$$\text{Act}(\text{rel}) = \frac{\overline{\text{CR}(\text{SAT})}}{\omega} \cdot E(\text{rel}) \cdot N \quad \text{at LMW}, \quad (\text{E3.2})$$

$$\phi_{\text{abs}} = K \text{Act}(\text{rel}) = \frac{N}{E \Sigma_a \frac{CW}{\rho}} \cdot \overline{\text{CR}(\text{SAT})}, \quad \text{at LMW}, \quad (\text{E3.3})$$

where

λ = decay constant of the radioactive isotope,

T_D = time between the irradiation and the counting of the foil,

T_R = irradiation time,

T_C = counting time,

PC = preset count,

BGD = background during counting,

CR(SAT) = counting rate due to the saturated activity of the foil,

$\overline{\text{CR}(\text{SAT})}$ = average value for CR(SAT) of a foil,

$E(\text{rel})$ = relative value of the counting efficiency during the counting of the foil obtained from the count rate of the RaD+E standard,

N = normalization constant for calculating the foil activity at LMW operation of the MITR. The quantity, N , was calculated from the count rate of the monitor foils in the thermal column,

Act(rel) = relative activity of the foil at LMW operation of the MITR,

K = conversion constant between the relative activity and the absolute flux,

E = counting efficiency,

Σ_a = absorption cross section,

W = weight of the foil,

ρ = density of the foil material,

C = correction factor for flux depression, self-shielding, and flux hardening.

The derivation and discussion of these equations are given in Appendix A2. The above nomenclature is also used in Chapters E4, E5, and E6. All of the values of the microscopic cross sections were obtained from BNL-325 (9), the decay constants and the description of the decay scheme from Sullivan's Trilinear Charts (10), and the correction factors and densities from ANL-5800 (11).

E3.4 Errors in the Flux Distribution Measurements

All foils in the assembly were counted three times with a preset count of at least 10,000. The monitor foils were counted for at least a total of 100,000 counts. The average count rate was found to be within the statistical error of the individual counting rates, so any error introduced by spurious counts was negligible. Equation (E3.3) is rewritten to include the maximum standard error due to counting statistics.

$$\phi_{\text{abs}} \pm 0.83\% = \frac{K}{W} \cdot (N \pm 0.14\%) \cdot [E(\text{rel}) \pm 0.58\%] \cdot [\overline{\text{CR}}(\text{SAT}) \pm 0.58\%] \quad (\text{E3.4})$$

The standard error of N was based on a total of 100,000 counts of the monitor foils and their accompanying RaD+E standard foil while the standard errors of E(rel) and $\overline{\text{CR}}(\text{SAT})$ were based on a total of 30,000 counts. Since the foils were sometimes counted for more than these number of counts, the standard error of ϕ_{abs} is the maximum error due to counting statistics.

No standard error is given for the conversion constant, K, for the absolute flux, or for the weight, W, of the foil. The weight of a foil was known within 1×10^{-4} gram, so the error was about 3×10^{-3} percent and contributed an insignificant error to ϕ_{abs} . This study is interested primarily in comparing the magnitude and distribution of the

flux in each assembly. Since all of the foils' activities were multiplied by K, the error in K does not enter into the comparison of the different values of the flux for different assemblies.

E3.5 Experimental Results

The values of the absolute flux, ϕ_{abs} , (at LMW operation of the MITR) determined in the 15 experiments are listed in Tables E3.2 through E3.36. The value of ϕ_{abs} for each foil is shown at the same location on the drawing that indicates the site on the surface where the foil was irradiated. The values of E(rel), N, and the reactor power at which the foils were irradiated are also indicated in the tables. Note in the tables the designation of the sides of the honeycomb and pedestal as the front, back, north side, and south side.

The values of ϕ_{abs} from Experiment #1 (thermal column face) are plotted for the six horizontal rows of foils in Figures E3.1a and E3.1b. The resulting flux distributions show that the neutron source is symmetrical about the vertical mid-line on the thermal column face. Since each cavity assembly is also symmetrical about the vertical mid-line, the flux distribution on the honeycomb surface and in the pedestal should be symmetrical about the center line from the front to the back edge of the honeycomb. Examination of the experimental points shows that this is the case. Figure E3.2 shows the vertical flux distribution on the thermal column face; only three vertical traverses are shown because of the symmetry about the vertical mid-line. The average value of the neutron source, obtained by graphical integration of the flux distribution in Chapter T4, is 1.348×10^9 n/cm²sec. The general shape of the distribution of the neutron source may be described by a function of the form $\cos x \cos y$, where x and y are proportional to the distances in the horizontal and vertical directions, respectively, from the center of the thermal column face.

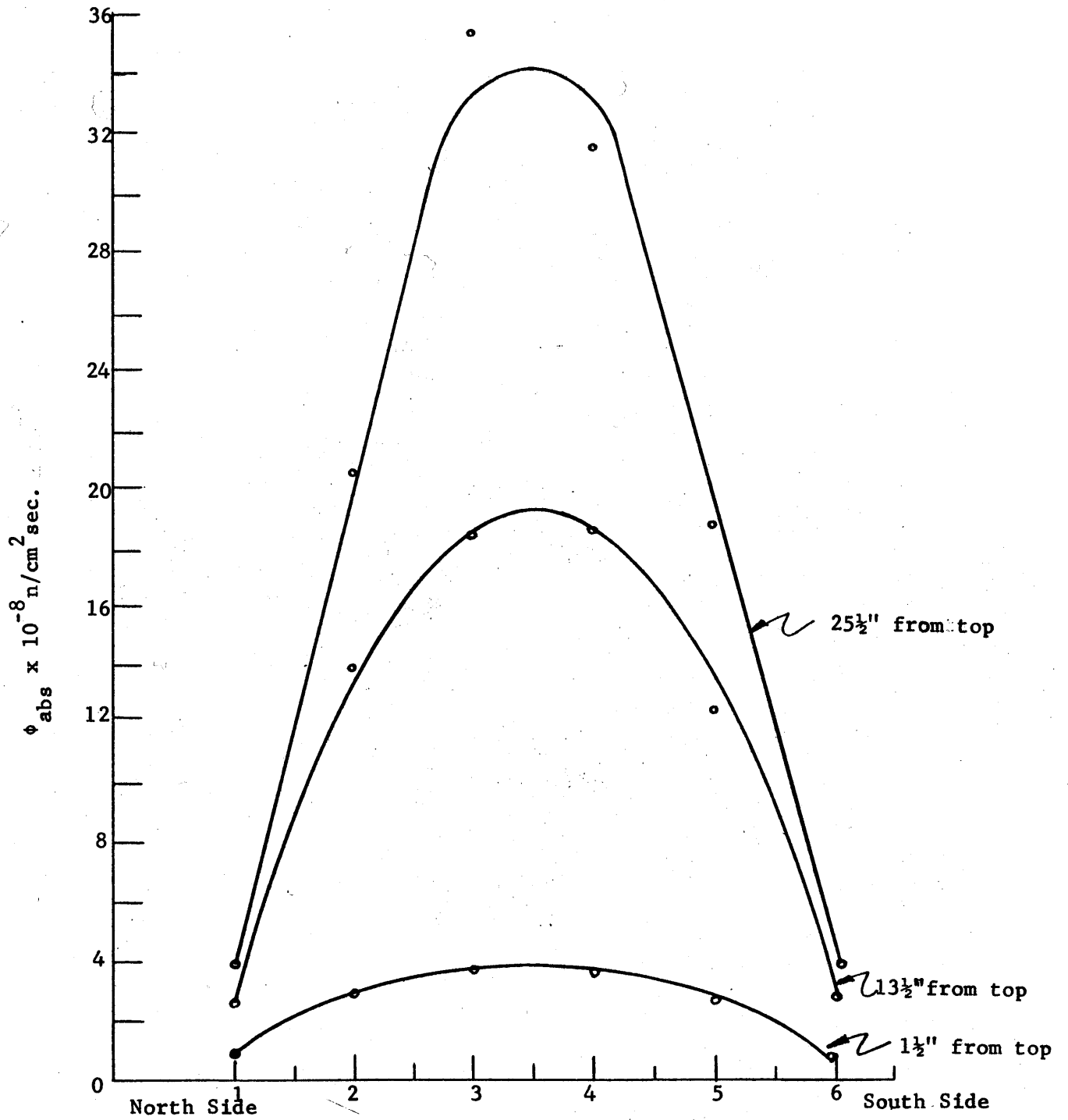


Figure #3.1a Horizontal Traverse Flux Distribution of Neutron Source (Experiment #1).

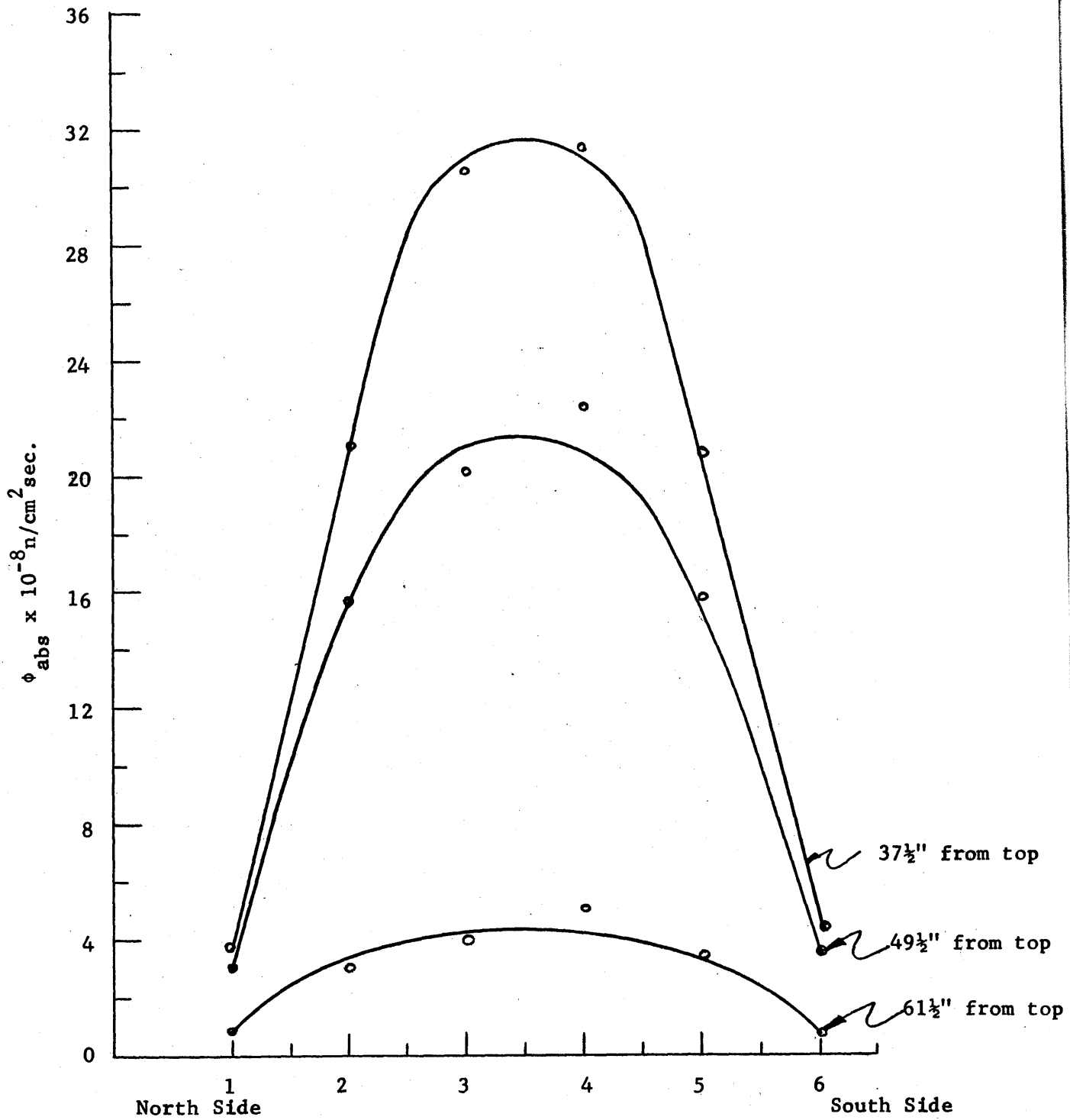


Figure E3.1b Horizontal Traverse of Flux Distribution of Neutron Source (Experiment #1)

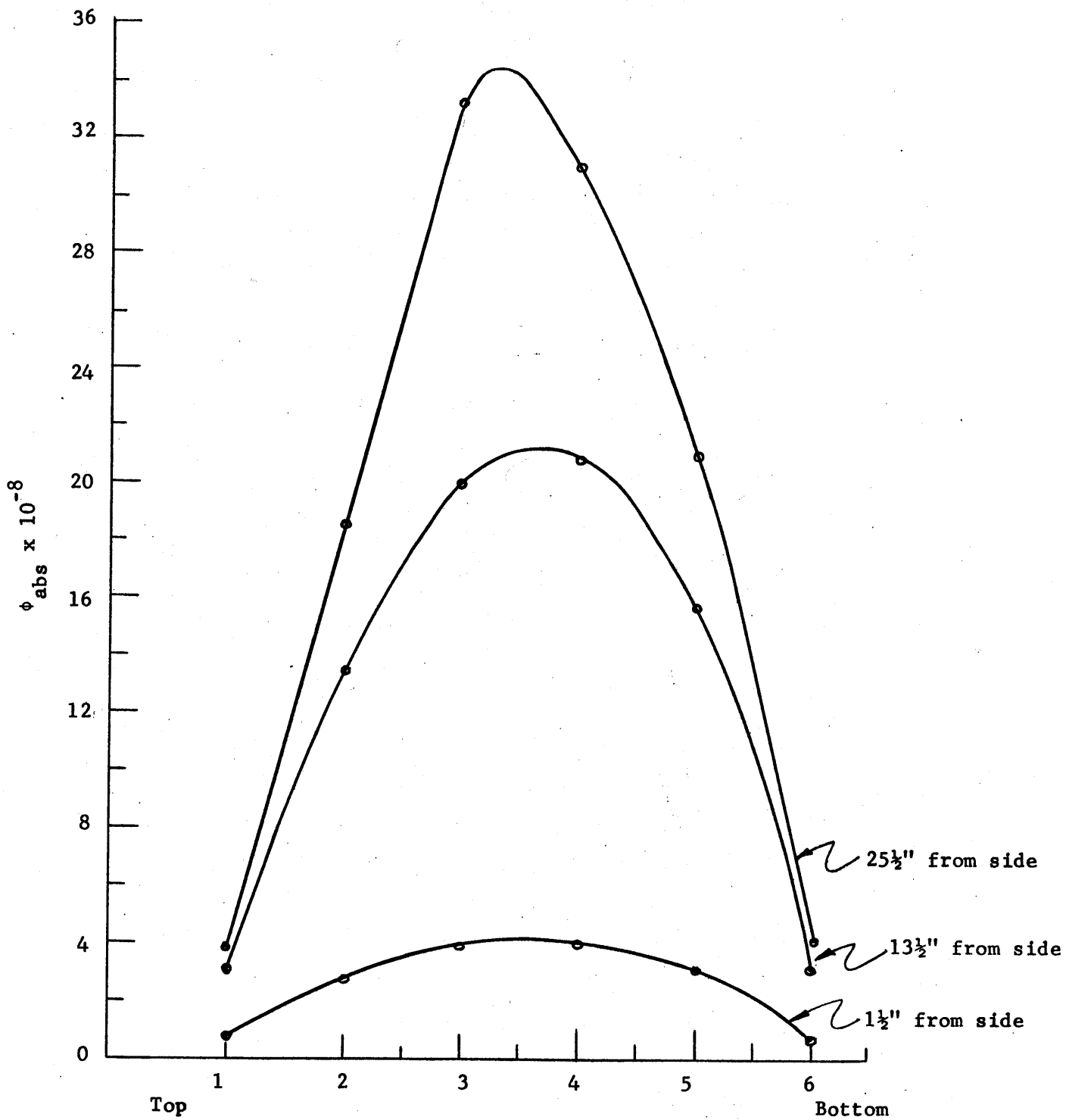


Figure E3.2 Vertical Traverse of Flux Distribution of Neutron Source (Experiment #1).

The values of ϕ_{abs} for the foils on the honeycomb in Experiments #2 through #13 are first plotted from the north to the south side of the honeycomb. In some cases, two sets of measurements were made for the same arrangement of the cavity assembly; the two sets of values of ϕ_{abs} are plotted together, as in Figure E3.3, which includes values of ϕ_{abs} from Experiments #10 and #11. A flux distribution symmetrical about the center line from the front to back edge of the honeycomb is drawn, and most of the values of the absolute flux lie within 1% of the plotted flux distribution. The number that appears just to the right of each curve indicates the distance (in inches) of the foils from the front edge of the honeycomb.

It seems likely that some of the discrepancies between the two values of ϕ_{abs} for the assembly are due to differences in the flux at a given point during the two irradiations. These differences may have been caused by small changes in the distribution of the neutron source which, in turn, were possibly caused by differences in the positions of the shim rods in the two experiments. There is no practical means of measuring small changes in the distribution of the neutron source during the irradiation. However, all but a few values of ϕ_{abs} lie close to the plotted distribution, so that the measured distribution should be accurate within the statistical errors of the values of ϕ_{abs} .

Next, the flux distribution is plotted from the front to the back edge of the honeycomb by using the value of ϕ_{abs} from the symmetrical flux distributions obtained by plotting the values of ϕ_{abs} from the north to the south side. The flux distribution, 6" from the center line, is plotted for all seven assemblies in Figure E3.4.

The flux distributions from the north side to the south side of the honeycomb, at 7" from the front edge and at 67" from the front edge are

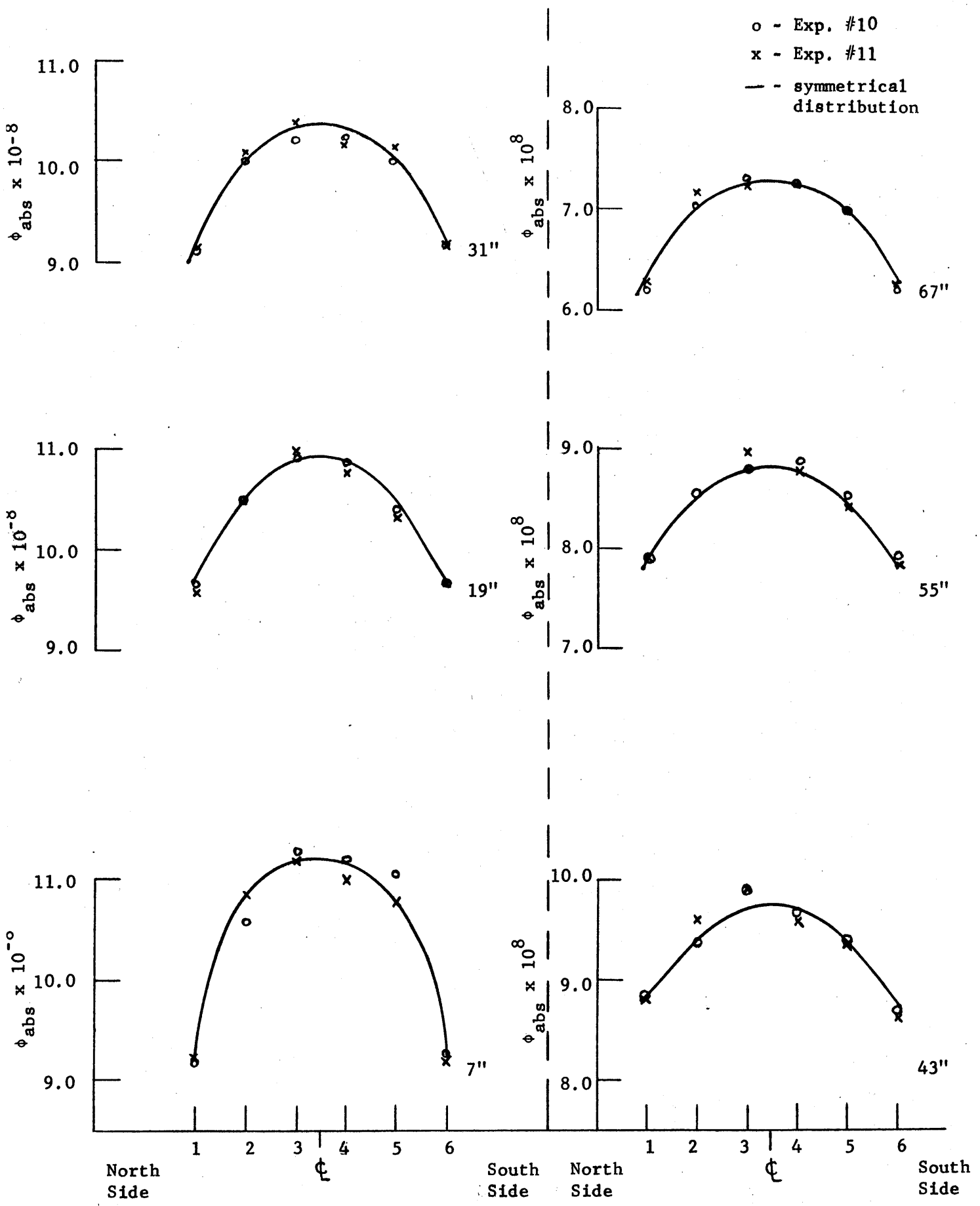


Figure E3.3 Symmetrical Flux Distribution Plotted from the Values of $\phi_{abs} \times 10^8$ for Experiments #10 and #11 on the Honeycomb.

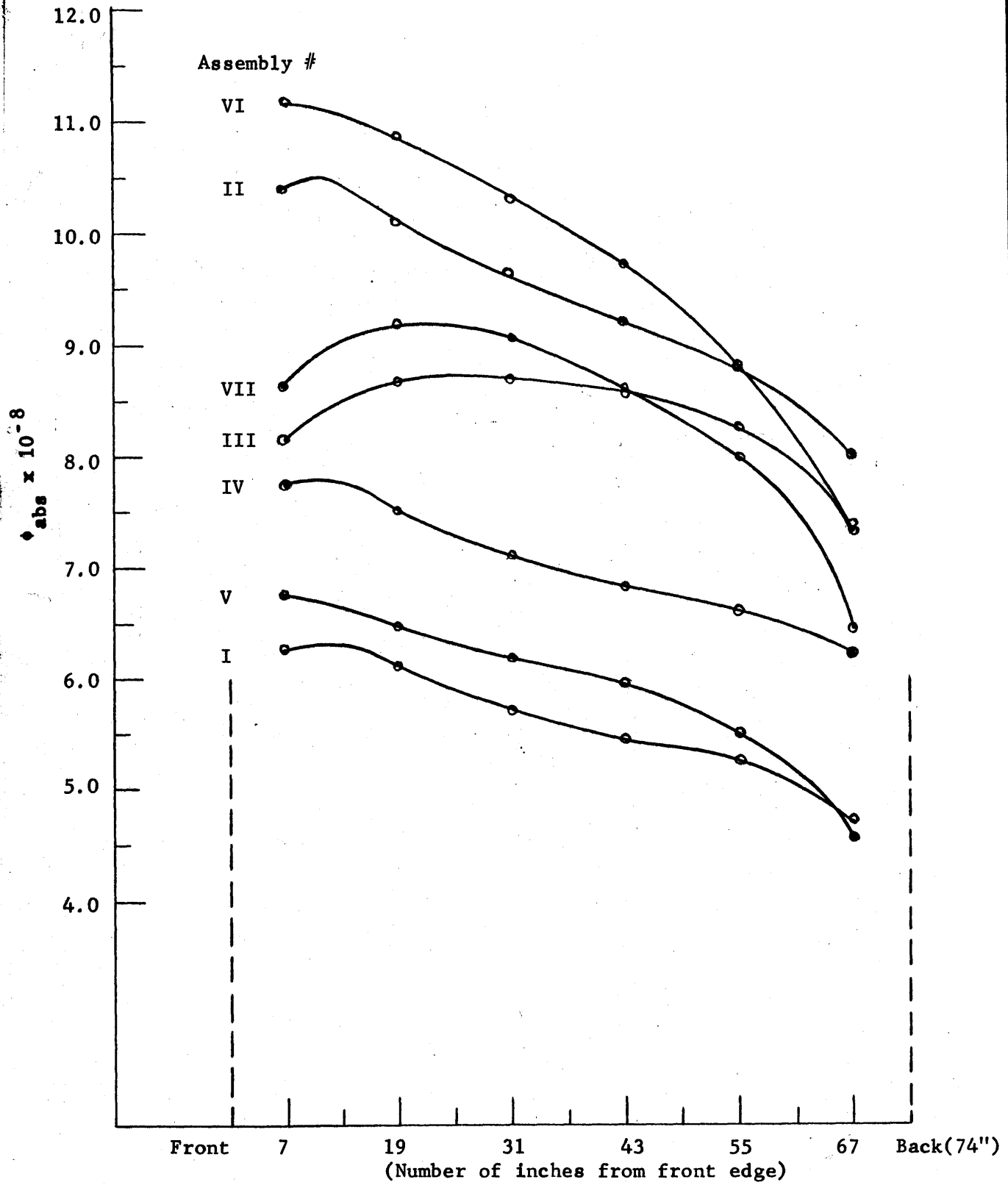


Figure E3.4 Flux Distribution on Honeycomb, 6" off Centerline for Assembly I through VII.

plotted for all seven assemblies in Figures E3.5 and E3.6, respectively.

It is of interest to compare the magnitude and the distribution of the flux obtained by the use of a cavity with the results that would be obtained if the cavity were filled with graphite. Figure E3.7 shows the cavity filled with graphite. The shaded area represents the graphite in Assembly I. In the representation of the solid graphite region, graphite was also considered to be added to the thermal column so that the graphite block has a constant cross-sectional area.

In general, for a finite block of graphite

$$\phi(x,y,z) = \phi_{oo} \cos \frac{\pi x}{a} \cos \frac{\pi y}{b} e^{-z/B_{11}} \left(1 - e^{-2(c-z)/B_{11}} \right), \quad (E3.5)$$

where

$$\frac{1}{L^2} = \frac{1}{B^2} - \frac{\pi^2}{a^2} - \frac{\pi^2}{b^2}.$$

The quantities a , b , and c are the extrapolated dimensions of the graphite on the x , y , and z directions, respectively. A value of 48 cm is used for diffusion length of graphite. The magnitude of the neutron source at the center of the thermal column face, ϕ_s , has been measured and is equal to 3.37×10^9 n/cm²sec (See Table E3.2). The magnitude of the flux, ϕ_o , at this point, when the graphite is placed in the cavity, is calculated from equation (E3.6).

$$\frac{\phi_o}{\phi_s} = \frac{\left[\phi_{oo} \cos \frac{\pi x}{a} \cos \frac{\pi y}{b} e^{-z/B_{11}} \left(1 - e^{-2(c-z)/B_{11}} \right) \right]_{\text{graphite}}}{\left[\phi_{oo} \cos \frac{\pi x}{a} \cos \frac{\pi y}{b} e^{-z/B_{11}} \left(1 - e^{-2(c-z)/B_{11}} \right) \right]_{\text{cavity}}} \quad (E3.6)$$

For the case of a cavity

$$\begin{aligned} x = 0, & \quad a = 63'' + 2(0.7\lambda_t), \\ y = 0, & \quad b = 63'' + 2(0.7\lambda_t), \\ z = z_o, & \quad c = 63'' + 0.7 \lambda_t, \end{aligned}$$

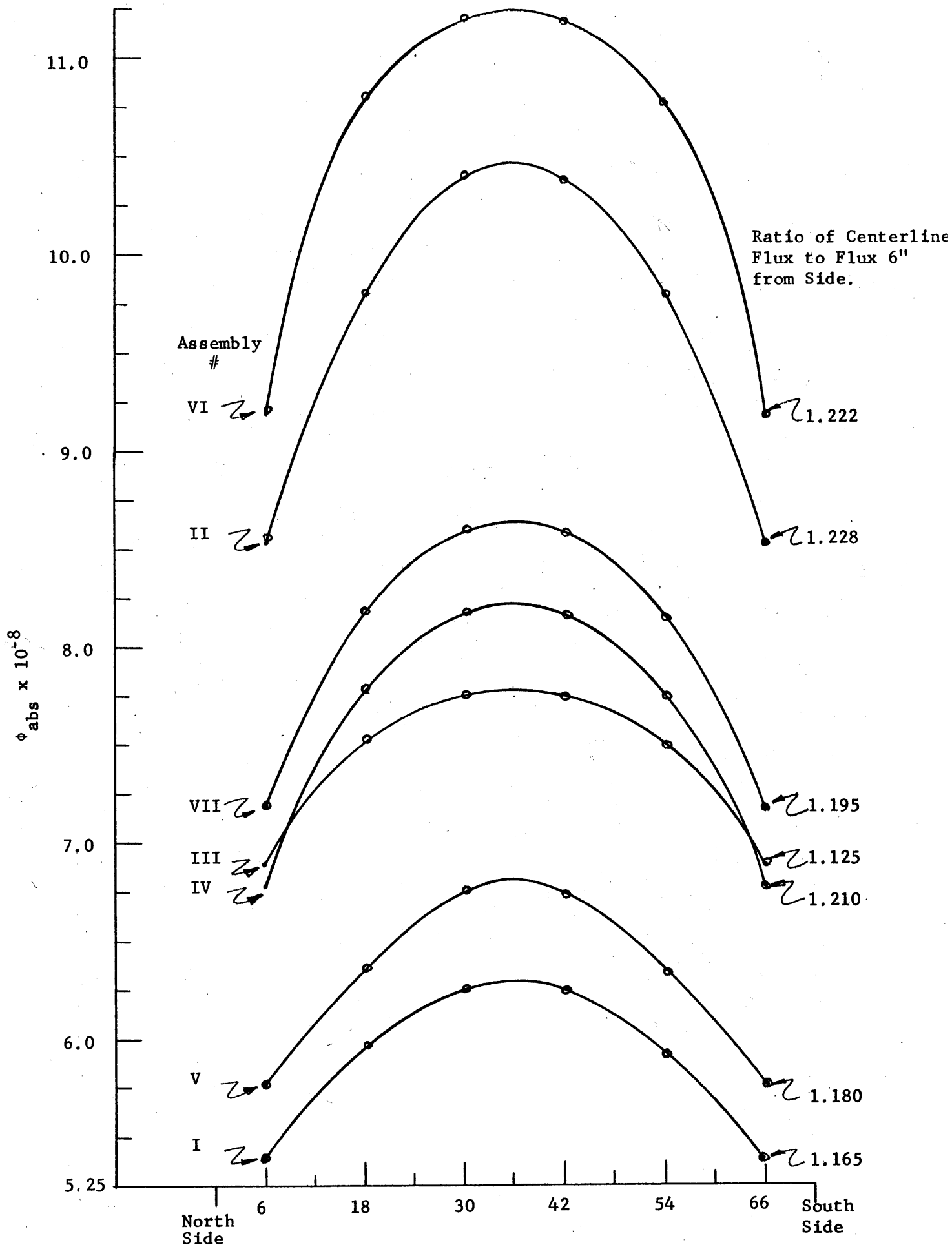


Figure E3.5 Flux Distribution on Honeycomb 7" from Front of Honeycomb for Assembly I and VII.

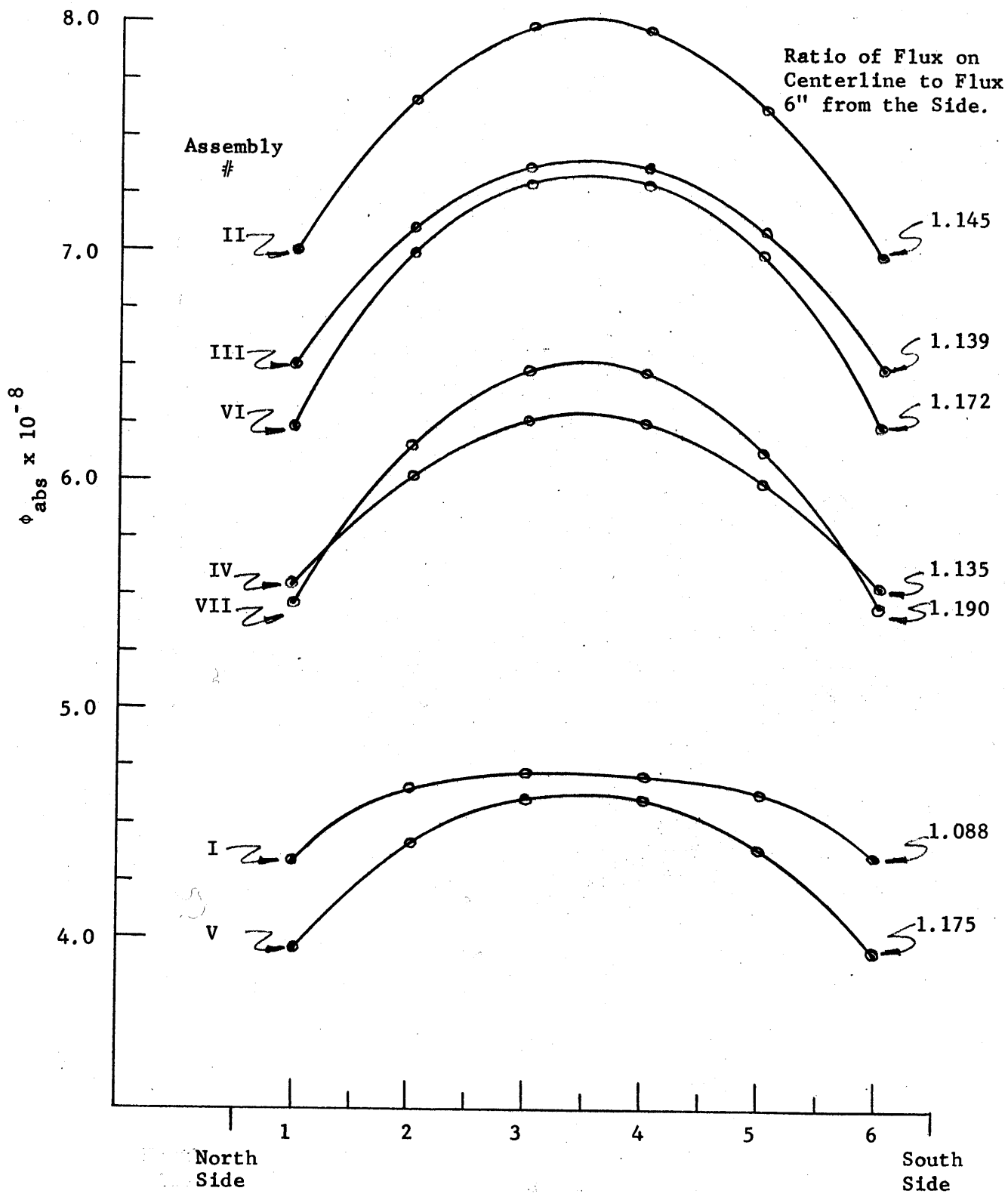


Figure E3.6 Flux Distribution on Honeycomb 67" from Front of Honeycomb for Assemblies I to VII.

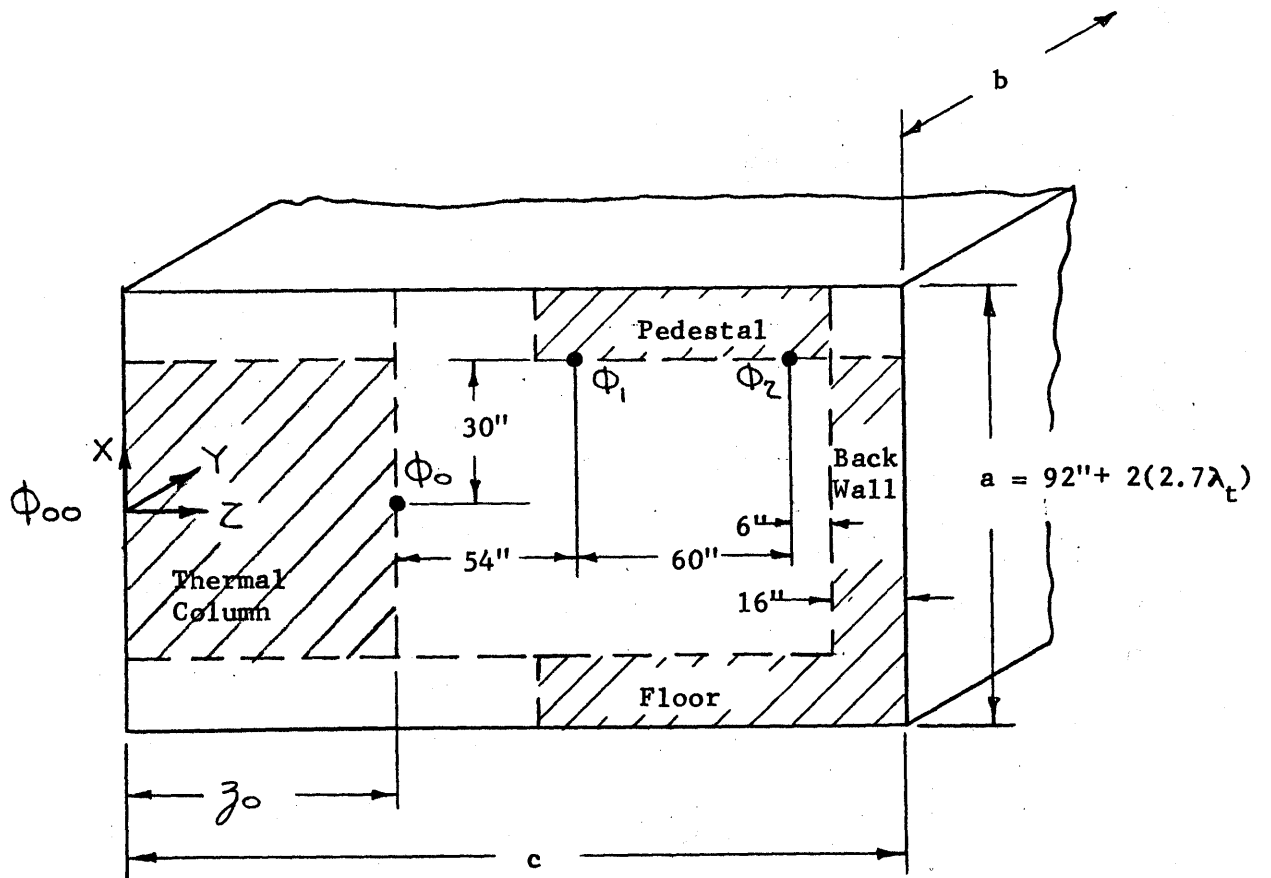


Figure E3.7 Vertical Section of the Graphite-Filled Cavity.

and for the graphite-filled cavity

$$\begin{aligned} x &= 0, & a &= 92'' + 2(0.7\lambda_t), \\ y &= 0, & b &= 92'' + 2(0.7\lambda_t), \\ z &= z_o, & c &= z_o + 136 + 0.7\lambda_t. \end{aligned}$$

Substituting these values in equation (E3.6), one obtains

$$\phi_o = 8.06 \phi_s = 2.72 \times 10^{10} \text{ n/cm}^2 \text{ sec.}$$

The flux, ϕ_1 , (see Figure E3.7) corresponds to the center line flux on the front of the honeycomb for the cavity assemblies. The value of ϕ_1/ϕ_o is calculated from equation (E3.7).

$$\phi_1/\phi_o = \cos \frac{\pi/x}{a} e^{-(z_1-z_o)/B_{11}} \frac{[1 - e^{-2(c-z_1)/B_{11}}]}{[1 - e^{-2(c-z_o)/B_{11}}]} \quad (\text{E3.7})$$

Substituting

$$\begin{aligned} y &= 0 \\ x &= 30'' \\ z_1 - z_o &= 54'' \\ c - z_1 &= 82'' + 0.7\lambda_t \\ c - z_o &= 136'' + 0.7\lambda_t \end{aligned}$$

into equation (E3.8) yields

$$\phi_1 = 0.0115 \phi_o = 3.12 \times 10^8 \text{ n/cm}^2 \text{ sec.}$$

The same procedure is used to calculate ϕ_2 , which corresponds to the flux on the back of the honeycomb for the cavity assemblies.

$$\phi_2 = 1.54 \times 10^{-4} \phi_o = 4.18 \times 10^6 \text{ n/cm}^2 \text{ sec.}$$

It can be seen from Figure E3.4 that the value of ϕ_1 is a factor of two smaller than any of the corresponding values of the flux in the cavity assemblies. The value of ϕ_2 is 100 times smaller than its corresponding value in the cavity assemblies.

Thus, the magnitude of the flux at the honeycomb is much greater when the cavity is used than it would be if the cavity were filled with graphite. The cavity also supplies neutrons with a distribution given approximately by a double cosine, while the distribution given by solid graphite would decrease approximately exponentially. Hence, both the magnitude and distribution of the flux are given more favorably by the cavity assembly.

Next, we consider in detail the effect of the geometrical and material arrangement of the cavity assembly on the magnitude and distribution of the neutron flux. We start with the flux distribution from the front to the back of the honeycomb. Two general characteristics of all of the cavity flux distributions are a higher value of the flux at the front than at the back edge of the honeycomb, and a larger gradient in the flux distribution near the back edge than at any other position. The higher value of the flux near the front edge is due to a greater contribution of the neutron source to this region than to the back edge, which is farther away. The large gradient in the flux distribution near the back edge is the result of neutron leakage from the back side of the pedestal. The effect of the leakage from the front side of the pedestal is compensated by the large contribution from the neutron source. Thus, the magnitude of the flux at a point on the honeycomb depends on the distance between the point and the edges of the pedestal, and between the point and the neutron source.

The effect of the inclined surface may be seen by comparing the flux distributions in Assemblies I and V, in Assemblies II and VI, and in Assemblies III and VII. In each case, the flux for the 45° cavity is higher at the front and lower at the back than the corresponding flux for the PARA cavity. Thus, the inclined surface of the 45° assemblies

produces a flux which has a greater magnitude, on the average, but a less symmetric distribution than the flux for the corresponding PARA assemblies.

The effect of the addition of the graphite frame and the tooth may be seen by comparing Assemblies I, II, and III for the PARA cavity, and Assemblies V, VI, and VII for the 45° cavity. The magnitude of the flux distribution is increased by a factor of about 1.7 by adding the graphite frame to Assemblies I and V. The neutrons reflected from the frame contributed only slightly more to the front edge than to the back edge in Assembly II. However, when the frame is added to Assembly V, the flux on the front part of the honeycomb is increased more than the flux on the back edge. The reason for this effect is that the additional flux on the inclined surface contributes more to the front than to the back of the honeycomb. This larger contribution to the front part of the honeycomb in Assembly V is shown by the fact that the flux curves for Assemblies II and VI cross each other closer to the front edge than do the flux distributions for Assemblies I and V.

When the tooth is added to the PARA and 45° cavities (Assemblies III and VII), the flux distribution from front to back becomes more symmetrical. The tooth reduces the number of source neutrons that strike the front part of the honeycomb from the thermal column face. The flux distribution of Assembly III may be described as a "tilted", symmetrical flux distribution with the back edge only about 10% lower than the front edge. Such a distribution should be useful as a source for an exponential assembly. The inclined plane in Assembly VII increases the distribution more at the front and thus produces a more "tilted", symmetrical distribution.

In Assembly VI, only the floor of the door space is covered with graphite, with the result that the magnitude of the flux lies between

those of Assemblies I and II. In addition, the pedestal is extended at the back, resulting in a smaller gradient of the flux near the back edge.

Figures E3.5 and E3.6 show that the flux distribution from the north side to the south side of the honeycomb is about the same for all of the assemblies; the magnitude of this flux has been already discussed. The shape of the flux distribution depends, in part, on the distribution of the neutron source ($\cos x \cos y$) and on the neutron leakage out of the sides of the square pedestal. Thus, all of the distributions are similar to a chopped-cosine distribution. In both figures the value of the ratio of the flux on the center line to the flux 6" from the side edge is shown at the right of the corresponding curve. The distribution of the flux from side to side, at 7" from the front edge, is not affected by the inclined surface, as can be seen by comparing the flux distributions in Assemblies III and VII. The values of the flux ratios are approximately the same for each pair of curves. A slightly higher ratio for the frame assemblies (I and VII) is due to the reflection of source neutrons by the frame. As would be expected, the lowest value of the ratio is that for Assembly IV, in which the pedestal was extended on the sides; since the pedestal is larger, there is less leakage and a flatter distribution results.

The flux distributions in Figure E3.6, at 67 inches from the front edge, have a smaller ratio of the flux on the center line to the flux 6" from the edge. This result is expected because the neutron source contributes a smaller fraction of the total flux and thus has a smaller influence on the flux distribution. For example, a large fraction of the neutrons in Assembly I comes from the back wall and hence does not show a strong influence of the distribution of the source neutrons. The frame

assemblies still have a slightly higher ratio than the bare assemblies, as they did in Figure E3.5.

A question of interest is how much of the flux incident on the honeycomb is lost in reaching the fundamental mode as the neutrons pass upward in the pedestal. The flux distributions from the front to the back, 6" from the center line, of the honeycomb and of the two layers of the pedestal are plotted for Assemblies II and III in Figures E3.8 and E3.9, respectively. As would be expected from the distribution on the honeycomb, the flux distribution in the upper layer of the pedestal of Assembly II is still slightly higher near the front. Although the magnitude of the flux on the honeycomb of Assembly II is, on the average, about 10% greater than that of Assembly III, most of this additional flux is lost in reaching the fundamental mode.

The flux distribution in the upper layer of the pedestal of Assembly III was fitted to a double cosine function. The equation for this function is:

$$\phi(x,y) = 2.15 \times 10^8 \cos \frac{\pi x}{100} \cos \frac{\pi y}{100}, \quad (\text{E3.8})$$

where the x coordinate defines the distance from the middle of the pedestal layer to the front and back boundaries, in inches, and the y coordinate defines the distance from the middle to the north or south boundaries of the pedestal, in inches.

The curves for $\phi(6'',y)$ and $\phi(x,6'')$ are drawn in Figures E3.10a and E3.10b, respectively, together with the corresponding values of ϕ_{abs} in the upper layer of the pedestal for Assembly III.

From Figure E3.10 it is evident that the distribution of the flux in the pedestal is well represented by the double cosine functions obtained

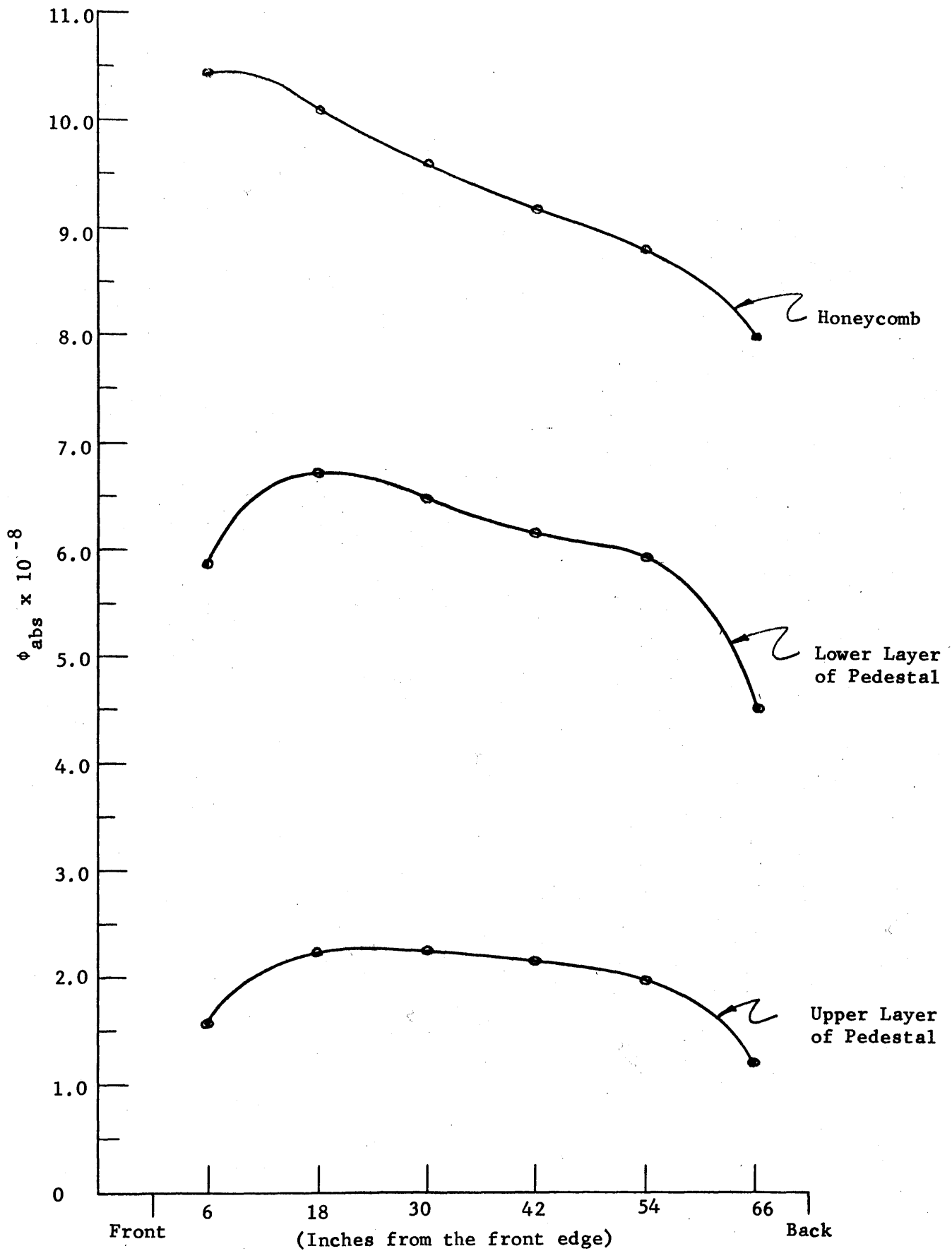


Figure E3.8 Flux Distribution for Assembly II from Front to Back, 6" off Centerline.

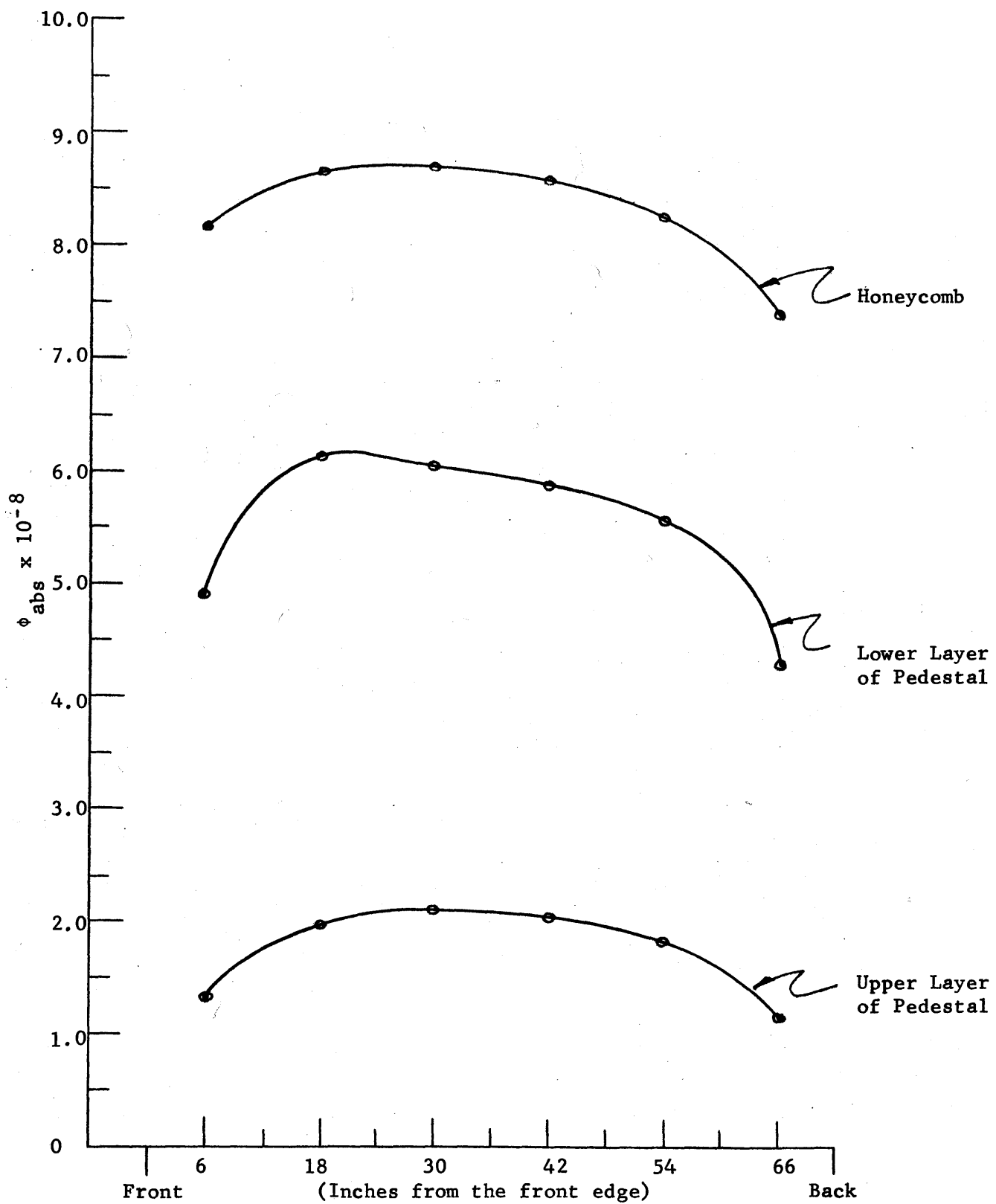


Figure E3.9 Flux Distribution for Assembly III from Front to Back, 6" off Centerline.

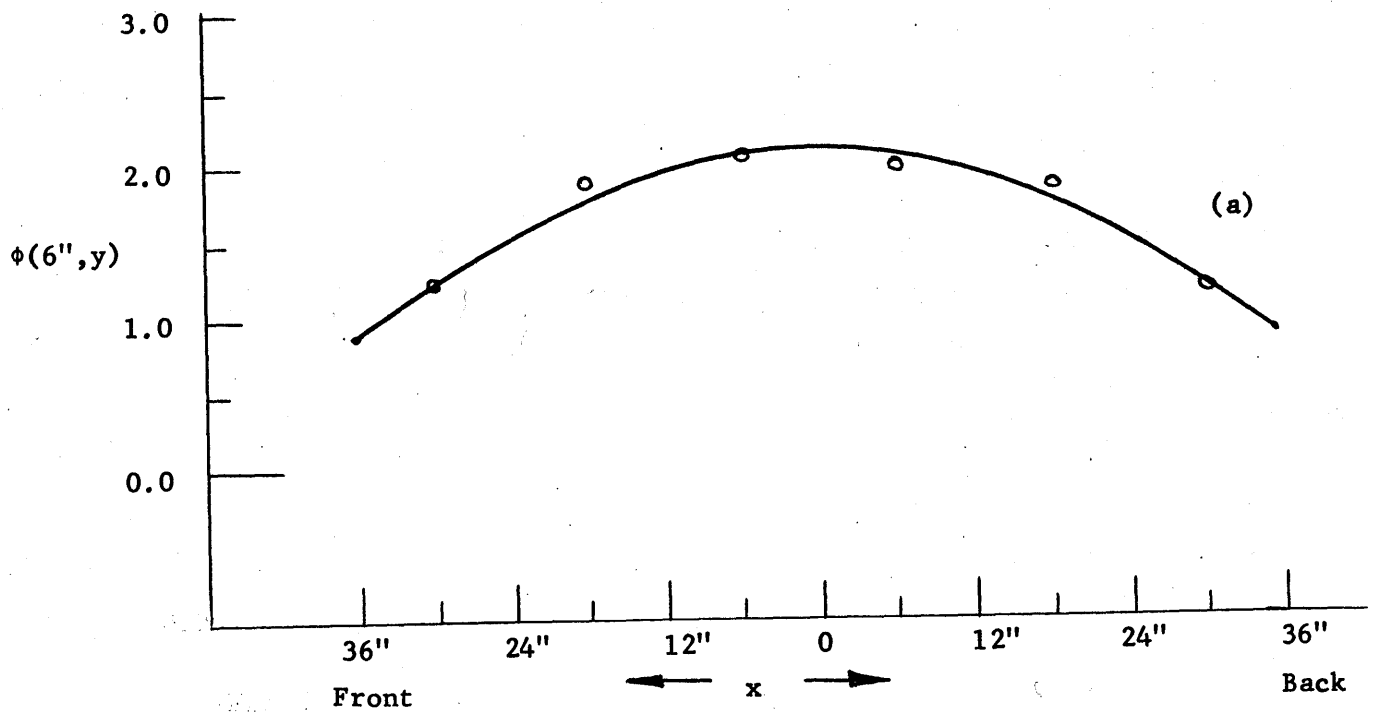
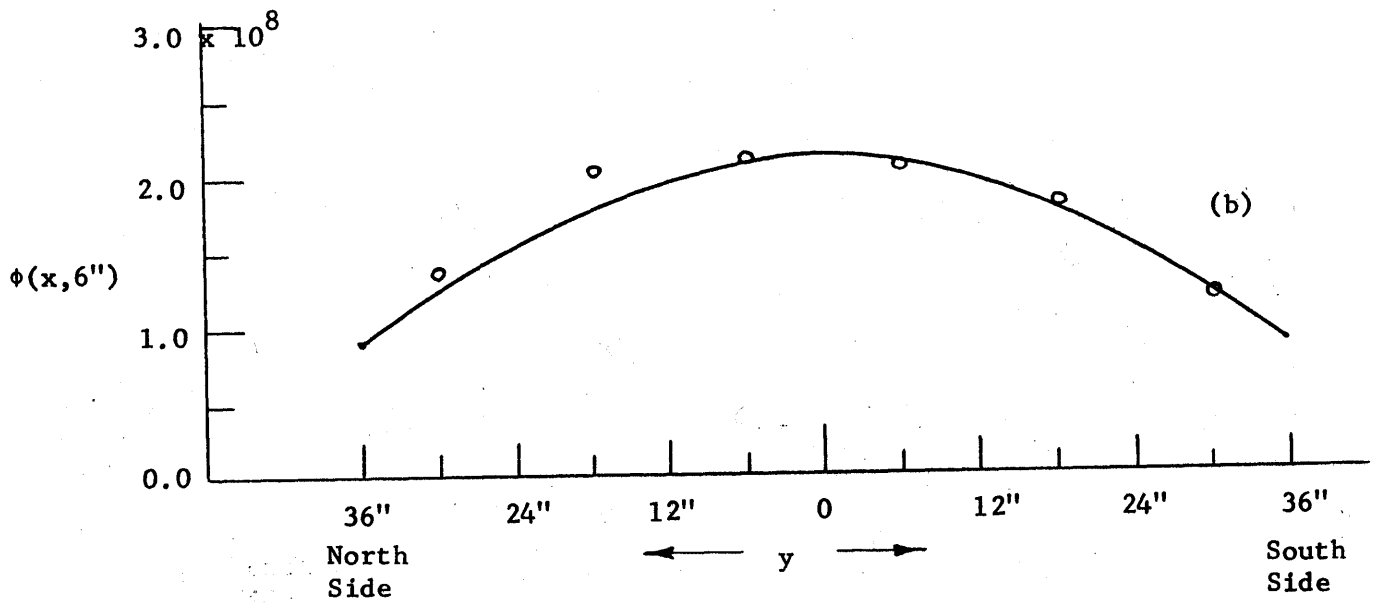


Figure E3.10 Fitting the Values of ϕ_{abs} in the Upper Layer of the Pedestal in Assembly III to the Cosine Curve, $\phi(x,y)$. The circles represent the values of ϕ_{abs} .

from equation (E3.8). Such a flux distribution is suitable for supplying neutrons to an exponential assembly whose fundamental mode is defined by a function of the form, $\cos x \cos y$.

The values of the absolute flux on all surfaces of Assembly II, obtained in Experiment #14, are shown in Table E3.35. The edge labeled "front" in the drawings is the edge closest to the thermal column face. The absolute flux has been normalized to agree with the results from Experiment #2 because of the flux depression in the cavity due to the foils, but the relative distribution on a given surface should not be seriously affected by the depression of the flux in the cavity.

Two general observations may be made from these results. First, the flux distribution is symmetrical about the vertical mid-plane of the cavity assembly. Second, the flux is almost flat on the floor of the cavity because the back and side walls reduce the number of neutrons leaking from the side and back edges of the floor. The same condition exists on the side and back walls. The neutron flux decreases less rapidly near the bottoms of the walls than near the tops, because the graphite floor reduces the leakage from the bottoms of the walls.

The values of ϕ_{abs} for the three arrays of foils irradiated in the cavity itself (Experiment #15) are given in Table E3.36. The greatest and smallest values of the flux differ by only 15% in each of the arrays. However, the influence of the distribution of the source neutrons is seen in the fact that the flux is greatest at the middle of the array and smallest on the outside of the array. The foils whose surfaces faced the thermal column usually had a slightly higher activity. From these data, it is concluded that magnitude of the flux in the cavity itself is fairly uniform, and that the angular distribution of the flux is influenced by

the source neutrons emitted from the thermal column face.

The practicality of extending and modifying the reactor neutron source has been established by these experimental results. From the seven arrangements of the cavity assembly, it is seen that a considerable variation in the magnitude and distribution of the extended source can be obtained by varying the geometrical arrangement of the assembly.

Table E3.2

The Values of $\phi_{abs} \times 10^{-8}$ Measured on the Face of the Thermal Column

Experiment #1
 E(rel) = 1.000
 N = 25.000
 Power = 40 kw

Top

| | | | | | |
|-------|--------|--------|--------|--------|-------|
| 0.841 | 3.024 | 3.745 | 3.622 | 2.727 | 0.709 |
| 2.747 | 14.026 | 18.451 | 18.733 | 12.533 | 2.809 |
| 3.890 | 20.644 | 35.596 | 31.605 | 18.788 | 3.829 |
| 3.810 | 21.030 | 30.592 | 31.411 | 20.778 | 4.160 |
| 3.110 | 15.606 | 20.176 | 22.402 | 15.848 | 3.381 |
| 0.807 | 3.067 | 3.960 | 5.091 | 3.420 | 0.856 |

North
Side

South
Side

1½"

12"

12"

12"

12"

12"

1½"

Bottom

1½"

12"

12"

12"

12"

12"

1½"

Table E3.3

The Value of $\phi_{abs} \times 10^{-8}$ Measured on the Honeycomb in Assembly I

Experiment #2
 E(rel) = 1.009
 N = 46.80
 Power = 20 kw

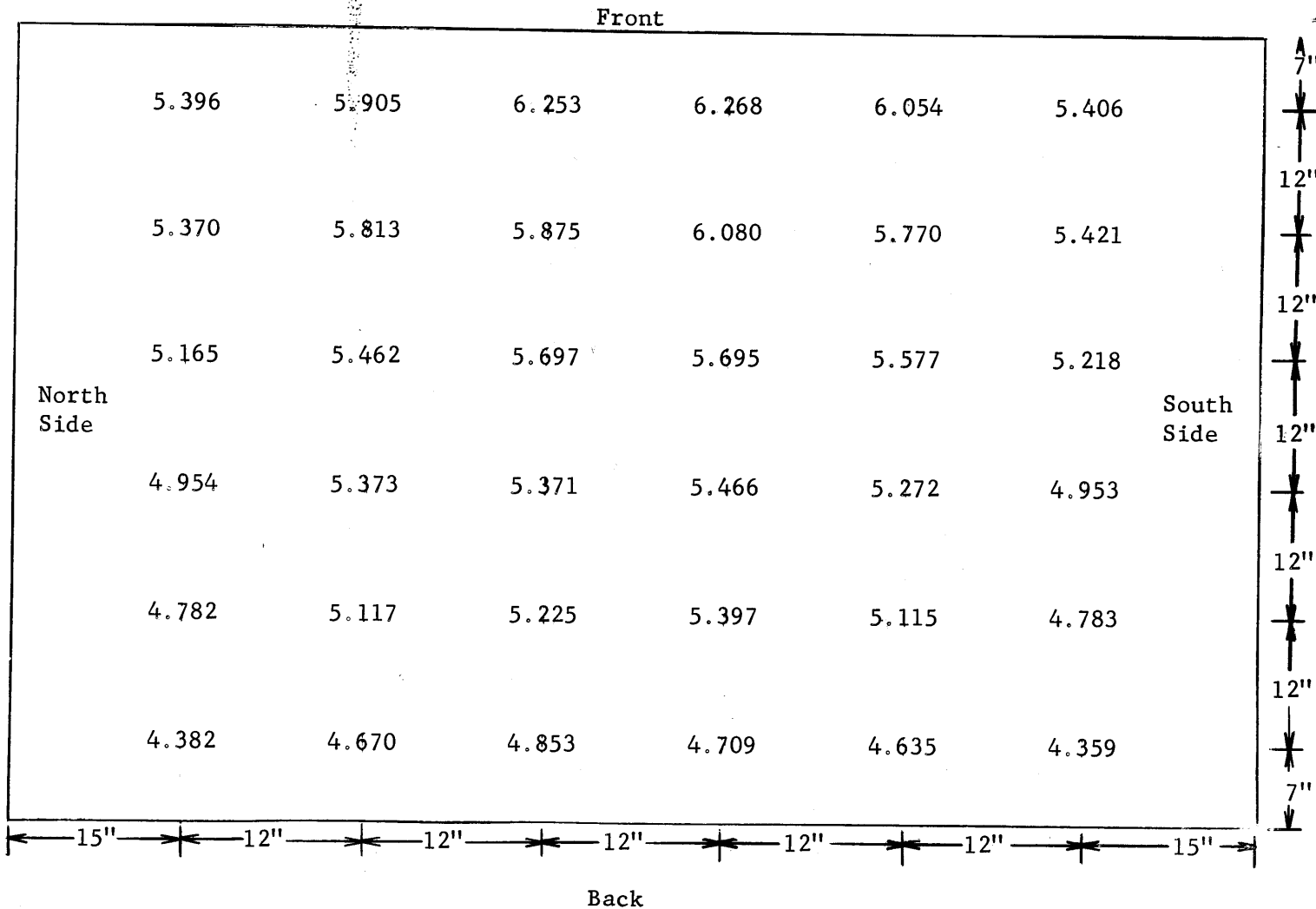


Table E3.4

The Values of $\phi_{abs} \times 10^{-8}$ Measured on the Honeycomb in Assembly II

| | | Front | | | | | | |
|--|------------|-------|--------|--------|--------|-------|-------|-----|
| Experiment #3 E(rel) = 0.9910 N = 24.77 Power = 40 kw | | 8.575 | 10.000 | 10.477 | 10.416 | 9.772 | 8.560 | 4" |
| | | | | | | | | 12" |
| | | 8.914 | 9.892 | 10.089 | 10.047 | 9.607 | 8.914 | 12" |
| | | | | | | | | 12" |
| | North Side | 8.415 | 9.280 | 9.662 | 9.501 | 9.207 | 8.525 | 12" |
| | | 8.354 | 8.973 | 9.202 | 9.032 | 8.907 | 8.268 | 12" |
| | | 7.873 | 8.570 | 8.753 | 8.895 | 8.757 | 7.853 | 12" |
| | 6.998 | 7.735 | 7.926 | 7.976 | 7.638 | 7.042 | 12" | |
| | | | | | | | 7" | |
| | | 15" | 12" | 12" | 12" | 12" | 12" | 15" |
| | | Back | | | | | | |

Table E3.6

The Values of $\phi_{abs} \times 10^{-8}$ Measured in the Upper Layer of the Pedestal in Assembly II

Experiment #3
 E(rel) = 0.984
 N = 24.77
 Power = 40 kw

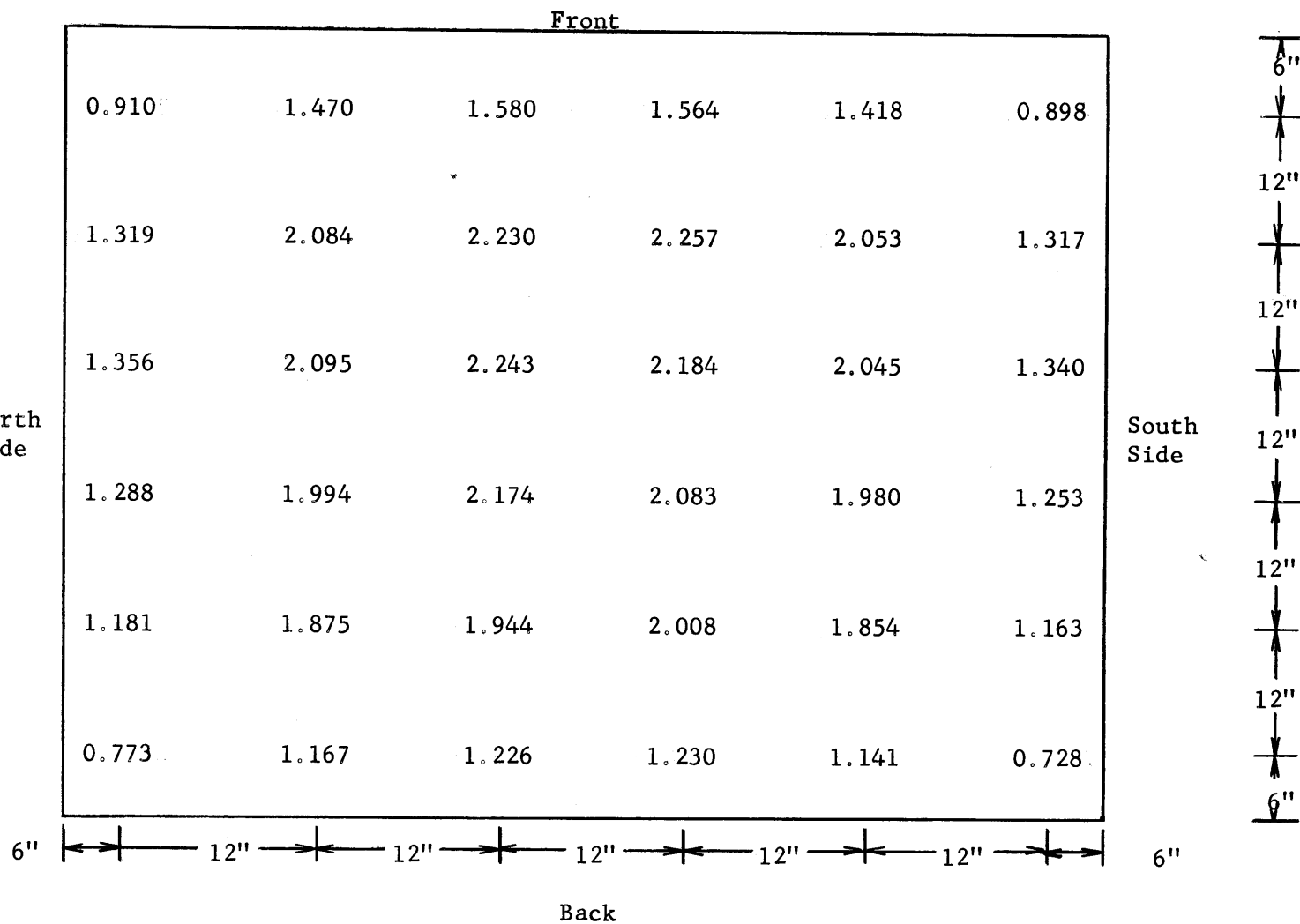


Table E3.7

The Value of $\phi_{abs} \times 10^{-8}$ Measured on the Honeycomb in Assembly II with the Pedestal Extended in the Back

| | | Front | | | | | | |
|---|------------|------------|-------|--------|--------|-------|-------|-----|
| Experiment #4 E(rel) = 1.001 N = 25.25 Power = 40 kw | | 8.607 | 9.832 | 10.499 | 10.384 | 9.747 | 8.499 | 7" |
| | | | | | | | | 12" |
| | | 9.078 | 9.807 | 10.122 | 10.075 | 9.628 | 8.924 | 12" |
| | | | | | | | | 12" |
| | North Side | 8.687 | 9.382 | 9.733 | 9.730 | 9.394 | 8.650 | 12" |
| | | 8.388 | 9.075 | 9.368 | 9.269 | 8.972 | 8.307 | 12" |
| | | 7.921 | 8.512 | 8.772 | 9.118 | 8.809 | 8.172 | 12" |
| | 7.392 | 8.213 | 8.291 | 8.374 | 8.161 | 7.473 | 12" | |
| | | | | | | | 7" | |
| | | 15" | 12" | 12" | 12" | 12" | 12" | 15" |
| | | Back | | | | | | |
| | | South Side | | | | | | |

Table E3.8

The Values of $\phi_{abs} \times 10^{-8}$ in the Lower Layer of the Pedestal on Assembly II
with the Pedestal Extended in the Back

Experiment #2
E(rel) = 0.991
N = 25.25
Power = 40 kw

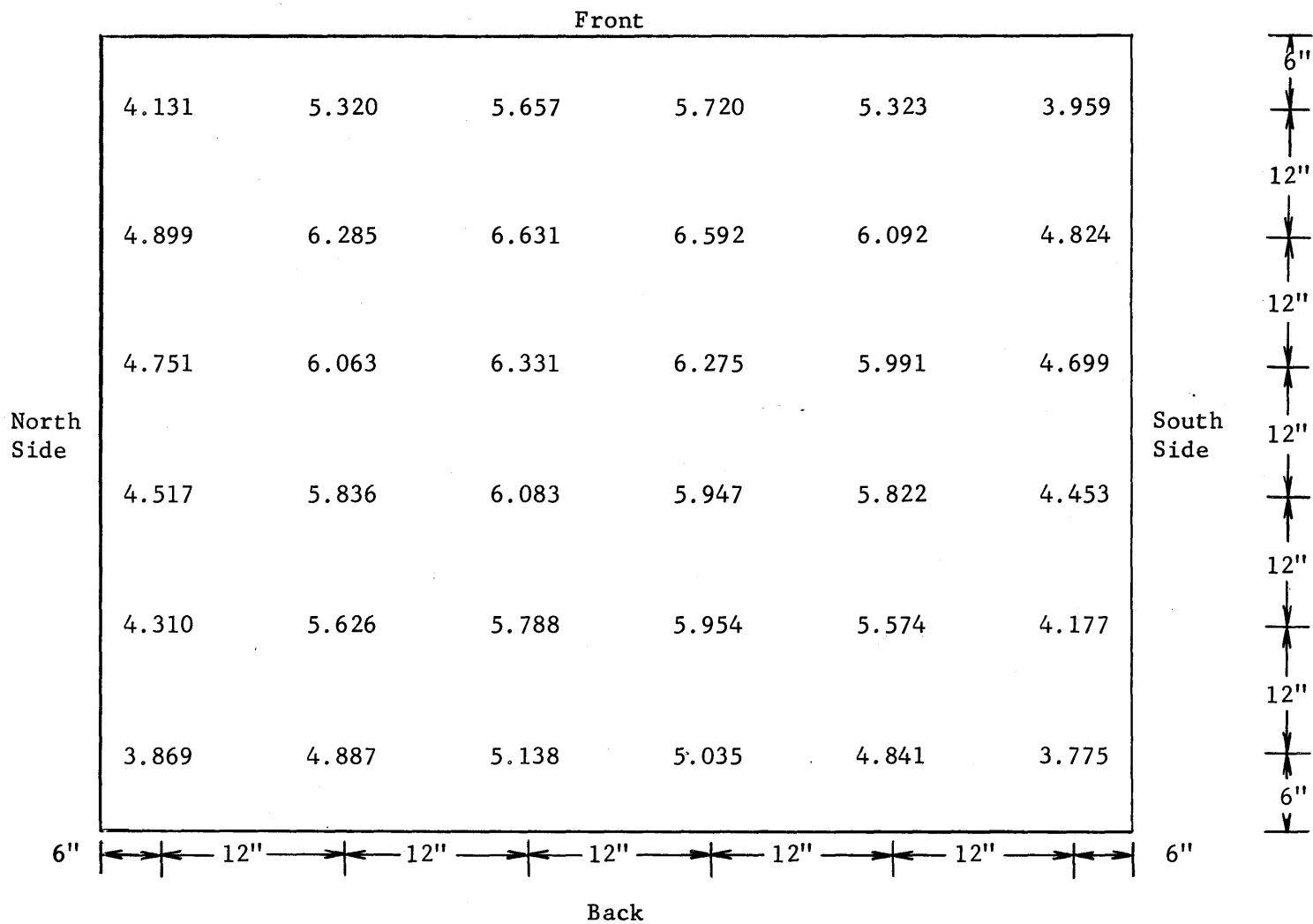


Table E3.9

The Values of $\phi_{abs} \times 10^{-8}$ in the Upper Layer of the Pedestal in Assembly II
with the Pedestal Extended in the Back

Experiment #4
 E(rel) = 0.998
 N = 25.25
 Power = 40 kw

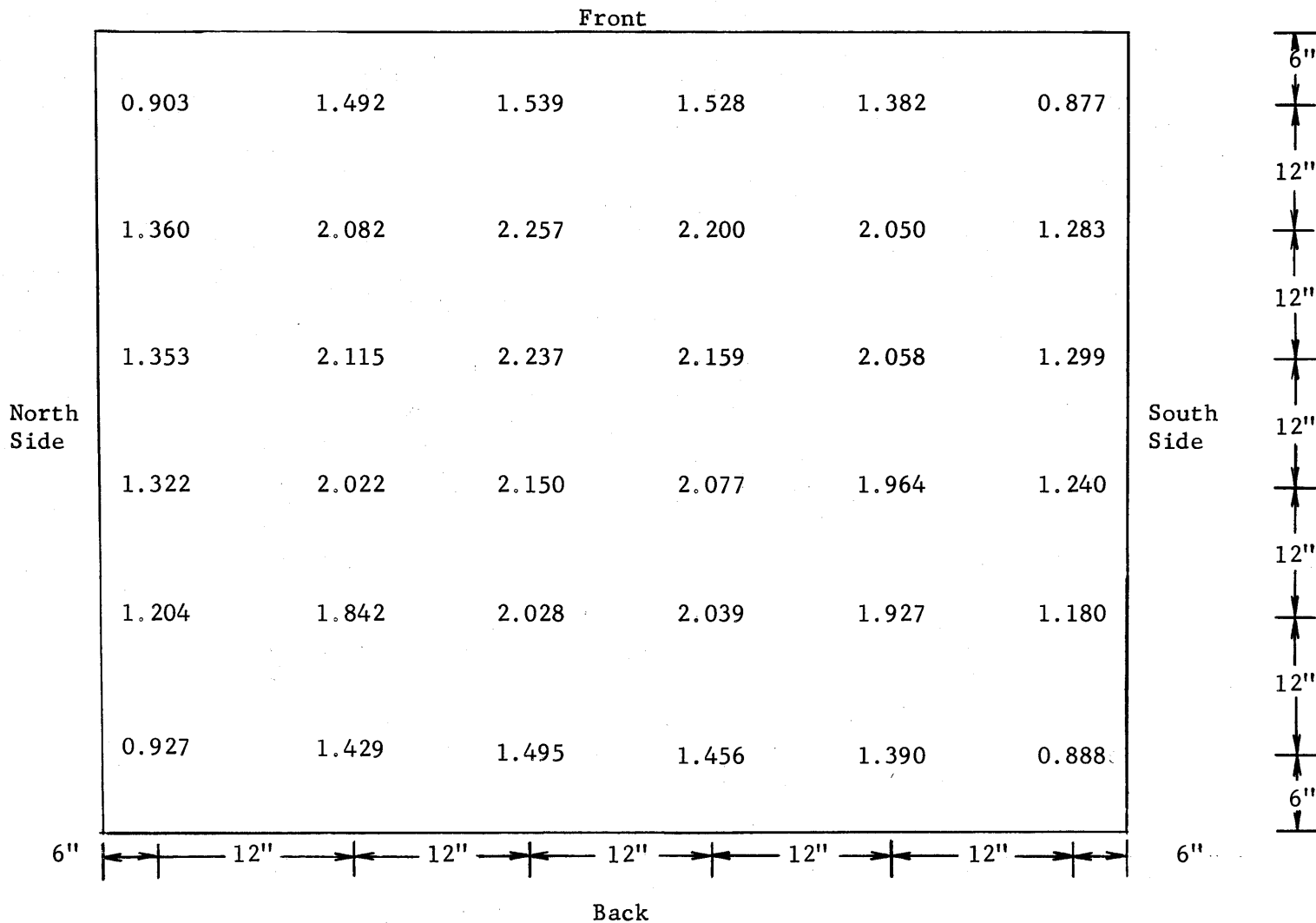


Table E3.10

The Values of $\phi_{abs} \times 10^{-8}$ Measured on the Honeycomb of Assembly III

Experiment #5
 E(rel) = 1.004
 N = 28.23
 Power = 40 kw

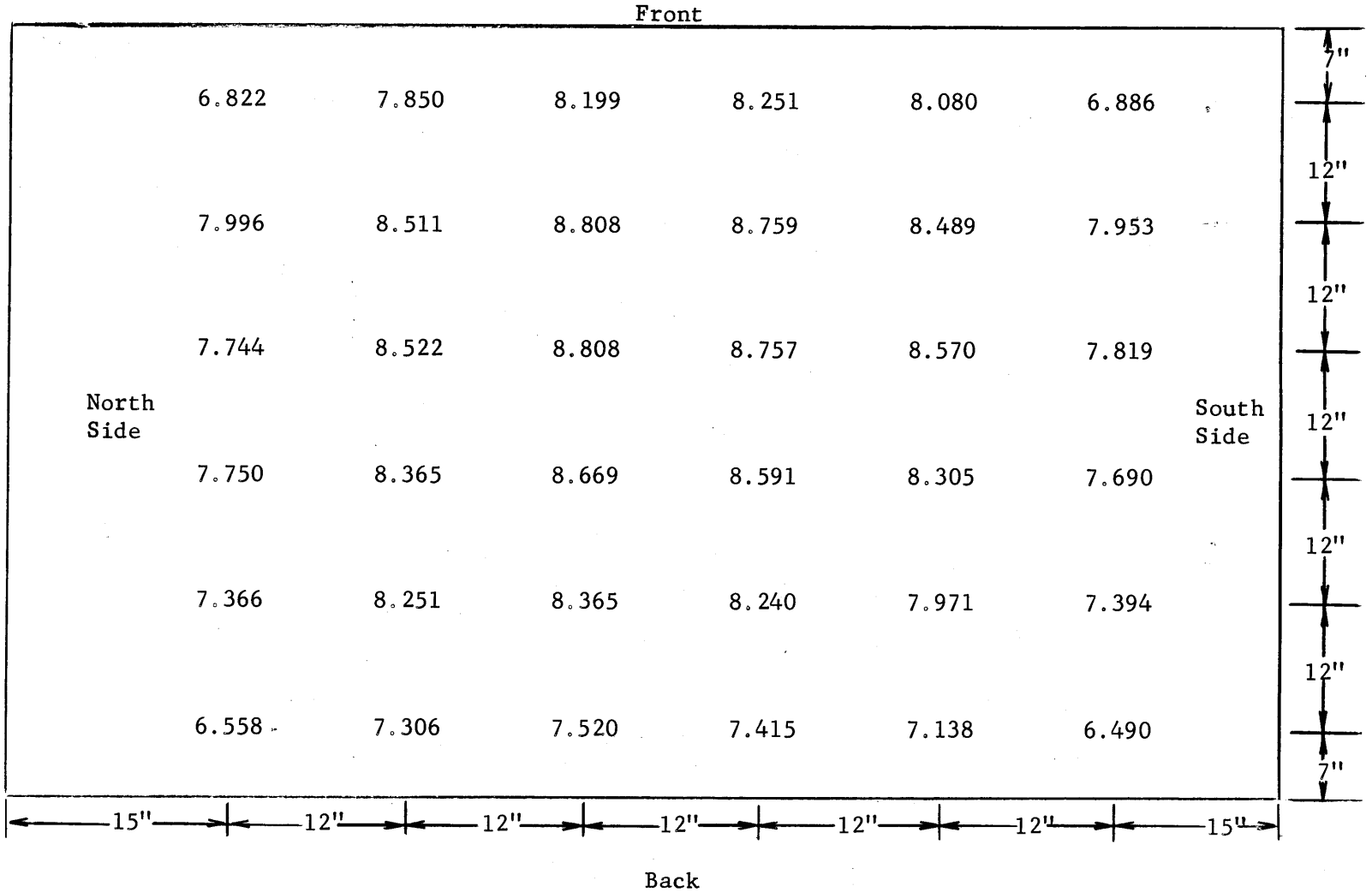


Table E3.11

The Values of $\phi_{abs} \times 10^{-8}$ Measured in the Lower Layer of the Pedestal in Assembly III

57

Experiment #5
 E(rel) = 1.0107
 N = 28.23
 Power = 40 kw

North
Side

Front

| | | | | | |
|-------|-------|-------|-------|-------|-------|
| 3.590 | 4.583 | 4.845 | 4.937 | 4.747 | 3.449 |
| 4.611 | 5.724 | 6.129 | 6.166 | 5.755 | 4.420 |
| 4.466 | 5.856 | 6.034 | 6.012 | 5.758 | 4.511 |
| 4.424 | 5.722 | 5.920 | 5.793 | 5.526 | 4.316 |
| 4.212 | 5.456 | 5.629 | 5.525 | 5.285 | 4.018 |
| 3.199 | 4.077 | 4.267 | 4.150 | 4.042 | 3.126 |

South
Side

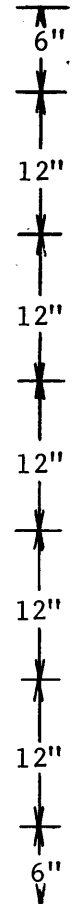
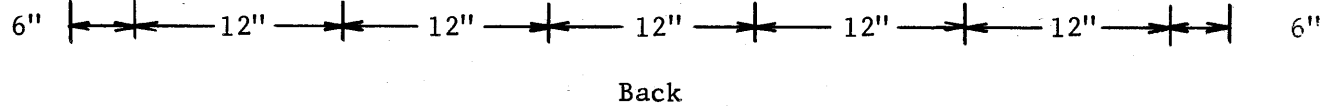


Table E3.13

The Values of $\phi_{abs} \times 10^{-8}$ Measured on the Honeycomb in Assembly III

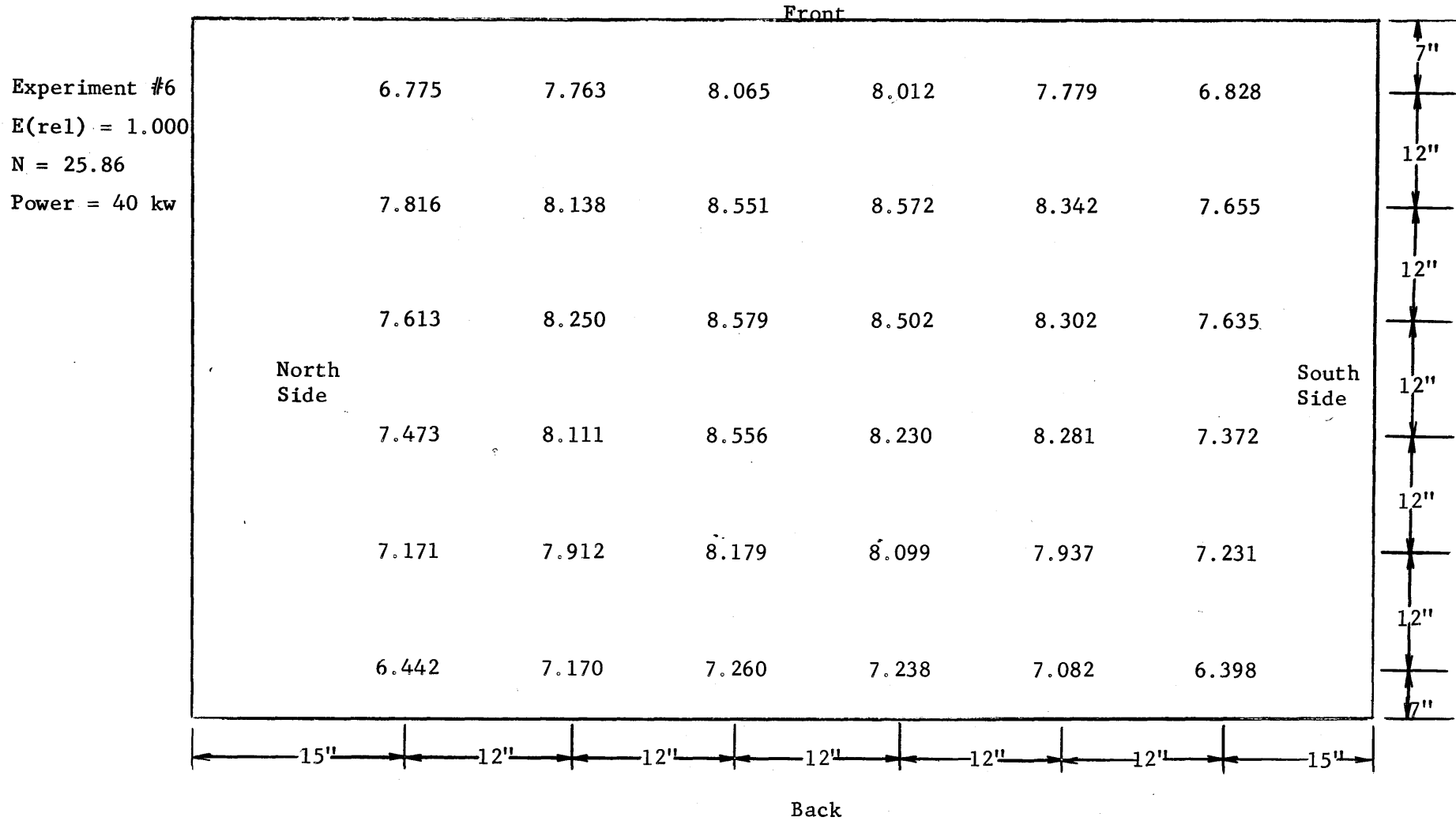


Table E3.15

The Values of $\phi_{abs} \times 10^{-8}$ Measured in the Lower Layers of the Pedestal in Assembly IV

Experiment #7
 E(rel) = 1.001
 N = 25.76
 Power = 40 kw

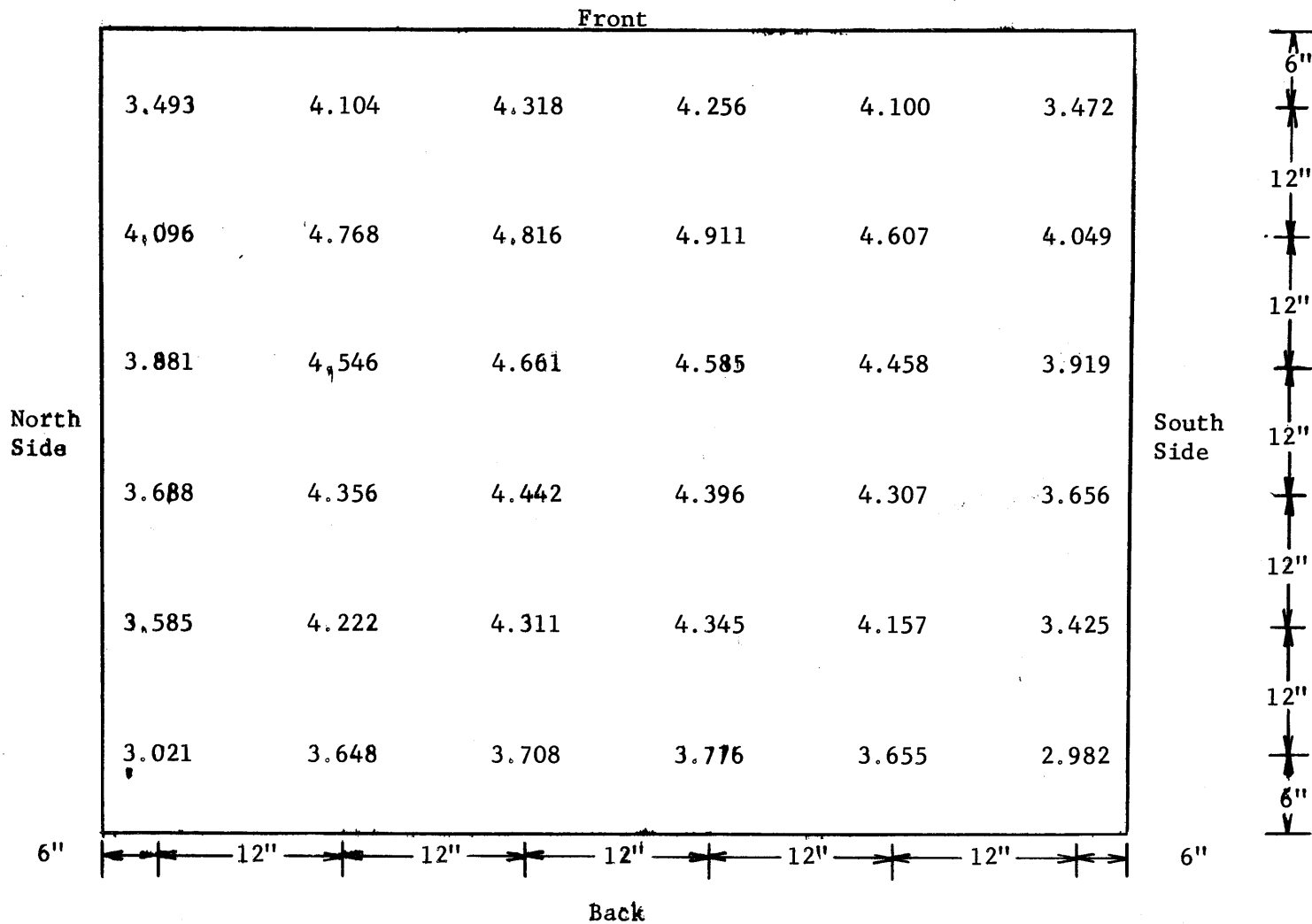


Table E3.16

The Values of $\phi_{abs} \times 10^{-8}$ Measured in the Upper Layer of the Pedestal in Assembly IV

Experiment #7
 E(rel) = 0.9973
 N = 25.76
 Power = 40 kw

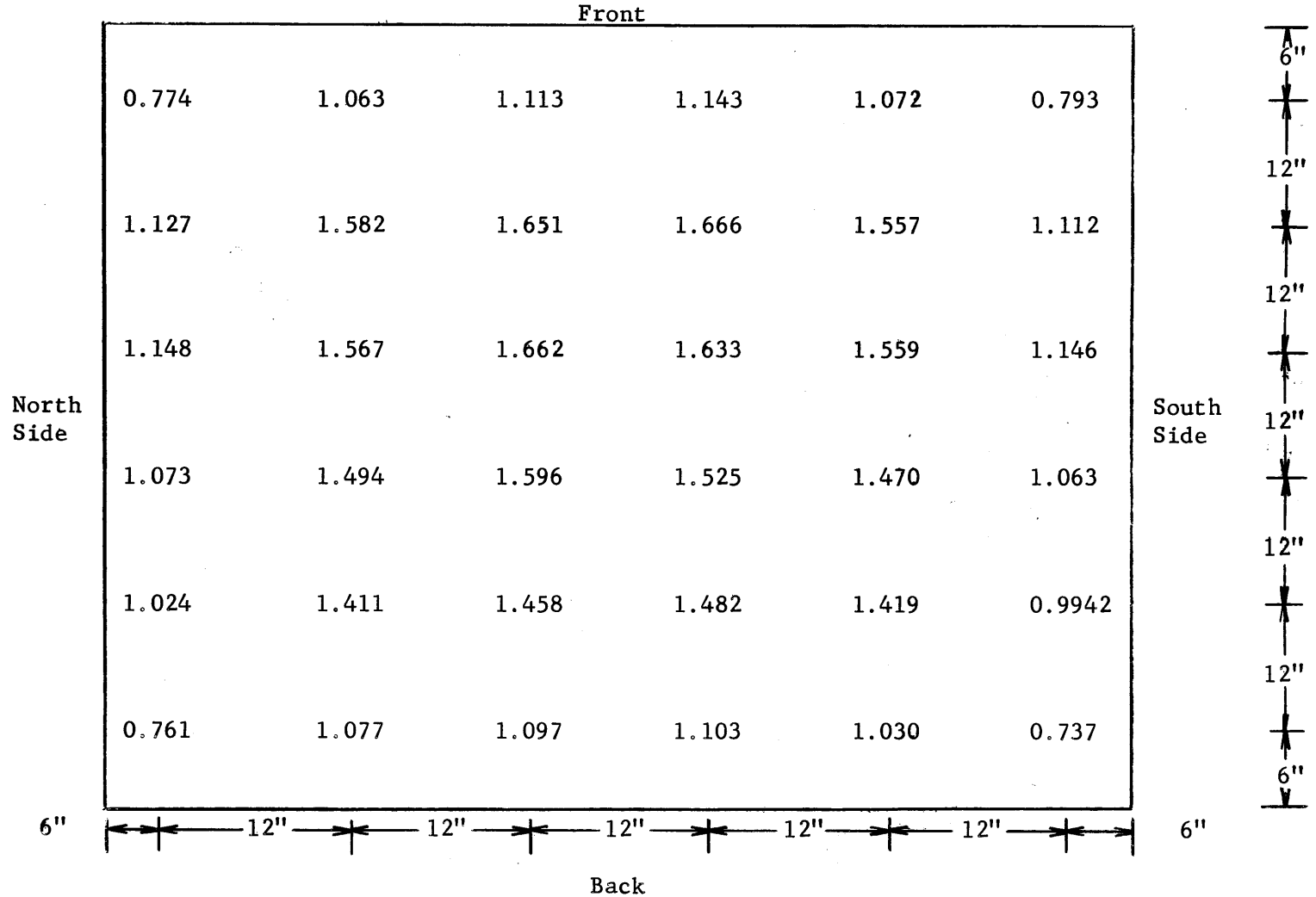


Table E3.19

The Values of $\phi_{abs} \times 10^{-8}$ Measured in the Upper Layer of the Pedestal in Assembly V

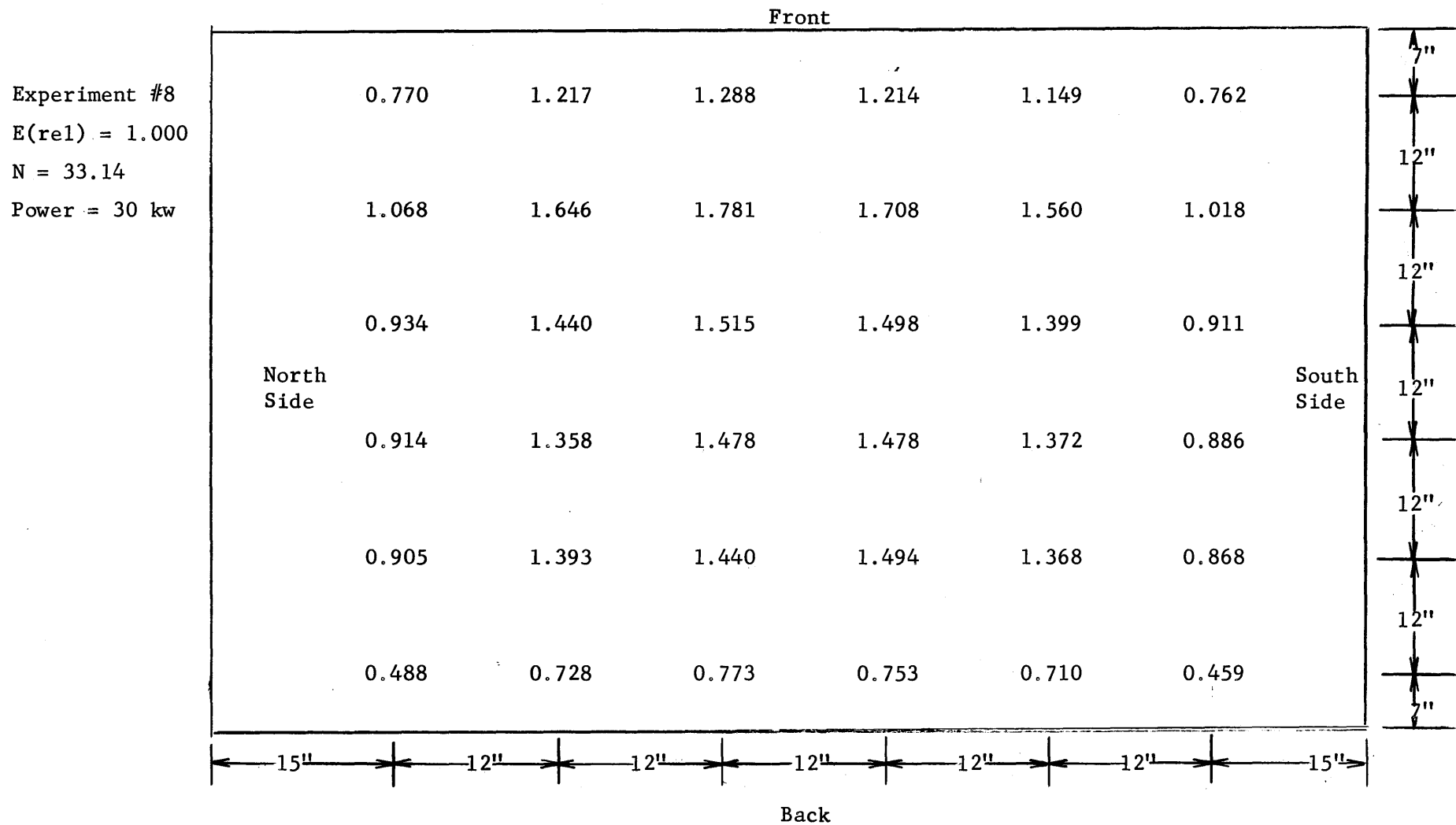


Table E3.20

The Values of $\phi_{abs} \times 10^{-8}$ Measured on the Honeycomb in Assembly V

Experiment #9
 E(rel) = 1.011
 N = 31.32
 Power = 30 kw

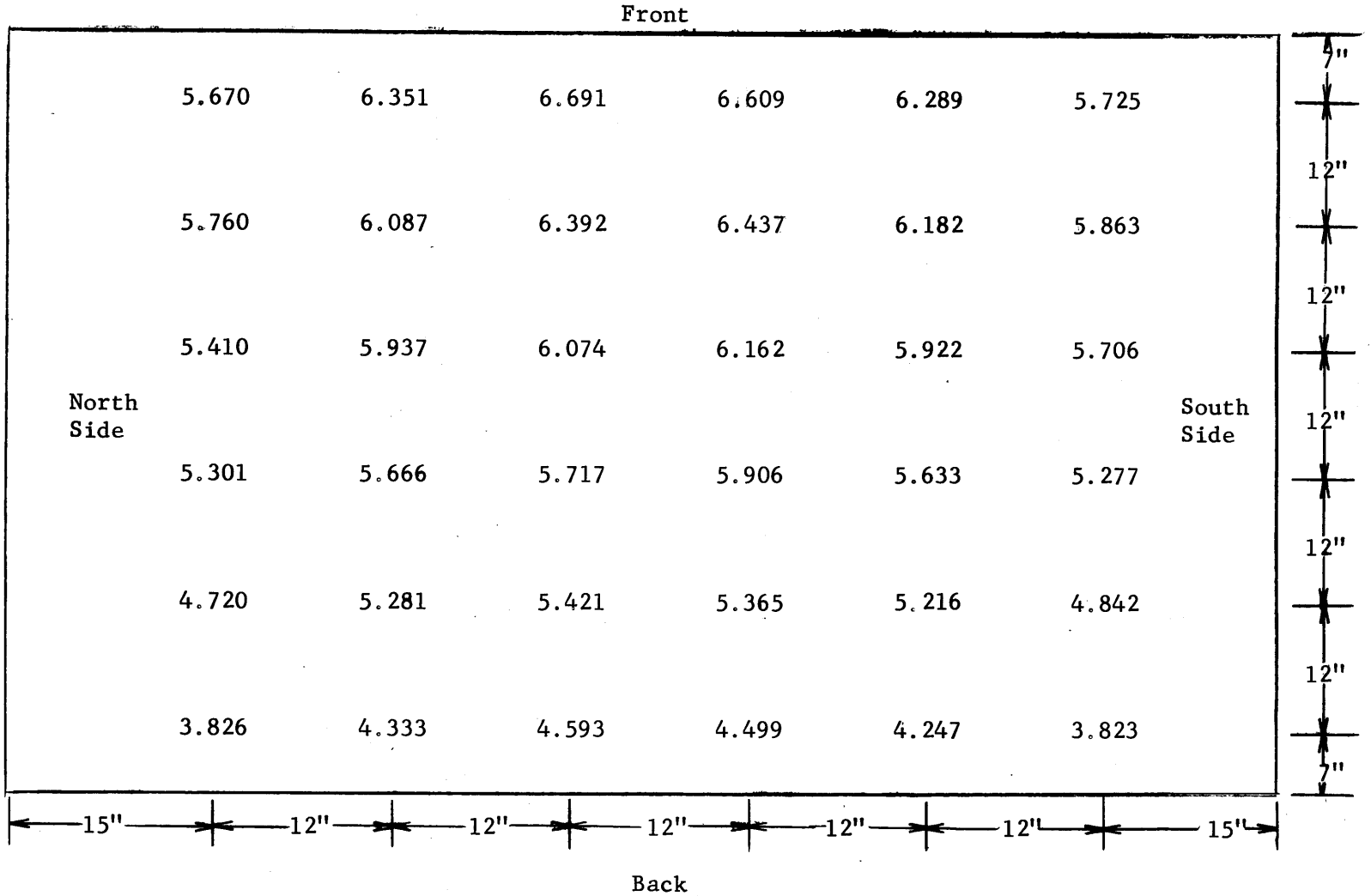


Table E3.21

The Values of $\phi_{\text{obs}} \times 10^{-8}$ Measured in the Lower Layer of the Pedestal in Assembly V

| | | Front | | | | | | |
|--|---------------|-------|-------|-------|-------|-------|-------|---------------|
| Experiment No. 9 E(rel) = 1.011 N = 31.32 Power = 30 kw | North Side | 3.124 | 4.144 | 4.336 | 4.166 | 3.948 | 3.036 | 6" |
| | | 3.204 | 4.120 | 4.207 | 4.130 | 3.960 | 3.034 | 12" |
| | | 3.066 | 3.909 | 4.030 | 3.967 | 3.887 | 3.020 | 12" |
| | | 2.947 | 3.616 | 3.997 | 3.850 | 3.677 | 2.825 | 12" |
| | | 2.681 | 3.326 | 3.593 | 3.554 | 3.363 | 2.575 | 12" |
| | | 1.876 | 2.468 | 2.538 | 2.482 | 2.383 | 1.855 | 6" |
| | | Back | | | | | | South Side |
| | | 6" | 12" | 12" | 12" | 12" | 12" | 6" |

Table E3.22

The Values of $\phi_{abs} \times 10^{-8}$ Measured in the Upper Layer of the Pedestal in Assembly V

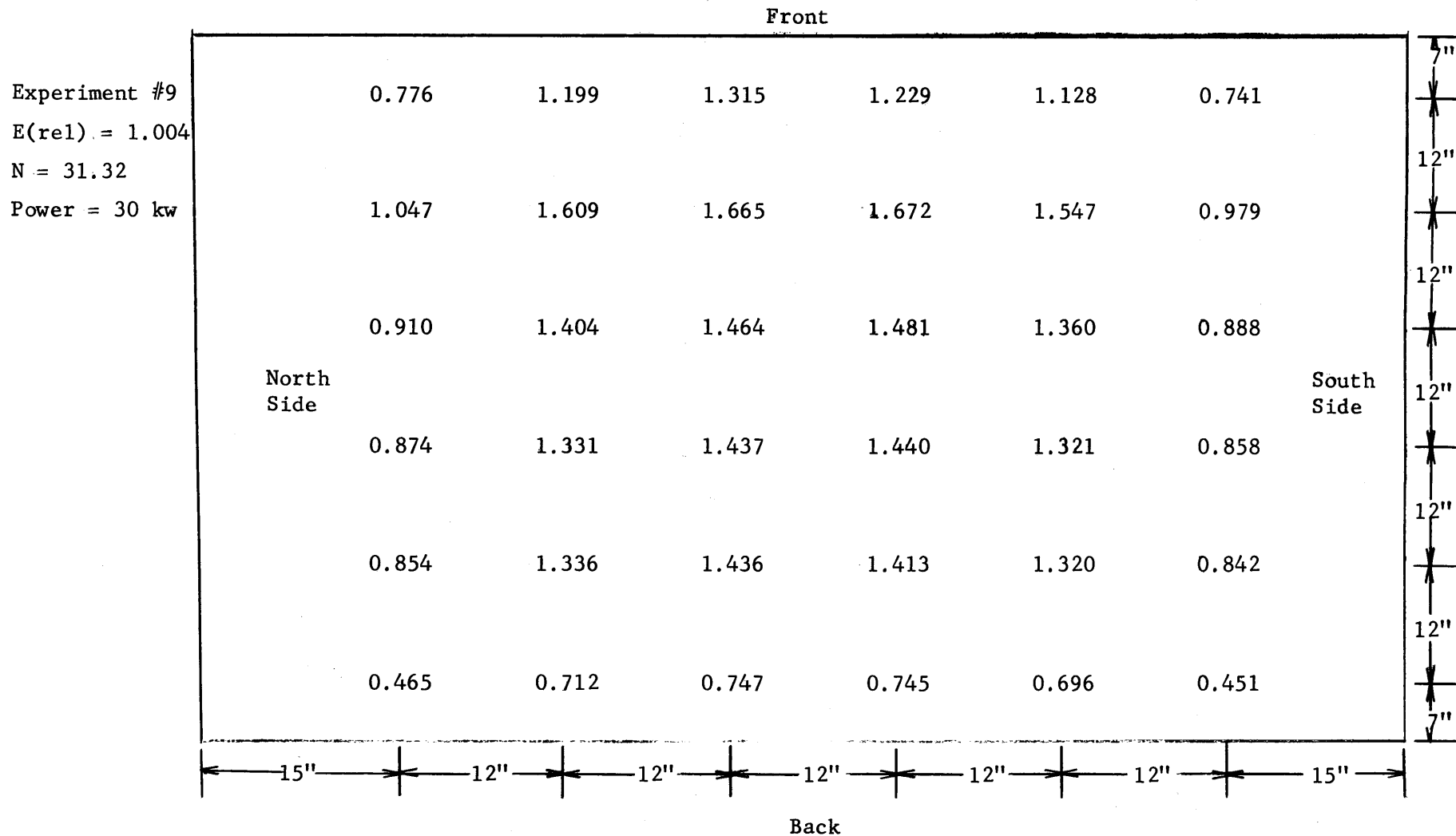


Table E3.23

The Values of $\phi_{abs} \times 10^{-8}$ Measured on the Honeycomb of Assembly VI

| | | Front | | | | | | |
|---|------------|-------|--------|--------|--------|--------|-------|------------|
| Experiment #10 E(rel) = 0.9907 N = 36.15 Power = 30 kw | | 9.133 | 10.606 | 11.289 | 11.177 | 11.104 | 9.270 | 7" |
| | | 9.442 | 10.504 | 10.903 | 10.861 | 10.375 | 9.632 | 12" |
| | | 9.163 | 10.038 | 10.224 | 10.241 | 9.986 | 9.153 | 12" |
| | North Side | 8.866 | 9.345 | 9.843 | 9.666 | 9.398 | 8.640 | 12" |
| | | 7.860 | 8.550† | 8.781 | 8.893 | 8.763 | 7.880 | 12" |
| | | 6.253 | 7.063 | 7.376 | 7.281 | 7.028 | 6.183 | 12" |
| | | | | | | | | 7" |
| | | | | | | | | 15" |
| | | | | | | | | 12" |
| | | | | | | | | 12" |
| | | | | | | | | 12" |
| | | | | | | | | 12" |
| | | | | | | | | 15" |
| | | | | | | | | Back |
| | | | | | | | | South Side |

Table E3.25

The Values of $\phi_{abs} \times 10^{-8}$ Measured in the Upper Layer of the Pedestal of Assembly VI

Experiment #10
 E(rel) = 0.9573
 N = 36.15
 Power = 30 kw

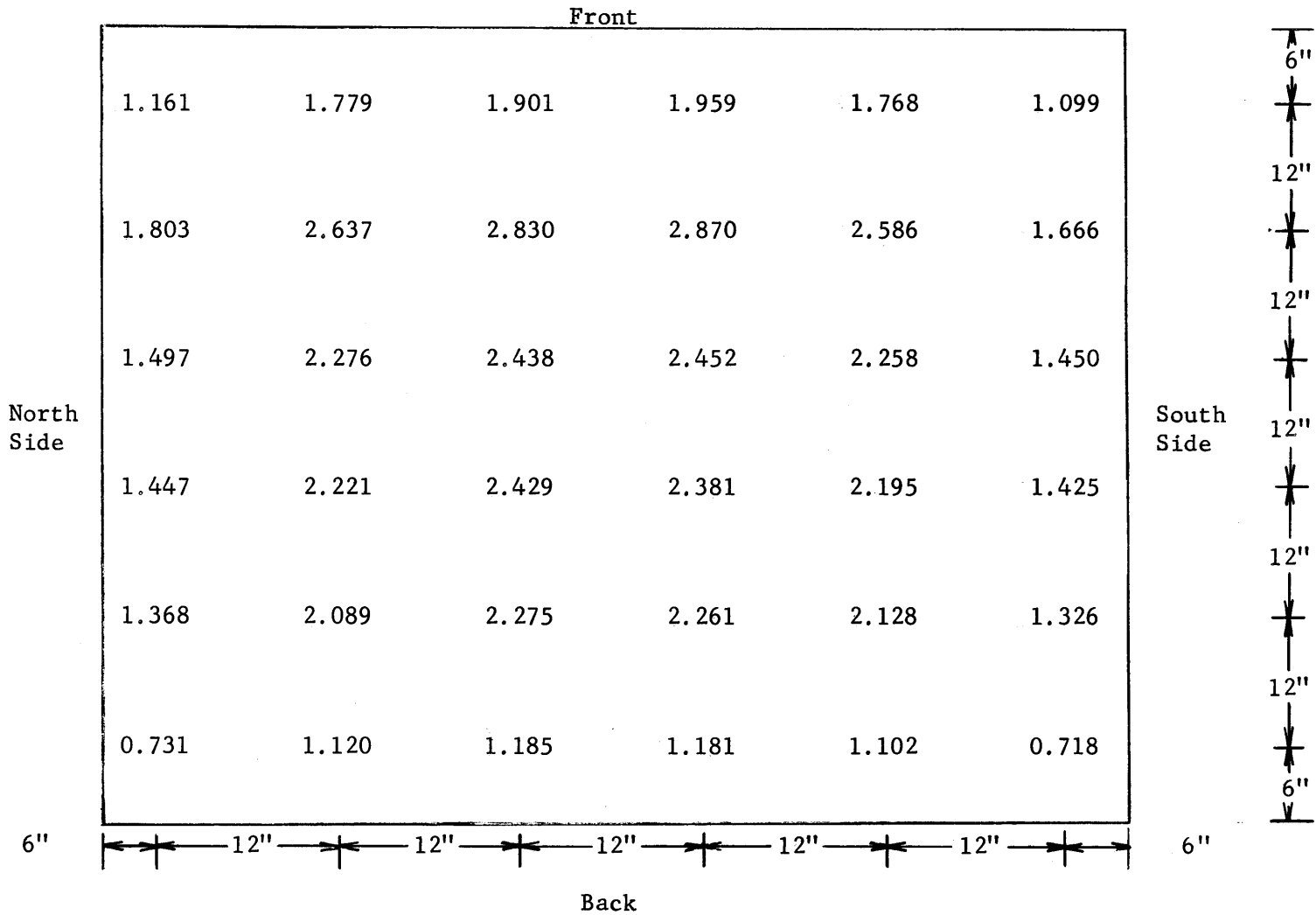


Table E3.26

The Values of $\phi_{abs} \times 10^{-8}$ Measured on the Honeycomb in Assembly VI

| | | Front | | | | | | |
|---|------------|-------|--------|--------|--------|--------|-------|-----|
| Experiment #11 E(rel) = 0.9747 N = 34.82 Power = 30 kw | | 9.185 | 10.863 | 11.204 | 10.949 | 10.818 | 9.211 | 7" |
| | | | | | | | | 12" |
| | | 9.582 | 10.525 | 10.985 | 10.753 | 10.290 | 9.643 | 12" |
| | | | | | | | | 12" |
| | North Side | 9.167 | 10.124 | 10.410 | 10.180 | 10.150 | 9.167 | 12" |
| | | 8.838 | 9.623 | 9.913 | 9.572 | 9.363 | 8.587 | 12" |
| | | 7.919 | 8.488 | 8.967 | 8.769 | 8.416 | 7.860 | 12" |
| | 6.290 | 7.188 | 7.293 | 7.284 | 6.992 | 6.241 | 7" | |
| | | | | | | | 7" | |
| | | 15" | 12" | 12" | 12" | 12" | 12" | 15" |
| | | Back | | | | | | |

Table E3.27

The Values of $\phi_{abs} \times 10^{-8}$ Measured in the Lower Layer of the Pedestal in Assembly VI

73

Experiment #11
 E(rel) = 0.981
 N = 34.82
 Power = 30 kw

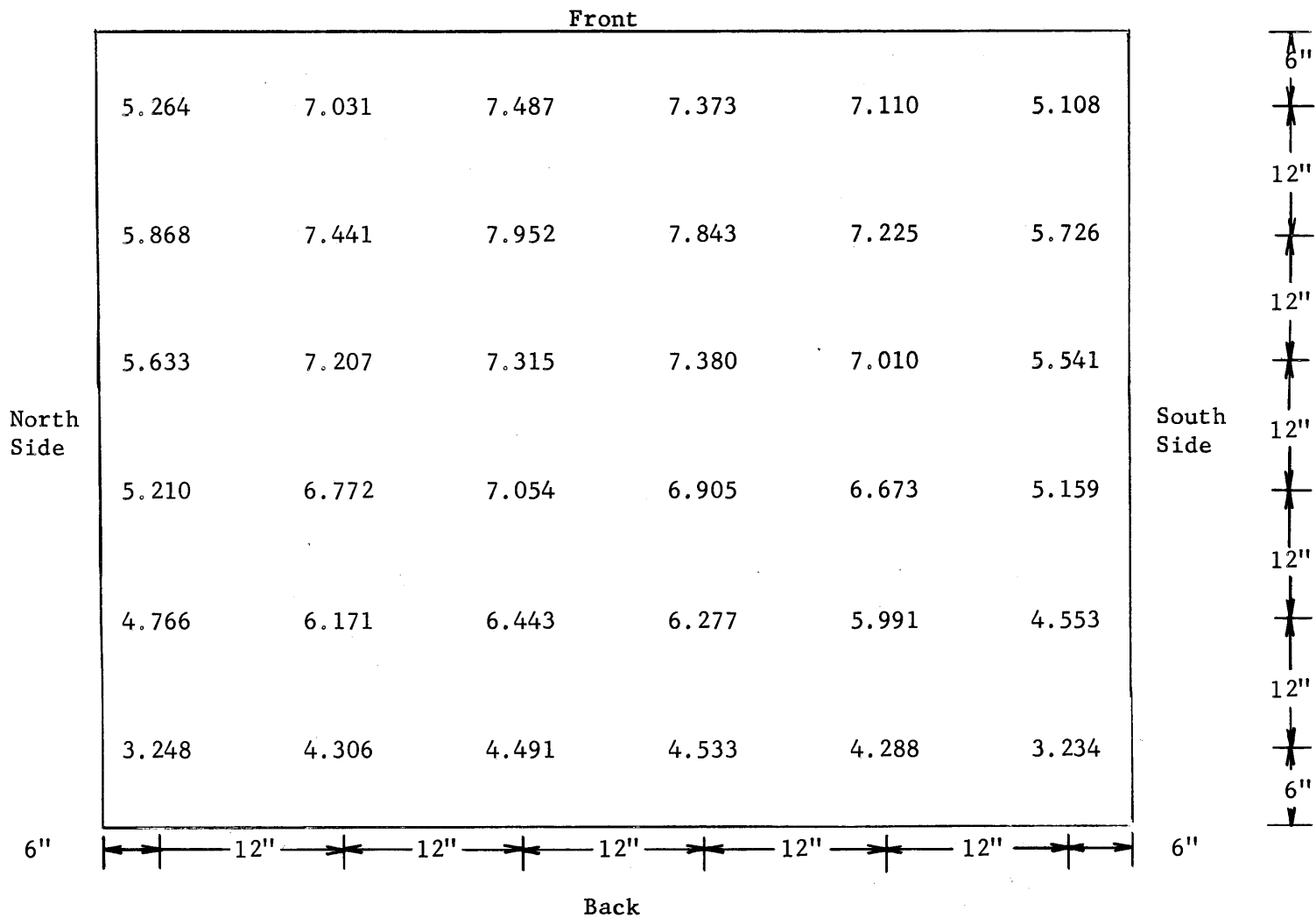
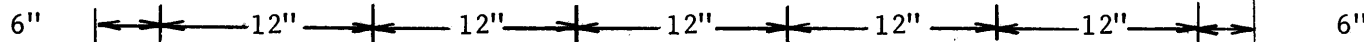
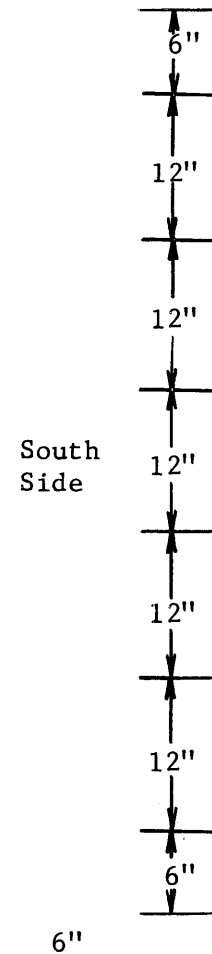


Table E3.28

The Values of $\phi_{abs} \times 10^{-8}$ in the Upper Layer of the Pedestal in Assembly VI

Experiment #11
 E(rel) = 0.9627
 N = 34.82
 Power = 30 kw

| | | Front | | | | | |
|---------------|--|-------|-------|-------|-------|-------|-------|
| North Side | | 1.178 | 1.825 | 1.965 | 1.954 | 1.850 | 1.131 |
| | | 1.727 | 2.649 | 2.928 | 2.848 | 2.634 | 1.665 |
| | | 1.550 | 2.355 | 2.548 | 2.487 | 2.327 | 1.537 |
| | | 1.458 | 2.199 | 2.434 | 2.328 | 2.210 | 1.403 |
| | | 1.446 | 2.271 | 2.402 | 2.384 | 2.259 | 1.420 |
| | | 0.775 | 1.158 | 1.224 | 1.221 | 1.136 | 0.749 |
| | | Back | | | | | |



71

Table E3.29

The Values of $\phi_{abs} \times 10^{-8}$ Measured on the Honeycomb of Assembly VII

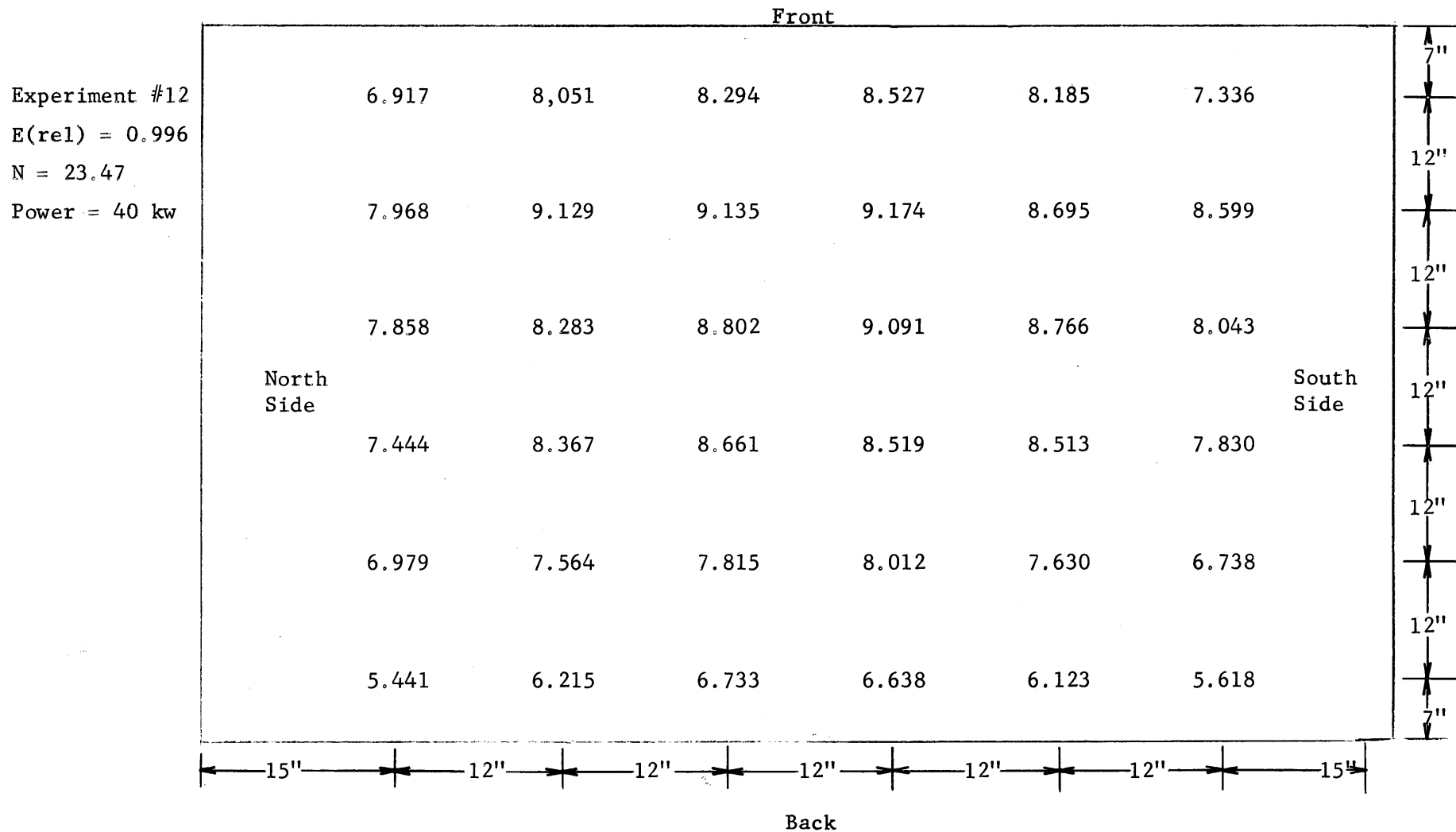


Table E3.31

The Values of $\phi_{abs} \times 10^{-8}$ Measured in the Upper Layer of the Pedestal in Assembly VII

77

Experiment #12
 E(rel) = 0.9813
 N = 23.47
 Power = 40 kw

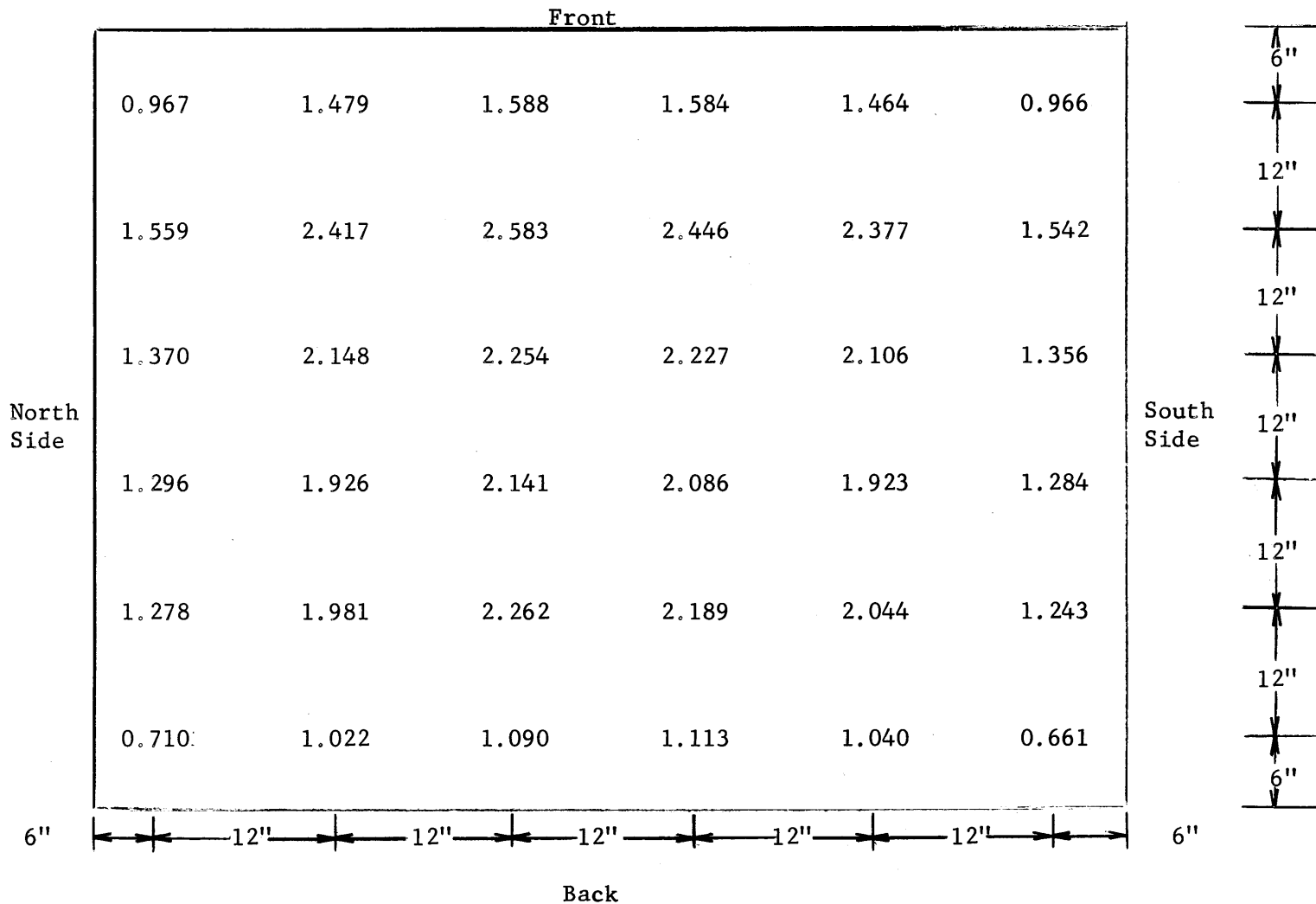


Table E3.34

The Values of $\phi_{abs} \times 10^{-8}$ Measured in the Upper Layer of the Pedestal of Assembly VII

Experiment #13
 $E(rel) = 0.9867$
 $N = 26.57$
 Power = 40 kw

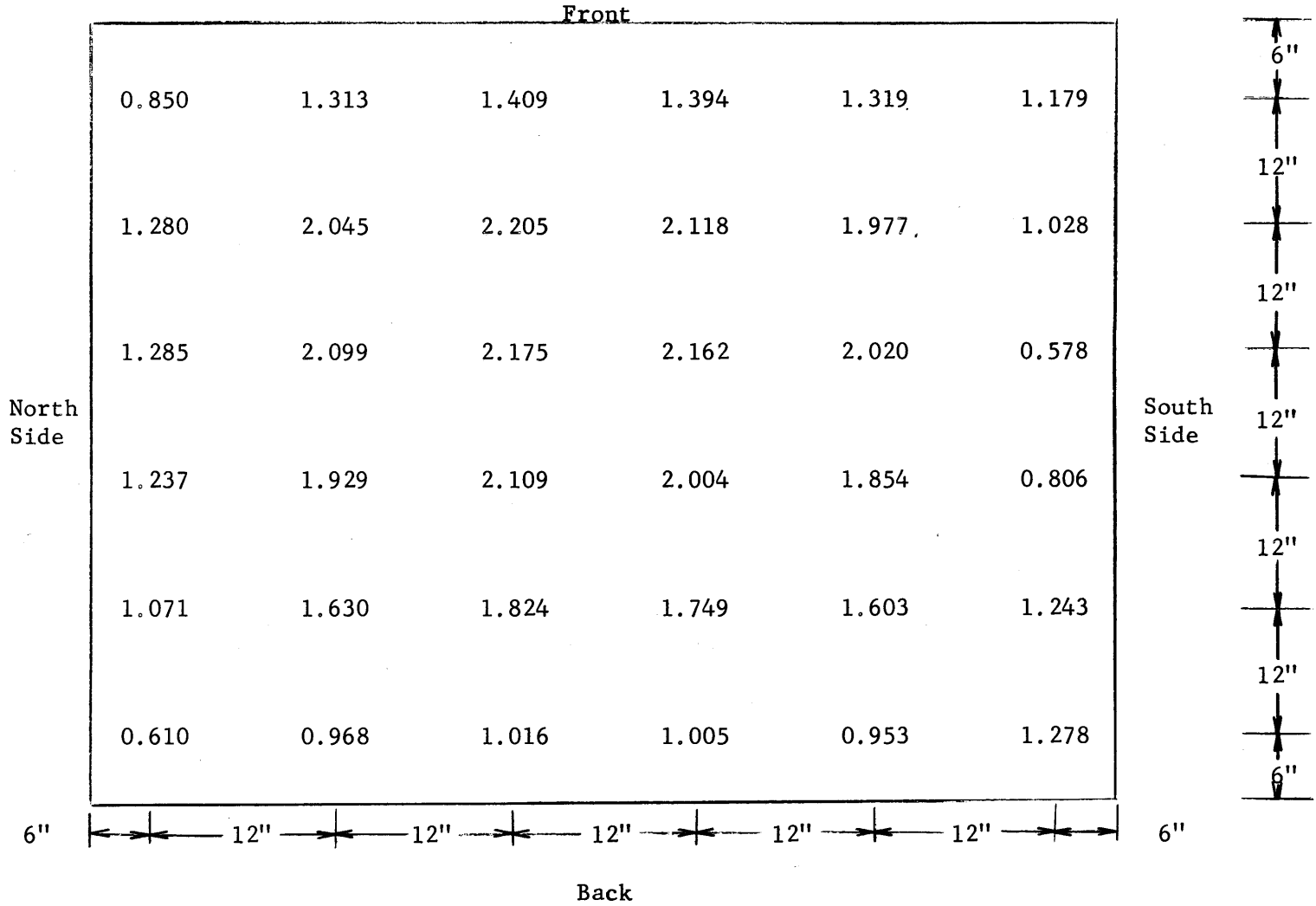


Table E3.35

The Values of $\phi_{abs} \times 10^{-8}$ Obtained in Experiment #14

Top

| | | | | | | | |
|-------|--------|--------|-------|-------|-------|-------|------|
| | 8.972 | 9.504 | 9.131 | 8.757 | 8.181 | 7.864 | |
| Front | 10.169 | 9.713 | 9.435 | 8.725 | 8.763 | 8.991 | Back |
| | 9.859 | 10.049 | 9.435 | 8.909 | 8.650 | 8.434 | |

Side Wall - North

Top

| | | | | | | | |
|-------|--------|--------|-------|-------|-------|-------|------|
| | 8.852 | 9.099 | 8.789 | 8.434 | 8.092 | 7.985 | |
| Front | 10.150 | 9.897 | 9.397 | 8.858 | 8.485 | 8.498 | Back |
| | 10.093 | 10.077 | 9.276 | 8.795 | 8.504 | 8.257 | |

Side Wall - South

Table E3.35 (continued)

Top

| | | | | | | | |
|------------|-------|-------|-------|-------|-------|-------|------------|
| | 8.375 | 8.713 | 9.000 | 8.894 | 8.688 | 8.269 | |
| South Side | 9.194 | 9.250 | 9.444 | 9.375 | 9.306 | 9.263 | North Side |
| | 8.981 | 9.511 | 9.377 | 9.364 | 9.140 | 8.987 | |

Back Wall

Front

| | | | | | |
|------------|-------|--------|--------|--------|------------|
| | 9.868 | 10.992 | 11.451 | 10.066 | |
| | 9.492 | 9.811 | 9.766 | 9.575 | |
| | 8.949 | 9.134 | 9.192 | 9.160 | |
| North Side | 8.432 | 8.579 | 8.738 | 8.700 | South Side |
| | 8.196 | 8.432 | 8.445 | 8.355 | |
| | 7.992 | 8.279 | 8.451 | 8.349 | |

Back

Floor

Table E3.35 (continued)

Front

| | | | | | |
|------------|-------|--------|--------|-------|------------|
| | 9.225 | 10.650 | 10.394 | 8.725 | |
| | 9.494 | 10.006 | 9.844 | 9.269 | |
| North Side | 9.150 | 9.413 | 9.388 | 8.788 | South Side |
| | 8.856 | 9.019 | 9.013 | 8.431 | |
| | 8.144 | 8.613 | 8.750 | 8.106 | |
| | 7.563 | 8.263 | 7.944 | 7.363 | |

Honeycomb Surface

Top

| | | | | | |
|------------|--------|--------|--------|--------|------------|
| | 35.829 | 49.218 | 49.268 | 36.469 | |
| | 48.352 | 70.007 | 69.599 | 48.766 | |
| North Side | 48.810 | 67.675 | 76.579 | 50.894 | South Side |
| | 37.053 | 53.097 | 51.195 | 38.509 | |

Bottom

Thermal Column Face

Table E3.35 (continued)

| | | | |
|--------------------|--------|--------|------|
| | Top | | |
| Front | 31.742 | 27.966 | Back |
| | 36.796 | 30.681 | |
| | 36.469 | 30.362 | |
| | 30.889 | 27.180 | |
| Frame - North Side | | | |

| | | | |
|--------------------|--------|--------|------|
| | Top | | |
| Front | 31.065 | 27.06 | Back |
| | 35.471 | 30.249 | |
| | 35.672 | 29.709 | |
| | 30.437 | 26.621 | |
| Frame - South Side | | | |

| | | | | |
|-------------|--------|--------|--------|--------|
| | Back | | | |
| Front | 27.901 | 31.448 | 31.441 | 27.449 |
| | 33.959 | 41.617 | 38.830 | 31.686 |
| Frame - Top | | | | |

| | | | | |
|----------------|--------|--------|--------|--------|
| | Back | | | |
| Front | 25.685 | 29.209 | 29.371 | 27.272 |
| | 31.412 | 35.765 | 36.114 | 29.156 |
| Frame - Bottom | | | | |

Table E3.36

The Values of $\phi_{\text{abs}} \times 10^{-8}$ Obtained in Experiment #15

Top

| | | | | | |
|----------------|--------|--------|--------|--------|--------|
| Front Array | 9.873 | 9.810 | 10.476 | 9.790 | 10.483 |
| | 9.914 | 10.830 | 10.476 | 10.310 | 10.143 |
| | 10.879 | 10.574 | 11.559 | 10.247 | 10.310 |
| | 11.004 | 10.733 | 10.997 | 10.976 | 11.822 |
| | 10.920 | 11.781 | 11.309 | 10.511 | 11.316 |

Bottom

Top

| | | | | | |
|-----------------|--------|--------|--------|--------|-------|
| Middle Array | 9.274 | 9.599 | 9.835 | 9.989 | 8.942 |
| | 9.828 | 9.572 | 9.523 | 9.952 | 9.288 |
| | 9.544 | 10.278 | 10.056 | 9.419 | 9.987 |
| | 10.243 | 9.862 | 9.641 | 10.181 | 9.689 |
| | 9.918 | 9.696 | 9.696 | 10.112 | 9.966 |

Bottom

Table E3.36 (continued)

| | Top | | | | |
|------------|-------|-------|-------|-------|-------|
| Back Array | 8.672 | 8.664 | 9.228 | 8.862 | 8.357 |
| | 9.345 | 9.236 | 9.455 | 9.389 | 8.738 |
| | 9.660 | 9.843 | 9.411 | 9.580 | 9.638 |
| | 9.280 | 9.739 | 9.441 | 9.280 | 9.477 |
| | 9.748 | 9.455 | 9.338 | 9.514 | 9.177 |

Bottom

Chapter E4

Absolute Flux

The conversion factor between the absolute flux, ϕ_{abs} , and the relative activity, $\text{Act}(\text{rel})$, calculated by Equation E3.2, was obtained by irradiating a cobalt foil and a copper foil in the same flux. The absolute disintegration rate of the cobalt foil was measured by coincidence counting, and from the absolute disintegration rate, the absolute flux which irradiated the cobalt foil was calculated. The conversion factor was obtained by comparing this absolute flux to the value of $\text{Act}(\text{rel})$ for the copper foil irradiated in the same flux.

E4.1 Irradiation Procedure

A 5 mil, 1" diameter cobalt foil was punched, filed, cleaned and weighed. It was placed in one of the two locations in the thermal column used for the copper monitor foils for the flux distribution experiments; a copper foil was placed in the other position. The two copper monitor foils used in the flux distribution experiments were found to have the same activity within 0.5% and thus the flux was the same in both locations in the thermal column. The procedure for irradiating the copper and cobalt foils was the same as that used in the flux distribution measurements.

E4.2 Determination of the Absolute Disintegration Rate

After the 10.5 min isomer of Co^{60} was allowed to decay, the absolute decay rate was measured by a coincidence counting of the two gammas from Co^{60} . The coincidence system, built by Mr. A. Weitzberg, counts the photoelectric peaks due to the 1.17 and 1.33 Mev gamma rays entering the two detectors of the system. The base line of each channel was set at about 1.0 Mev, with an infinite channel width. The correction for dead time, which is about 27 μc (12), was negligible for these count rates.

Table E4.1

Results from Coincidence Countings of $\frac{1}{2}$ μc Co^{60} Standard
and the Cobalt Foil in the Thermal Column

| <u>Sample</u> | <u>Durations</u> | <u>Total Counts</u> | | | <u>Absolute Disintegration Rate</u> |
|------------------------------------|------------------|---------------------|-------------------|--------------------|---|
| | | <u>Channel #1</u> | <u>Channel #2</u> | <u>Coincidence</u> | |
| Background | 30 min. | 606 | 633 | 1 | - |
| $\frac{1}{2}$ μc Source | 60 min. | 173,586 | 195,932 | 289 | 1.635×10^4 dis/sec. |
| Co foil | 300 mm | 650,343 | 693,432 | 1147 | 1.082×10^4 dis/sec. |

Coincidence counts were also taken for $\frac{1}{2}\mu\text{c Co}^{60}$ source and for the background.

The equation for the absolute disintegration rate, R_{abs} , is

$$R_{\text{abs}} = \frac{R_1 R_2}{2R_c} \quad (\text{E4.1})$$

where

R_1 = the count rate in Channel #1 corrected for background,

R_2 = the count rate in Channel #2 corrected for background,

R_c = coincidence count rate corrected for background.

The results of the coincidence counting are given in Table E4.1.

E4.3 Calculation of the Absolute Flux

Equation(E4.2) gives the standard relationship between the flux activating a foil and the foil activity for the case of $\lambda T_r \ll 1$.

(See Chapter E3.4 for the nomenclature):

$$\phi_s = \frac{\text{Act (dis/sec)}}{\frac{C W \Sigma_a \lambda T_r}{\rho}} \quad (\text{E4.2})$$

The absorption cross section, Σ_a , is rewritten as

$$\Sigma_a = \frac{\sigma_a \rho N_o}{A} \quad (\text{E4.3})$$

where

Σ_a = the absorption cross section of Co^{59} ,

N_o = Avogadro's number,

A = atomic weight of Co^{59} ,

ρ = density of cobalt, gm/cm^3 .

The activation experiments with a $1/v$ absorber actually measure the neutron density, n . For these calculations the 2200 m/s, absorption cross section, $\sigma_a(2200)$, is used to obtain the neutron flux :

$$\phi_{2200} = n v_{2200} \text{ m/s} = \frac{\text{Act}}{C W \Sigma_a \left[\frac{2200}{N_o} \lambda T_r \right]} \quad (\text{E4.4})$$

The correction for flux depression, F_{sp} , and self-shielding, F_{iso} , were calculated from the equations given in ANL-5800 (11).

Insertion of the values:

$$C = F_{iso} F_{sp} = (1.0134)^{*7}, \quad \lambda = 2.4877 \times 10^6 \text{ min}^{-1},$$

$$\sigma_a \left[\frac{2200}{N_o} \right] = 37 \text{ barns}, \quad T_r = 30 \text{ min},$$

$$W = 0.5688 \text{ gm}, \quad A = 59,$$

$$N_o = 6.025 \times 10^{23} \text{ atoms/gm-moles},$$

$$\text{Act} = 1.082 \times 10^4 \text{ dis/dic}$$

into equation (E4.4) yields:

$$\phi_{2200} = 7.356 \times 10^9 \text{ n/cm}^2 \text{ sec. at 40 hw.}$$

The relative activity, $\text{Act}(\text{rel})$, of the copper foil exposed to the same flux in the thermal column was calculated from equation (E3.2) and was found to be $1.0826 \times 10^8 \text{ dis/min gm}$. The conversion factor, K , between $\text{Act}(\text{rel})$ and the absolute flux was found to be

$$K = \frac{7.356 \times 10^9}{1.0826 \times 10^8} = 67.95 .$$

The relative activity of the copper foils was multiplied by K to obtain the absolute value of the flux in the flux distribution experiments.

Chapter E5

The Cadmium Ratio Experiment

E5.1 Introduction

The cadmium ratio for gold foils was measured on the thermal column face, the floor, side and back walls, the honeycomb, and in the pedestal. The high values of the cadmium ratio obtained on all the surfaces indicated that the neutrons in the cavity are, indeed, thermal. The theoretical model that will be used later is based on the assumption that all the neutrons are thermal. The activity of copper, whose cross section does not display any appreciable low-energy resonances, was considered to be due only to thermal neutrons, and was therefore used to measure the thermal flux distribution in the assembly.

E5.2 Selection of the Foil Material

The cadmium ratio was measured with $\frac{1}{2}$ " diameter, 3 mil gold foils, covered with 20 mil cadmium. Gold is commonly used for cadmium ratio experiments, and was well suited for this one. A bare gold foil after an irradiation of 30 minutes at a reactor power of 40 Kw, produced a count rate of about 5000 CPM, ample for good counting statistics. An accurately measured thermal cross section of 97 barns and an effective resonance integral of 1558 barns mean that gold is activated by both epithermal and thermal neutrons.

E5.3 Foil Preparation

The procedure for punching, cleaning, and weighing the gold foils was the same as that described for copper foils (see Appendix A1). A gold foil was placed between two 20 mil cadmium covers and the covers were pressed tightly together. The cadmium covered foils were inspected

under a magnifying glass to determine whether the cadmium covers completely sealed off the gold.

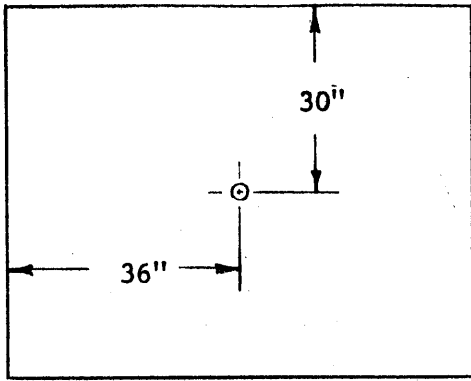
E5.4 Positioning of the Foil

The experiment was performed in two irradiations, one with all of the bare foils, and one with all of the cadmium covered foils. The bare and cadmium covered foils were irradiated separately because the cadmium perturbs the thermal flux and thus the activity of the bare foils; a perturbation in the thermal flux has no influence on the activity of the cadmium covered foil. The bare foils were located on the surfaces of the cavity and in the pedestal as illustrated in Figure E5.1. The number and the position of each foil was recorded in the data book. (See Appendix A1 of the thesis for the details of the experimental procedure.) After the bare foils had been irradiated and removed, the cadmium covered foils were put within 1/8" of the same location and irradiated. All of the foils were held in place with mylar tape on the surfaces of the cavity assembly or were placed in the notches drilled in the graphite stringers of the pedestal.

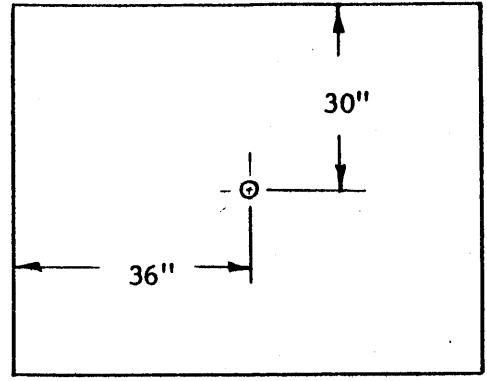
Two monitor foils were located on the graphite frame in each irradiation; they measured the neutron flux level in the cavity assembly during each irradiation. The activities of the bare and cadmium covered foils were compared on the basis of the same neutron flux by means of these monitor foils. The irradiation procedure in the cadmium ratio experiments was identical to that described for the flux distribution measurements.

E5.5 Counting Equipment

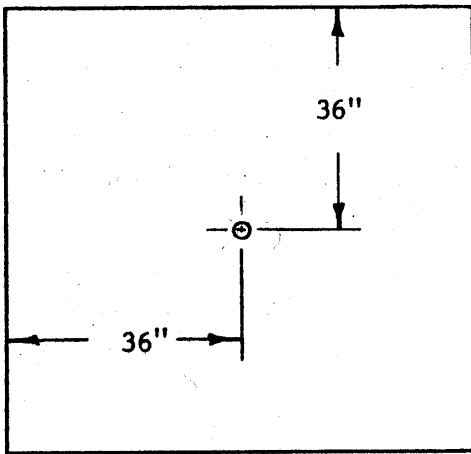
The only differences in the counting equipment used in the cadmium ratio and the flux distribution experiments was that a scintillation detector was substituted for the gas flow detector and time delay controller.



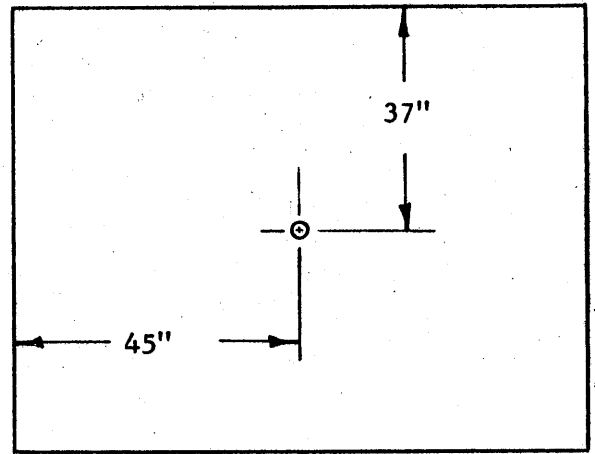
Side Wall (72" x 60")



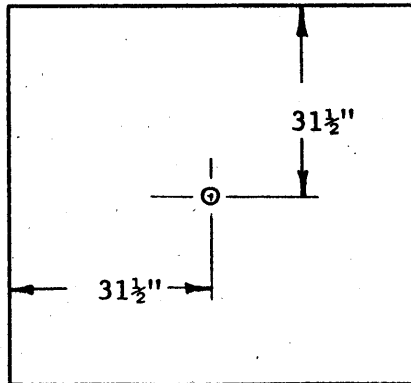
Back Wall (72" x 60")



Floor (72" x 72")



Honeycomb (90" x 74")



Thermal Column Face
(63" x 63")

Figure E5.1 The Locations on the Walls of the Assembly at which the Cadmium Ratio was measured.

A scintillation detector was used because it is much more sensitive to gamma rays than to beta particles.

The advantage of counting gamma rays lies in the fact that very few gammas are absorbed in the 3 mil thick gold foil. Thus, the thickness of the foil, which may be difficult to measure accurately, does not enter into the calculations, and the count rate for gamma rays was taken to be proportional to the weight of the gold foil.

E5.6 Counting Procedure

The cadmium was removed from the covered foils. All of the foils were cleaned and placed in planchets. The $\frac{1}{2}$ " diameter foils were positioned in the center of the 1-1/16" diameter planchets and were held in position with vaseline. The foils irradiated without covers and those irradiated with covers were counted separately. Two different background counts were taken, one with only bare foils in the automatic sample changer, and the other with only cadmium-covered foils in the automatic sample changer. The activity of the covered foils was very low and an accurate background was needed to determine this activity. The order in which the foils were counted, the time at the start of counting, and the preset count were recorded on the paper tape of the printer. A Co^{60} standard foil, a gamma emitter, was used to measure any variations in the counter efficiency. Except for using a Co^{60} foil instead of a RaD+E foil as a standard, the procedure for counting the foil was the same as that described for the copper foils.

E5.7 Data Reduction

The cadmium ratio is the ratio of the activity of the bare foil to that of the cadmium covered foil, or

$$R_{cd} = \frac{\left[\frac{\text{Act}(\text{rel})}{\text{Act}(\text{rel})} \right]_{\text{bare}}}{\left[\frac{\text{Act}(\text{rel})}{\text{Act}(\text{rel})} \right]_{\text{covered}}} \quad (\text{E5.1})$$

When the expression for the saturated activity, equation(E3.2.) is substituted in equation(E5.1), the resulting equation for the case of the same value of T_r is:

$$R_{cd} = \frac{\left[\frac{\text{PC-BGD}}{T_C} \cdot \frac{\lambda T_C}{1 - e^{-\lambda T_C}} \cdot e^{+\lambda T_D} \cdot E(\text{rel}) \cdot N/W \right]_{\text{bare}}}{\left[\frac{\text{PC-BGD}}{T_C} \cdot \frac{\lambda T_C}{1 - e^{-\lambda T_C}} \cdot e^{+\lambda T_D} \cdot E(\text{rel}) \cdot N/W \right]_{\text{covered}}} \quad (\text{E5.2})$$

Since the quantity T_C is very much less than unity, equation(E5.2) takes the form:

$$R_{cd} = \frac{\left[\frac{\text{PC-BGD}}{T_C} \cdot e^{\lambda T_D} \cdot E(\text{rel}) \cdot N/W \right]_{\text{bare}}}{\left[\frac{\text{PC-BGD}}{T_C} \cdot e^{\lambda T_D} \cdot E(\text{rel}) \cdot N/W \right]_{\text{covered}}} \quad (\text{E5.3})$$

The ratio of the counting efficiencies, $\frac{E(\text{rel})_{\text{bare}}}{E(\text{rel})_{\text{covered}}}$, for the bare and covered foils is obtained from the ratio of the counting rates of the Co^{60} standard, $\frac{(\text{SCR}_{\text{bare}})}{(\text{SCR}_{\text{covered}})}$, where SCR is the count rate of the standard Co^{60} foil during the counting of the foils. The ratio of the normalization constants, $\frac{N_{\text{bare}}}{N_{\text{covered}}}$, is equal to the ratio of the count ratio for the two sets of copper monitor foils, $\frac{\left[\frac{E(\text{rel}) \cdot \text{CR}(\text{SAT})}{W} \right]_{\text{covered}}}{\left[\frac{E(\text{rel}) \cdot \text{CR}(\text{SAT})}{W} \right]_{\text{bare}}}$.

As was the case for copper foils, no dead time correction was necessary because the count rates did not exceed 20,000 CPM. The values of the cadmium ratio in the cavity assembly were calculated by using equation (E5.3) and the results are given in Table E5.1.

Table E5.1

Results of the Cadmium Ratio Measurements

| | <u>Bare - CPM/gm</u> | <u>Covered - CPM/gm</u> | <u>Cadmium Ratio</u> |
|------------------------|----------------------|-------------------------|----------------------|
| Upper Pedestal | 967 ± 10 | 1.63 ± 1.46 | 593 ± 531 |
| Lower Pedestal | 2897 ± 29 | 2.90 ± 1.49 | 999 ± 514 |
| Honeycomb | 4455 ± 45 | 4.86 ± 1.51 | 917 ± 285 |
| Floor | 4426 ± 44 | 3.41 ± 1.50 | 1298 ± 571 |
| Back Wall | 4402 ± 44 | 5.62 ± 1.52 | 783 ± 212 |
| Side Wall (north) | 4223 ± 42 | 2.75 ± 1.49 | 1536 ± 833 |
| Side Wall (south) | 4219 ± 42 | 2.78 ± 1.49 | 1518 ± 814 |
| Thermal Column Face | 9120 ± 91 | 7.36 ± 1.54 | 1239 ± 259 |

E5.8 Discussion of Experimental Results

In all cases the count rates of the covered foils were within seven counts of the background rate of 63.4 ± 0.73 CPM. The highest count rates were obtained on the thermal column face and thus the smallest uncertainty in the cadmium ratio was in the value of 1239 for the thermal column face.

Since the source neutrons entered through this surface, the cadmium ratio of 1239 shows that the source neutrons had a thermal spectrum, and thus the neutrons on the other surfaces must also have had thermal spectrum. All of the cadmium ratios were close to 1000, except for those measured in the back wall and in the upper layer of the pedestal. The uncertainty in the background and the count rates of the covered foil explain the low cadmium ratio in the upper pedestal. The cadmium ratio should be highest in this position and should be higher than that of the source neutrons. However, an accurate cadmium ratio in the upper pedestal was difficult to measure because of the small magnitude of the flux. The background rate was 63.4 ± 0.7 CPM; the count rate for the foil in the upper pedestal and its standard error are: $(65.04 \pm 0.73) \pm (63.41 \pm 0.73) = 1.63 \pm 1.46$ CPM. Since the total activity was so close to the background activity, the foil activity had a probable error of almost 100 percent.

The standard error in the cadmium ratio on the thermal column face, which had about ten times more flux, is given by:

$$R_{cd} = \frac{9120 \pm 91}{7.36 \pm 1.54} = 1239 \pm 259$$

The fact that the lower limit of the cadmium ratio on the thermal column face was about 1000 shows that the neutrons entering the cavity are thermal, and thus the neutrons in the entire assembly are thermal.

Chapter E6

Measurement of the Albedo of Graphite

E6.1 Discussion of the Experiment

The albedo of the material forming the walls of the cavity is used in the theoretical model (see Chapter T3) for calculating the flux distribution on the surface of the cavity. The general definition of the albedo of a medium A is the ratio of the current leaving medium A to the current entering medium A. If J_{out} refers to the current leaving and J_{in} refers to the current entering, the albedo β is defined by the relation:

$$\beta = J_{out} / J_{in} . \quad (E6.1)$$

The albedo may refer to the ratio of the current at a point or over an area on the interface of two media. The albedo of graphite has been measured by foil activation inside a large slab, with the aid of a correction for the perturbation caused by the foil; in this case Medium A and the adjoining medium are both graphite. In the cavity assemblies of the present study, the adjoining media are graphite and air, and information is needed about the albedo of the graphite. An experiment was designed to measure the albedo over the area of a foil on the surface of a graphite wall in such a way that no correction for the perturbation caused by the foil was needed.

Consider a wall on which a neutron current, J_{in} , is incident, and from which a neutron current, J_{out} , is leaving. See Figure E6.1a. Four sets of foils were used to measure the ratio of these currents. The experiment consisted of irradiating each set of foils at the same place on a graphite surface. The sets of foils consisted of: (1) a bare gold foil, (2) a gold foil with a cadmium foil between the wall and the gold

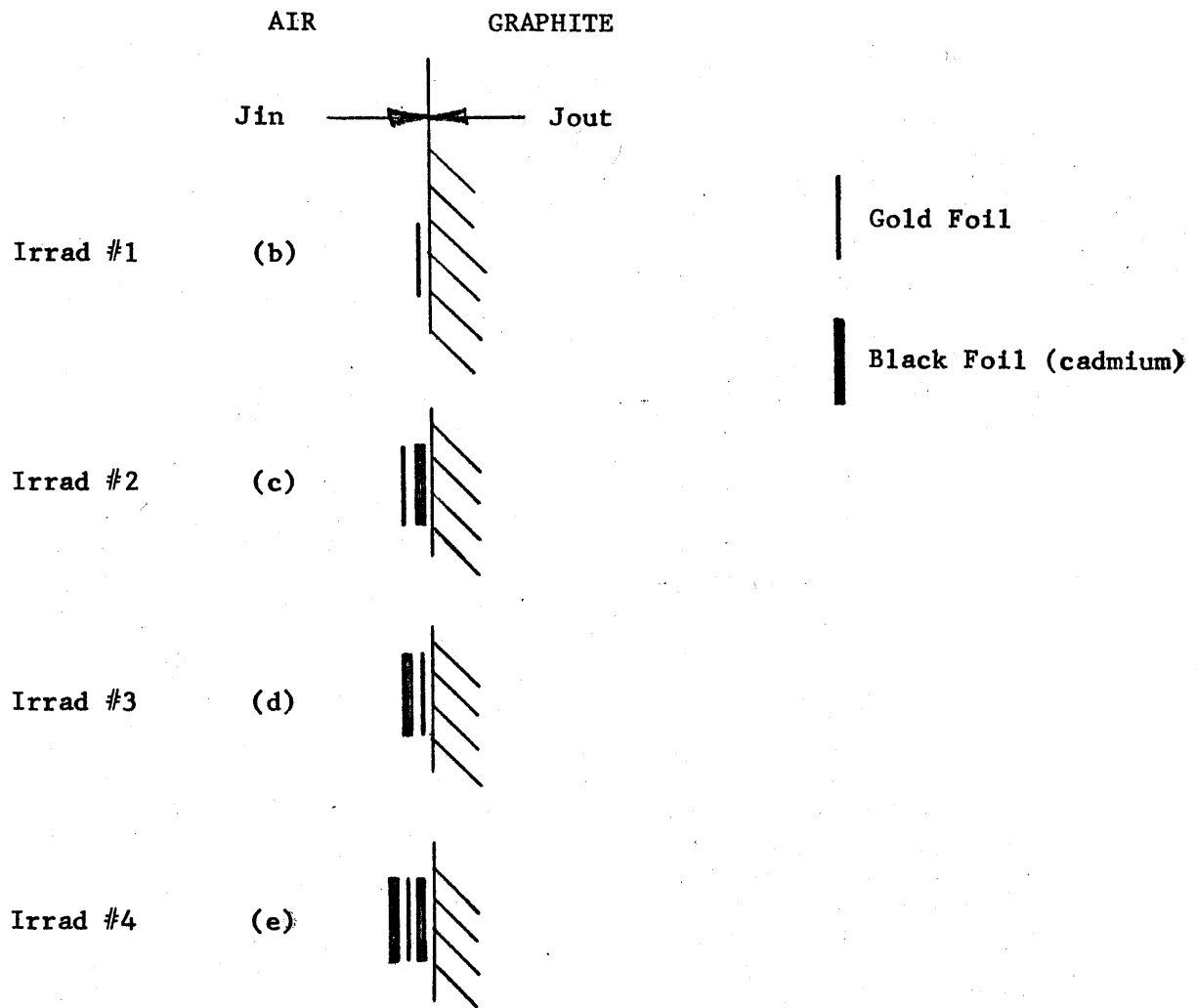


Figure E6.1 Arrangement of the Foils for the Four Irradiations of the Albedo Experiments.

foil, (3) a gold foil between a cadmium foil and the wall, (4) a gold foil between two cadmium foils. The arrangements are shown in Figure E6.1 with arrows indicating the unperturbed values of J_{in} and J_{out} . The currents, J_{in} and J_{out} , are considered to be composed only of thermal neutrons. Note that the cadmium and gold foils have the same diameter. The following nomenclature is used:

"Act" is the activity of the gold foil due to the absorption of neutrons,

" f_{in} " is the fraction of J_{in} that is absorbed in the gold foil,

" f_{out} " is the fraction of J_{out} that is absorbed in the gold foil,

"fast effect" is the activity of the gold foil due to fast neutrons,

"P" is the fraction of J_{in} which contributes to J_{out} ; note that J_{in}

and J_{out} refer to the currents incident on the foil and not on the entire wall,

"edge effect" is the activity due to neutrons striking the edge of the gold foils.

In irradiation #1, the activity, Act.1, is due to the fraction of J_{in} absorbed, plus the fraction of the perturbed value of J_{out} absorbed, plus the fast and side effects. The quantity J_{out} , however, is reduced by the fraction of J_{in} which does not contribute to J_{out} because it was absorbed by the bare gold foil. Then,

$$\text{Act.1} = f_{in} J_{in} + f_{out} (J_{out} - f_{in} J_{in} P) + \text{fast effects} + \text{edge effects.} \quad (\text{E6.2})$$

Since the cadmium is assumed to be black to thermal neutrons and transparent to fast neutrons, Act.2 is due to $f_{in} J_{in}$, plus the edge and fast effects:

$$\text{Act.2} = f_{in} J_{in} + \text{fast effects} + \text{edge effects.} \quad (\text{E6.3})$$

Activity #3 (Figure E6.1c) is due to absorption of the perturbed value of J_{out} . Since $f_{in} = 1.0$ in this case, Act. 3 is given by:

$$\text{Act.3} = f_{out} (J_{out} - PJ_{in}) + \text{fast effects} + \text{edge effects.} \quad (\text{E6.4})$$

Since no thermal neutrons strike the sides of the gold foil, the activity in irradiation #4 is:

$$\text{Act.4} = \text{fast effects} + \text{edge effects.} \quad (\text{E6.5})$$

The quantity, Act.4, is subtracted from Act.1, Act.2, and Act.3, resulting in Act.1', Act.2', and Act.3', respectively.

The ratios of Act.1'/Act.2' and Act.3'/Act.2' are then obtained:

$$\frac{\text{Act.1}'}{\text{Act.2}'} = 1 + \frac{f_{out}}{f_{in}} \beta - f_{out} P, \quad (\text{E6.6})$$

and

$$\frac{\text{Act.3}'}{\text{Act.2}'} = \frac{f_{out}}{f_{in}} (\beta - P), \quad (\text{E6.7})$$

where $\beta = J_{out}/J_{in}$.

Equations (E6.6) and (E6.7) are combined to eliminate P and to obtain an expression for β :

$$\beta = \frac{\frac{(\text{Act.1} - \text{Act.4})}{(\text{Act.2} - \text{Act.4})} - 1 - f_{in} \frac{(\text{Act.3} - \text{Act.4})}{(\text{Act.2} - \text{Act.4})}}{\frac{f_{out}}{f_{in}} (1 - f_{in})} \quad (\text{E6.8})$$

If $f_{out} = f_{in}$, equation (E6.8) becomes:

$$\beta = \frac{\frac{(\text{Act.1} - \text{Act.4})}{(\text{Act.2} - \text{Act.4})} - 1 - f_{in} \frac{(\text{Act.3} - \text{Act.4})}{(\text{Act.2} - \text{Act.4})}}{1 - f_{in}} \quad (\text{E6.9})$$

If f_{in} is less than 0.10, equation(E6.9) is quite insensitive to the exact value of f_{in} . For example, let

$$\frac{\text{Act.1} - \text{Act.4}}{\text{Act.2} - \text{Act.4}} = 1.90 \quad \text{and} \quad \frac{\text{Act.3} - \text{Act.4}}{\text{Act.2} - \text{Act.4}} = 0.89 ,$$

both of which are realistic values. By substituting three values for f_{in} (0.05, 0.075, and 0.100) into equation(E6.9), the values of 0.8995, 0.9009 and 0.9011, respectively, are obtained for the albedo. A change by 100 percent in the value of f_{in} (0.05 to 0.10) results in a change of less than one percent in the value of the albedo. If the assumption of $f_{in} = f_{out}$ is justified, the albedo on the surface of a graphite slab can be measured accurately without any corrections for the perturbation of the currents J_{in} and J_{out} .

E6.2 Experimental Procedure

A 3 mil, $\frac{1}{2}$ " diameter gold foil was used in the experiments. These foils result in a high count rate (5000 cpm) and a value of about 0.10 for f_{in} or f_{out} . Gold is mainly an absorber and has an accurately measured absorption cross section for thermal neutrons. Both of these factors aid in the calculation of f_{in} or f_{out} . A 20 mil cadmium foil was used as a black foil. The gold foils were punched and the burrs were removed carefully so that the diameter of the gold and cadmium foils were the same. Each foil was inscribed with an identification number and then cleaned and weighed. The 20 mil, $\frac{1}{2}$ " diameter cadmium foils were attached to the gold foils with glyptal. The composite foil was examined under a magnifying glass to insure that the gold was completely covered by the cadmium foil.

Measurements were made on five surfaces of the cavity assembly: on the floor, side and back walls, and the bottom of the honeycomb; see

Figure E6.2 for the foil locations on these surfaces. The albedo experiment was performed in four irradiations, yielding the four activities, Act.1, Act.2, Act.3, and Act.4. In each of the four irradiations, one set of foils (see Figure E6.1), some with cadmium covers, was placed on each of the five surfaces of the cavity assembly. By placing the same number of bare and cadmium covered foils in the assembly for each irradiation, any small perturbations of the flux in the cavity were the same for each irradiation. Actually, only a very small perturbation would be expected from five $\frac{1}{2}$ " diameter foils on different surfaces, but as a precaution, the same amount of "poisoning" was introduced into each irradiation. The schedule for the irradiation is shown in Table E6.1.

The foils for each irradiation were placed in position with mylar tape and the location and number of each foil was recorded. The position of the four foils on each wall was reproducible within $\frac{1}{8}$ ". Two copper foils were placed on the bottom surface of the graphite frame for each irradiation and acted as monitors for the flux level in the cavity.

The irradiation procedure was the same as that used for the measurement of the flux distribution (Appendix A1 of the thesis). After all four irradiations were completed, the cadmium was removed from the composite foils and the glyptal on the gold was dissolved and removed. The foils were counted in two groups: the first group contained the copper monitor foils and the gold foils which were bare, or covered on only one side; the gold foils covered on both sides were counted separately because of their low activity.

The counting equipment and counting procedure for the foils were identical with those used in the cadmium ratio experiments discussed in

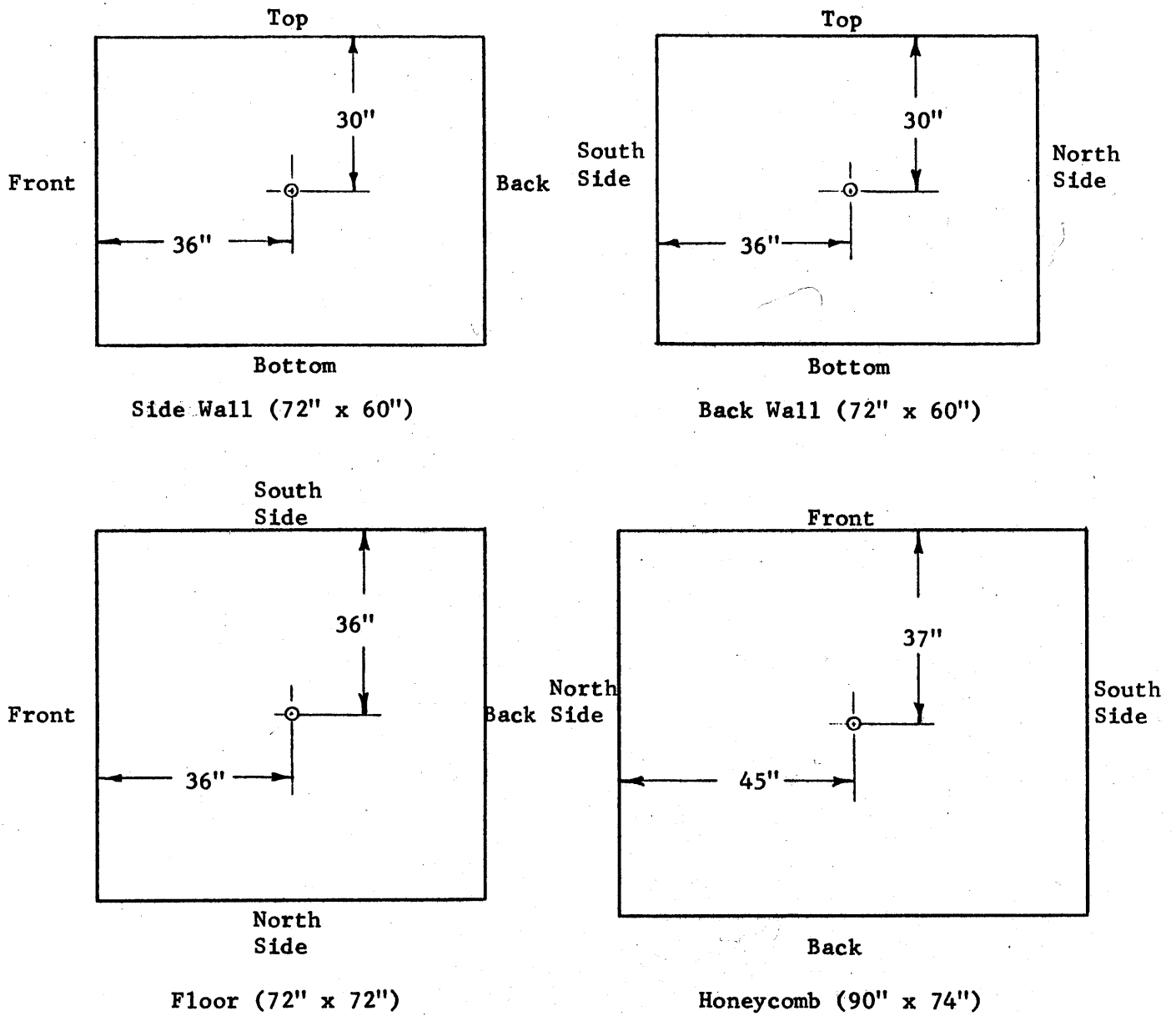


Figure E6.2 The Positions on the Walls of the Assembly at which the Albedo was measured.

Chapter E5, with one exception. A 1/4" thick steel plate was attached to the end of the scintillation crystal to prevent any beta particles from being counted. The reason for counting only gamma rays is best shown by an example. Consider a gold foil which was irradiated with one side covered with cadmium. Because neutrons enter the foil through only one surface of the foil, the number of radioactive nuclides, Au^{98} , falls off exponentially from this surface. The number of beta rays leaving one surface exposed to the flux is greater than the number leaving the other surface because the range of the beta ray is shorter than the thickness of the foil. The range of the gamma ray is much larger than the thickness of the foil and the same number leave each surface. The foils were counted on both sides in the scintillator and found to give the same count rate. Thus the gamma counting gave a count rate proportional to the total activity of the foil. A Co^{60} standard foil was used to correct for any variations in the counter efficiency.

E6.3 Data Reduction

Since only ratios of activities were required in Equations E6.8 and E6.9, the absolute values for Act.1, Act.2, Act.3, and Act.4 are not needed. The correction, N , for the differences in the magnitude of the flux level in the cavity for the four irradiations was made by means of the copper monitor foils. The corrections for the self-shielding were included in f_{in} and f_{out} . No correction was necessary for the perturbation in the flux caused by the foil. Using the nomenclature as defined in Chapter E3.4, we get the following equation for the relative activity of a gold foil:

$$\text{Act}(\text{rel}) = N \cdot E(\text{rel}) \cdot \frac{\text{PC-BGD}}{T_C} \times \frac{T_C}{1 - e^{-\lambda T_C}} \times \frac{e^{+\lambda T_d}}{1 - e^{-\lambda T_r}} \quad (\text{E6.10})$$

E6.4 Results and Discussion

The relative activities and the albedo calculated from equation (E6.9), with $f_{\text{in}} = 0.10$, are given in Table E6.2. The values of the albedo calculated from diffusion theory appear in the last row.

The measured values of the albedo disagree with those calculated from diffusion theory. An analysis of the counting statistics of the four activities showed that the probable error in the measured albedo is about ± 0.025 . None of the measured values of the albedo are within 0.025 of the albedo calculated by diffusion theory. In fact, one value is greater than unity, contrary to the definition of the albedo. The assumption that $f_{\text{in}} = f_{\text{out}}$ appears to be the main source of the error in the values of the albedo. The factors, f_{in} and f_{out} , depend on the absorption cross section, the thickness of the foil, and also on the angular distribution of the current incident on the foil. Although no exact information is available for the angular distribution of J_{in} and J_{out} , a rough calculation can be performed to indicate that the main part of the error results from the assumption that $f_{\text{in}} = f_{\text{out}}$.

The albedo on two surfaces, the back and north walls, is calculated for the case of $f_{\text{in}} = f_{\text{out}}$. The back wall is considered first. Detailed calculations (see Chapter T5.4) show that about one-third of the neutrons which strike the foil on the back wall are source neutrons from the thermal column face. In Figure E6.3, it is seen that these neutrons strike the foil perpendicularly. By assuming that the other neutrons ($2/3$ of J_{in}) strike the foil isotropically, an effective absorption cross

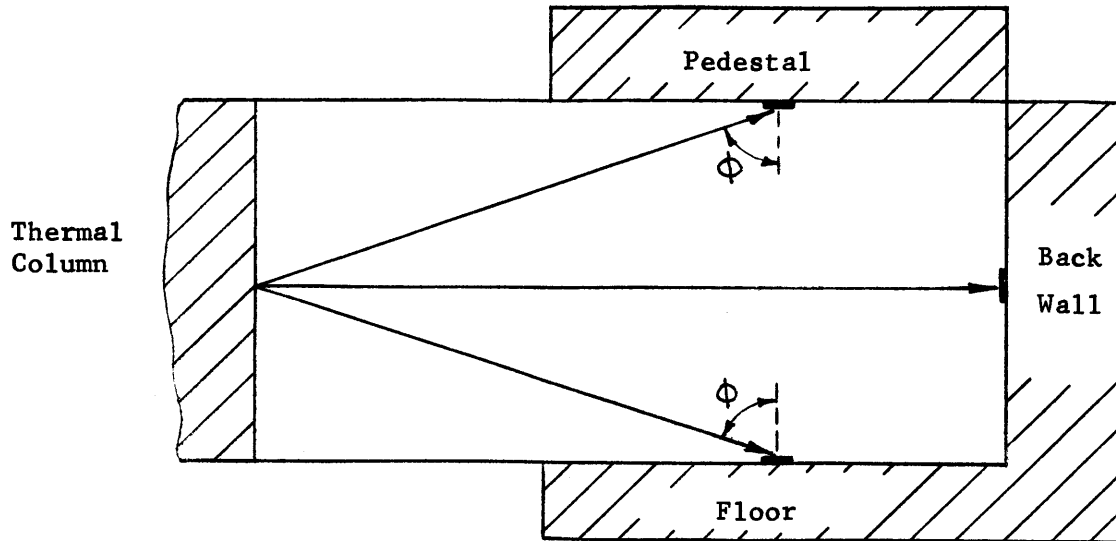


Figure E6.3 Vertical Section of the Cavity Assembly. The lines from the thermal column indicate the angle of incidence with which the source neutrons strike the foils.

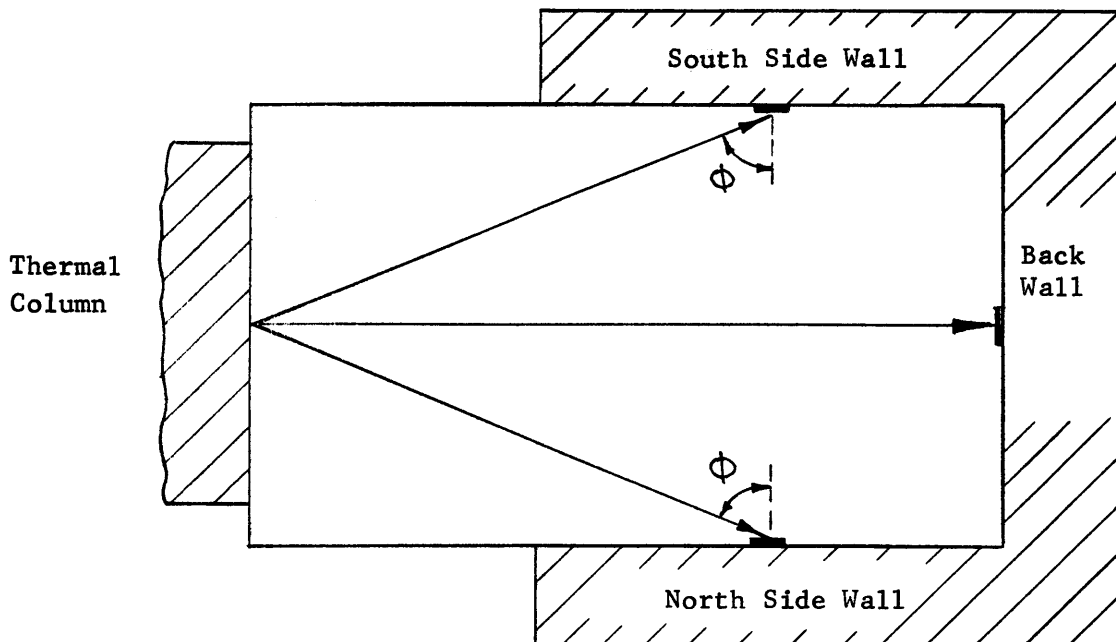


Figure E6.4 Vertical Section of the Cavity Assembly. The lines from the thermal column indicate the angle of incidence with which the source neutrons strike the foils.

Table E6.1

The Schedule for the Four Irradiations of the Albedo Experiments

| <u>Irrad.</u> | <u>Honeycomb</u> | <u>Back Wall</u> | <u>Floor</u> | <u>North Wall</u> | <u>South Wall</u> |
|---------------|------------------|------------------|--------------|-------------------|-------------------|
| 1 | bare | one-side | one-side | both-side | both-side |
| 2 | one-side | one-side | both-side | bare | bare |
| 3 | one-side | both-sides | bare | one-side | one-side |
| 4 | both-sides | bare | one-side | one-side | one-side |

Table E6.2

The Results of the Albedo Experiment

| | <u>Honeycomb</u> | <u>Back</u> | <u>Floor</u> | <u>Side Wall</u> | |
|--|------------------|-------------|--------------|------------------|--------------|
| | | | | <u>North</u> | <u>South</u> |
| <u>Act. 1-Act. 4</u> <u>Act. 2-Act. 4</u> | 1.762 | 2.1313 | 1.8649 | 1.8267 | 1.8310 |
| <u>Act. 3-Act. 4</u> <u>Act. 2-Act. 4</u> | 0.7534 | 0.9842 | 0.7397 | 0.7728 | 0.7918 |
| β from Eq. E29 | 0.7633 | 1.1480 | 0.8788 | 0.8327 | 0.8352 |
| β from diff. theory | 0.9124 | 0.9124 | 0.8926 | 0.9124 | 0.9124 |

section can be obtained. Since the effective cross section for an isotropic beam is approximately $2\Sigma_a$ (11), the effective cross section Σ_{in} for J_{in} on the back wall is:

$$\Sigma_{in} = (2/3) (2\Sigma_a) + 1/3 \Sigma_a = 1.67 \Sigma_a .$$

If it is assumed that the J_{out} is distributed isotropically on the surface of the foil, Σ_{out} is:

$$\Sigma_{out} = 2\Sigma_a .$$

The ratio of f_{in}/f_{out} is very nearly $\frac{\Sigma_{in}}{\Sigma_{out}}$, because all the foils have the same thickness. Substituting

$$\frac{f_{in}}{f_{out}} = \frac{1.67 \Sigma}{2.0 \Sigma}$$

into equation (E6.8) and using the same values of the activities that were used in calculating the values of the albedo listed in Table E6.2 and f_{in} , results in an albedo of 0.953.

Roughly one-fourth of the current J_{in} that strikes the foil on the side wall (north) is composed of source neutrons. By assuming that all of the source neutrons are emitted in the center of the thermal column face, (see Figure E6.4) we find that the cosine of the angle of incidence of the source neutrons is 0.333. The effective absorption cross section for a beam is $\frac{\Sigma_a}{\cos \phi}$ or $3\Sigma_a$ for the source neutrons in this case. The value of Σ_{in} is

$$\Sigma_{in} = 3/4 (2\Sigma_a) + 1/4 (3\Sigma_a) = 2.25 \Sigma_a .$$

The corrected value for the albedo is obtained by the same procedure as

used before and is 0.955. The corrected value for the albedo on the other side wall is also 0.955. By applying the same procedure, corrected values of the albedo on the honeycomb and the floor are obtained which are closer to the theoretical values. Even though the method of correcting the albedo is approximate, it does demonstrate that a significant error is introduced by assuming that $f_{in} = f_{out}$. The correction is in the right direction and is approximately of the correct magnitude to explain the values of the albedo in Table E6.2.

The purpose of the albedo experiment was to measure the albedo at many points on all of the surfaces, especially near the corners of the surfaces. The albedo varies most rapidly near the corners where it can not be accurately calculated by diffusion theory. Unfortunately, the theoretical model also has its greatest uncertainty at the corners, and thus the angular distribution of J_{in} calculated from the results of the theoretical model may be in serious error. No references were found which gave the angular distribution for a situation corresponding to that of J_{out} . As long as the angular distribution of J_{in} and J_{out} are not accurately known, the experimental results cannot be corrected accurately enough to obtain an albedo with an uncertainty less than $\pm 5\%$. The uncertainty may be even greater in the corners of the assembly. An uncertainty of this magnitude is not acceptable and, therefore, a more precise theoretical method of obtaining the albedo was used; it is discussed in Chapter T3.

THEORETICAL SECTION

Chapter T1

Derivation of the Theoretical Model

The aim of this section is the development of a theoretical model capable of predicting accurately the magnitude and distribution of the neutron flux on the surfaces of a hohlraum or cavity. The equation for the flux distribution obtained from the theoretical model has been programmed for an electronic computer and solved for the particular cavity assemblies in which the flux distributions were measured.

Many problems, both of practical importance and of academic interest, have been studied successfully in the field of reactor physics. The problems have involved complicated arrangements of fissionable, fertile, moderating, poisoning, and structural materials. The method of solution has ranged from one group diffusion theory to a numerical solution of the transport equation requiring hours of computer time. It has often been necessary to determine the neutron flux distributions in these complicated systems. It may be surprising, then, that the problem of predicting the flux distribution on the surfaces bounding a cavity has received little attention, especially since this information would be useful in many reactor physics calculations. While the determination of the transmission of neutrons and gamma rays through certain simple ducts in shields, and of the effect of gas coolant channels on the flux distribution in nuclear reactors has been carried out (13) by other means, little has been done to solve this type of problem by calculating the flux distribution on the surface of a cavity. Because of this lack of previous study it is necessary to develop, in some detail, a method for predicting the flux distribution on the surfaces of a cavity.

The method developed in this thesis is derived from an approximate equation for the equilibrium current striking the surface. In the interest of a logical development, the exact equation for the equilibrium current is derived first. In attempting to develop the model, difficulties are encountered at the outset because a neutron travels in a straight line in a cavity rather than by diffusion due to scattering, so that the existing solutions of diffusion and transport theory are not applicable to this problem. Another approach must, therefore, be used.

The system to be studied is a cavity or hohlraum surrounded by a partially reflecting material or materials. In order that the development of the model be general, the arrangement of the cavity assembly and the material composition of the walls are not specified at this stage.

Throughout this study, the hohlraum or cavity is the air space itself, and the cavity or hohlraum assembly is the cavity together with the material surrounding it. An incident, or incoming neutron, is one that travels from the cavity into the surrounding wall material, while a re-entering, or outgoing neutron, is one that leaves the surrounding material and goes into the cavity. By the surface of the cavity is meant the surface of the wall bounding the cavity. Let r define the position of a point on the surface of the cavity; let $J(r)$ be the neutron current ($n/cm^2 \cdot sec$) incident on the surface at the point r , and let $A(r)$ (cm^2) be the area on which the current is incident. The quantity $J(r)$ is considered to be a function of position, r , on the surface, but not of the angular distribution of the neutrons which comprise the incident current. The number of neutrons per second incident on $A(r)$ is $J(r) A(r)$. The neutrons that re-enter the cavity everywhere on the surface contribute in some degree to

$J(r) A(r)$, and this contribution is expressed mathematically by the equation:

$$J(r) A(r) = \int_{\text{all surfaces}} J(r') K(r, r') dA(r') + \int_{\text{source surface}} S(r') L(r, r') dA(r') \quad (T1.1)$$

where

r' is a point on the surface from which neutrons contribute to

$J(r) A(r)$,

$J(r')$ is the neutron current ($n/cm^2 \cdot sec$) incident on the surface at r' ,

$A(r')$ is the area at r' on the surface,

$K(r, r')$ is the kernel defining the contribution that the neutron current $J(r')$ makes to $J(r)$; when r and r' are on the same plane surface, $K(r, r') = 0$,

$L(r, r')$ is the kernel defining the contribution that the source $S(r')$ makes to $J(r)$; when r and r' are on the same plane surface, $L(r, r') = 0$,

$S(r')$ is the surface distributed neutron source ($n/cm^2 \cdot sec$) entering the cavity at r' .

The number of neutrons that contribute to $J(r)$ from the differential area $dA(r')$ is given by $J(r') K(r, r') dA(r')$ and $S(r') L(r, r') dA(r')$, if $dA(r')$ is on the surface of the neutron source. In equation (T1.1), $J(r') K(r, r') dA(r')$ is integrated over all the surfaces of the cavity, and $S(r') L(r, r') dA(r')$ is integrated over only the surface of the neutron source to obtain the total number of incident neutrons at r .

To make clear the physical significance of the kernels, $K(r,r')$ and $L(r,r')$, the behavior of a neutron in the hohlraum assembly will be described. A neutron originates at a point r' on the source surface, and travels in a straight line through the cavity to another surface; $L(r,r')$ is the probability that a neutron starting at r' on the source surface will be incident at the point r on the other surface by traveling in a straight line, and depends on the relative position of r and r' , and also on the angular distribution of the neutrons leaving the source $S(r')$. The neutron, upon reaching the surface, may go through the wall without a collision, or may undergo one or more collisions in the wall. It is either captured in the wall material, or leaks out of the cavity assembly, or returns to the cavity and then impinges upon another surface. The neutron continues to undergo collisions and traversals of the cavity until it is eventually either captured somewhere inside the assembly, or lost outside of the assembly. The kernel $K(r,r')$ defines the probability that a neutron incident on the surface at r' will return to the cavity, pass through it, and then impinge upon the surface at r . If a neutron incident at r' re-enters the cavity by leaving the surface at r'' , for example, the probability that the neutron will then impinge on the surface at r depends on the relative position of r and r'' , and also on the angular distribution of the neutrons re-entering the cavity.

Clearly then, the kernels are very complicated functions, and the integrals would be difficult to evaluate. Even if $K(r,r')$ and $L(r,r')$ could be expressed as easily integrable expressions, the solution of equation (T1.1) for the current $J(r)$ would still offer a strong challenge for even a simple cubic cavity such as that shown in Figure T1.1. Each of the six surfaces has its own coordinate system as shown on the drawing. The

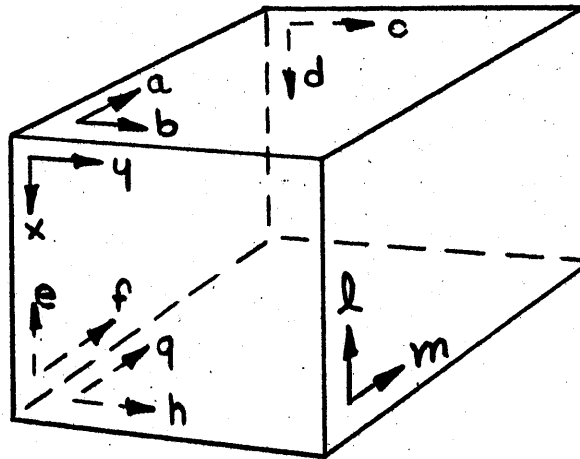


Figure T1.1 Cubic Cavity with a Coordinate System for Each Surface.

source is located on the surface designated by (1,m) and the equation (Tl.2) can be written for the current incident on the (x,y) surface.

$$\begin{aligned}
 J(x,y) A(x,y) = & \iint_{A(a,b)} J(a,b) K(x,y|a,b) dA(a,b) \\
 & + \iint_{A(c,d)} J(c,d) K(x,y|c,d) dA(c,d) + \iint_{A(e,f)} J(e,f) K(x,y|e,f) dA(e,f) \\
 & + \iint_{A(g,h)} J(g,h) K(x,y|g,h) dA(g,h) + \iint_{A(1,m)} J(1,m) K(x,y|1,m) dA(1,m) \\
 & + \iint_{A(1,m)} S(1,m) L(x,y|1,m) dA(1,m) \tag{Tl.2}
 \end{aligned}$$

Similar equations are written for the other five surfaces, and the neutron distribution on all surfaces can be obtained from this set of six integral equations, at least in theory. In practice, however, an equation like equation (Tl.2) is very difficult to solve, and the problem will be treated in another way.

Before discussing the method used to solve equation (Tl.1), it is worth mentioning an analytical treatment of a problem somewhat similar to the present one. Simon and Clifford (14) derived an expression for the neutron transmission through a cylindrical duct having partially reflecting walls and open at the two ends. The equation they solved involves an integration over one variable, the length of the duct, rather than over two variables on each of five surfaces as does equation (Tl.2). Their paper was the only one found that treated analytically the case of multiple scattering from the walls bounding a cavity; the method could not be used because of the greater complexity of the present problem.

Several methods could be used to calculate the flux distribution on the surface of a cavity. One method is to simplify equation (T1.1) by means of suitable approximations and solve for the equilibrium incident current. A second method would be to use a Monte Carlo calculation which follows many neutrons through the cavity assembly and deduces the flux distribution from the history of the neutrons. In a third method, each surface could be divided into small areas, all the neutrons in each area lumped into a group, and the different groups followed around the assembly. A Monte Carlo code, although it can be very accurate, is time-consuming, and should not be used if another method is available which is accurate and simpler. The same is true for the method which follows groups of neutrons in a system in which the neutrons are predominantly scattered rather than absorbed. In the cavity assemblies treated in this study each neutron in a group of neutrons would have to be followed, on the average, through about 10 crossings of the cavity to obtain its complete history, and the calculation would be time-consuming and expensive. Hence, the method suggested first was used, that is, an approximate solution of equation (T1.1) was undertaken.

To solve the general equation (T1.1), the integrals are replaced by summations:

$$J_i A_i = \sum_j^{\text{all surfaces}} J_j A_j K_{ji} + \sum_j^{\text{source surface}} S_j A_j L_{ji} \quad (\text{T1.3})$$

The quantities A_j and A_i are small sub-areas on which the neutron currents J_j and J_i , respectively, are incident, and K_{ji} and L_{ji} define the contribution from A_j to A_i . It is assumed that the incident currents J_i and J_j are constant over the small sub-areas A_i and A_j , respectively.

The kernel K_{ji} is now separated into two factors. The first factor defines the probability that a neutron, incident on a wall in the sub-area A_j , will eventually re-enter the cavity, and the second factor defines the probability that the neutron upon re-entering the cavity will then strike the sub-area A_i . The first factor is called the albedo, β , and the second the "view factor", F_{ji} . Since L_{ji} defines the probability that a source neutron, which enters the cavity through the sub-area A_j , will pass through it and strike the surface within the sub-area A_i , it is the same, by definition, as F_{ji} . On substituting $K_{ji} = \beta_j F_{ji}$ and $L_{ji} = F_{ji}$, equation (T1.3) becomes:

$$J_i A_i = \sum_j^{\text{all surfaces}} \beta_j J_j A_j F_{ji} + \sum_j^{\text{source surface}} S_j A_j F_{ji} \quad (\text{T1.4})$$

Equation (T1.4) is the approximate form of equation (T1.1) used to obtain the flux distribution on the surfaces of the cavity. The sizes of the sub-areas are chosen to make the variation of the current within each sub-area small enough so that the summation is a good approximation to the integration. The magnitude of the variation in the currents that is acceptable will be discussed in Chapters T2 and T3.

The values of the albedos, view factors, and source terms are computed; then equation (T1.4) is written for each sub-area on the surface of the cavity, resulting in a set of simultaneous, algebraic equations. The number of equations in this set is equal to the number of sub-areas on all of the surfaces. This set of equations is solved for the unknowns, the J_i 's, from which the flux distribution can be calculated. Before describing the method of solution and the results obtained, the calculation of the view factors, albedos, and the source will be discussed.

Chapter T2

View Factors

T2.1 Derivation of the General Equation Defining the View Factor

The use of view factors is not new; they have been used extensively in the field of radiant heat transfer, and it is in this field that most of the literature (15,16) on the subject is found. Particles and rays travel in straight lines through a cavity, and the fraction of the radiation transmitted to a given surface bounding a cavity can be obtained by calculating the proper view factor.

While most books on heat transfer contain graphs of view factors for various geometrical arrangements of the emitting and receiving surfaces, the graphs cannot be read with the accuracy needed for the present study. Hence, expressions were derived for the view factors required for the determination of the flux distribution at the surface of a cavity, and numerical values were calculated on an electronic computer. A derivation of the general equation for view factors follows; a more complete discussion of view factors is found in Jacob's "Heat Transfer". (17) For simplicity, we shall use the term "radiation", instead of "number of neutrons".

In Figure T2.1, the view factor F_{12} defines the fraction of the radiation emitted from A_1 which reaches A_2 , so that $J_{out A_1} F_{12}$ is the quantity of radiation arriving at A_2 from A_1 . To derive an expression for F_{12} , the quantity of radiation arriving at A_2 from A_1 must first be written in differential form. For the case of the surface elements dA_1 and dA_2 , shown in Figure T2.2, the radiation striking dA_2 is equal to the fraction of the radiation emitted from dA_1 at the angle ϕ_1 multiplied by the probability of that radiation striking dA_2 . Lambert's Law, which states that the

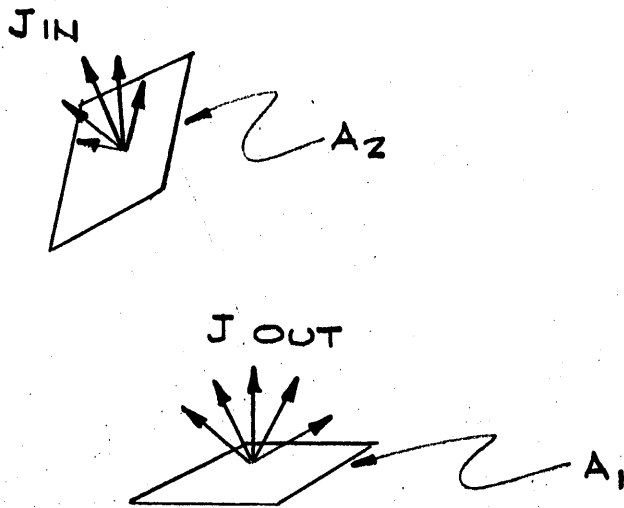


Figure T2.1 General Representation of the Areas A_1 and A_2 for which the View Factor, F_{12} , is derived.

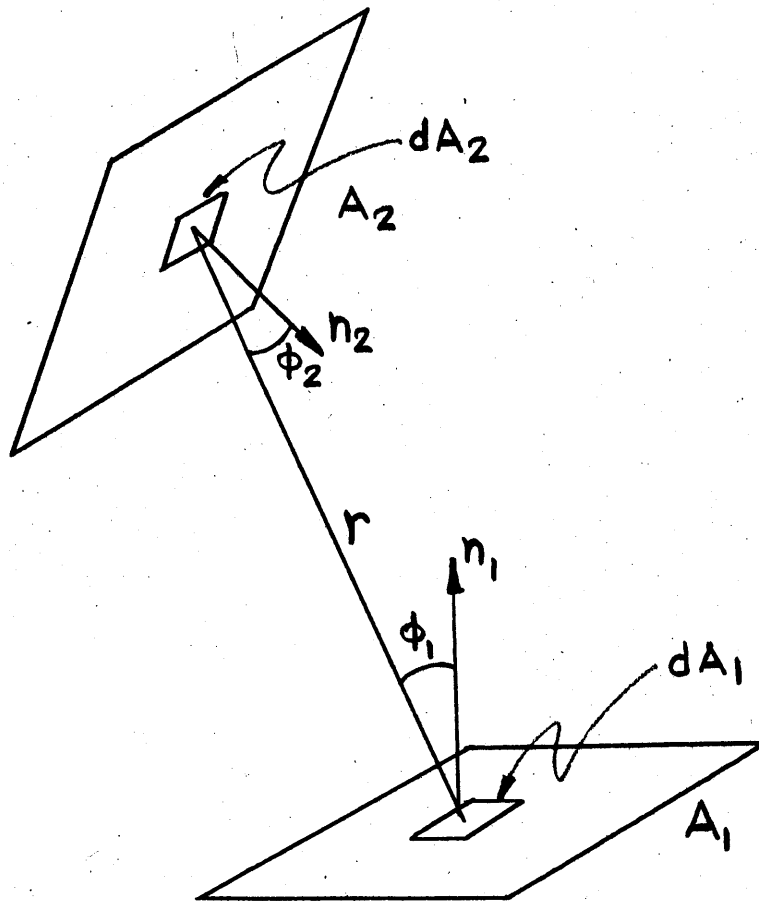


Figure T2.2 The General Representation of the Areas A_1 and A_2 with the Differential Areas, dA_1 and dA_2 .

fraction of radiation emitted from a surface at an angle ϕ_1 to the normal to that surface is proportional to $\cos \phi_1$, is assumed to hold. The validity of this assumption will be discussed at the end of this chapter. The fraction of the radiation emitted from dA_1 at the angle ϕ_1 is then $J_{out} \cos \phi_1 dA_1 / \pi$, where $1/\pi$ is a normalization constant; if $J_{out} \cos \phi_1 dA_1$ is integrated over a closed surface, the total radiation reaching the closed surface is $\pi J_{out} dA_1$, so that the use of the factor $1/\pi$ implies conservation of radiation. The probability that the radiation will strike dA_2 is given by $d\omega_2$, the differential solid angle subtended by dA_2 . The quantity of radiation striking dA_1 from dA_2 is $J_{in} dA_2$, which is given by:

$$J_{in} dA_2 = \frac{J_{out} \cos \phi_1 dA_1 d\omega_2}{\pi} . \quad (T2.1)$$

In equation (T2.1),

$$d\omega_2 = \frac{\cos \phi_2 dA_2}{r^2} , \quad (T2.2)$$

where

r is the distance between dA_1 and dA_2 ,

ϕ_1 is the angle between the normal to dA_1 and r ,

ϕ_2 is the angle between the normal to dA_2 and r ,

J_{in} is the current of radiation arriving at A_2 from A_1 ($n/cm^2, sec$),

J_{out} is the current emitted from A_1 .

Substitution of the expression for $d\omega_2$ into equation (T2.1) gives

$$J_{in} dA_1 = \frac{J_{out} \cos \phi_1 \cos \phi_2}{\pi r^2} dA_1 dA_2 . \quad (T2.3)$$

As mentioned earlier, the current incident on a particular sub-area is assumed constant within that sub-area. It will also be assumed that the current, J_{out} , leaving a given sub-area is constant over the sub-area. The validity of this assumption will be discussed in Section T2.2. Upon integrating equation (T2.3) over A_1 and A_2 , the following result is then obtained:

$$J_{in} A_2 = J_{out} \int_{A_2} \int_{A_1} \frac{\cos \phi_1 \cos \phi_2 dA_1 dA_2}{\pi r^2} \quad (T2.4)$$

Since $J_{in} A_2 = J_{out} F_{12} A_1$, equation (T2.4) becomes

$$F_{12} = \frac{1}{A_1} \int_{A_2} \int_{A_1} \frac{\cos \phi_1 \cos \phi_2}{\pi r^2} dA_1 dA_2. \quad (T2.5)$$

The differential form, $F(d1)2$, the view factor from dA_1 to A_2 is:

$$F(d1)2 = dA_1 \int_{A_2} \frac{\cos \phi_1 \cos \phi_2}{\pi r^2} dA_2. \quad (T2.6)$$

The view factor F_{12} can now be computed for a given geometrical arrangement of A_1 and A_2 .

View factors are required for thirteen distinct geometrical arrangements of A_1 and A_2 , and each of these thirteen view factors must be expressed as a function of the relative positions of A_1 and A_2 . As an example of a geometrical arrangement of A_1 and A_2 , consider the case of two squares, A_1 and A_2 , each having sides whose lengths are expressed as multiples of a unit length L , and situated in perpendicular planes (see Figure T2.3). The view factor, $F_l(I,J,K)$, is expressed as a function of three quantities, I , J , and K , which define the relative positions of

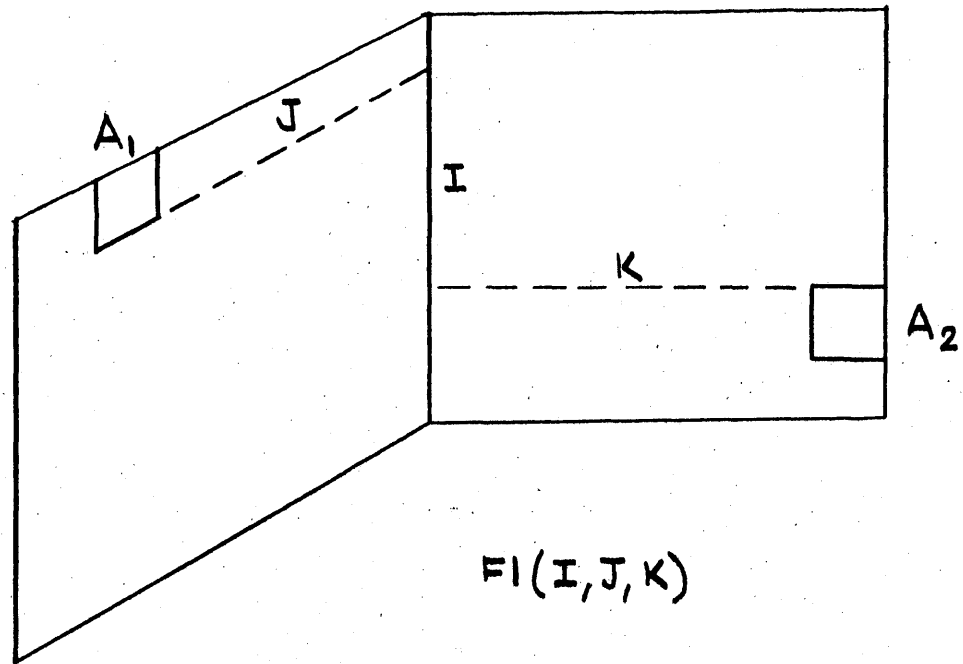


Figure T2.3 The Geometrical Arrangement of A_1 and A_2 Defined by I , J , and K , for $F_1(I, J, K)$.

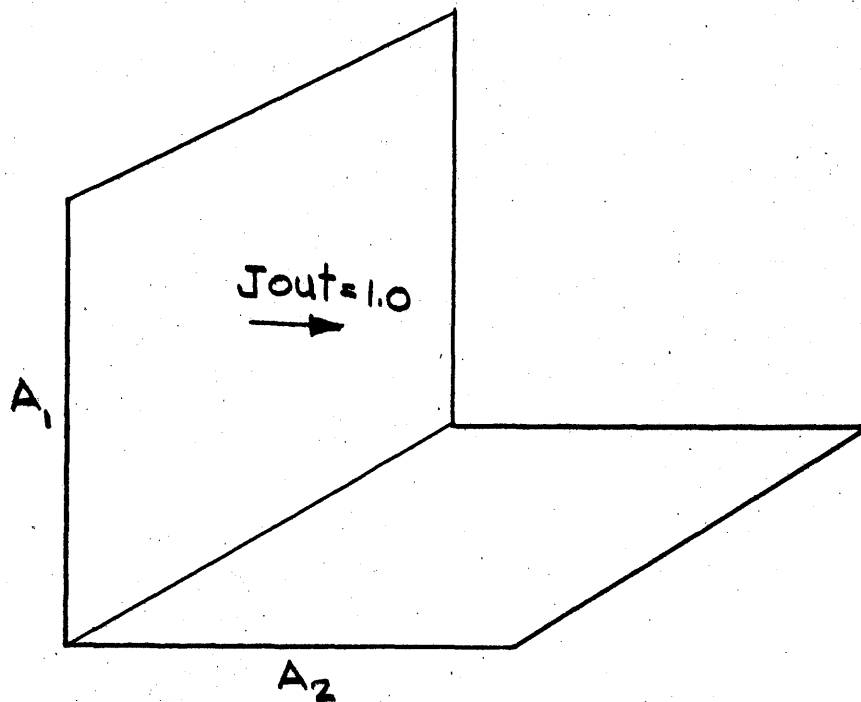


Figure T2.4 The Value of J_{out} is Constant and Equal to Unity on A .

A_1 and A_2 in terms of the unit length, L . The quantity K is the number of unit lengths between A_2 and the intersection of the two perpendicular planes; J is the number of unit lengths between A_1 and the intersection of the two planes, and I is the number of unit lengths along the line of intersection of the two planes in which A_1 and A_2 lie. The quantities I , J , and K uniquely define the view factor for two areas in perpendicular planes.

Since there are 13 different geometrical arrangements, the variables which establish the relative positions of the two areas for each view factor are defined differently, and are illustrated and defined in the appropriate drawing of each geometrical arrangement of A_1 and A_2 .

The derivation of the expressions for the 13 view factors, together with the drawings of the geometrical arrangements of A_1 and A_2 , appear in Appendix B1. The computer codes used to evaluate the view factors are discussed in Appendix B2.

In calculating the flux distribution it is convenient to use one symbol to represent the product of the view factor and the area. The computer codes, therefore, calculate the product, $A_1 F_{12}$, denoted by the symbol V . The quantity V is defined for the case of $F_1(I,J,K)$ as:

$V_1(I,J,K) = A_1 F_1(I,J,K)$. If the area A_1 is a square whose sides are of length L , then $V(I,J,K) = F(I,J,K)$. In all further discussion, the term "view factor" refers to the product $A_1 F_{12}$, unless stated otherwise. The values of V were calculated and punched on IBM cards which serve as input data for the calculation of the flux distribution.

T2.2 Discussion of the View Factors

In deriving the general expression for the view factor, equation (T2.5), two assumptions were made; these will be discussed in this section.

The first assumption is that the outgoing current, J_{out} , is constant over a given sub-area. It is, of course, unrealistic to consider that the current is constant over one sub-area, and then jumps to another constant value in an adjacent sub-area, and the question arises as to how much error is introduced by this assumption. The magnitude of this error is indicated by the use of two examples. In the first example, we consider the two squares shown in Figure T2.4. When the outgoing current on A_1 has a constant value of unity, the current incident on A_2 from A_1 is 0.20004. In Figure T2.5, A_1 is divided into sub-areas, and the outgoing current is varied from 0.95 to 1.05 as shown, but the average value is still unity. The incident current on A_2 from A_1 is now 0.19589, that is, there is a decrease of 2.27 per cent from the previous case. In the second example (see Figure T2.6), A_1 and A_2 are farther apart, and the difference in the current incident on A_2 from A_1 for the same change in the outgoing current is 0.7 per cent. In the first example, the two areas were as close together as possible, and the contribution of A_1 to A_2 (about 20 per cent of the total contribution to A_2) is in error by only 2.27 per cent. The contribution from areas two or three units away is in error by less than one per cent, as shown by the second example. In addition, it will be shown later that J_{out} usually does not vary within a sub-area by more than 10 per cent.

From these examples, it is concluded that the total current incident on a sub-area from all of the other sub-areas on the cavity surface is in error at most by about 1 per cent owing to a 10 per cent variation of J_{out} . In the case of a sub-area near the center of a cavity surface, the nearest sub-area which contributes to its incident current is two or three units

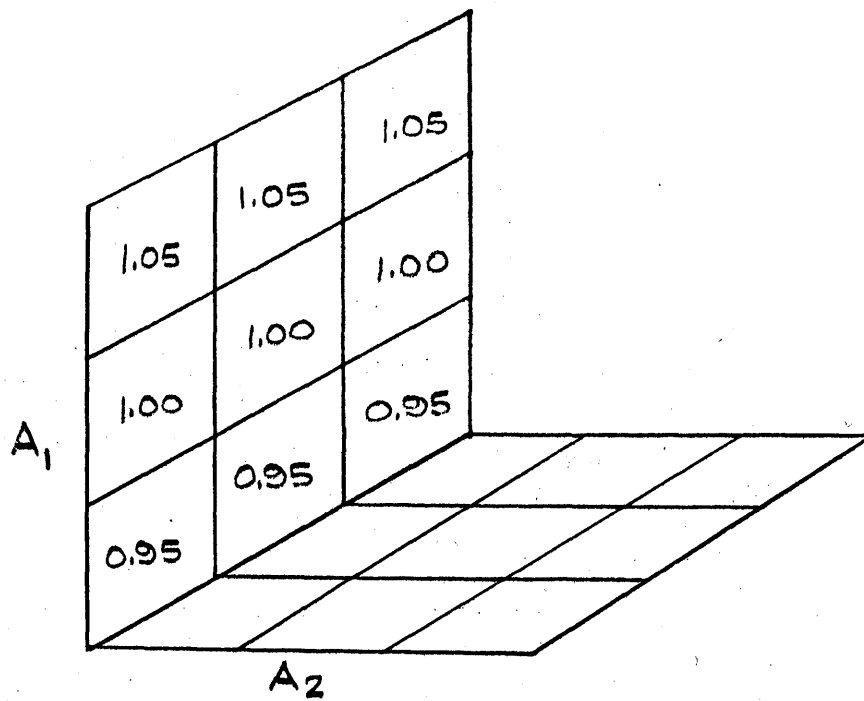


Figure T2.5 The Value of Jout for the Sub-areas varies Over A_1 .

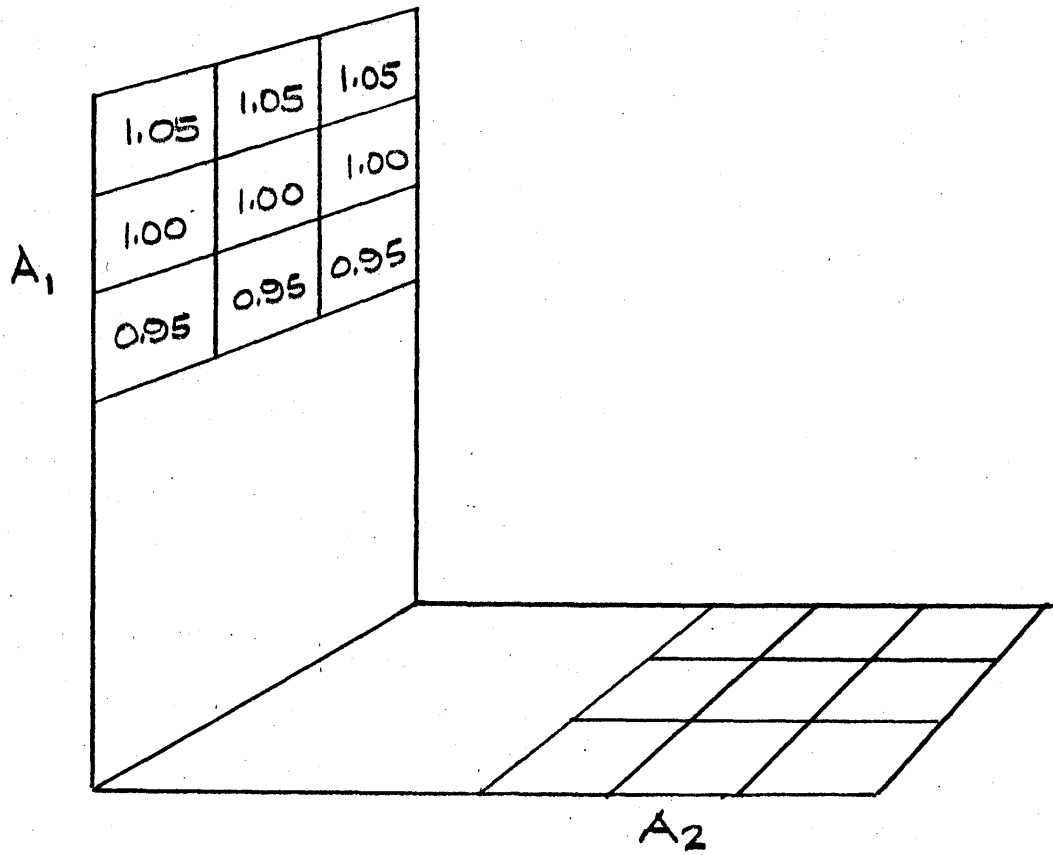


Figure T2.6 The Two Areas, A_1 and A_2 , are Farther Apart than in Figure T2.5. The Value of Jout for the Sub-areas Varies over A_1 .

away, so that the error in the total incident current is less than 0.7 per cent. The worst case was used as an example, the case of a sub-area bordering a corner of the cavity surfaces. If all of the sub-areas have a 10 per cent variation in the outgoing current in such a way that all of the error is in the same direction, the error in the total current incident on a sub-area in a corner is about one to two per cent. This result can be obtained by means of the following rough calculation. Twenty per cent of the incident current is in error by 2.27 per cent, and the rest (80 per cent) is in error by approximately one per cent, resulting in a 1.25 per cent error in the total incident current. It may be inferred from these examples that so long as the sub-areas are made small enough to limit the variation of the outgoing current to 10 per cent, the error introduced by assuming a constant outgoing current is acceptable.

The second assumption in the derivation of equation (T2.5) is that the neutron current leaving a surface has an angular distribution such that Lambert's Law holds. This law states that the amount of radiation leaving a surface at an angle ϕ with the normal to the surface is proportional to $\cos \phi$. According to Jacob (17), diffuse radiation from a surface has a distribution described by Lambert's Law; in diffuse radiation the radiant flux density is equally distributed to all directions of the space. To determine whether or not Lambert's Law may be applied to neutrons leaving a surface of the cavity, the angular distributions of two different groups of neutrons, S and J_{out} , entering the cavity will be examined.

The source neutrons, S , enter the cavity after diffusing through the 52" long, graphite thermal column. Pigford et al (18) measured the angular distribution of the neutrons emitted from the surface of a graphite slab with a neutron source deep inside. They obtained good agreement with the

theoretical distribution obtained from Placzek's solution (19) of the Milne problem. Since the source neutrons entering the cavity are emitted from a large graphite slab with a neutron source deep inside, the angular distribution of these neutrons should be the same as the distribution measured by Pigford et al and calculated by Placzek. Figure T2.7 presents two angular distributions, one obtained from Placzek's calculations, and the other from Lambert's Law. Placzek's distribution shows that the neutrons have a preferentially forward direction. This preference for large values of $\cos \phi$ is reasonable. The neutron population in a graphite slab decreases rapidly near the surface, indicating that some of the neutrons have left the slab without undergoing a collision near the surface. Because the probability of escaping through the surface from a distance x within the slab is proportional to $e^{-\Sigma t x / \cos \phi}$, the neutrons with large values of $\cos \phi$ are more likely to escape. Placzek's distribution is composed of neutrons which have made their last collision near the surface and are isotropically distributed, and neutrons from deeper inside the slab scattered preferentially forward.

The view factors for the source neutrons should be evaluated by using the Placzek distribution. But the algebraic form of this distribution is complicated, and an analytical expression for the view factor cannot be obtained. An approximate method can, however, be used. When $\cos \phi$ in equation (T2.5) is nearly constant in the integration over A_1 and A_2 , the view factor, derived by using Lambert's Law, can be corrected for Placzek's distribution in the following way. Let $V(x,y,z)$ be a view factor calculated from equation (T2.5) and let $P(\cos \phi)$ represent Placzek's distribution. If A_1 and A_2 are distant (5 or more units), the view factor $V'(x,y,z)$ which includes Placzek's distribution may be written:

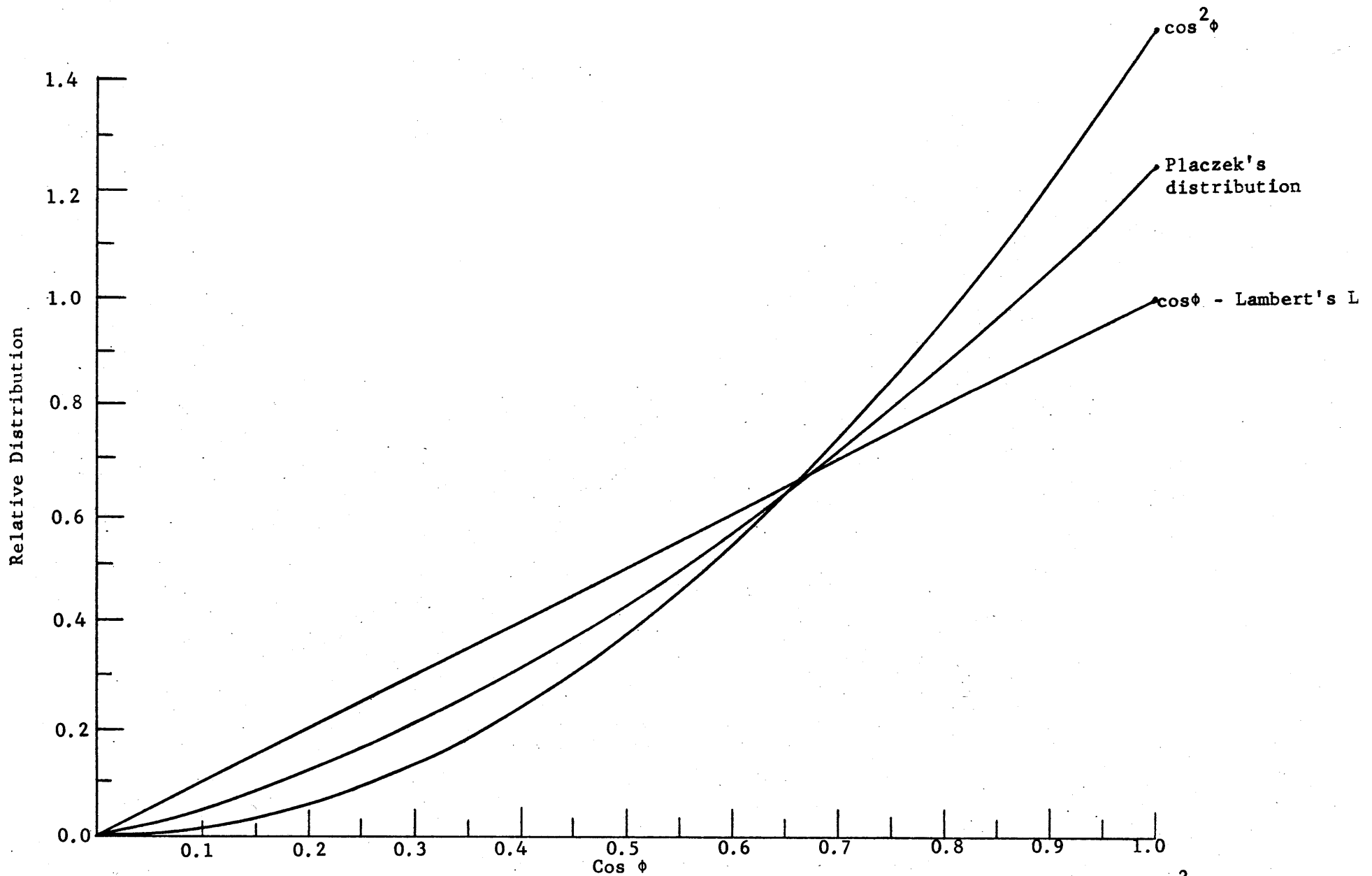


Figure T2.7 The Relative Angular Distribution vs $\cos \phi$ for Placzek's Distribution, $\cos \phi$, and $\cos^2 \phi$.

$$V'(x,y,z) = V(x,y,z) \frac{P(\cos \phi)}{\cos \phi_1} .$$

Suppose that $x = 1$, $y = 3$, and $z = 5$; a line between the centers of A_1 and A_2 forms an angle with the normal whose cosine is 0.8742. From Figure T2.7, $P(\cos \phi) = 1.004$, so that

$$V'(1,3,5) = V(1,3,5) \times 1.1484.$$

The view factors from the thermal column face to the bottom of the honeycomb were corrected in this way for Placzek's distribution. The resulting correction in the flux at the honeycomb, due to the neutron source with the reactor operating at 1 Mw, is shown for the case of 12" sub-areas in Table T2.1, and for 6" sub-areas in Table T2.2. The flux on each of the surfaces must be corrected, and the correction affects, in turn, the flux at the honeycomb. The magnitude of this secondary effect depends upon the particular configuration of the cavity, and will be discussed in Chapter T5.3, where the results for all the different cavities are given.

The second group of neutrons, represented by J_{out} , consists of neutrons reflected from graphite surfaces, in contrast to those that came directly from a neutron source deep inside the graphite thermal column. The angular distribution of such neutrons has not been measured, and we have not been able to find a theoretical treatment which can easily be applied to the present problem. A Monte Carlo code was, therefore, written for this problem; the code has the same mathematical representation of the neutron interaction as does the Milne problem, that is, monoenergetic neutrons undergoing isotropic scattering in a semi-infinite medium.

Table T2.1

Correction to the Flux (1×10^8) on the 12" Sub-areas on the Honeycomb

Due to Placzek's Distribution of the Neutron Source

Front

| | | | | | |
|--------|--------|--------|--------|--------|--------|
| 0.1536 | 0.2666 | 0.3272 | 0.3272 | 0.2666 | 0.1536 |
| 0.1686 | 0.2511 | 0.2955 | 0.2955 | 0.2511 | 0.1686 |
| 0.1527 | 0.2088 | 0.2143 | 0.2143 | 0.2088 | 0.1527 |
| 0.1119 | 0.1686 | 0.1673 | 0.1673 | 0.1686 | 0.1119 |
| 0.1077 | 0.1346 | 0.1459 | 0.1459 | 0.1346 | 0.1077 |
| 0.0843 | 0.1014 | 0.1085 | 0.1085 | 0.1014 | 0.0843 |

Back

Table T2.2

Correction to the Flux (1×10^8) in the 6" Sub-areas on the Honeycomb

Due to Placzek's Distribution of the Neutron Source

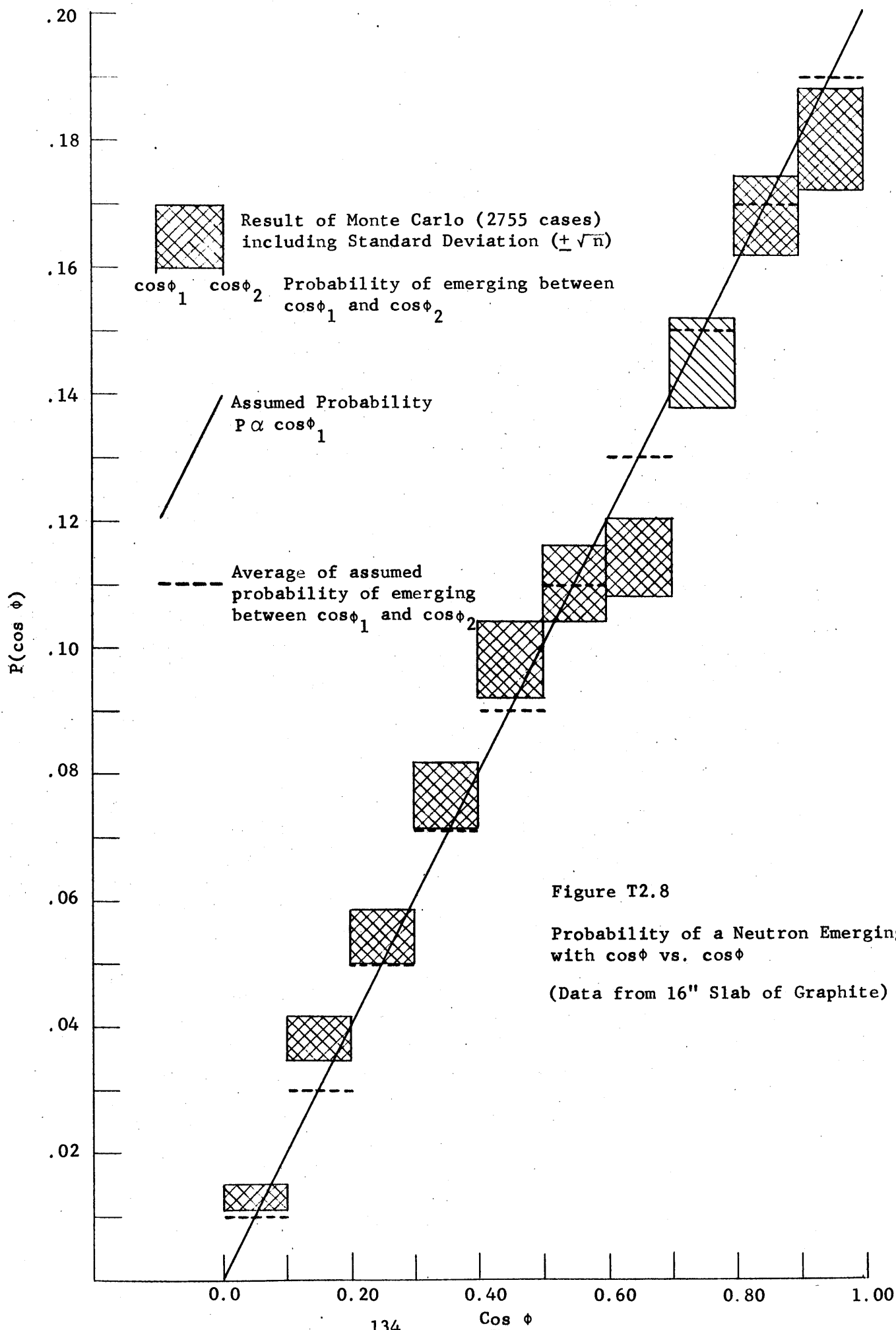
(Only one-half of the surface is shown. The other half is symmetric around the center line.)

| Front | | | | | |
|-------|-------|-------|-------|-------|-------|
| 0.112 | 0.180 | 0.241 | 0.289 | 0.318 | 0.337 |
| 0.132 | 0.191 | 0.249 | 0.292 | 0.323 | 0.333 |
| 0.141 | 0.191 | 0.241 | 0.278 | 0.293 | 0.300 |
| 0.151 | 0.191 | 0.227 | 0.258 | 0.262 | 0.269 |
| 0.149 | 0.185 | 0.210 | 0.233 | 0.232 | 0.237 |
| 0.110 | 0.166 | 0.192 | 0.200 | 0.194 | 0.194 |
| 0.102 | 0.138 | 0.174 | 0.182 | 0.176 | 0.177 |
| 0.095 | 0.126 | 0.155 | 0.163 | 0.158 | 0.158 |
| 0.092 | 0.123 | 0.136 | 0.148 | 0.152 | 0.154 |
| 0.091 | 0.105 | 0.122 | 0.133 | 0.137 | 0.141 |
| 0.090 | 0.099 | 0.105 | 0.111 | 0.115 | 0.120 |
| 0.070 | 0.079 | 0.092 | 0.097 | 0.099 | 0.100 |

Back

Since the theory of the Milne problem could be applied successfully to the problem of the angular distribution of the neutrons emerging from the surface of a reasonably large block of graphite with a source deep inside, it was thought that a directly analogous theoretical treatment with only the source changed should give the information necessary for approximating the angular distribution of the current re-entering the cavity, J_{out} . The Monte Carlo code was applied to the problem of a beam of neutrons with an isotropic angular distribution incident on the surface of a graphite slab, and the cosine of the angle of emergence was recorded for each returning neutron. The justification for the assumption of an isotropic incident beam will be given below. A complete description of the code is found in the next chapter. The values of the cosine of the angle of emergence were divided into ten groups (0.0 to 0.10, 0.10 to 0.20, etc.) and the number of neutrons in each group was obtained from the output information. The probability of a neutron emerging in any one of these groups was calculated and the results were plotted as a function of the cosine of the angle (see Figure T2.8). The assumed distribution from Lambert's Law is also plotted along with its average value in each of the ten groups. The average value of the assumed distribution lies within the standard deviation of the Monte Carlo results in five of the groups and is close in two other groups. Because of limitations on machine time, only 2755 neutrons were used to calculate the probability, so that the standard deviation is large. However, the results do show that the calculated distribution is close to that given by Lambert's Law, and may be approximated by using that law.

It seems reasonable that the neutrons re-entering the cavity should be more evenly distributed in angle than those which originate from a neutron source deep inside the graphite. The re-entering neutrons consist



mainly of neutrons that are incident on the surface and are then scattered just below the surface. This fact is shown by the Monte Carlo results: one-fourth of the incident neutrons return to the cavity after a single collision and about two-thirds of the returning neutrons have suffered less than eight collisions in the graphite. Since most of the neutrons comprising the outgoing current make their last collision near the surface, the forward direction is not nearly so preferred as in the Placzek distribution.

In the cavity assembly for which the flux distribution was calculated, the neutrons incident upon any sub-area arrive from all of the sub-areas on the other surfaces. The neutrons may, therefore, be incident on the sub-area with any angle between 0° and 90° . The exact distribution of the incident neutrons has not been obtained from either the theoretical or experimental results. The theoretical results do show, however, that the neutrons are distributed fairly uniformly on all of the surfaces, so that no angle of incidence should be strongly preferred for any sub-area. As will be seen in the next chapter, the value of the albedo for graphite is only slightly affected by the distribution of the incident neutrons. It may also be argued that the angular distribution of the neutrons leaving the graphite is also only slightly dependent upon the angular distribution of the incident neutrons. Because of the limitation on computer time, the magnitude of this dependence was not investigated. In view of the above discussion, however, it was thought that the assumption of an isotropic beam source would not introduce any significant error. The excellent agreement ultimately found between theory and experiment supports this statement.

Lambert's Law describes an angular distribution similar to that produced by the Monte Carlo results and has an algebraic form which allows for an analytical solution of the view factor equation. Hence, the distribution of the re-entering neutrons, J_{out} , is approximated by assuming that Lambert's Law holds.

At this point it is of interest to return to the first discussion of the view factor (see Chapter T1). In deriving equation (T1.4), L_{ji} was equated to F_{ji} . It may seem that they are equal by definition because both express the fraction of neutrons (J_{out} for F_{ji} and S for L_{ji}) which leave the sub-area A_j and strike the sub-area A_i . They have different numerical values, however, because J_{out} and S have different angular distributions.

T2.3 Testing for Error in the View Factors

Most of the values of $V1$ and $V2$ and the values of all of the other eleven view factors were calculated for the first time in the present study. To insure that the numerical values of the view factors are correct, the equations and computer programs were checked in seven ways:

- (1) The value of each view factor must lie between 0.0 and 1.0.

Most errors in the equations or computer programs for the view factors result in a few numbers of a large array which are negative or greater than unity. All view factors were, therefore, scanned to be sure they lay within the value of 0.0 and 1.0.

- (2) The symmetry of $V1(I,J,K)$ in the J and K directions and of $V2(I,J,K)$ and $V12(I,J,K)$ in the I and J directions affords a method of verifying both the equation and the numerical value of these view factors. These variables were interchanged in the algebraic and FORTRAN equations

for V_1 , V_2 , and V_{12} , without altering the form of the equation. The numerical values of each symmetrical pair of these view factors were found to be identical. The requirement of symmetry was, therefore, fulfilled in these cases.

(3) The numerical values of all view factors should decrease as the distance between the two areas increases, if $\cos \phi_1$, and $\cos \phi_2$ remain constant. Several values of each view factor have been successfully checked for this type of consistency.

(4) The equations for special cases of V_1 and V_2 appeared in Jacob's "Heat Transfer". For instance, equation (B1.3) was written with $I = 0$, $J = 0$, $K = 0$, and was found to agree with the corresponding equation in Jacob.

(5) The equations (B1.3) and (B1.6) were evaluated by hand calculations for several values of I , J , and K , and compared to the values obtained with the computer; the values were in close agreement. The FORTRAN equation for each view factor was solved by a hand calculation for a number of cases and agreed with the computer results. A graphical integration was performed and found to agree with the numerical integration in the code for $V_4(1,1,1)$.

(6) When the two areas for which the view factor is calculated are distant, the following approximations may be made:

$$\frac{1}{2} V_1(I,J,K) \approx V_4(I,J,K) \approx V_5(I,J,K)$$

$$\frac{1}{2} V_2(I,J,K) \approx V_{12}(I,J,K) \approx V_{13}(I,J,K) = V_9(I,J,K)$$

The results of the computer calculations agreed with these approximations.

(7) The sum of the view factors from all of the sub-areas on a closed surface to any sub-area is equal to unity. This sum was computed for all sub-areas in the parallelepiped and 45° cavities, for which the flux distribution was computed; this sum differed from unity by 0.00008000 in the worst case.

Chapter T3

Calculation of the Albedo and Discussion of the Neutron Source

T3.1 Calculation of the Albedo

In equation (T1.4) the number of neutrons arriving at A_i from A_j is written as $\beta_j J_j F_{ji} A_j$, if A_j does not include a source. The view factor, F_{ji} , is defined as that fraction of the current leaving A_j which is incident upon A_i . Thus, $\beta_j J_j$ must represent the magnitude of the current re-entering the cavity through A_j , and corresponds to J_{out} in the derivation of the view factor equation. In this model the term, β_j , the albedo, is then defined as the ratio of the outgoing to incident currents in the sub-area A_j . The model assumes, therefore, that the current re-entering through A_j may be expressed as a function of the current incident on A_j and not of the currents incident on adjoining sub-areas. The validity of this assumption is discussed later in the chapter.

The albedo for a particular sub-area on the surface of the cavity depends upon several factors. One factor is the nuclear properties of the wall materials, and another is the thickness of the wall. The location of the sub-area is also a factor: if the sub-area borders the edge of the surface, the albedo is smaller than if the sub-area is near the center of the surface. The reason for a smaller albedo near the edges of a surface is that some of the incident neutrons, instead of re-entering the cavity, leak through the sides of the wall and escape from the assembly. Since the albedo depends on where the incident current strikes the surface, it must be averaged over a sub-area. As was seen in the last chapter, the angular distribution of the re-entering neutrons is needed in order to calculate the view factor. Also, the effect of the angular distribution of the incident current on the numerical value of the albedo is of interest.

A Monte Carlo code was written (a) to obtain the average value of the albedo for each of the sub-areas on the cavity surface, (b) to investigate the validity of expressing the albedo of a sub-area as a function of the current incident only upon that sub-area, (c) to obtain the angular distribution of the re-entering current, and (d) to study the effect of the angular distribution of the incident current.

The following information is printed out by the Monte Carlo code:

- (1) The number of neutrons incident at a specified point on the surface of a slab,
- (2) The number of neutrons that return through the same surface on which they were incident,
- (3) The location where each neutron leaves the surface,
- (4) The cosine of the angle at which each neutron leaves the surface,
- (5) The cosine of the angle at which each neutron strikes the surface.

The code was applied to slabs of various materials and dimensions, and for various locations of the incident neutrons.

The ratio of (2)/(1) is called the reflectivity in this study. The reflectivity is then the fraction of neutrons incident at a point on the surface, which return through the same surface. The albedo of a sub-area, which was defined earlier in this chapter, is obtained by averaging the reflectivity over the sub-area. The other information desired of the Monte Carlo code (b, c, and d) is given directly by the data in groups (3), (4), and (5) above. The interpretation of this information is discussed later in the chapter.

The model for neutron interaction used in this code assumes isotropic scattering in the lab-system for a one-velocity group of neutrons.

Graphite scatters neutrons almost isotropically in the lab-system, so that isotropic scattering is frequently assumed for graphite. (20) Since the cadmium ratio measurements (see Chapter E5) show that the neutrons entering the cavity from the thermal column are well thermalized, it is not necessary to include slowing down in the code. The model is the same as that used in the Milne problem, the solution of which has been found to be accurate for predicting the spatial and angular distribution of neutrons in a large slab of graphite. The solution of the Milne problem for spatial and angular distribution near the surface of a slab must be accurate in order to determine the albedo; this has been found to be the case since the extrapolated distance and angular distribution of the flux at the surface are accurately predicted by the solution of the Milne problem. In view of the above observations, it was thought that a Monte Carlo code based on this model for neutron interaction should be able to give the information listed above.

In the Monte Carlo code, a beam of neutrons is incident on a rectangular slab and the neutrons are followed, one by one, through the slab until they leave. No neutron absorption is included in the code because the slab material was usually graphite which has a very small ratio of absorption to scattering (5.9×10^{-4}). A correction for absorption was made later, but was less than 1 per cent of the value of the reflectivity. Because the neutrons are assumed to scatter isotropically in the lab-system, there is no need to use a center-of-mass coordinate system. The coordinate system used defines the dimensions of the slab and also the positions of the neutrons in the slab. The surface of the slab on which the neutrons are incident is divided into squares and the position at which a neutron

enters and leaves the surface is defined in terms of the square through which it passes. A drawing of the slab which includes the squares drawn on the surface and the coordinate system appears in Figure T3.1.

The flow sheet for the code is shown in Figure T3.2. The input data contain the following information: the number of neutrons to be followed, the number of squares in the y,z plane, the location of the incident beam, the dimensions of the squares in collision mean free paths (Σt^{-1}), the thickness of the slab in collision mean free paths, and three optional transfers. The computer first clears the storage locations in which the history of the neutrons will be recorded. The dimensions of the slab in the y,z plane and the position of the incident beam are calculated in terms of collision mean free paths. The incident beam is always located at the center of the designated squares. Now a neutron is ready to be followed through the graphite. The initial values of x,y,z, the location of the beam on the surface (x=0) is stored, and an isotropic or unidirectional beam is selected. The value of $\cos \phi_x$, the cosine in the x direction, is selected from a random number between 0.0 to 1.0 for an isotropic source. The random number generator is an MIT library subroutine (21) which produces random numbers between zero and one. The crow flight distance in collision mean free paths is obtained from the log of a random number. The other directional cosines, $\cos \phi_y$ and $\cos \phi_z$, are randomly selected by means of the semi-circle technique. (20) From the directional cosines and the crow flight distance, the location in terms of x, y, and z of the next collision is calculated. The computer then determines if this new location is within the slab. If it is, the procedure is repeated until the neutron escapes. The value of $\cos \phi_x$ is randomly selected

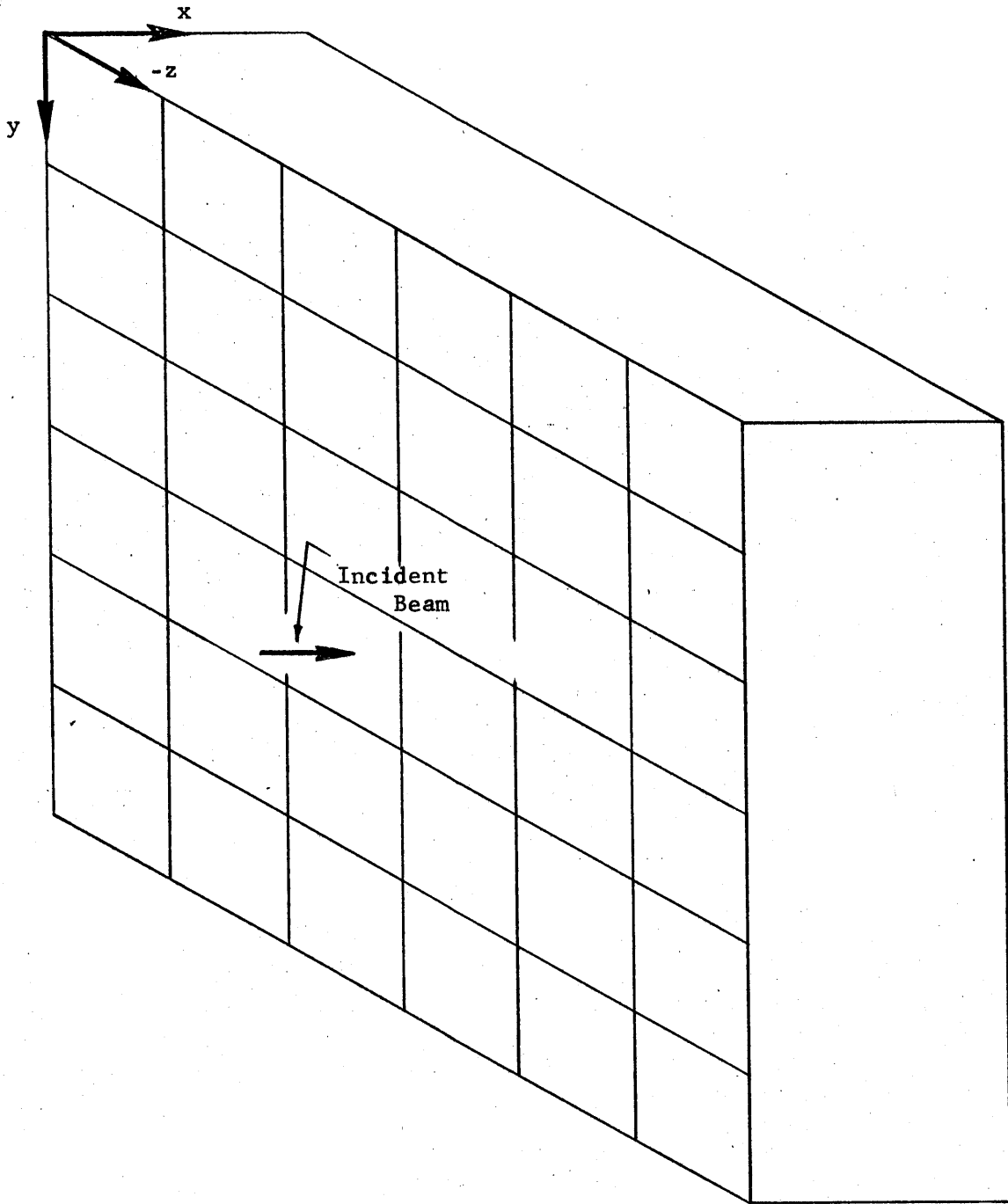


Figure T3.1 The Slab with the Coordinate System, Squares and Direction of Incident Neutrons Shown.

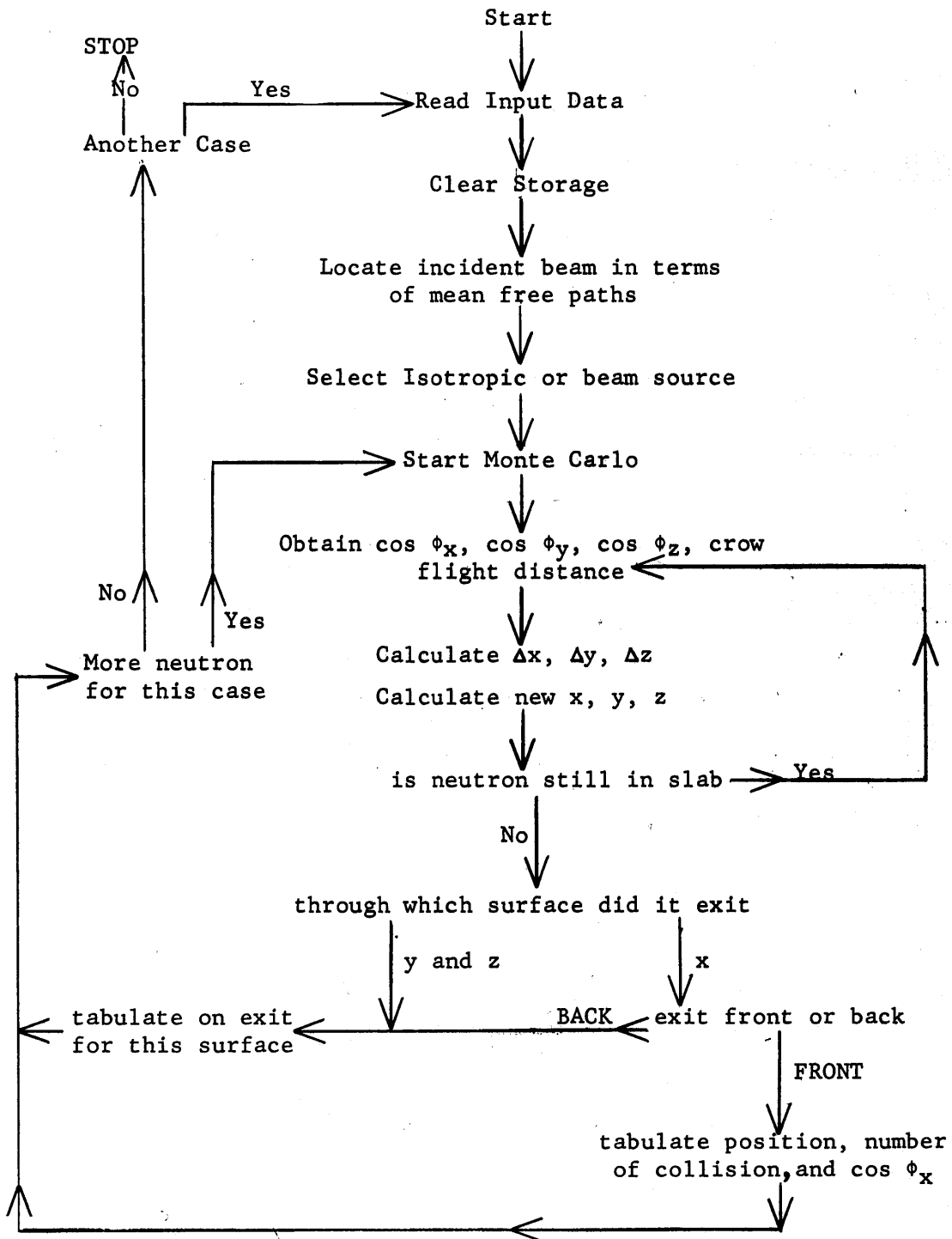


Figure T3.2 Flow Diagram for the Monte Carlo Code which Calculated the Reflectivity

between 1.0 and -1.0 after the first collision. If the neutron is not within the slab, a test is made to determine the surface through which the neutron left. If the neutron left the surface on which it was initially incident before leaving any other surface, the following information is recorded: the square through which it left, the initial and final value of $\cos \phi_x$, and the number of collisions which it suffered before leaving. If the neutron leaves through another surface, it is added to those which have previously left through that surface. After the information about a departing neutron has been recorded, the next neutron is followed, starting from the point of incidence on the surface. After the desired number of neutrons has been followed, the stored history is printed out and the program gives an option of doing another Monte Carlo calculation or stopping.

One part of the data from the Monte Carlo code predicts the fraction of the incident neutrons that return through the surface on which they were incident. The results of the program for different materials, different dimensions of the slab, and different locations of the incident beam are tabulated in Table T3.1. The final value of the reflectivity has been corrected for absorption by the procedure described next.

Let the number of collisions which a neutron suffered before returning be n , which is denoted in the code by ICOL and is part of the output information. The probability, P , that a neutron has suffered n collisions and has not been absorbed is

$$P = (1-q)^n,$$

where q is the probability of absorption per collision; q is equal to $\bar{\sigma}_a/\sigma_t$ where $\bar{\sigma}_a$ is the average microscopic cross section and σ_t is the

Table T3.1

Values of the Reflectivities for the 21 Cases of the Monte Carlo Code

| Case No. | Material | Σ_T (cm ⁻¹) | Dimensions of Slab (in.) | | | Position of Source (in.) | | Reflectivity | Reflectivity (including absorption) |
|----------|------------|--------------------------------|-----------------------------|----|----|-----------------------------|----|--------------|---|
| | | | x | y | z | y | z | | |
| 1 | Graphite | 0.385 | 16 | 72 | 72 | 2 | 6 | 0.6870 | 0.6844 |
| 2 | Graphite | 0.385 | 16 | 72 | 72 | 2 | 18 | 0.7070 | 0.7037 |
| 3 | Graphite | 0.385 | 16 | 72 | 72 | 6 | 6 | 0.8230 | 0.8189 |
| 4 | Graphite | 0.385 | 16 | 72 | 72 | 6 | 18 | 0.8660 | 0.8550 |
| 5 | Graphite | 0.385 | 16 | 72 | 72 | 6 | 30 | 0.8590 | 0.8595 |
| 6 | Graphite | 0.385 | 16 | 72 | 72 | 18 | 18 | 0.9170 | 0.9065 |
| 7 | Graphite | 0.385 | 16 | 72 | 72 | 18 | 30 | 0.9140 | 0.9035 |
| 8 | Graphite | 0.385 | 16 | 72 | 72 | 30 | 30 | 0.9220 | 0.9137 |
| 9 | Graphite | 0.385 | 12 | 72 | 72 | 6 | 18 | 0.8450 | 0.8393 |
| 10 | Graphite | 0.385 | 12 | 72 | 72 | 6 | 30 | 0.8510 | 0.8460 |
| 11 | Graphite | 0.385 | 12 | 72 | 72 | 18 | 18 | 0.8900 | 0.8837 |
| 12 | Graphite | 0.385 | 12 | 72 | 72 | 30 | 30 | 0.9030 | 0.8944 |
| 13 | Graphite | 0.385 | 8 | 36 | 72 | 2 | 6 | 0.6840 | 0.6817 |
| 14 | Graphite | 0.385 | 8 | 36 | 72 | 2 | 18 | 0.7010 | 0.6955 |
| 15 | Graphite | 0.385 | 8 | 36 | 72 | 2 | 30 | 0.6950 | 0.6925 |
| 16 | Graphite | 0.385 | 8 | 36 | 72 | 6 | 6 | 0.8080 | 0.8045 |
| 17 | Graphite | 0.385 | 8 | 36 | 72 | 6 | 18 | 0.8320 | 0.8274 |
| 18 | Graphite | 0.385 | 8 | 36 | 72 | 6 | 30 | 0.8320 | 0.8280 |
| 19 | Graphite | 0.385 | 8 | 36 | 72 | 18 | 18 | 0.8650 | 0.8562 |
| 20 | Al (Boral) | 0.098 | 1/8 | 72 | 72 | 18 | 18 | 0.0480 | 0.0412 |
| 21 | Cadmium | - | - | - | - | - | - | - | 0.0005 |

total microscopic cross section. Since the neutrons are well thermalized, the absorption cross section is averaged over a Maxwell-Boltzmann distribution at room temperature. For graphite $q = 5.908 \times 10^{-4}$ and, since $q \ll 1$, $(1-q)^n$ may be approximated by $1-nq$:

$$P = (1-q)^n \cong (1-nq).$$

The total number of neutrons absorbed is equal to the product of the total number of collisions and q . If M is the total number of returning neutrons, with absorption neglected, and if n_i is the number of collisions suffered by the i^{th} neutron, the number of neutrons, M' , which return if absorption is included, is

$$M' \cong M \left[1 - \left(\sum_i n_i \right) q \right]$$

The results of the Monte Carlo code indicated that when the neutrons are incident on a graphite surface at a point 30" or more away from any edge, only one out of 1000 neutrons leak out the side, so that the surface is essentially infinite in area. For the case of infinite surface area, reflectivity and albedo are identical. The albedo can be obtained from diffusion theory for the case of a slab of finite thickness, but of infinite area. The equation for the albedo from diffusion theory is:

$$\beta = \frac{J_{\text{out}}}{J_{\text{in}}} = \frac{1 - 2\kappa D \coth \kappa a}{1 + 2\kappa D \coth \kappa a},$$

where

$\kappa = 1/L =$ reciprocal of the diffusion length,

$D =$ diffusion coefficient,

$a =$ thickness of the slab.

If $L = 50$ cm, and $D = 0.01444$, which are consistent with the values of

$\bar{\sigma}_a/\sigma_s$ and σ_s used in the Monte Carlo code, the albedo for a 16" thick graphite slab is 0.9175 and for a 12" thick graphite slab is 0.8991. The albedo is not sensitive to the value of L: if $L = 48$, the albedo changes only by 0.25 per cent. The Monte Carlo code, using 1000 neutrons in each case, predicts values of the albedo of 0.9137 and 0.8944, respectively, both of which agree with diffusion theory within the standard deviation of the Monte Carlo results (± 0.0333).

The value of reflectivity obtained from the Monte Carlo code for twenty-one different cases is presented in Table T3.1. As mentioned previously, the albedo, β_j , as it is used in equation (T1.4), is equal to the ratio of the outgoing to incident current in the sub-area, A_j . Hence, the reflectivities in Table T3.1 must be averaged over the sub-areas in such a way that $\beta_j J_i A_i$ is equal to the number of neutrons re-entering the sub-area through A_j . Since J_j is assumed constant over A_j , and β_j is considered to be a function of the current incident only on A_j , the reflectivity is weighted only with the area A_j . The values of the reflectivity obtained from the above data are plotted as a function of the location of the incident beams and the average value of the albedo is obtained by a graphical integration over the sub-area in question.

The reflectivity of an incident beam varies slowly over the surface of a graphite slab, with the exception of a neutron beam incident within 6" of an edge of the surface. Because of this slow variation, the graphical integration can be performed accurately. The average values of the albedo, obtained by the graphical integration of the reflectivities, are given in Figures T3.3 through T3.7 for 8", 12", 16" thick graphite slabs. The average values of the albedo for the 8" and 16" slabs are given for 4"

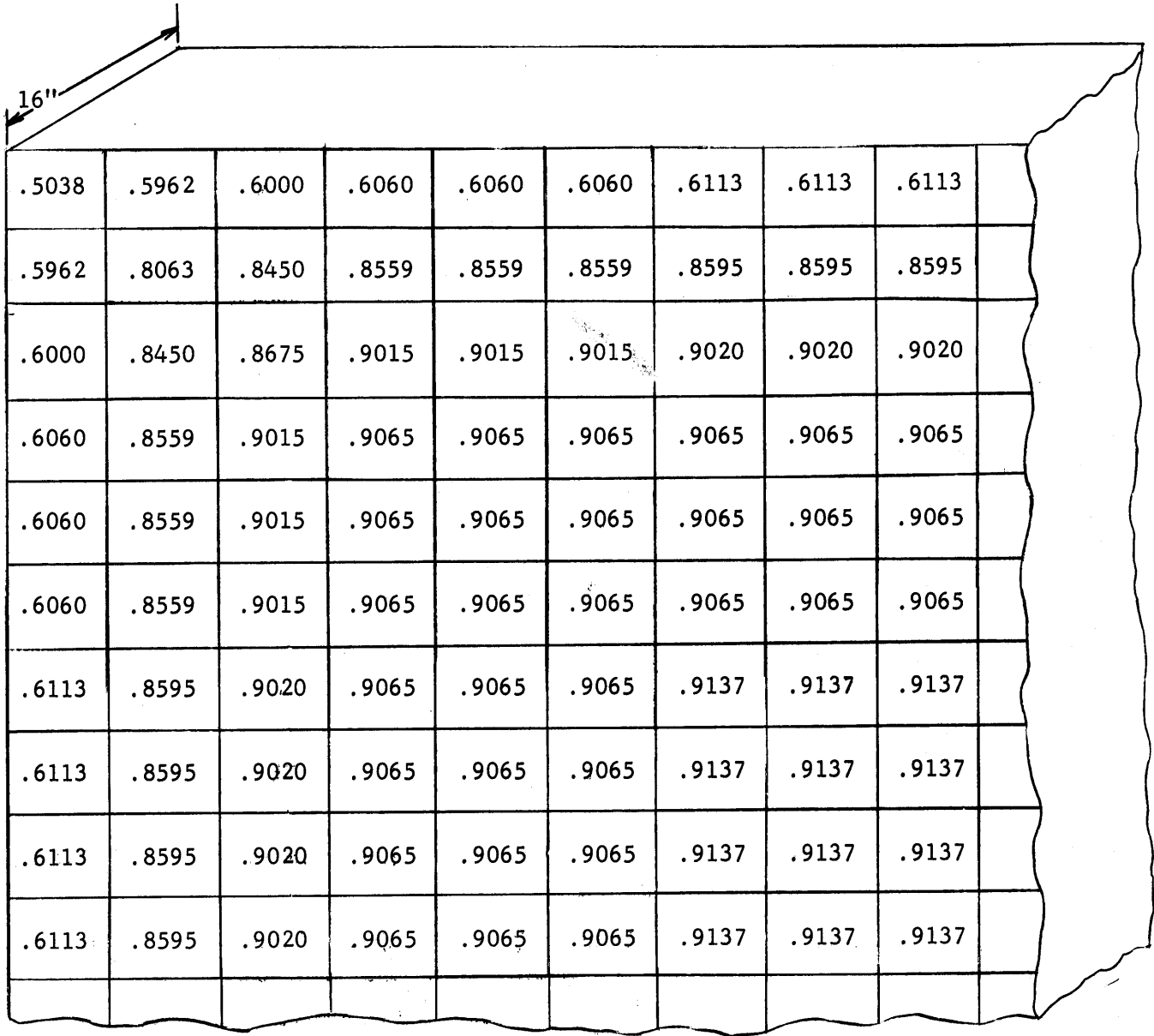


Figure T3.3 Average Albedo for Surface of a 16" Thick, Infinite Area, Graphite Slab Divided into 4" Sub-Areas
Average Albedo is Shown for Each Sub-Area

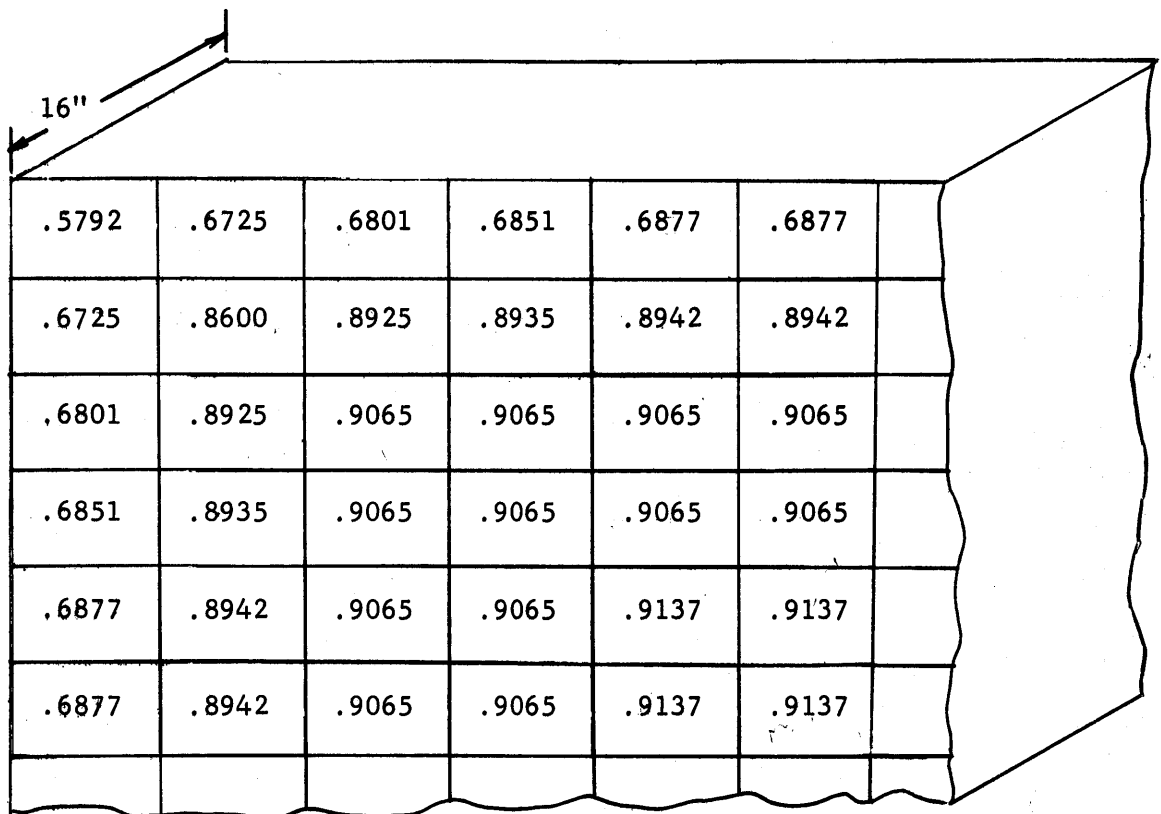


Figure T3.4 Average Albedo for 6" Sub-Areas on a 16" Thick, Infinite Area Graphite Slab

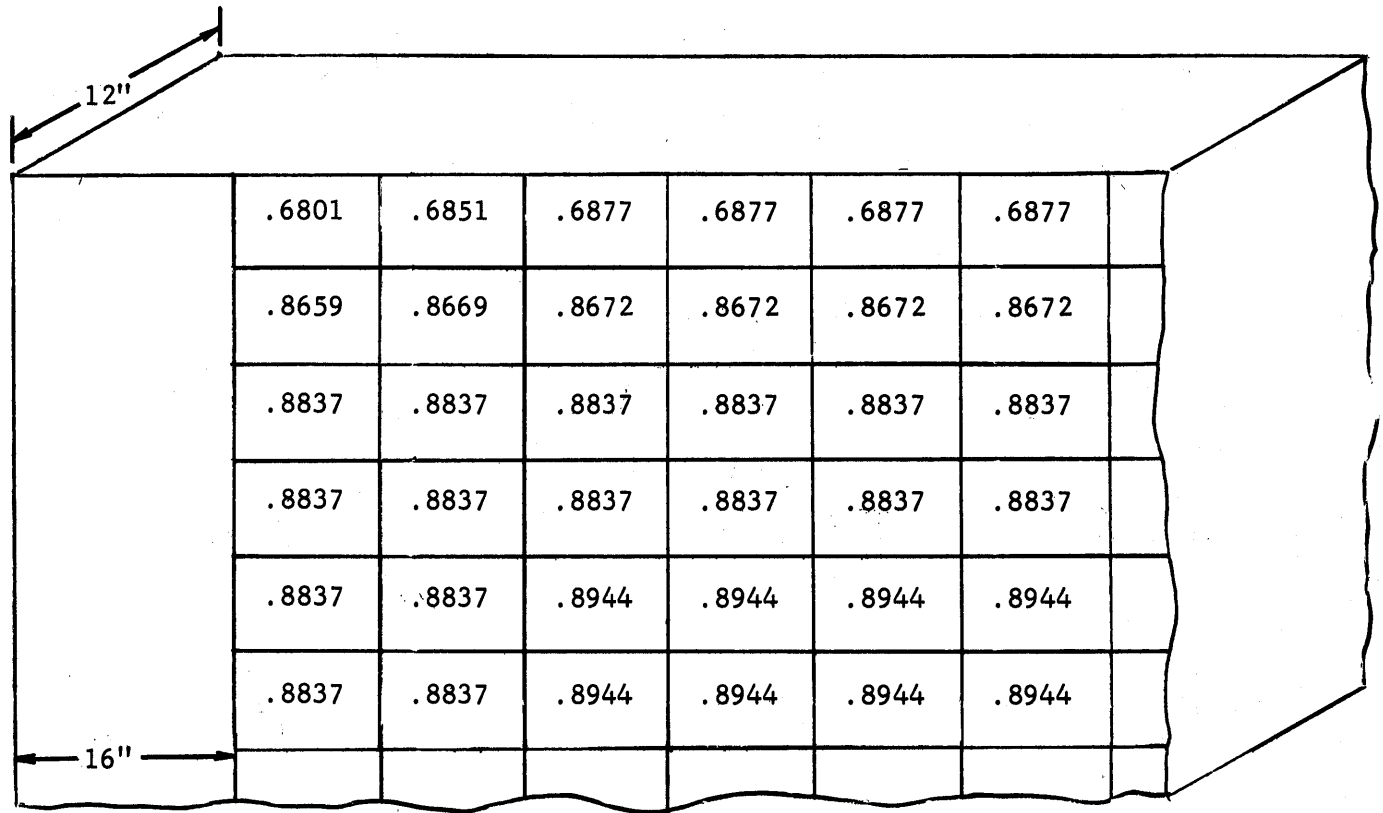


Figure T3.5 The Average Albedo for 6" Sub-Areas on 12" Thick Graphite Slab Surface of the Slab is Infinite in Area with 16" Border on the Left.

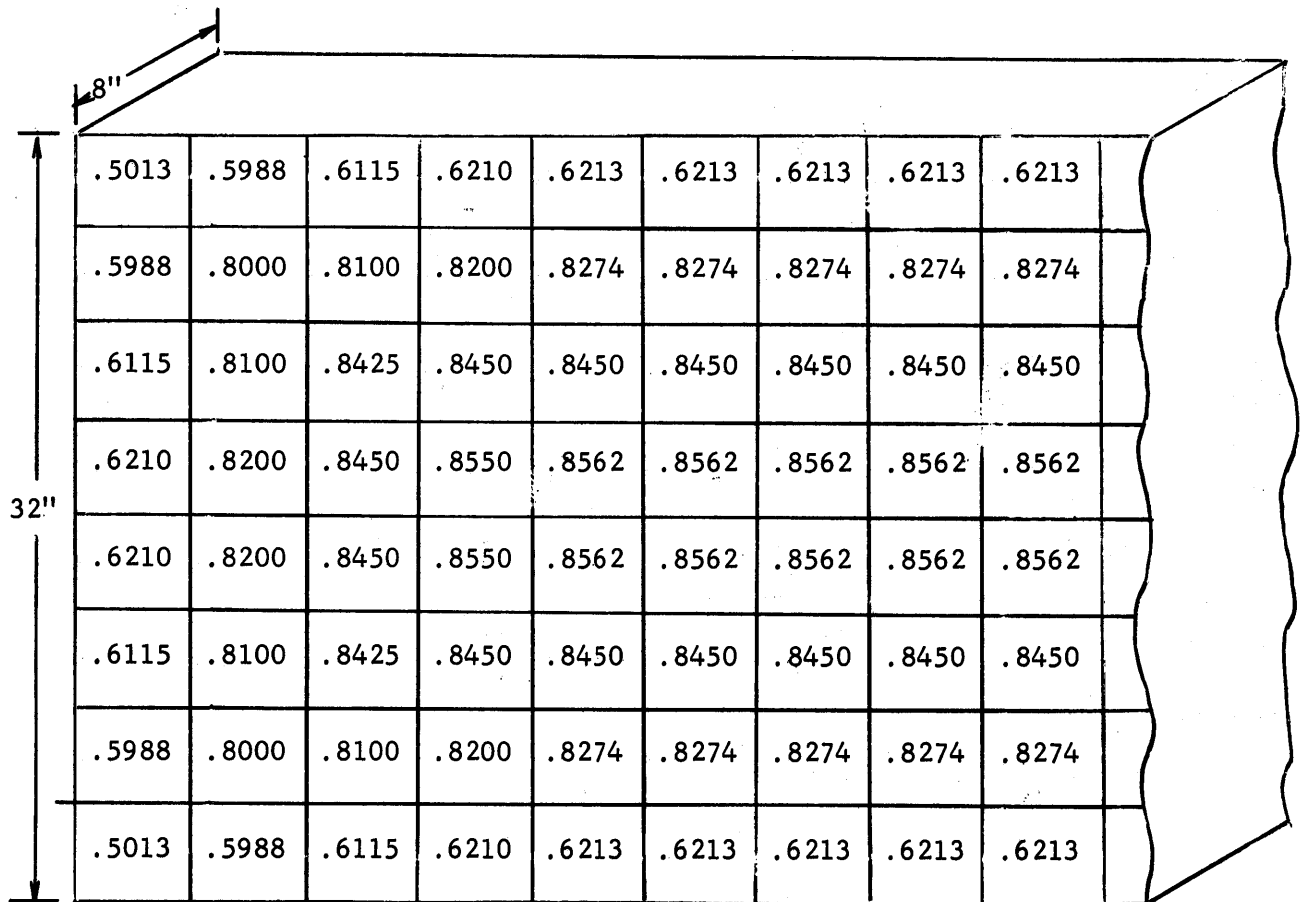


Figure T3.6 Average Albedo for 4" Sub-Areas on the Graphite Frame which is 8" Thick, 32" Wide, 72" Long

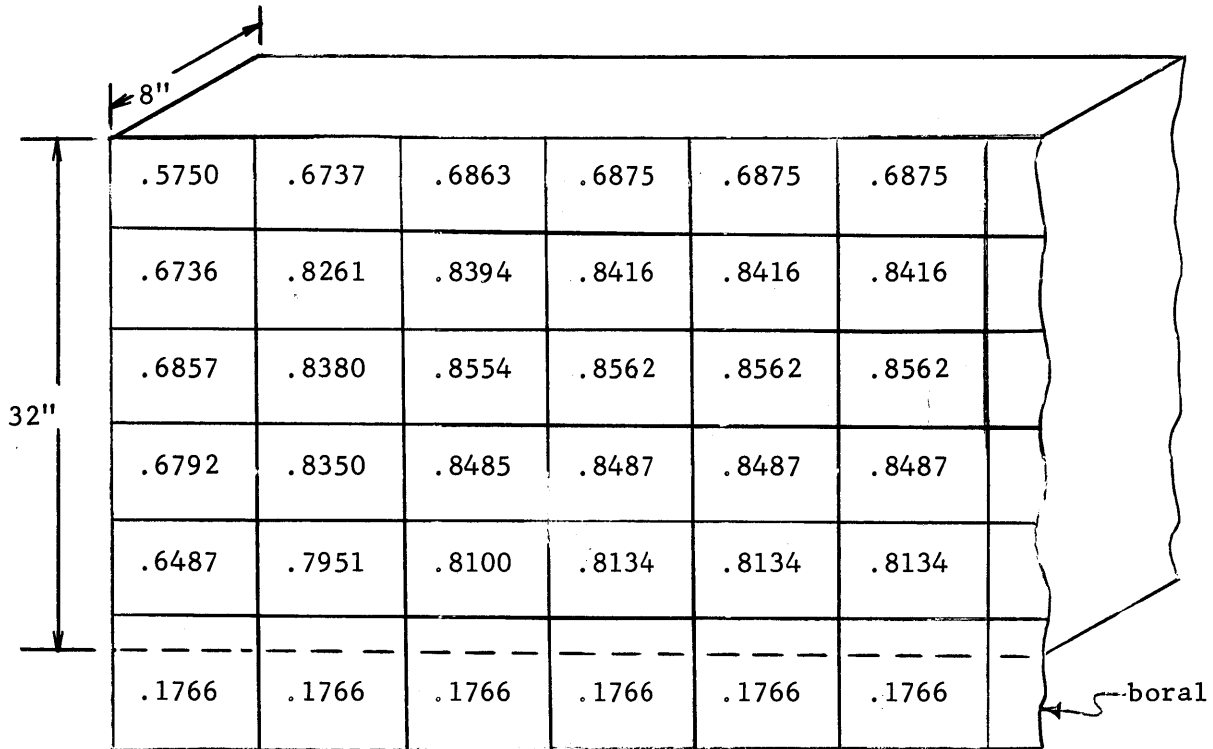


Figure T3.7 Average Albedo for 6" Sub-Areas on 8" Thick Graphite Frame (32"x72")
 The Bottom Row of Sub-Areas is a Combination of Graphite and Boral.

and 6" square sub-areas. For the 12" slab, only 6" square sub-areas were used.

The average values of the albedo given in these figures are used to assign the proper albedo to the sub-area on the cavity surfaces. As an example, consider a 6" sub-area on the cavity surface which is 6", 12", 54", and 60", respectively, from the four edges of a 72" by 72", 16" thick graphite slab. Almost no neutrons leak out the edges which are 54" and 60" away, so that these dimensions do not effect the albedo. Referring to Figure T3.4, the average albedo of the sub-area in the same location is 0.8925. In the next chapter, the sub-areas on the surface of cavities of interest are illustrated and average values of the albedos are assigned to each sub-area.

The reflectivity for boral and cadmium (Cases #20 and #21) does not vary significantly over the surface. Because the absorption rate is so high, the edges which are a few mean free paths from the location of the incident neutrons have little effect on the reflectivity. The values of the reflectivity and the albedo were, therefore, taken to be identical for boral and cadmium.

As mentioned before, the current re-entering the cavity through a sub-area is expressed only as a function of the average albedo and J_1 , and not of the current incident in the adjoining sub-area. This assumption was investigated by using the results in group (3) of the information produced by the code. The code records the number of neutrons incident at a point which leave through each square on the surface. These data for Case #8, described in Table T3.1, are given in Figure T3.8. The percentage of neutrons leaving each 4" square is written in the corresponding square. The

beam of neutrons is incident on the center of the square, and 62.4 per cent of the neutrons return to the cavity through this square. Another 16.2 per cent of the neutrons return through the adjoining squares, so that about 85 per cent of the neutrons re-entering the cavity leave within a radius of 6" from where they entered the slab. The neutrons incident in the surrounding sub-areas compensate for those neutrons which do not leave the same sub-area as they entered, as long as all of the incident currents are of the same magnitude. As an example of this compensation, consider two cases: the first is shown in Figure T3.9. A large surface of a 16" thick slab of graphite is divided into 12" square sub-areas, on each of which there is an incident current of 1.00. The ratio of the outgoing to incident current for the shaded sub-area in Figure T3.9 is equal to 0.9137, which is the same as the average albedo for this sub-area; 79.2 per cent of the returning neutrons were initially incident on that sub-area and the remaining 20.8 per cent were incident on the adjoining sub-areas, which have the same albedo.

In the second example the only difference is that the magnitude of the current incident on one of the adjoining sub-areas is changed to 1.10. The ratio of outgoing to incident current is now 0.9258, or an increase of 1.32 per cent over 0.9137. The effect of the currents incident in adjoining sub-areas is additive. If the incident currents in two adjoining sub-areas have values of 1.10, the albedo increases by 2.64 per cent over the value of 0.9137. The validity of assuming that currents incident on adjoining sub-areas do not affect the albedo will be determined by averaging the values of these currents, and comparing the average to the current incident on the sub-area in question. Since the effect of these currents is

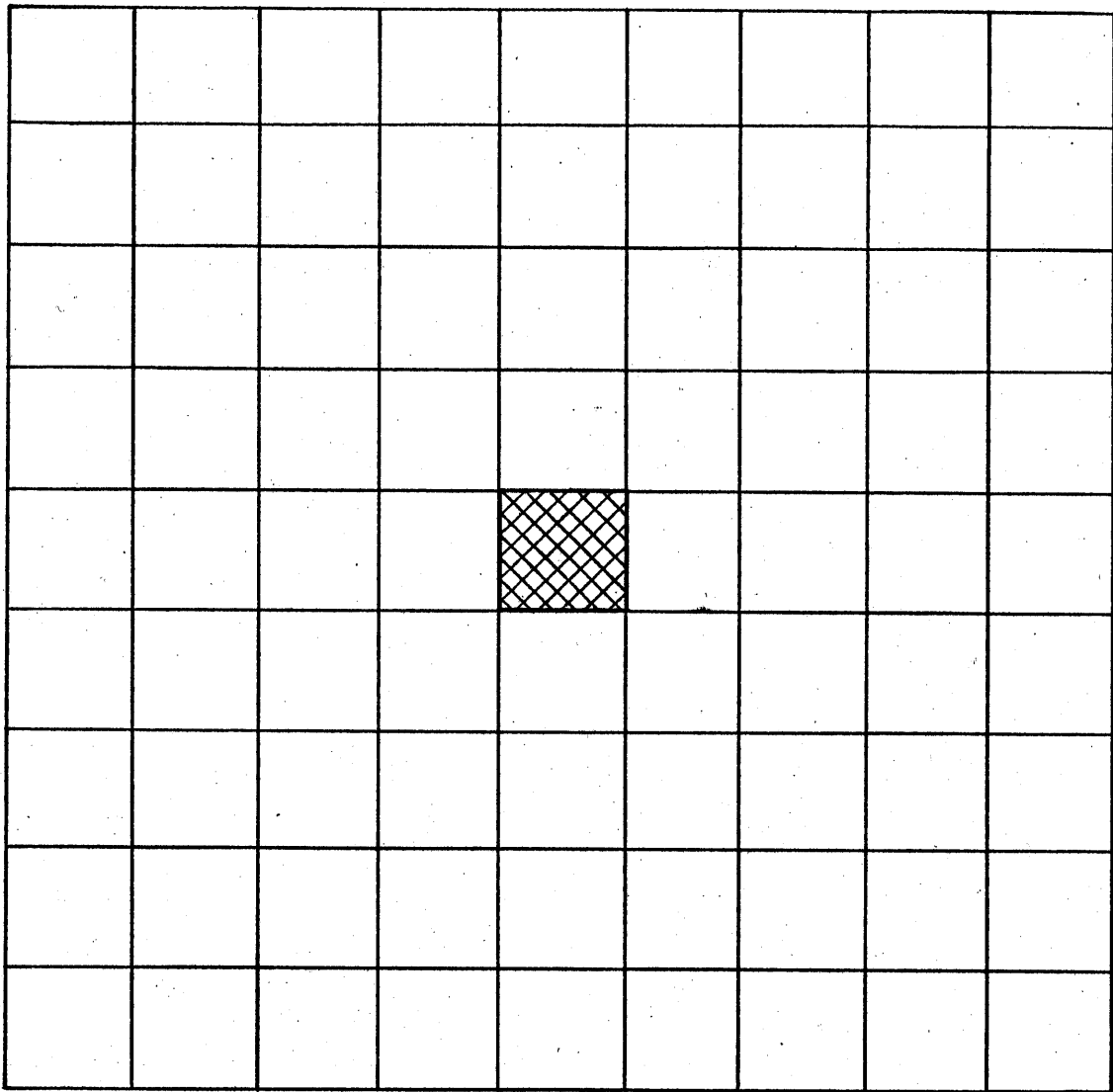


Figure T3.9 Surface of 16" Thick, Large Graphite Slab,
Divided into 12" Sub-Area.

additive, a 10 per cent difference in the average value of the currents and the current in question results in a 1.32 per cent difference in the assigned value of the albedo. In Section T5.3 the error in the albedo will be investigated by this method.

The effect of the angular distribution of the incident current on the value of the reflectivity was also investigated. The Monte Carlo code uses an isotropic beam source, but the current incident on a sub-area bordering the cavity may favor a particular angle rather than being isotropic. Using the output data of the Monte Carlo code, the incident neutrons were placed in one of two groups according to their angle, $\cos \phi_x = 0.0$ to 0.50 or $\cos \phi_x = 0.50$ to 1.00 . The reflectivity for each group was then determined. Case #8 was again selected as an example. The reflectivity for the case of an isotropic source, not corrected for absorption, is 0.9220 . The reflectivity for the neutrons with $\cos \phi_x$ between 0.0 and 0.50 is 0.9037 , while for $\cos \phi_x$ between 0.50 and 1.00 it is 0.9401 . This example demonstrates that even an extremely anisotropic angular distribution of incident neutrons, such as a distribution between 60° and 90° , changes the reflectivity by only 2 per cent. The error introduced into the value of the flux at the surface because of a 2 per cent error in the albedo is about 1 per cent, because the flux is equal to $(1 + \beta)$ times the incident current. The effect of the angular distribution of the incident neutrons on the albedo was, therefore, neglected in this study.

The last piece of information obtained from the code is the angular distribution of the returning neutrons. This topic was discussed in the last chapter which dealt with the view factors.

As a result of the code, a numerical value for the ratio of the outgoing to ingoing currents, β_j , can be determined for each sub-area on the cavity surface, and the validity of expressing β_j as a function of the current incident only on A_j was established. Since the β_j and F_{ji} have been evaluated, the only remaining input information is S_j , which describes the source neutrons.

T3.2 Discussion of the Neutron Source

The values of the flux on the surfaces of a cavity assembly are calculated for a given magnitude and distribution of the neutron source. The magnitude of the neutron source entering the cavity through the sub-area, A_j , is equal to the quantity, S_j . The distribution of the source is represented by a variation of the magnitude of the S 's from sub-area to sub-area. The error introduced into the calculated flux by representing a continuous distribution of the neutron source by a discontinuous one is discussed in Section T5.3.

To determine whether the theoretical model can be successfully applied to the cavity assemblies described in Chapter E1, the values of the flux were calculated for these assemblies. The magnitude and distribution of the neutron source feeding these assemblies were measured, and the results of the measurements were used to calculate the values of S_j . The method and the results of calculating the values of S_j are given in Section T4.5.

Chapter T4

Calculation of the Flux Distribution

T4.1 Introduction

Now that the calculation of quantities β_j , F_{ji} and S_j has been discussed, equation (T1.4) can be used to determine the equilibrium values of the current incident on each sub-area. From the value of the incident current, the neutron flux for each sub-area, A_i , is calculated by means of the equation

$$\phi_i = J_i (1 + \beta_i) \quad (T4.1)$$

The incident current J_i is constant over A_i , and ϕ_i represents a constant value of the neutron flux in the sub-area A_i .

An equation of the form of equation (T1.4) may be written for every sub-area on the cavity surface so that a set of simultaneous equations is formed. Such a set contains at least 140 equations having as many as 280 terms, and the values of the incident currents are obtained by using an electronic computer. The set of equations is solved by means of an iteration technique. The solution by matrix reduction of a set of equations this large takes more time than the iteration technique, and was therefore not used. Usually only three iterations are required to obtain the required convergence. Since the solution converges so rapidly, no special techniques are employed to accelerate convergence.

T4.2 Representation of the Cavity in the Theoretical Model

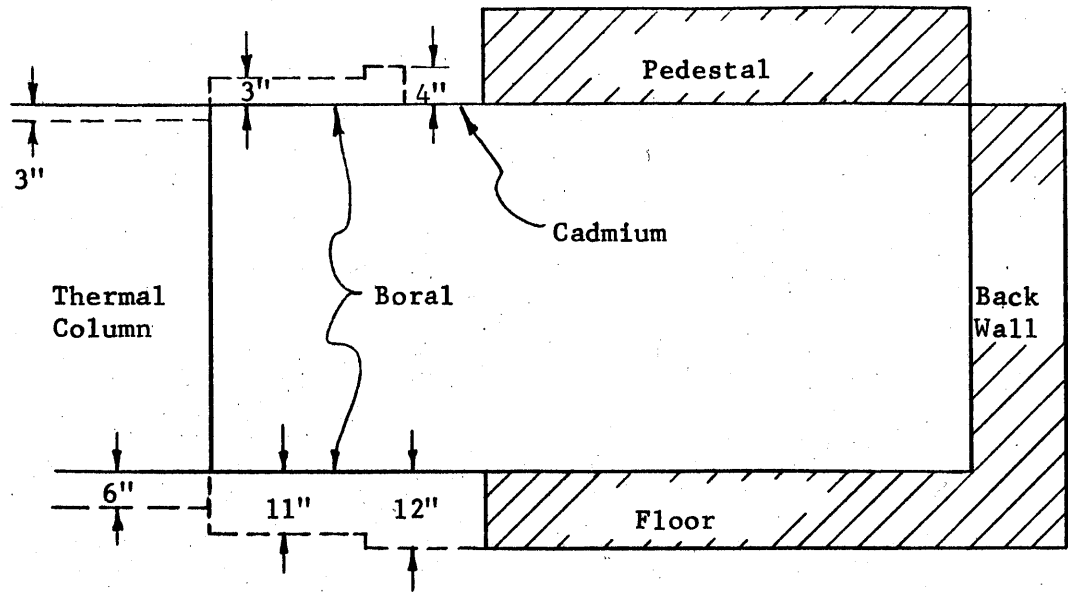
Before explaining the calculation of the incident current it is necessary to discuss how the geometrical arrangements of the hohlraum or cavity assemblies in which the flux distribution was measured are represented in the theoretical model. In the theoretical model, the cavity surfaces are

divided into sub-areas the lengths of whose sides are expressed integral multiples of a unit length L . To have an integral number of sub-areas on each surface, the dimension of the surface must be an integral multiple of L . If L is chosen equal to 6" or 12", most surfaces meet this requirement quite closely. The dimensions of the graphite walls which were built outside the thermal column door space are integral multiples of 6" and 12". (Floor, 72" x 72"; side walls, 60" x 72"; back wall, 60" x 72"; honeycomb surface, 72" x 72".)

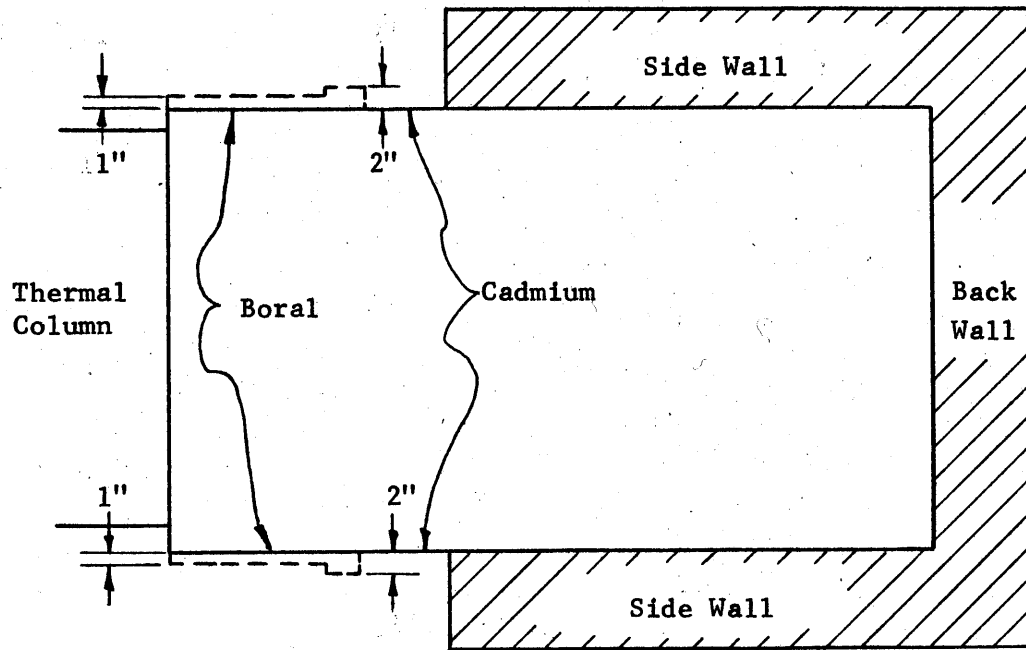
The dimensions of the thermal column door space cannot be expressed as integral multiples of L , so that approximate dimensions must be used in the theoretical representation. The difference in the dimensions of the physical assembly and its theoretical representation is shown in Figures T4.1 and T4.2. The theoretical representation of the cavity assembly is shown in solid lines. The dashed lines are drawn where the physical and theoretical representations differ and they indicate the actual dimension of the assembly. The number of inches written in the figures refers to the distance between the actual and theoretical representation of a surface.

The dimensions of the assembly are approximated in the door space region in order that the surfaces of the cavity be continuous; the calculation of the flux distribution on the surfaces of a cavity is greatly simplified if the surfaces are continuous. If there are sharp discontinuities in the surface, the solution of the equation for the flux distribution derived in this paper may be difficult to obtain.

In Figure T4.1, the boral-lined walls in the door space are represented as being continuous with the other walls in the assembly. The dashed lines in Figure T4.1 indicate that there are differences in the

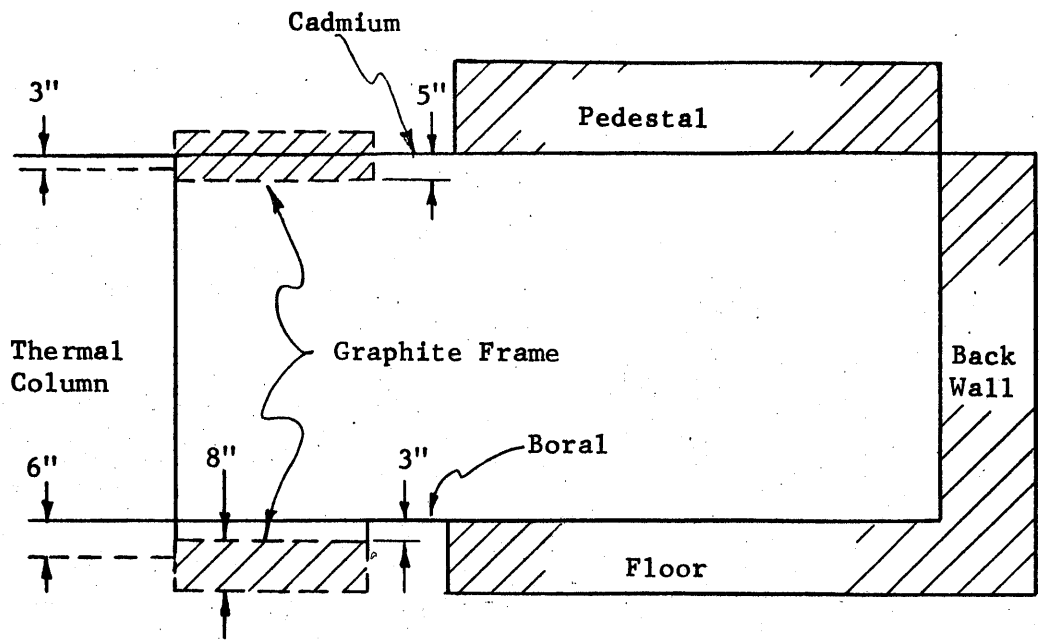


Vertical Section

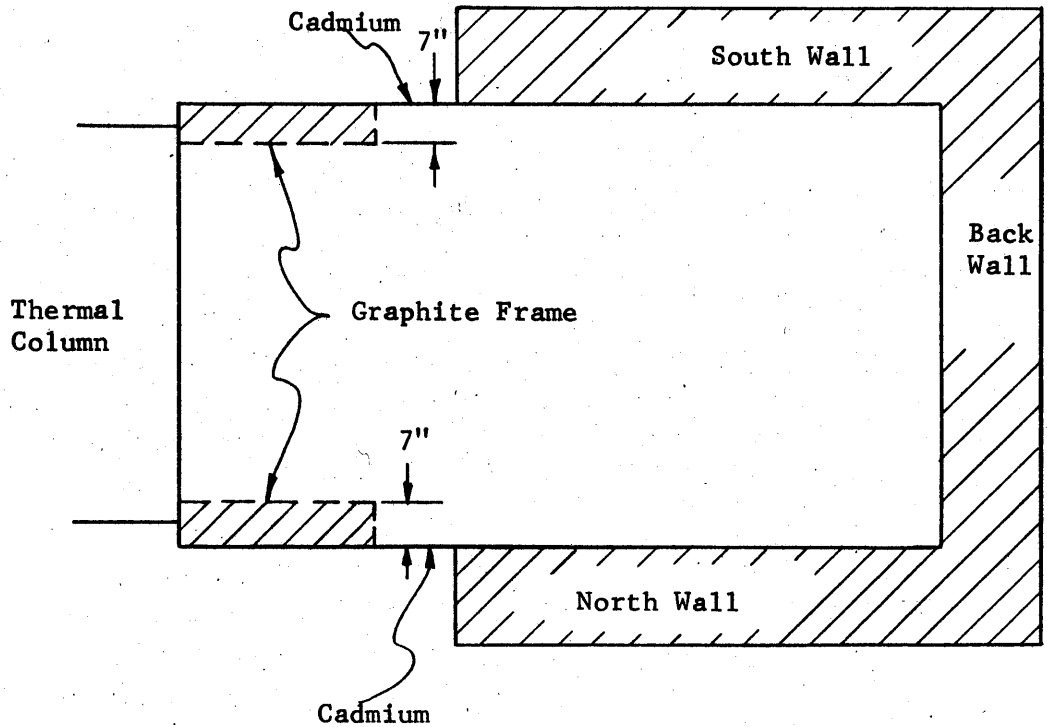


Horizontal Section

Figure T4.1 The Theoretical Representation of Assembly I. Differences between the theoretical and actual representation is indicated by dashed lines.



Vertical Section



Horizontal Section

Figure T4.2 The Theoretical Representation of Assembly II. Differences between the theoretical and actual representation is indicated by dashed lines.

representation of the boral-lined walls. Since 96 per cent of the neutrons which strike the boral-lined walls are absorbed, and thus do not contribute to the flux on the other surfaces, the approximate dimensions of these walls do not significantly affect the flux distribution on the other surface.

The theoretical representation of the hohlraum assembly with the graphite frames in place is shown in Figure T4.2. The surfaces of the frame are not quite continuous with the other surfaces, and the effect of this representation on the flux distribution is discussed in Section T5.3, where the results of the calculations are presented. Since many of the neutrons striking the graphite frame contribute later on to the flux on other surfaces, the argument used above for the bare door space does not apply. The graphite frame (see Figure T4.2) blocks off two inches on the borders of the thermal column face. However, very few source neutrons are emitted within 2" of the edge of the thermal column and these entered the cavity through the frame. The effect of the frame "blocking" off the thermal column face on the flux distribution should be very small. The location and dimensions of the thermal column face in the horizontal plane are exactly reproduced in the theoretical representation. In the vertical plane, however, the theoretical location and dimensions of the thermal column face differ somewhat from the actual ones. The difference in dimension is corrected in the calculation of the source neutrons emitted from the thermal column face. The source terms, S_j , are calculated by averaging the measured distribution of the source neutrons in such a way that the same magnitude and distribution of neutrons are emitted from the 63" x 60" surface of the theoretical representation as were emitted from the 63" x 63" thermal column face. However, the neutron sources on the thermal column

face are still located 3" lower in the theoretical representation, and this difference of 3" is the most serious discrepancy between the actual assembly and its theoretical representation; the effect of the discrepancy is discussed together with the results in Section T5.3.

As explained earlier in the experimental section, there are two cavity arrangements, Assemblies I and V, from which the other geometrical arrangements are obtained by adding graphite. These two cavities are named PARA and 45°, respectively, and are pictured in Figures T4.3 and T4.4, respectively. PARA refers to the parallelepiped arrangement of the cavity, and 45° refers to the 45° inclined plane. The stepped arrangement of graphite stringers is approximated by an inclined plane in the theoretical model, because of the difficulty in treating theoretically a stepped arrangement. The theoretical representation of the PARA assembly is pictured in Figure T5.5 for the case of the "frame" arrangement. The 45° assembly is identical except for the inclined plane, which is shown by the dashed line in Figure T5.5. Note that there is a notch in the back wall. This notch is due to cadmium-covered angle irons which are used to support the honeycomb.

In order to avoid confusion, a few definitions are repeated. The surface of the cavity refers to that part of the surface of the graphite slab which bounds the cavity and these bounding surfaces are shown in Figures T4.3 and T4.4. It is the cavity surfaces which are divided into sub-areas. Since the slabs overlap at certain edges, not all of the surface of a cavity determines the extent of the slab. This can be seen from the drawing of the cavity assembly, where part of the surface of the floor slab is joined with the back wall. This distinction is important because the albedo of a sub-area is a function of the location of the sub-area on the surface

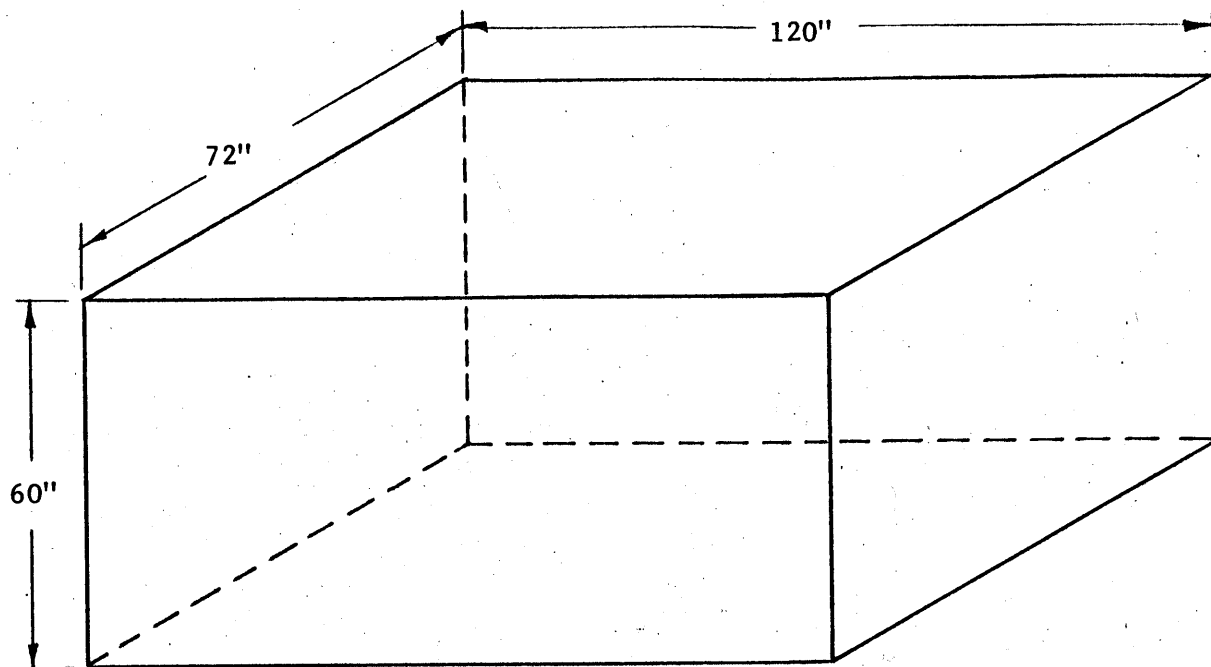


Figure T4.3 Theoretical Representation of the Parallelepiped Cavity.

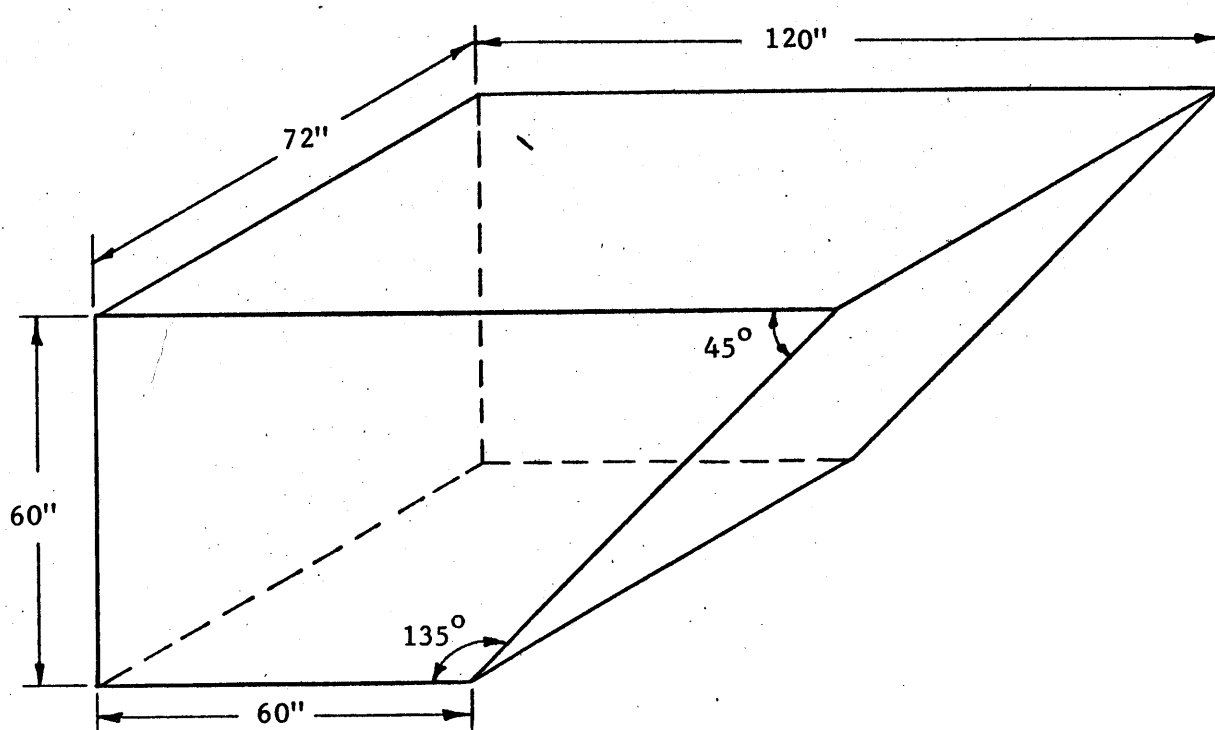


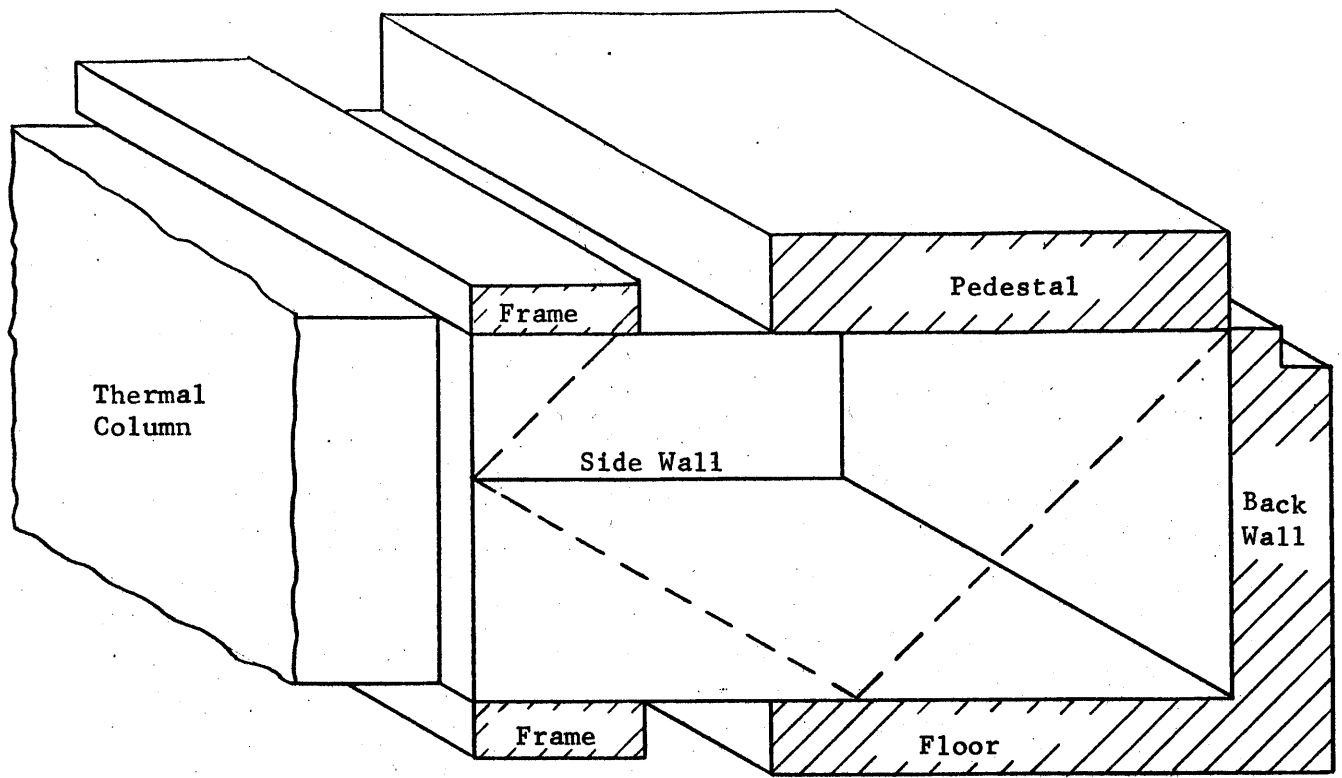
Figure T4.4 Theoretical Representation of the 45° Cavity.

of the slab, but not on the surface of the cavity. In determining the proper albedo, the floor slab, for example, is assumed to continue through the back wall. Since the back wall is 16" thick, the sub-areas on the cavity surface are at least 16" from the back edge of the floor surface. Figures T4.6 and T4.7 show drawings of the walls of the PARA and 45° cavities, respectively. The surface of the wall which bounds the cavity, that is, the cavity surface, is divided into 12" sub-areas. The surface of the slab which does not bound the cavity is shaded in the drawing.

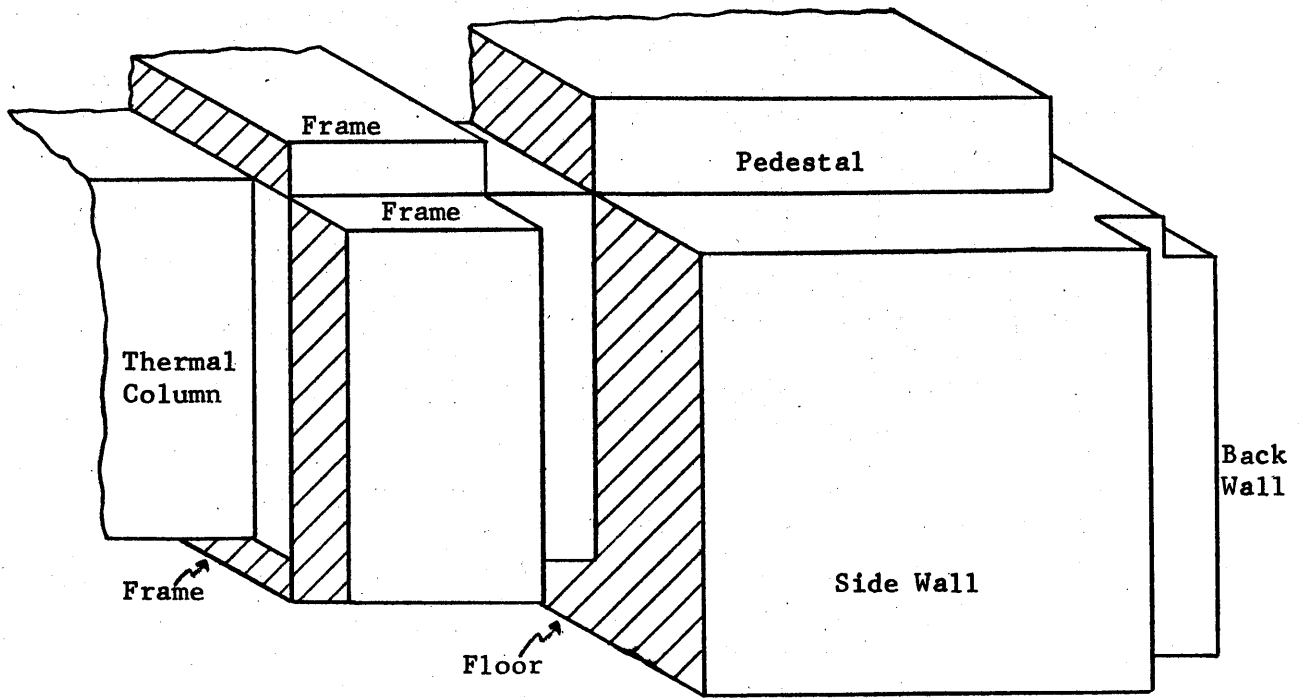
Surface #1 includes the thermal column face (63" x 60") and 4½" of boral at each side. The graphite in the thermal column is considered to be infinitely thick. Surface #2 is the surface of the back wall, and includes the area where the back wall joins with the side walls and the floor. Note that the side walls are only 8" thick at this point because of the vertical angle irons. Surface #3 is the top surface, part of which corresponds to the bottom of the honeycomb. Note that no other walls join with the top wall as can be seen in Figure T4.5. Surface #4 is the bottom surface of the hohlraum assembly, which includes the bottom part of the frame and the floor. The side and back walls join with the floor. Again, note the notches in the side walls because of the vertical angle irons. Surface #6 is one of the side walls of the cavity assembly. It includes the side graphite wall and side of the graphite frame. The floor and back wall join with the side wall. The coordinate system drawn on each surface defines the location of the sub-area on the surface. The type of material and its thickness for each of the walls is noted with the drawings.

T4.3 Selection of Unit Length

As is true in many approximate calculations, a compromise is made between increased accuracy and the additional time required. The computer

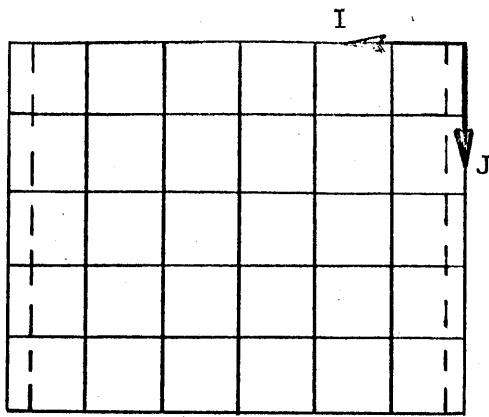


(a)



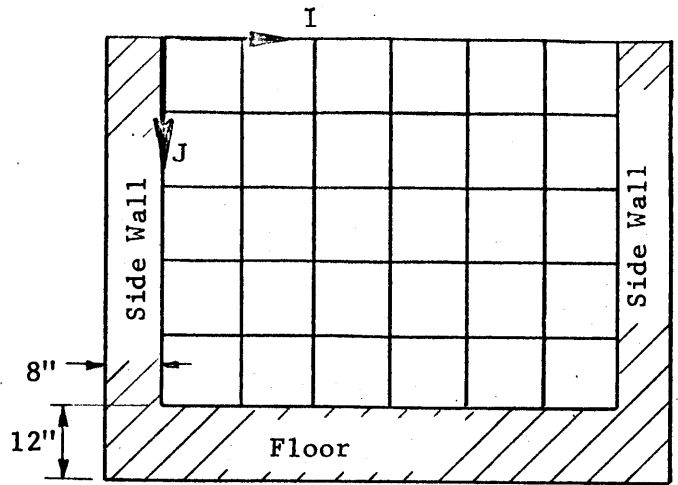
(b)

Figure T4.5 Theoretical Representation of Assembly II.
The dashed line in (a) indicates the representation of Assembly VI.



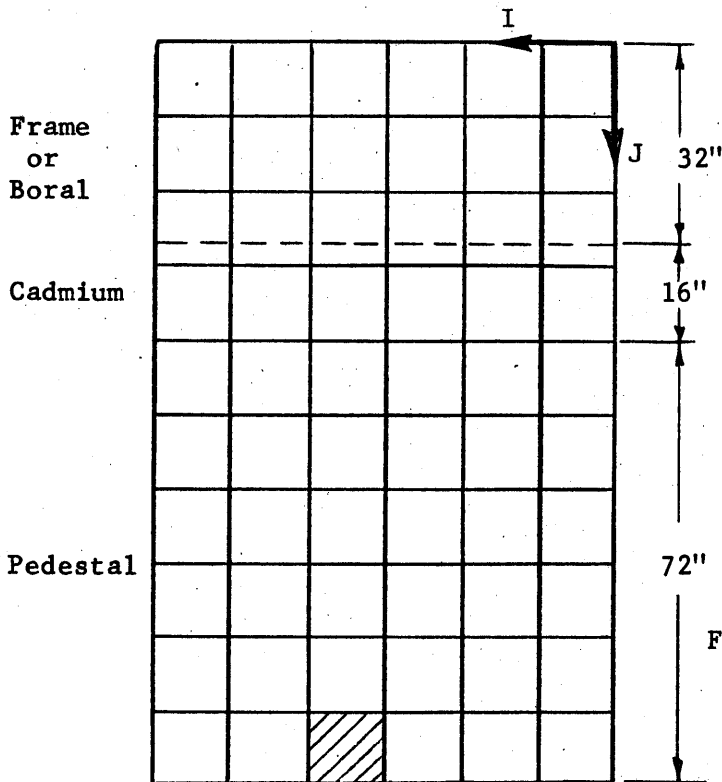
Surface #1

Thermal Column Face
63"x60" graphite, 4½" of
boral on each side.



Surface #2

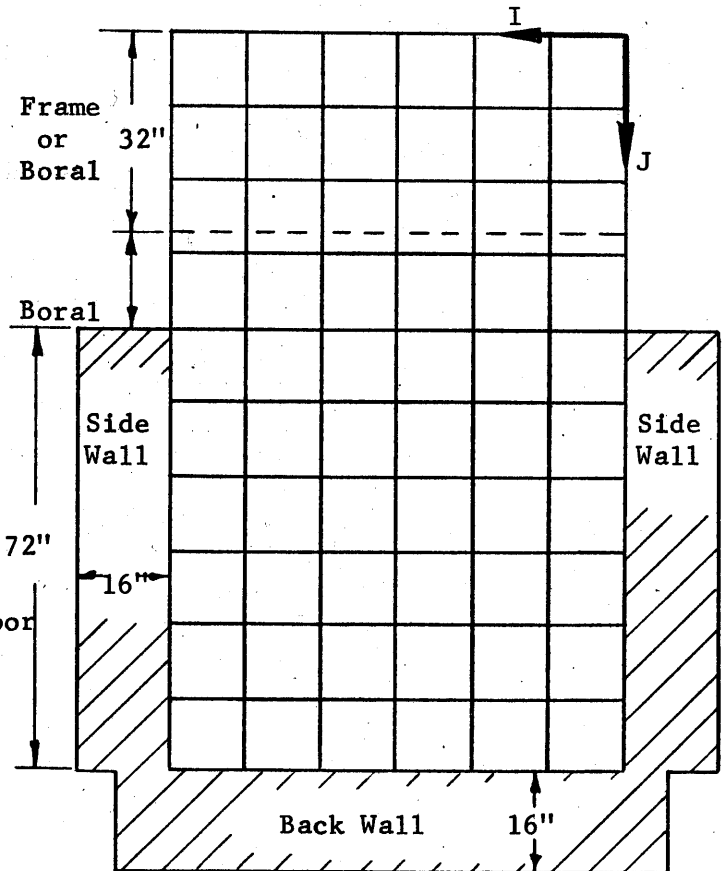
Back Wall
16" thick graphite except
at top where there is a
notch.



Surface #3

Top Surface

Pedestal - 16" thick graphite
Frame - 8" thick graphite



Surface #4

Bottom Surface

Floor - 12" thick graphite
Frame - 8" thick graphite

Figure T4.6 The Walls of the PARA Cavity Assembly with 12" Sub-Areas.

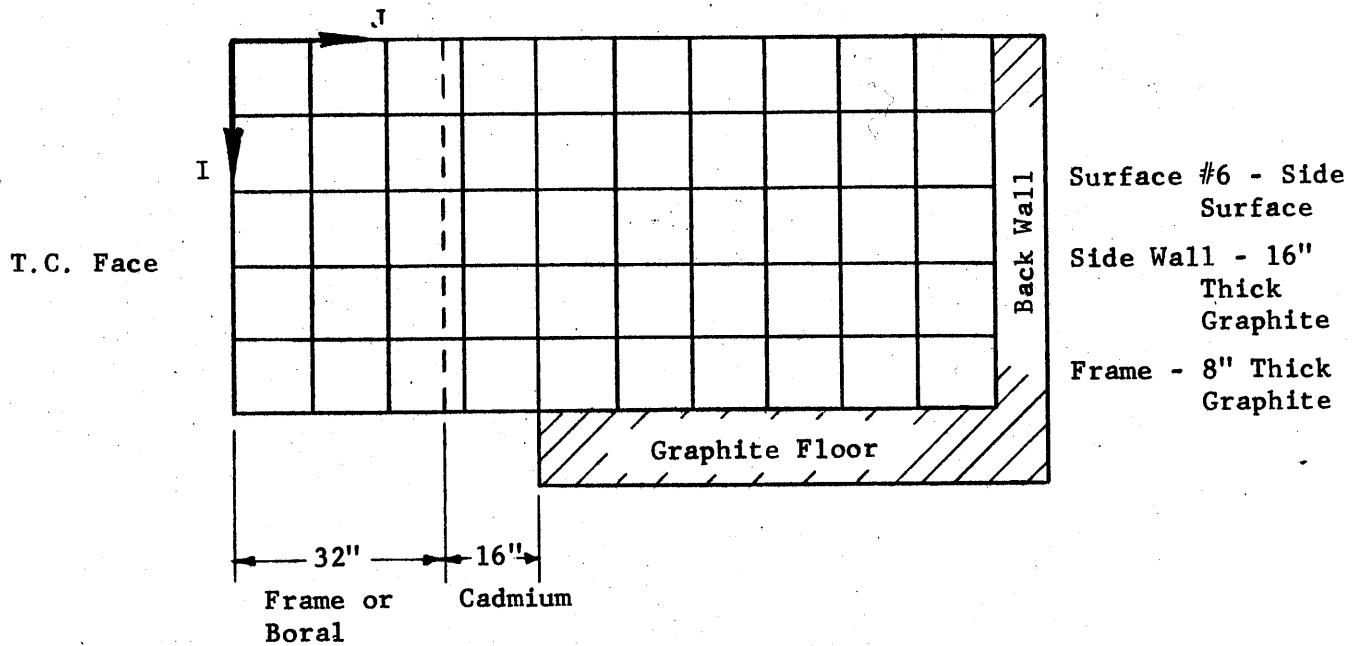
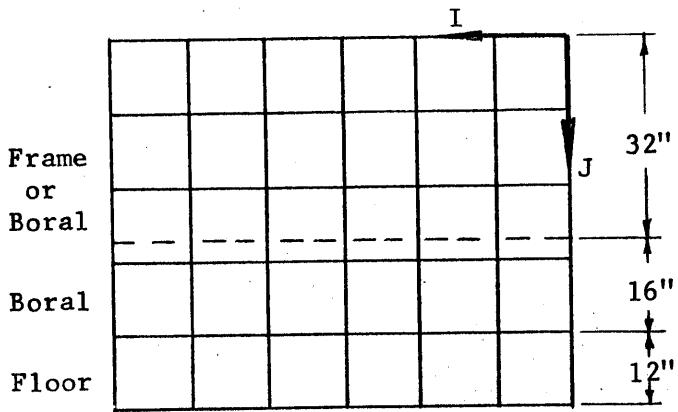
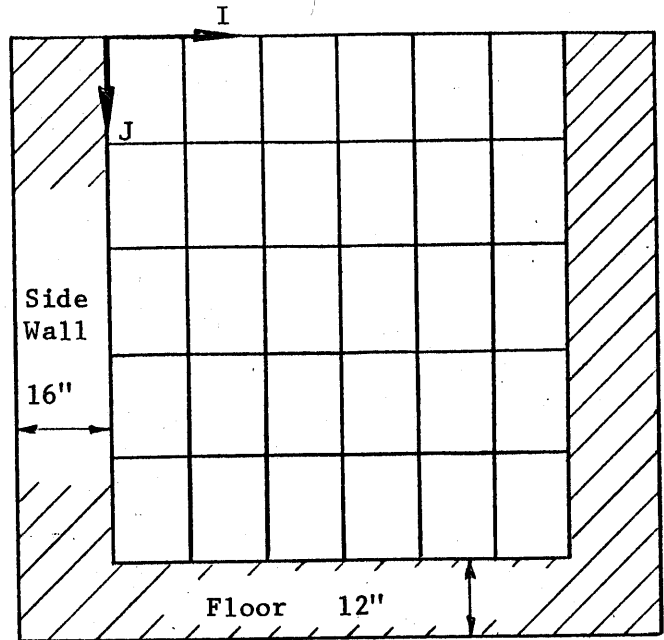


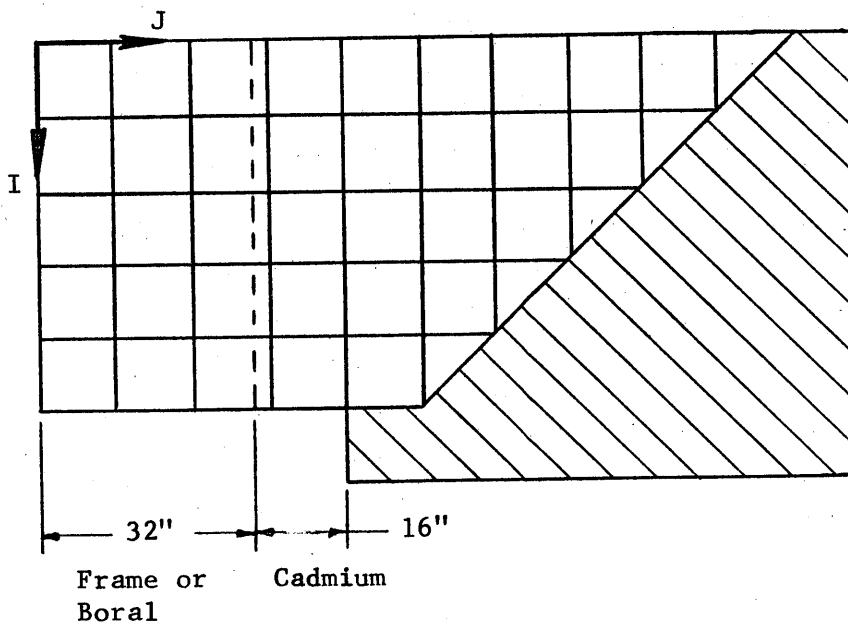
Figure T4.6 (Continued)



Surface #4 - Bottom Surface
 Floor - 12" Thick Graphite
 Frame - 8" Thick Graphite



Surface #2 - Inclined Surface
 At Least 16" Thick Graphite



Surface #6 - Side Surface
 Side Wall - 16" Thick
 Graphite
 Frame - 8" Thick Graphite

Figure T4.7 Walls of the 45° Cavity Assembly with 12" Sub-areas.
 Surface #1 and #3 are the same as those in Figure T4.6.

time required for a calculation is approximately inversely proportional to the cube of the unit dimension. A solution with $L = 6''$ requires 33 minutes, or eight times as much computer time as a calculation with $L = 12''$ (four to five minutes). A calculation with $L = 4''$, the next smallest integral unit of the cavity dimension, would require over one and one-half hours of computer time. As will be seen later, the additional accuracy which would be expected does not justify an hour and a half of computer time. The flux distribution has therefore been calculated for $L = 6''$ and $L = 12''$. The effect of the size of the sub-area on the accuracy of the flux distribution is discussed in Section T5.2.

T4.4 Assignment of the Average Value for the Albedo of a Sub-area

A value of the albedo will now be given for each of the sub-areas. The type and thickness of the wall material and the location of the sub-area on the surface of the wall is obtained from Figures T4.6 and T4.7. With this information the value of the average albedo is obtained from Figures T3.3 through T3.7 in Chapter T3. The shaded $12''$ sub-area on surface #3 in Figure T4.6 is used as an example. It borders one edge of the pedestal and is $24''$, $36''$, and $60''$ away, respectively, from the other three edges. The material is graphite and it is $16''$ thick. Referring to Figure T3.4, one obtains an albedo of 0.7909 for this sub-area.

There are five different assemblies for which the flux distribution was computed. There are three variations of the PARA cavity and two variations of the 45° cavity, as shown in Figure T4.8. For each variation, the surfaces are divided into sub-areas and the value of the albedo is written in its corresponding sub-area in Figures T4.9 through T4.15. The flux distribution for the "tooth" arrangement was not calculated for this variation, because the model cannot treat the case of neutron diffusion through the "tooth".

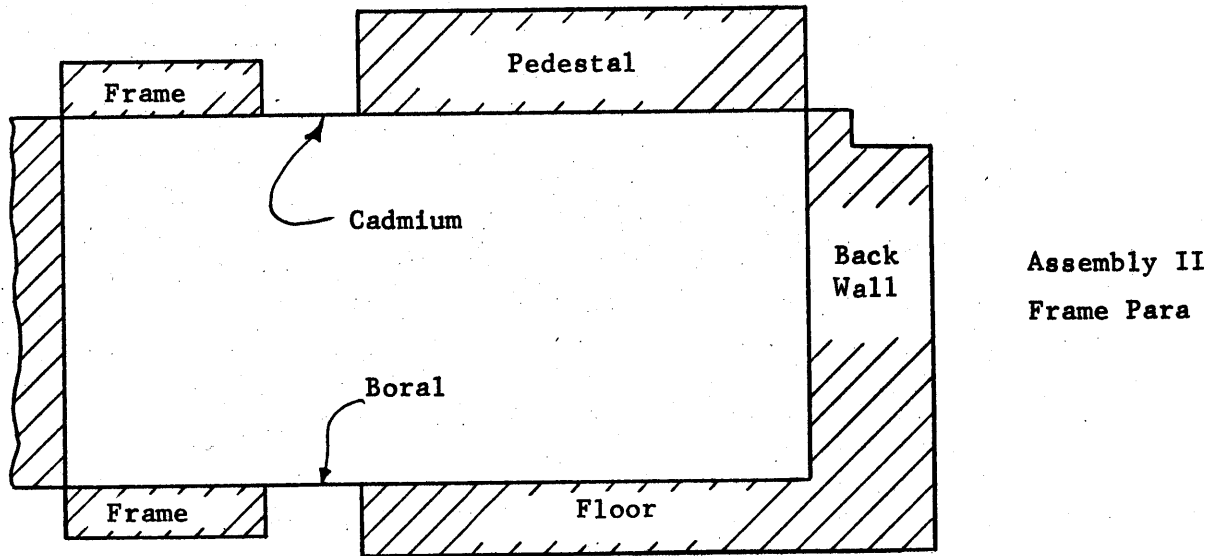
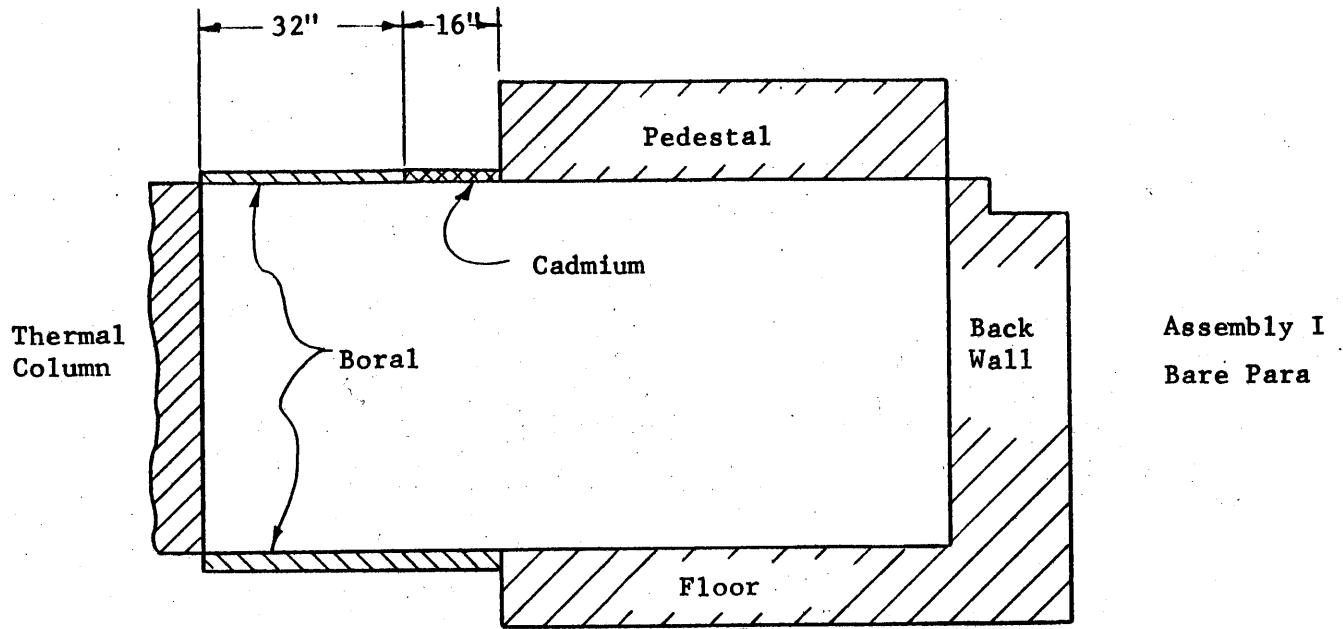
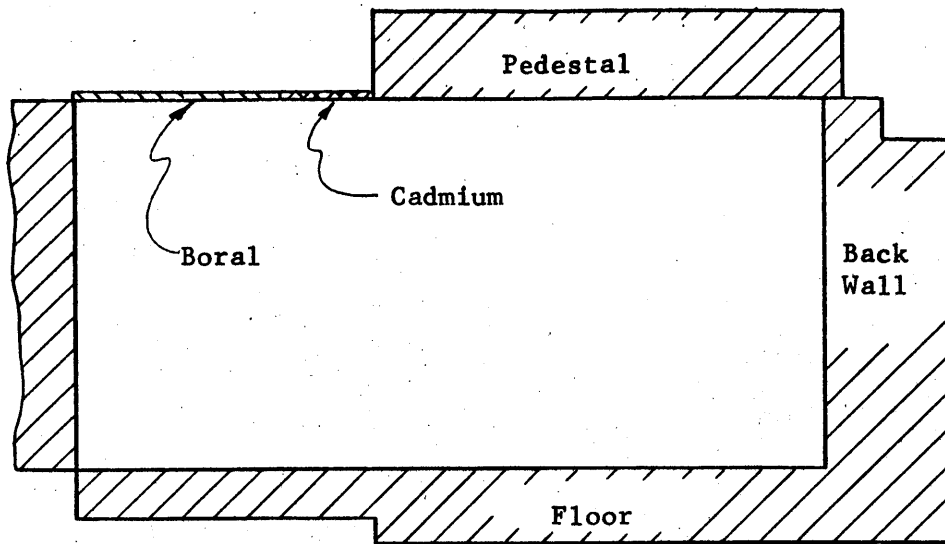
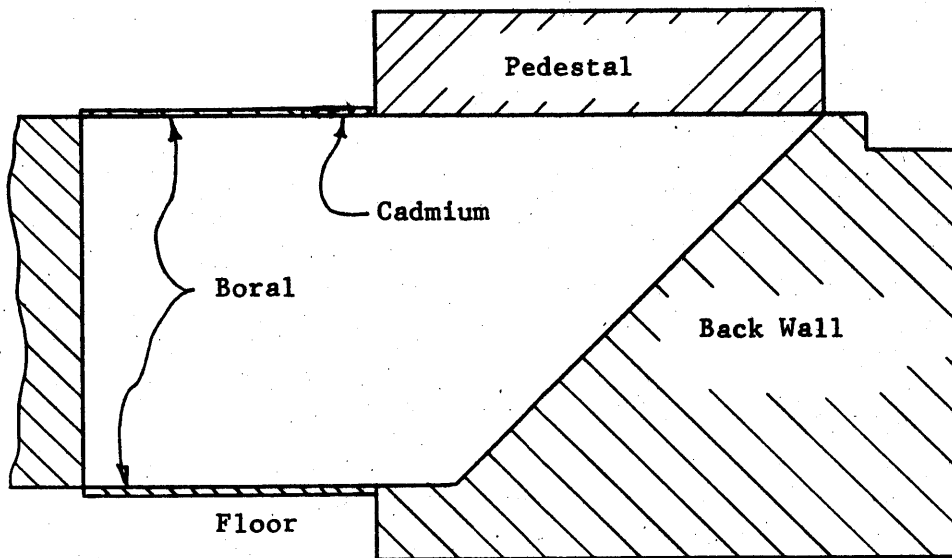


Figure T4.8 Theoretical Representation of Cavity Assemblies I, II, IV, V, and VI.

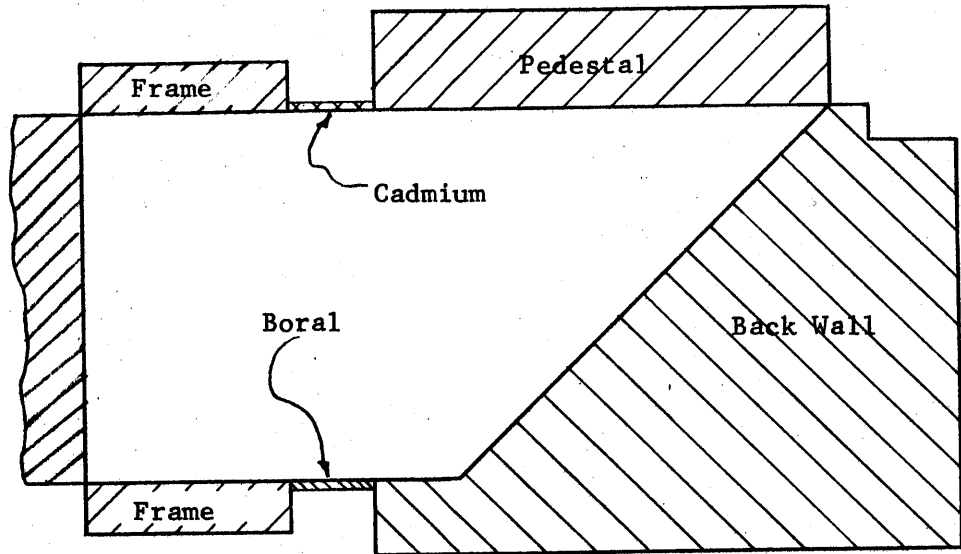


Assembly IV
 Extended Floor
 and Pedestal



Assembly V
 Bare 45°

Figure T4.8 (Continued)



Assembly VI
Frame 45°

Figure T4.8 (Continued)

| | | | | | |
|-------|-------|-------|-------|-------|---------|
| | | | | | I |
| .8978 | .8978 | .8972 | .8506 | .6687 | ◁.1010 |
| .9352 | .9352 | .9352 | .9352 | .8506 | .1010 ▽ |
| .9352 | .9352 | .9352 | .9352 | .8972 | .1010 |
| .9352 | .9352 | .9352 | .9352 | .8978 | .1010 |
| .9352 | .9352 | .9352 | .9352 | .8978 | .1010 |
| .9352 | .9352 | .9352 | .9352 | .8978 | .1010 |
| .9352 | .9352 | .9352 | .9352 | .8978 | .1010 |
| .9352 | .9352 | .9352 | .9352 | .8972 | .1010 |
| .9352 | .9352 | .9352 | .9352 | .8506 | .1010 |
| .8978 | .8978 | .8972 | .8506 | .6687 | .1010 |

Half of Surface #1 $\beta_1(I,J)$

| | | | | | | |
|---|--------|-------|-------|-------|-------|-------|
| | I | | | | | |
| | | ▷ | | | | |
| J | .6687 | .6801 | .6826 | .6860 | .6875 | .6875 |
| | ▽.8506 | .8669 | .8672 | .8672 | .8672 | .8672 |
| | .8972 | .9065 | .9065 | .9065 | .9065 | .9065 |
| | .8978 | .9065 | .9065 | .9065 | .9065 | .9065 |
| | .8978 | .9065 | .9065 | .9137 | .9137 | .9137 |
| | .8978 | .9065 | .9065 | .9137 | .9137 | .9137 |
| | .8978 | .9065 | .9065 | .9137 | .9137 | .9137 |
| | .8978 | .9065 | .9065 | .9065 | .9065 | .9065 |
| | .8978 | .9065 | .9065 | .9065 | .9065 | .9065 |
| | .8972 | .9065 | .9065 | .9065 | .9065 | .9065 |

Half of Surface #2 $\beta_2(I,J)$

Figure T4.9 The Average Value of the Albedo for the 6" Sub-Areas in Assembly I Only Half of Surfaces #1, #2, #3 and #4 are Shown Due to Symmetry in the I Direction.

| | | | | | | | |
|-------|-------|-------|-------|-------|-------|---|---|
| .0412 | .0412 | .0412 | .0412 | .0412 | .0412 | I | J |
| .0412 | .0412 | .0412 | .0412 | .0412 | .0412 | | |
| .0412 | .0412 | .0412 | .0412 | .0412 | .0412 | | |
| .0412 | .0412 | .0412 | .0412 | .0412 | .0412 | | |
| .0412 | .0412 | .0412 | .0412 | .0412 | .0412 | | |
| .0141 | .0141 | .0141 | .0141 | .0141 | .0141 | | |
| .0005 | .0005 | .0005 | .0005 | .0005 | .0005 | | |
| .0005 | .0005 | .0005 | .0005 | .0005 | .0005 | | |
| .6877 | .6877 | .6851 | .6801 | .6725 | .5792 | | |
| .8942 | .8942 | .8935 | .8925 | .8600 | .6725 | | |
| .9065 | .9065 | .9065 | .9065 | .8925 | .6801 | | |
| .9065 | .9065 | .9065 | .9065 | .8935 | .6851 | | |
| .9137 | .9137 | .9065 | .9065 | .8942 | .6877 | | |
| .9137 | .9137 | .9065 | .9065 | .8942 | .6877 | | |
| .9137 | .9137 | .9065 | .9065 | .8942 | .6877 | | |
| .9137 | .9137 | .9065 | .9065 | .8942 | .6877 | | |
| .9065 | .9065 | .9065 | .9065 | .8935 | .6851 | | |
| .9065 | .9065 | .9065 | .9065 | .8925 | .6801 | | |
| .8942 | .8942 | .8935 | .8925 | .8600 | .6725 | | |
| .6877 | .6877 | .6851 | .6801 | .6725 | .5792 | | |

Half of Surface #3 $\beta_3(I,J)$

Figure T4.9 (continued)

| | | | | | | |
|-------|-------|-------|-------|-------|-------|---|
| .0412 | .0412 | .0412 | .0412 | .0412 | .0412 | I |
| .0412 | .0412 | .0412 | .0412 | .0412 | .0412 | J |
| .0412 | .0412 | .0412 | .0412 | .0412 | .0412 | |
| .0412 | .0412 | .0412 | .0412 | .0412 | .0412 | |
| .0412 | .0412 | .0412 | .0412 | .0412 | .0412 | |
| .0412 | .0412 | .0412 | .0412 | .0412 | .0412 | |
| .0412 | .0412 | .0412 | .0412 | .0412 | .0412 | |
| .0412 | .0412 | .0412 | .0412 | .0412 | .0412 | |
| .6877 | .6877 | .6877 | .6877 | .6851 | .6801 | |
| .8672 | .8672 | .8672 | .8672 | .8669 | .8659 | |
| .8837 | .8837 | .8837 | .8837 | .8837 | .8837 | |
| .8837 | .8837 | .8837 | .8837 | .8837 | .8837 | |
| .8944 | .8944 | .8944 | .8944 | .8837 | .8837 | |
| .8944 | .8944 | .8944 | .8944 | .8837 | .8837 | |
| .8944 | .8944 | .8944 | .8944 | .8837 | .8837 | |
| .8944 | .8944 | .8944 | .8944 | .8837 | .8837 | |
| .8944 | .8944 | .8944 | .8944 | .8837 | .8837 | |
| .8837 | .8837 | .8837 | .8837 | .8837 | .8837 | |
| .8837 | .8837 | .8837 | .8837 | .8837 | .8837 | |

Half of Surface #4 $\beta_4(I,J)$

Figure T4.9 (continued)

| | | | | | | | | | I | J | |
|-------|-------|-------|-------|-------|-------|-------|-------|-------|---|-------|---|
| .0412 | .0412 | .0412 | .0412 | .0412 | .0412 | .0412 | .0412 | .0412 | ◁ | .0412 | ▷ |
| .0412 | .0412 | .0412 | .0412 | .0412 | .0412 | .0412 | .0412 | .0412 | | .0412 | ▽ |
| .0412 | .0412 | .0412 | .0412 | .0412 | .0412 | .0412 | .0412 | .0412 | | .0412 | |
| .0412 | .0412 | .0412 | .0412 | .0412 | .0412 | .0412 | .0412 | .0412 | | .0412 | |
| .0412 | .0412 | .0412 | .0412 | .0412 | .0412 | .0412 | .0412 | .0412 | | .0412 | |
| .0141 | .0141 | .0141 | .0141 | .0141 | .0141 | .0141 | .0141 | .0141 | | .0141 | |
| .0005 | .0005 | .0005 | .0005 | .0005 | .0005 | .0005 | .0005 | .0005 | | .0005 | |
| .0005 | .0005 | .0005 | .0005 | .0005 | .0005 | .0005 | .0005 | .0005 | | .0005 | |
| .6801 | .6851 | .6877 | .6877 | .6877 | .6877 | .6851 | .6801 | .6725 | | .5742 | |
| .8925 | .8935 | .8942 | .8942 | .8942 | .8942 | .8935 | .8925 | .8600 | | .6725 | |
| .9065 | .9065 | .9065 | .9065 | .9065 | .9065 | .9065 | .9065 | .8925 | | .6801 | |
| .9065 | .9065 | .9065 | .9065 | .9065 | .9065 | .9065 | .9065 | .8935 | | .6851 | |
| .9065 | .9065 | .9137 | .9137 | .9137 | .9137 | .9065 | .9065 | .8942 | | .6877 | |
| .9065 | .9065 | .9137 | .9137 | .9137 | .9137 | .9065 | .9065 | .8942 | | .6877 | |
| .9065 | .9065 | .9137 | .9137 | .9137 | .9137 | .9065 | .9065 | .8942 | | .6877 | |
| .9065 | .9065 | .9137 | .9137 | .9137 | .9137 | .9065 | .9065 | .8937 | | .6860 | |
| .9065 | .9065 | .9065 | .9065 | .9065 | .9065 | .9065 | .9065 | .8928 | | .6826 | |
| .9065 | .9065 | .9065 | .9065 | .9065 | .9065 | .9065 | .9065 | .8708 | | .6801 | |
| .8972 | .8978 | .8978 | .8978 | .8978 | .8978 | .8978 | .8972 | .8506 | | .6687 | |

All of Surface #6 $\beta_6(I,J)$

Figure T4.9 (continued)

| | | | | | | |
|---|-------|-------|-------|-------|-------|-------|
| | I | | | | | |
| J | .5750 | .6737 | .6863 | .6875 | .6875 | .6875 |
| | .6737 | .8261 | .8394 | .8416 | .8416 | .8416 |
| | .6857 | .8383 | .8554 | .8562 | .8562 | .8562 |
| | .6792 | .8350 | .8485 | .8487 | .8487 | .8487 |
| | .6487 | .7951 | .8100 | .8134 | .8134 | .8134 |
| | .1495 | .1495 | .1495 | .1495 | .1495 | .1495 |
| | .0005 | .0005 | .0005 | .0005 | .0005 | .0005 |
| | .0005 | .0005 | .0005 | .0005 | .0005 | .0005 |

Half of Surface #3 $\beta_3(I,J)$
Frame Section

| | | | | | | |
|---|-------|-------|-------|-------|-------|-------|
| | I | | | | | |
| J | .5750 | .6737 | .6863 | .6875 | .6875 | .6875 |
| | .6737 | .8261 | .8394 | .8416 | .8416 | .8416 |
| | .6857 | .8380 | .8554 | .8562 | .8562 | .8562 |
| | .6792 | .8350 | .8485 | .8487 | .8487 | .8487 |
| | .6487 | .7951 | .8100 | .8134 | .8134 | .8134 |
| | .1766 | .1766 | .1766 | .1766 | .1746 | .1746 |
| | .0412 | .0412 | .0412 | .0412 | .0412 | .0412 |
| | .0412 | .0412 | .0412 | .0412 | .0412 | .0412 |

Half of Surface #4 $\beta_4(I,J)$
Frame Section

Figure T4.10 The Average Value of the Albedo for 6" Sub-Areas in Assembly II
Only the Frame Section is Given Here. The Value of the Albedo
for other Surfaces is Identical to those Given in Figure T4.9.

| | | | | | | | | | | |
|---|-------|-------|-------|-------|-------|-------|-------|-------|-------|-------|
| | I | | | | | | | | | |
| J | .5750 | .6737 | .6863 | .6875 | .6875 | .6875 | .6875 | .6863 | .6737 | .5750 |
| | .6737 | .8261 | .8394 | .8416 | .8416 | .8416 | .8416 | .8394 | .8261 | .6737 |
| | .6857 | .8383 | .8554 | .8562 | .8562 | .8562 | .8562 | .8554 | .8383 | .6857 |
| | .6792 | .8350 | .8485 | .8487 | .8487 | .8487 | .8487 | .8485 | .8350 | .6792 |
| | .6487 | .7951 | .8100 | .8134 | .8134 | .8134 | .8134 | .8100 | .7951 | .6487 |
| | .1495 | .1495 | .1495 | .1495 | .1495 | .1495 | .1495 | .1495 | .1495 | .1495 |
| | .0005 | .0005 | .0005 | .0005 | .0005 | .0005 | .0005 | .0005 | .0005 | .0005 |
| | .0005 | .0005 | .0005 | .0005 | .0005 | .0005 | .0005 | .0005 | .0005 | .0005 |

Surface #6 $\beta_6(I,J)$
 Frame Section

Figure T4.10 (continued)

| | | | |
|---|-------|-------|-------|
| | I | | |
| | ▶ | | |
| J | .6956 | .7878 | .7909 |
| ▼ | .7878 | .9352 | .9352 |
| | .7909 | .9352 | .9352 |
| | .7878 | .9352 | .9352 |
| | .6956 | .7878 | .7909 |

Half of Surface #1 $\beta_1(I,J)$

| | | | |
|---|-------|-------|-------|
| | I | | |
| | ▶ | | |
| J | .7582 | .7637 | .7637 |
| ▼ | .8550 | .9065 | .9065 |
| | .8595 | .9065 | .9137 |
| | .8595 | .9065 | .9137 |
| | .8520 | .9065 | .9065 |

Half of Surface #2 $\beta_2(I,J)$

| | | | |
|---|-------|-------|-------|
| | I | | |
| | ▶ | | |
| J | .0412 | .0412 | .0412 |
| ▼ | .0412 | .0412 | .0412 |
| | .0276 | .0276 | .0276 |
| | .0005 | .0005 | .0005 |
| | .6956 | .7878 | .7909 |
| | .7878 | .9065 | .9065 |
| | .7909 | .9065 | .9137 |
| | .7909 | .9065 | .9137 |
| | .7878 | .9065 | .9065 |
| | .6956 | .7878 | .7909 |

Half of Surface #3 $\beta_3(I,J)$

Figure T4.11 The Average Value of the Albedo for 12" Sub-Areas in Assembly I

| | | | |
|---|-------|-------|-------|
| | I | | |
| | | ▶ | |
| | .0412 | .0412 | .0412 |
| J | .0412 | .0412 | .0412 |
| ▼ | .0412 | .0412 | .0412 |
| | .7757 | .7780 | .7780 |
| | .8837 | .8837 | .8837 |
| | .8837 | .8944 | .8944 |
| | .8837 | .8944 | .8944 |
| | .8837 | .8944 | .8944 |
| | .8837 | .8944 | .8944 |
| | .8837 | .8837 | .8837 |

Half of Surface #4 $\beta_4(I,J)$

| | | | | | |
|---|-------|-------|-------|-------|-------|
| | I | | | | |
| | | ▶ | | | |
| | .0412 | .0412 | .0412 | .0412 | .0412 |
| J | .0412 | .0412 | .0412 | .0412 | .0412 |
| ▼ | .0276 | .0276 | .0276 | .0276 | .0276 |
| | .0005 | .0005 | .0005 | .0005 | .0005 |
| | .6956 | .7878 | .7909 | .7909 | .7878 |
| | .7878 | .9065 | .9065 | .9065 | .9065 |
| | .7909 | .9065 | .9137 | .9137 | .9065 |
| | .7909 | .9065 | .9137 | .9137 | .9065 |
| | .7909 | .9065 | .9065 | .9065 | .9065 |
| | .7693 | .8880 | .8893 | .8893 | .8880 |

Surface #6 $\beta_6(I,J)$

Figure T4.11 (continued)

| | | | |
|---|-------|-------|-------|
| | I | | |
| J | .6956 | .7878 | .7909 |
| ▽ | .7878 | .9352 | .9352 |
| | .7909 | .9352 | .9352 |
| | .7878 | .9352 | .9352 |
| | .6956 | .7878 | .7909 |

Half of Surface #1 $\beta_1(I,J)$

| | | | |
|---|-------|-------|-------|
| | I | | |
| J | .7604 | .7646 | .7646 |
| ▽ | .9048 | .9065 | .9065 |
| | .9053 | .9137 | .9137 |
| | .9053 | .9137 | .9137 |
| | .9048 | .9065 | .9065 |

Half of Surface #2 $\beta_2(I,J)$

| | | | |
|---|-------|-------|-------|
| | I | | |
| J | .6871 | .7637 | .7646 |
| ▽ | .7595 | .8522 | .8525 |
| | .4356 | .4822 | .4831 |
| | .0005 | .0005 | .0005 |
| | .6956 | .7878 | .7909 |
| | .7878 | .9065 | .9065 |
| | .7909 | .9065 | .9137 |
| | .7909 | .9065 | .9137 |
| | .7878 | .9065 | .9065 |
| | .6956 | .7878 | .7909 |

Half of Surface #3 $\beta_3(I,J)$

Figure T4.12 The Average Value of the Albedo for 12" Sub-Areas in Assembly II

| | | | |
|---|-------|-------|-------|
| | I | | |
| J | .6871 | .7637 | .7646 |
| | .7595 | .8522 | .8525 |
| | .4493 | .4958 | .4966 |
| | .0412 | .0412 | .0412 |
| | .7757 | .7780 | .7780 |
| | .8837 | .8837 | .8837 |
| | .8837 | .8944 | .8944 |
| | .8837 | .8944 | .8944 |
| | .8837 | .8944 | .8944 |
| | .8837 | .8837 | .8837 |

Half of Surface #4 $\beta_4(I,J)$

| | | | | | |
|---|-------|-------|-------|-------|-------|
| | I | | | | |
| J | .6871 | .7637 | .7646 | .7637 | .6871 |
| | .7595 | .8522 | .8525 | .8522 | .7595 |
| | .4356 | .4822 | .4831 | .4822 | .4356 |
| | .0005 | .0005 | .0005 | .0005 | .0005 |
| | .6956 | .7878 | .7909 | .7909 | .7878 |
| | .7878 | .9065 | .9065 | .9065 | .9065 |
| | .7909 | .9065 | .9137 | .9137 | .9065 |
| | .7909 | .9065 | .9137 | .9137 | .9065 |
| | .7909 | .9065 | .9065 | .9065 | .9065 |
| | .7822 | .9048 | .9053 | .9053 | .9048 |

Surface #6 $\beta_6(I,J)$

Figure T4.12 (continued)

| | | | |
|---|-------|-------|-------|
| | I | | |
| J | .6956 | .7878 | .7909 |
| | .7878 | .9352 | .9352 |
| | .7909 | .9352 | .9352 |
| | .7878 | .9352 | .9352 |
| | .6956 | .7878 | .7909 |

Half of Surface #1 $\beta_1(I,J)$

| | | | |
|---|-------|-------|-------|
| | I | | |
| J | .7582 | .7637 | .7637 |
| | .8520 | .9065 | .9065 |
| | .8595 | .9065 | .9137 |
| | .8595 | .9065 | .9137 |
| | .8520 | .9065 | .9065 |

Half of Surface #2 $\beta_2(I,J)$

| | | | | | |
|---|-------|-------|-------|-------|-------|
| | I | | | | |
| J | .0412 | .0412 | .0412 | .0412 | .0412 |
| | .0412 | .0412 | .0412 | .0412 | .0412 |
| | .0276 | .0276 | .0276 | .0276 | .0276 |
| | .0005 | .0005 | .0005 | .0005 | .0005 |
| | .6956 | .7878 | .7909 | .7909 | .7878 |
| | .7878 | .9065 | .9065 | .9065 | .9065 |
| | .7909 | .9065 | .9137 | .9137 | .9065 |
| | .7909 | .9065 | .9137 | .9137 | .9065 |
| | .7909 | .9065 | .9065 | .9065 | .9065 |
| | .7693 | .8880 | .8893 | .8893 | .8880 |

Surface #6 $\beta_6(I,J)$

Figure T4.13 The Average Value of the Albedo in the 12" Sub-Areas in Assembly IV

| | | | |
|---|-------|-------|-------|
| | I | | |
| J | .0412 | .0412 | .0412 |
| | .0412 | .0412 | .0412 |
| | .0276 | .0276 | .0276 |
| | .0005 | .0005 | .0005 |
| | .7693 | .7884 | .7909 |
| | .8880 | .9065 | .9065 |
| | .8893 | .9065 | .9137 |
| | .8893 | .9065 | .9137 |
| | .8882 | .9065 | .9065 |
| | .8650 | .8820 | .8893 |

Half of Surface #3 $\beta_3(I,J)$

| | | | |
|---|-------|-------|-------|
| | I | | |
| J | .6871 | .7637 | .7646 |
| | .7595 | .8522 | .8525 |
| | .7646 | .8522 | .8525 |
| | .7646 | .8522 | .8525 |
| | .8837 | .8944 | .8944 |
| | .8837 | .8944 | .8944 |
| | .8837 | .8944 | .8944 |
| | .8837 | .8944 | .8944 |
| | .8837 | .8944 | .8944 |
| | .8837 | .8837 | .8837 |

Half of Surface #4 $\beta_4(I,J)$

Figure T4.13 (continued)

| | | | |
|---|-------|-------|-------|
| | I | | |
| J | .6956 | .7878 | .7909 |
| ▽ | .7878 | .9352 | .9352 |
| | .7909 | .9352 | .9352 |
| | .7878 | .9352 | .9352 |
| | .6956 | .7878 | .7909 |

Half of Surface #1 $\beta_1(I,J)$

| | | | |
|---|-------|-------|-------|
| | I | | |
| J | .7604 | .7646 | .7646 |
| ▽ | .9352 | .9352 | .9352 |
| | .9352 | .9352 | .9352 |
| | .9352 | .9352 | .9352 |
| | .9352 | .9352 | .9352 |

Half of Surface #2 $\beta_2(I,J)$

| | | | |
|---|-------|-------|-------|
| | I | | |
| J | .0412 | .0412 | .0412 |
| ▽ | .0412 | .0412 | .0412 |
| | .0412 | .0412 | .0412 |
| | .0412 | .0412 | .0412 |
| | .7757 | .7780 | .7780 |

Half of Surface #4 $\beta_4(I,J)$

Figure T4.14 The Average Value of the Albedo for 12" Sub-Areas in Assembly V

| | | | |
|-----|-------|-------|-------|
| | I → | | |
| J ↓ | .0412 | .0412 | .0412 |
| | .0412 | .0412 | .0412 |
| | .0276 | .0276 | .0276 |
| | .0005 | .0005 | .0005 |
| | .6956 | .7878 | .7909 |
| | .7878 | .9065 | .9065 |
| | .7909 | .9065 | .9137 |
| | .7909 | .9065 | .9137 |
| | .7878 | .9065 | .9065 |
| | .6956 | .7878 | .7909 |

Half of Surface #3 $\beta_3(I,J)$

| | | | | | |
|-----|-------|-------|-------|-------|-------|
| | I → | | | | |
| J ↓ | .0412 | .0412 | .0412 | .0412 | .0412 |
| | .0412 | .0412 | .0412 | .0412 | .0412 |
| | .0276 | .0276 | .0276 | .0276 | .0276 |
| | .0005 | .0005 | .0005 | .0005 | .0005 |
| | .6956 | .7878 | .7909 | .7909 | .7878 |
| | .7878 | .9065 | .9065 | .9065 | .9065 |
| | .7909 | .9065 | .9137 | .9137 | |
| | .7909 | .9065 | .9137 | | |
| | .7909 | .9065 | | | |
| | .7822 | | | | |

Surface #6 $\beta_6(I,J)$

Figure T4.14 (continued)

| | | | |
|---|-------|-------|-------|
| | I | | |
| J | .6956 | .7878 | .7909 |
| | .7878 | .9352 | .9352 |
| | .7909 | .9352 | .9352 |
| | .7878 | .9352 | .9352 |
| | .6956 | .7878 | .7909 |

Half of Surface #1 $\beta_1(I,J)$

| | | | |
|---|-------|-------|-------|
| | I | | |
| J | .7604 | .7646 | .7646 |
| | .9352 | .9352 | .9352 |
| | .9352 | .9352 | .9352 |
| | .9352 | .9352 | .9352 |
| | .9352 | .9352 | .9352 |

Half of Surface #2 $\beta_2(I,J)$

| | | | |
|---|-------|-------|-------|
| | I | | |
| J | .6871 | .7637 | .7646 |
| | .7595 | .8522 | .8525 |
| | .4493 | .4958 | .4966 |
| | .0412 | .0412 | .0412 |
| | .7757 | .7780 | .7780 |

Half of Surface #4 $\beta_4(I,J)$

Figure T4.15 The Average Value of the Albedo for 12" Sub-Areas in Assembly VI

| | | | |
|---|-------|-------|-------|
| | I | | |
| J | .6871 | .7637 | .7646 |
| | .7595 | .8522 | .8525 |
| | .4356 | .4822 | .4831 |
| | .0005 | .0005 | .0005 |
| | .6956 | .7878 | .7909 |
| | .7878 | .9065 | .9065 |
| | .7909 | .9065 | .9137 |
| | .7909 | .9065 | .9137 |
| | .7878 | .9065 | .9065 |
| | .6956 | .7878 | .7909 |

Half of Surface #3 $\beta_3(I,J)$

| | | | | | |
|---|-------|-------|-------|-------|-------|
| | I | | | | |
| J | .6871 | .7637 | .7646 | .7637 | .6871 |
| | .7595 | .8522 | .8525 | .8522 | .7595 |
| | .4356 | .4958 | .4966 | .4958 | .4356 |
| | .0005 | .0005 | .0005 | .0005 | .0005 |
| | .6956 | .7878 | .7909 | .7909 | .7878 |
| | .7878 | .9065 | .9065 | .9065 | .9065 |
| | .7909 | .9065 | .9137 | .9137 | |
| | .7909 | .9065 | .9137 | | |
| | .7909 | .9065 | | | |
| | .7822 | | | | |

Surface #6 $\beta_6(I,J)$

Figure T4.15 (continued)

T4.5 Calculation of the Neutron Source Terms

The experimental and theoretical results will be compared on the basis of the same neutron source; the values of the source and the flux on the honeycomb were both multiplied by the same conversion factor between relative and absolute flux, so any error in this conversion constant does not effect the comparison of the theoretical and experimental results.

The neutron source terms, S_j , for each sub-area on the thermal column face were calculated from the measured distribution of the neutron source shown in Figures E3.1 and E3.2. A graphical double integration of the distribution was performed to obtain an average value of the neutron source in each sub-area. The symmetry in the neutron source around the vertical mid-line of the thermal column face was taken into account so that only half of the values of S were actually calculated. In Figure T4.16 the positions of the foils which measured the neutron flux are shown on the 72" x 60" surface. The solid lines indicate the location of the 12" sub-areas, while the dotted lines indicate the boundaries of the thermal column. As mentioned in Chapter T1, the neutron source was averaged over the 72" x 60" surface so that the S_j represent the same distribution that was measured on the 63" x 63" thermal column face. The values of S_j for the 12" and 6" sub-areas are shown in Tables T4.1 and T4.2, respectively.

The theoretical model is based on the assumption that a given S_j is constant over a sub-area A_j . From Figures E3.1 and E3.2 it is evident that the magnitude of the neutron source varies appreciably over the thermal column face. Even for the 6" sub-areas, the variation of the neutron source over a sub-area A_j may be as high as 50 per cent of the average value, S_j . A smaller dimension than 6" could not be used for the sub-areas

Table T4.1

Neutron Source Terms (1×10^8) for 12" Sub-Areas on Surface #1

The numbers represent the average value of the neutron source at 1 Mw operation of the M.I.T.R. for each 12" sub-area.

| | | | | | | |
|---|-------|--------|--------|--------|--------|-------|
| | I | | | | | |
| | | ▶ | | | | |
| | 2.163 | 8.652 | 10.959 | 10.959 | 8.652 | 2.163 |
| J | 3.845 | 17.544 | 25.594 | 25.594 | 17.544 | 3.845 |
| | 4.446 | 22.110 | 32.684 | 32.684 | 22.110 | 4.446 |
| | 3.965 | 18.505 | 25.955 | 25.955 | 18.505 | 3.965 |
| | 2.307 | 10.190 | 13.266 | 13.266 | 10.190 | 2.307 |

Table T4.2

Neutron Source Terms (1×10^8) for 6" Sub-Areas on Surface #1

The numbers represent the average value of the neutron source at 1 Mw operation of the M.I.T.R. for each 6" sub-area.

| | | | | | | | | | | | | | |
|---|---|-------|-------|--------|--------|--------|--------|--------|--------|--------|--------|-------|-------|
| I | ▶ | | | | | | | | | | | | |
| J | ▼ | 0.131 | 2.391 | 4.782 | 6.457 | 7.175 | 7.652 | 7.652 | 7.175 | 6.457 | 4.782 | 2.391 | 0.131 |
| | | 0.287 | 4.543 | 9.087 | 12.436 | 14.348 | 15.305 | 15.305 | 14.348 | 12.436 | 9.087 | 4.543 | 0.287 |
| | | 0.406 | 6.217 | 12.913 | 17.935 | 21.044 | 22.957 | 22.957 | 21.044 | 17.935 | 12.913 | 6.217 | 0.406 |
| | | 0.526 | 7.533 | 16.262 | 23.196 | 28.218 | 30.610 | 30.610 | 28.218 | 23.196 | 16.262 | 7.533 | 0.526 |
| | | 0.598 | 8.250 | 18.174 | 25.827 | 32.523 | 35.393 | 35.393 | 32.523 | 25.827 | 18.174 | 8.250 | 0.591 |
| | | 0.598 | 8.393 | 18.174 | 25.349 | 31.567 | 34.437 | 34.437 | 31.567 | 25.349 | 18.174 | 8.393 | 0.598 |
| | | 0.535 | 8.083 | 16.979 | 23.436 | 28.457 | 30.610 | 30.610 | 28.457 | 23.436 | 16.979 | 8.083 | 0.535 |
| | | 0.419 | 7.175 | 14.389 | 19.848 | 23.196 | 24.871 | 24.871 | 23.196 | 19.848 | 14.389 | 7.175 | 0.419 |
| | | 0.281 | 5.500 | 10.522 | 14.348 | 16.740 | 17.935 | 17.935 | 16.740 | 14.348 | 10.522 | 5.500 | 0.281 |
| | | 0.143 | 2.750 | 5.500 | 7.652 | 8.609 | 9.087 | 9.087 | 8.609 | 7.652 | 5.500 | 2.750 | 0.143 |

because of the limitation of computer time. The error introduced by assuming that the neutron source is constant over each sub-area is discussed with the theoretical results in Section T5.3.

T4.6 Introduction to the Discussion of the Computer Code

The representation of the cavity assemblies has been discussed and each sub-area has been assigned an average albedo. The computer code is discussed next. The nomenclature used in the code is defined, and the general plan for the calculation of the flux distribution is explained. A detailed description of the code for the 45° cavity appears in Appendix B3.

As was stated in the introduction to this chapter, the incident current for each sub-area, J_i , is obtained from a set of simultaneous equations by means of an iteration technique. The constant value of the flux for each sub-area is calculated from the value of J_i , and the average value of the albedo β_i is obtained from equation (T4.1).

The nomenclature of the iteration program follows.

$A_1(I,J)$ = sub-area on surface #1 at the position I,J = 1.0 unit of area,

$J_1(I,J)$ = current incident on $A_1(I,J)$ in $n/cm^2 \cdot sec$,

$C_1(I,J)$ = number of neutrons incident on $A_1(I,J)$ per second = $J_1(I,J) \cdot A_1(I,J)$,

$T_1(I,J)$ = the current re-entering through $A_1(I,J)$ in $n/cm^2 \cdot sec$,

$\beta_1(I,J)$ = average value of the albedo for $A_1(I,J) = T_1(I,J)/J_1(I,J)$,

$F(I,J)$ = number of source neutrons entering through $A_1(I,J)$ in $n/cm^2 \cdot sec$,

$AL_1(I,J) = \beta_1(I,J)$,

$D_1(I,J) = 1 - \beta_1(I,J)$,

$V_1(N_1, N_2, N_3) = \text{view factor} \times \text{area} = A_j F_{ji}$.

It should be noted that the area of a square is unity, of a triangle is $\frac{1}{2}$, and of a slanted rectangle is 1.414.

In Chapter T2, the product of the view factor, $F(I,J,K)$ and the area A was represented by $V(I,J,K)$; this product was calculated and punched on IBM cards. The convenience of using the product arises from the relationship,

$$A_i F_{ij} = A_j F_{ji}, \quad (T4.2)$$

from which, for unit areas, it follows that

$$V_{ij} = V_{ji}.$$

The quantity V_{ij} is used to calculate the contribution from A_i to A_j and also from A_j to A_i and thus only half of the V_{ij} need to be calculated.

Each sub-area $A(I,J)$, and the corresponding values of J , C , T , F , β , AL , and D , are defined in terms of the coordinate system drawn on the cavity surfaces in Figures T4.6 through T4.7. The arguments of $V_1(N_1, N_2, N_3)$ represent two pieces of information. First, they define the relative position of A_i and A_j which, in turn, uniquely define the value of $V_1(N_1, N_2, N_3)$; this was seen in Figure T2.3, where the definition of I , J , and K was given for $F_1(I,J,K)$. Second, N_1 , N_2 , and N_3 are the indices of an indexed variable in a computer program, and consequently define the storage location of $V_1(N_1, N_2, N_3)$. To understand the indices of the view factors as they are written in the program, one must be familiar with the definition of the coordinate system used to define each view factor.

Equation (T1.4) is rewritten in terms of the above nomenclature without specifying the surface numbers:

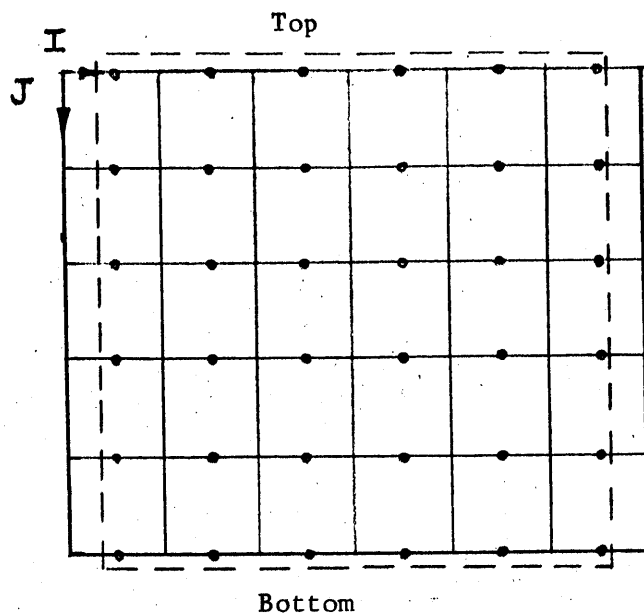


Figure T4.16 The Thermal Column Face (dashed lines) and the Foil Locations (circles) Superimposed on Surface #1

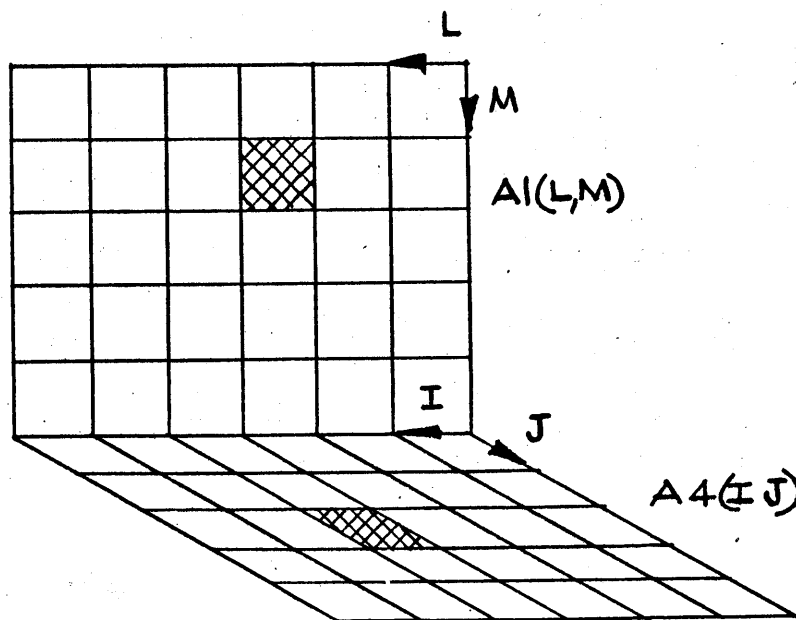


Figure T4.17 Surfaces #1 and #4 with 12" sub-areas. The Coordinates I,J and L,M define the location of the sub-areas, $A4(I,J)$ and $A1(L,M)$, respectively

$$\begin{aligned}
C(I,J) = J(I,J) \times A(I,J) = & \sum_{L,M}^{\text{all other surfaces}} T(L,M) \cdot V(N1, N2, N3) \\
& + \sum_{L,M}^{\text{source surface}} F(L,M) \times V(N4, N5, N6), \quad (T4.3)
\end{aligned}$$

where

$$T(L,M) = \beta(L,M) \times J(L,M) = A(L,M) \times C(L,M). \quad (T4.4)$$

As an example of the form of these equations as they appear in the FORTRAN code, the contribution from Surface #1 to Surface #4 is written for the case of the 45° cavity (see Figure T4.17).

$$C4(I,J) = \sum_{L,M}^{\text{all } A1(L,M)} [T1(L,M) + F(L,M)] V1(|I-L| + 1, 6-M, J) + \sum_{L,M}^{\text{other surfaces}} \quad (T4.5)$$

Surface #1, which is the thermal column face, has source neutrons, $F(L,M)$, and reflected neutrons, $T1(L,M)$, entering the cavity. The quantities, $|I-L| + 1$, $6-M$, and J , correspond to the I , J , and K coordinates, respectively, shown in Figure T2.3. For the particular case of $I = 4$, $J = 3$, $L = 3$, and $M = 2$, equation (T4.5) has the following form:

$$C4(4,3) = [T1(3,2) + F(3,2)] V1(3,4,3) + \text{other surfaces}. \quad (T4.6)$$

$A1(3,2)$ and $A4(4,3)$ appear as shaded sub-areas in Figure T4.17. The equations for the current incident on all of the surfaces have the same form.

T4.7 Description of the General Flow Diagram of the Computer Code

Now that the nomenclature of the program has been discussed, the program itself is described. Separate programs were written for the PARA and 45° hohlraum, and each contains a main routine and seven sub-routines. The general flow diagram, shown in Figure T4.18, is identical for both programs and is discussed first. Parts of the code are discussed in detail in Appendix B3.

The first step in the general flow diagram is the reading of input data. The V's, AL's, D's, and F's are stored in the computer according to their indices. Also, the dimensions of the cavity surfaces, and a few additional quantities, which will be explained in Appendix B3, are read into storage. Each re-entering current is given an initial value for the first iteration. The values of C(I,J) are calculated for the sub-areas on each surface by using equations such as equation (T4.3). After all of the C(I,J) have been calculated, they are normalized to preserve a neutron balance in the cavity. The resulting values of the C(I,J) are converted into the corresponding values of T(I,J) by means of equation (T4.4). The new values of T(I,J), calculated from their corresponding C(I,J)'s, are compared with the assumed values. If each of the new and old T(I,J) agrees within a specified range, the iteration is completed and the output information is printed. If the new and old values of the T(I,J) do not agree, the new values of the T(I,J) are used to calculate a new set of C(I,J) for each sub-area. A test of agreement is made again, and the iteration procedure continues until the desired agreement has been obtained.

The symmetry of the incident and re-entering currents permits the number of calculations to be reduced because the incident currents on only

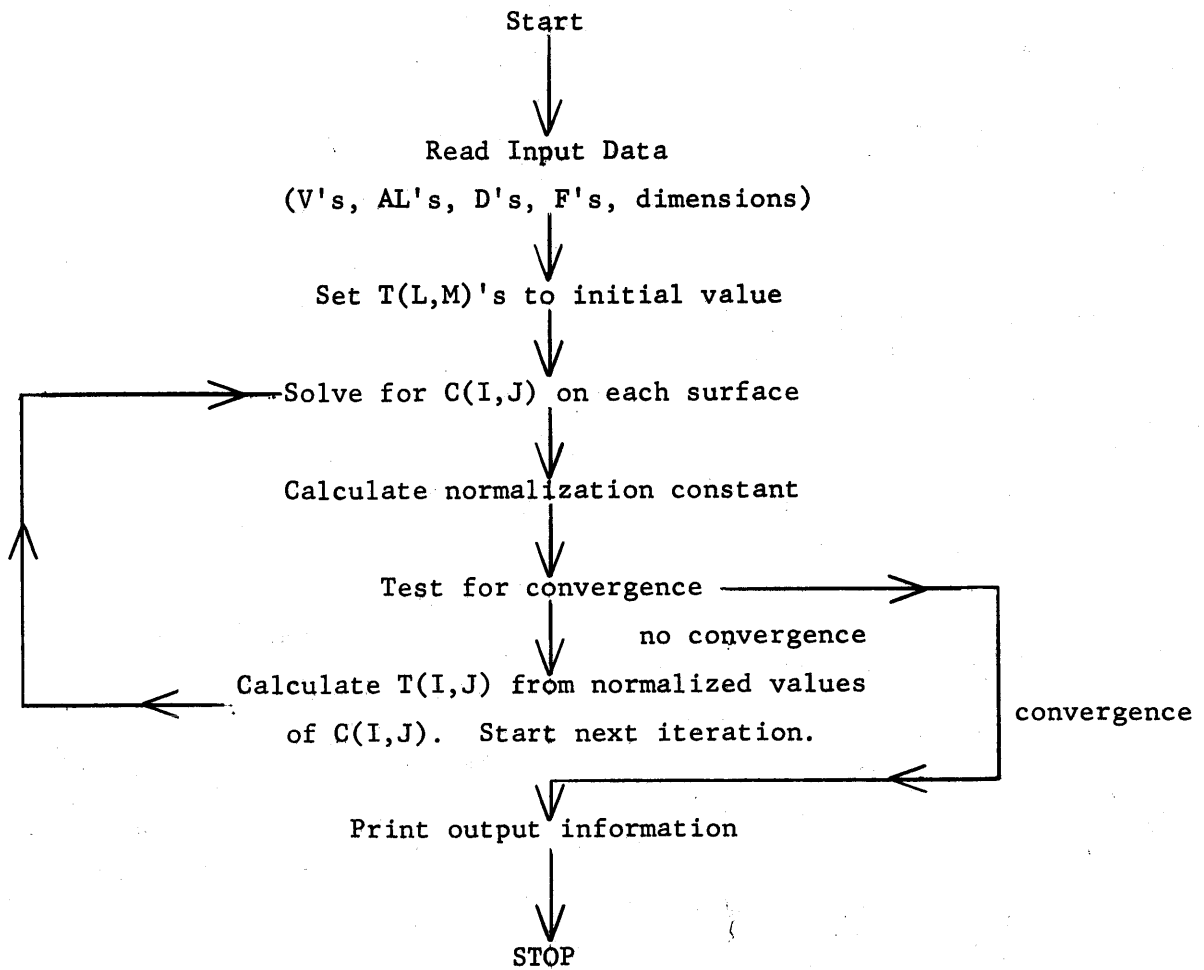


Figure T4.18 General Flow Diagram for the Computer Code that Calculates the Flux Distribution

half of the sub-areas must be determined. The currents are symmetrical about a vertical plane running from the middle of the thermal column face (Surface #1) to the surface of the back wall (Surface #2). This symmetry results from the fact that the neutron source is symmetrical about the vertical mid-line on the thermal column face, and the assembly on one side of the plane of symmetry is identical to that on the other side. The $C(I,J)$'s are calculated on only half of Surfaces 1, 2, 3 and 4; $C6(I,J)$ is calculated for the entire surface, and is identical to $C5(I,J)$ which is therefore not calculated. This symmetry is present for all of the assemblies.

Chapter T5

Theoretical Results

T5.1 Tabulation of the Results

The values of the flux on the honeycomb were calculated for Assemblies I, II, IV, V and VI by means of the computer program described in the previous chapter. The flux was calculated for 6" and 12" sub-areas in Assemblies I and II, and for 12" sub-areas in Assemblies I, II, IV, V and VI. The values were corrected for the forward anisotropy of the angular distribution of the neutrons as discussed in Section T2.2.

The location of a sub-area, $A_3(I,J)$, on the honeycomb and its corresponding constant value of flux, $\phi_3(I,J)$, are defined by the coordinate system (I,J) , shown in Figures T5.1 and T5.2 for the 6" and 12" sub-areas, respectively. The location at which the flux was measured is indicated by circles in these figures. Note the designation of the sides of the honeycomb as the front, back, north and south sides. The theoretical values of $\phi_3(I,J)$ for each of the five cavity assemblies are given in Tables T5.1 through T5.3, as functions of the coordinates (I,J) . Since the calculated flux, $\phi_3(I,J)$, is symmetrical about the mid-line running from the front to the back of the honeycomb, only the values of $\phi_3(I,J)$ for $I = 1$ to 3 in the case of 12" sub-areas and for $I = 1$ to 6 in the case of 6" sub-areas are listed.

T5.2 Comparison of the Results for the 6" and 12" Sub-areas

The influence of the size of the sub-area on the value of the calculated flux may be studied by comparing the results for sub-areas of different size in the same cavity assembly. The values of the flux on the honeycomb, calculated for 6" and 12" sub-areas in Assembly II, are compared

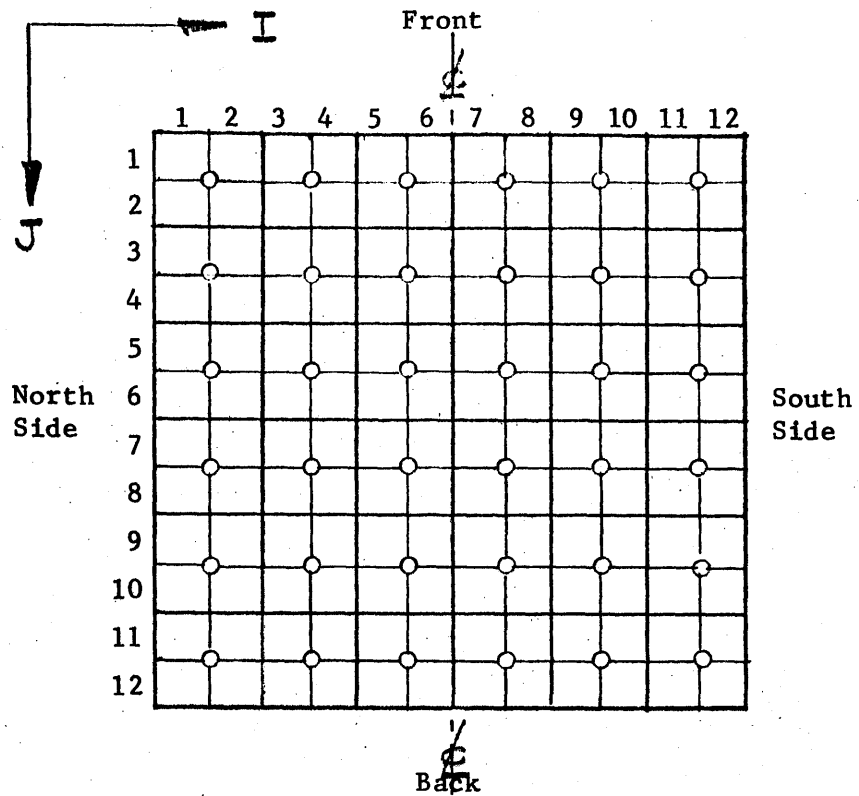


Figure T5.1 Location of the 6" Sub-Areas on the Honeycomb, Defined by the I,J Coordinates. The circles represent the foil locations.

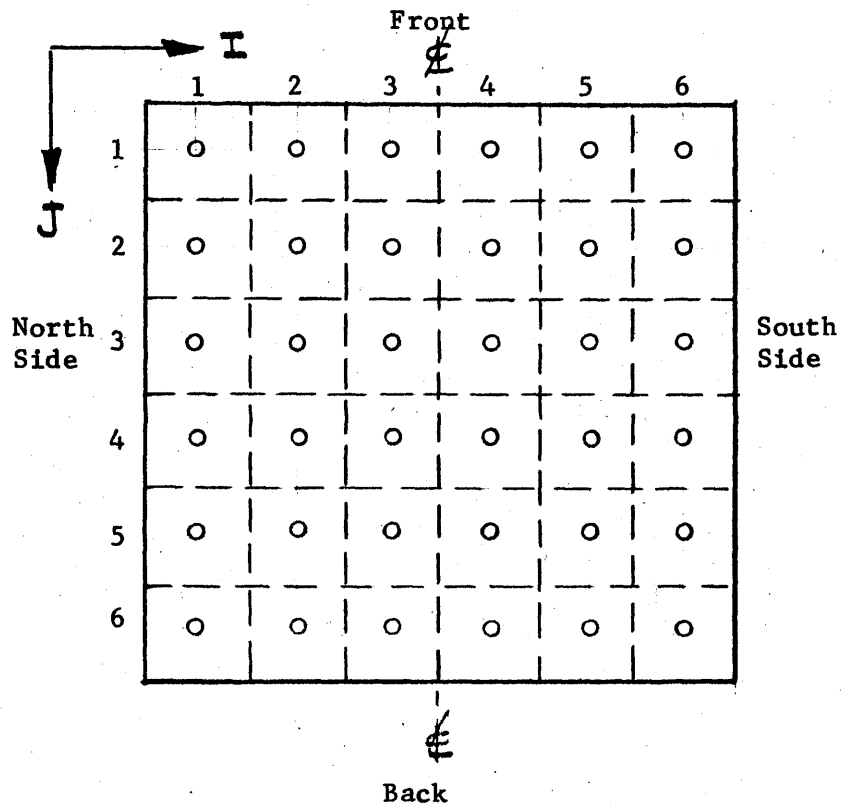


Figure T5.2 Location of the 12" Sub-Areas on the Honeycomb, Defined by the I,J Coordinates. The circles represent the foil locations.

Table T5.1

The Values of the Flux, $\phi_3(I,J) \times 10^8$, in the 6" Sub-Areas
on the Honeycomb of Assembly I

| | | I | | | | | |
|---|----|-------|-------|-------|-------|-------|-------|
| | | 1 | 2 | 3 | 4 | 5 | 6 |
| J | 1 | 4.314 | 4.880 | 5.218 | 5.502 | 5.697 | 5.799 |
| | 2 | 4.775 | 5.501 | 5.876 | 5.947 | 6.082 | 6.146 |
| | 3 | 4.768 | 5.587 | 5.744 | 5.843 | 5.909 | 5.944 |
| | 4 | 4.704 | 5.529 | 5.662 | 5.727 | 5.756 | 5.777 |
| | 5 | 4.615 | 5.450 | 5.577 | 5.626 | 5.661 | 5.674 |
| | 6 | 4.493 | 5.359 | 5.493 | 5.530 | 5.560 | 5.566 |
| | 7 | 4.402 | 5.266 | 5.422 | 5.464 | 5.495 | 5.501 |
| | 8 | 4.342 | 5.196 | 5.357 | 5.405 | 5.440 | 5.448 |
| | 9 | 4.290 | 5.141 | 5.296 | 5.356 | 5.383 | 5.396 |
| | 10 | 4.207 | 5.061 | 5.234 | 5.307 | 5.331 | 5.346 |
| | 11 | 3.972 | 4.875 | 4.989 | 5.158 | 5.191 | 5.210 |
| | 12 | 3.557 | 4.122 | 4.263 | 4.335 | 4.370 | 4.381 |

Table T5.2

The Values of the Flux, $\phi_3(I,J) \times 10^8$, in the 6" Sub-Areas
on the Honeycomb of Assembly II

| | | I | | | | | |
|---|----|-------|-------|-------|--------|--------|--------|
| | | 1 | 2 | 3 | 4 | 5 | 6 |
| J | 1 | 7.211 | 8.289 | 8.903 | 9.365 | 9.668 | 9.817 |
| | 2 | 7.971 | 9.284 | 9.794 | 10.092 | 10.309 | 10.416 |
| | 3 | 7.956 | 9.377 | 9.693 | 9.868 | 9.996 | 10.052 |
| | 4 | 7.839 | 9.274 | 9.517 | 9.635 | 9.708 | 9.744 |
| | 5 | 7.788 | 9.121 | 9.346 | 9.438 | 9.518 | 9.541 |
| | 6 | 7.501 | 8.954 | 9.189 | 9.261 | 9.325 | 9.343 |
| | 7 | 7.353 | 8.796 | 9.048 | 9.125 | 9.190 | 9.205 |
| | 8 | 7.239 | 8.669 | 8.923 | 9.006 | 9.073 | 9.088 |
| | 9 | 7.129 | 8.553 | 8.807 | 8.901 | 8.948 | 8.968 |
| | 10 | 6.984 | 8.408 | 8.685 | 8.809 | 8.840 | 8.860 |
| | 11 | 6.747 | 8.067 | 8.423 | 8.531 | 8.594 | 8.614 |
| | 12 | 5.932 | 6.797 | 7.028 | 7.143 | 7.202 | 7.220 |

Table T5.3

The Values of the Flux, $\phi_3(I,J) \times 10^8$, in the 12" Sub-Areas
on the Honeycomb of Assemblies I, II, IV, V and VI

| | | | | |
|---|---|---------------------|-------|-------|
| | | I \longrightarrow | | |
| | | 1 | 2 | 3 |
| J | 1 | 4.977 | 5.638 | 5.949 |
| | 2 | 5.345 | 5.833 | 5.945 |
| | 3 | 5.238 | 5.709 | 5.762 |
| | 4 | 5.102 | 5.612 | 5.667 |
| | 5 | 5.011 | 5.535 | 5.597 |
| | 6 | 4.621 | 5.056 | 5.118 |

$\phi_3(I,J) \times 10^8$
 Assembly I

| | | | | |
|---|---|---------------------|-------|-------|
| | | I \longrightarrow | | |
| | | 1 | 2 | 3 |
| J | 1 | 6.278 | 7.146 | 7.536 |
| | 2 | 6.596 | 7.253 | 7.411 |
| | 3 | 6.318 | 6.933 | 7.018 |
| | 4 | 6.021 | 6.666 | 6.748 |
| | 5 | 5.791 | 6.448 | 6.538 |
| | 6 | 5.544 | 6.139 | 6.261 |

$\phi_3(I,J) \times 10^8$
 Assembly IV

| | | | | |
|---|---|---------------------|--------|--------|
| | | I \longrightarrow | | |
| | | 1 | 2 | 3 |
| J | 1 | 9.055 | 10.465 | 11.022 |
| | 2 | 9.658 | 10.771 | 11.040 |
| | 3 | 9.377 | 10.425 | 10.620 |
| | 4 | 8.905 | 9.974 | 10.167 |
| | 5 | 8.113 | 9.144 | 9.336 |
| | 6 | 6.520 | 7.381 | 7.584 |

$\phi_3(I,J) \times 10^8$
 Assembly VI

Table T5.3 (continued)

| | | I → | | |
|-----|---|-------|-------|-------|
| | | 1 | 2 | 3 |
| J ↓ | 1 | 8.069 | 9.210 | 9.648 |
| | 2 | 8.345 | 9.366 | 9.536 |
| | 3 | 8.253 | 9.060 | 9.190 |
| | 4 | 7.994 | 8.830 | 8.958 |
| | 5 | 7.739 | 8.629 | 8.739 |
| | 6 | 6.962 | 7.748 | 7.881 |

$\phi_3(I,J) \times 10^8$
Assembly II

| | | I → | | |
|-----|---|-------|-------|-------|
| | | 1 | 2 | 3 |
| J ↓ | 1 | 5.283 | 6.048 | 6.392 |
| | 2 | 5.705 | 6.317 | 6.470 |
| | 3 | 5.574 | 6.179 | 6.278 |
| | 4 | 5.313 | 5.957 | 6.059 |
| | 5 | 4.871 | 5.495 | 5.606 |
| | 6 | 3.941 | 4.460 | 4.580 |

$\phi_3(I,J) \times 10^8$
Assembly V

by plotting the values from the front to the back of the honeycomb. The relationship between the 6" and 12" sub-areas on the honeycomb is shown in Figure T5.3, in which the solid lines represent the 12" sub-areas, and the broken lines represent the 6" sub-areas. In comparing the results for the 6" and 12" sub-areas, an average value of the flux in the 6" sub-areas must be used. For example, the value of $\phi_3(3,J)$ for the 12" sub-areas (see Figure T5.2) is compared to the average value of $\phi_3(5,J)$ and $\phi_3(6,J)$ for the 6" sub-areas (see Figure T5.1). The average value of the flux for the 6" sub-areas is obtained by first plotting the values of $\phi_3(I,J)$ from $I = 1$ to 6 for each value of J ; Figure T5.4 shows the value of $\phi_3(I,1)$ plotted in this manner. The average values of $\phi_3(5,1)$ and $\phi_3(6,1)$, of $\phi_3(3,1)$ and $\phi_3(4,1)$, and of $\phi_3(1,1)$ and $\phi_3(2,1)$ are taken to be the value of the flux at 6", 18" and 30", respectively, from the center line of the honeycomb. The average values of the flux in the 6" sub-areas are obtained for $J = 1$ to 12 and plotted in Figure T5.5, along with the values of $\phi_3(I,J)$ for the 12" sub-areas.

The values of the flux in the 12" sub-areas which do not border the edges of the honeycomb agree with the results calculated for the 6" sub-areas. In this region, the calculated flux distribution does not vary much within a single 12" sub-area and the use of sub-areas of this size does not introduce any serious errors as compared with the results based on the use of 6" sub-areas. The results for the 6" sub-areas do, however, predict a sharp decrease in the flux within 6" of the edges of the honeycomb. The value of the flux obtained for a 12" sub-area is an average value for the sub-area and consequently cannot predict variations in the flux near the edges of the honeycomb. A discrepancy exists, therefore,

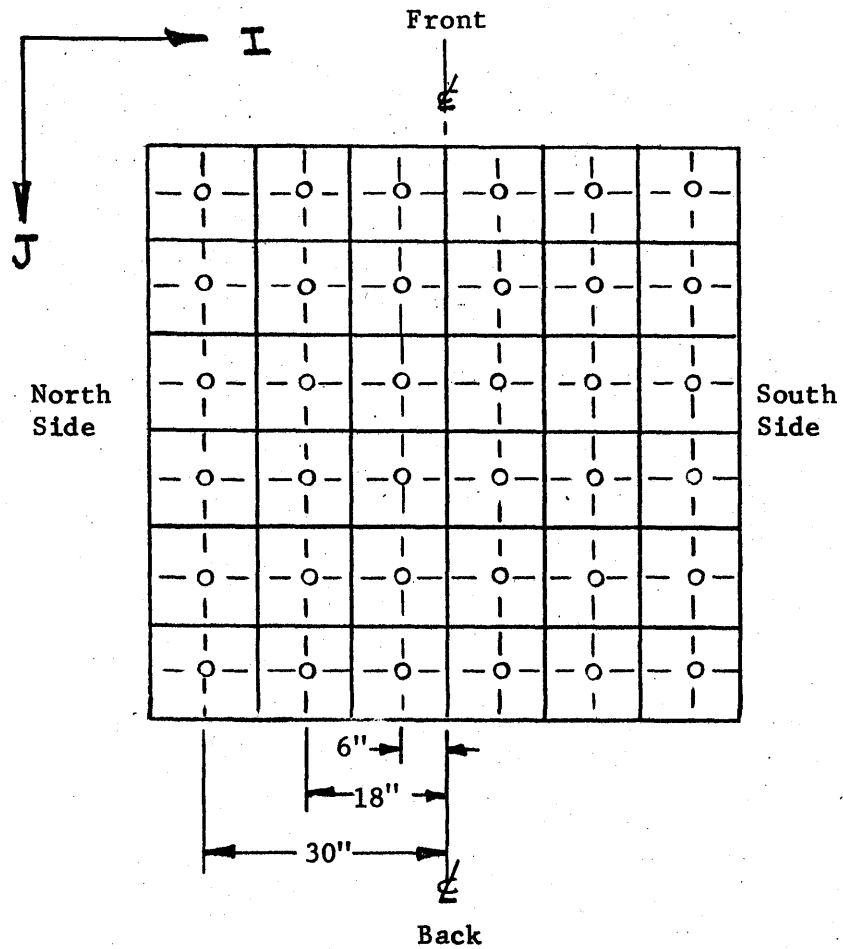


Figure T5.3 Location of the 6" and 12" Sub-Areas on the Honeycomb Surface. The circles represent the location at which the flux was measured.

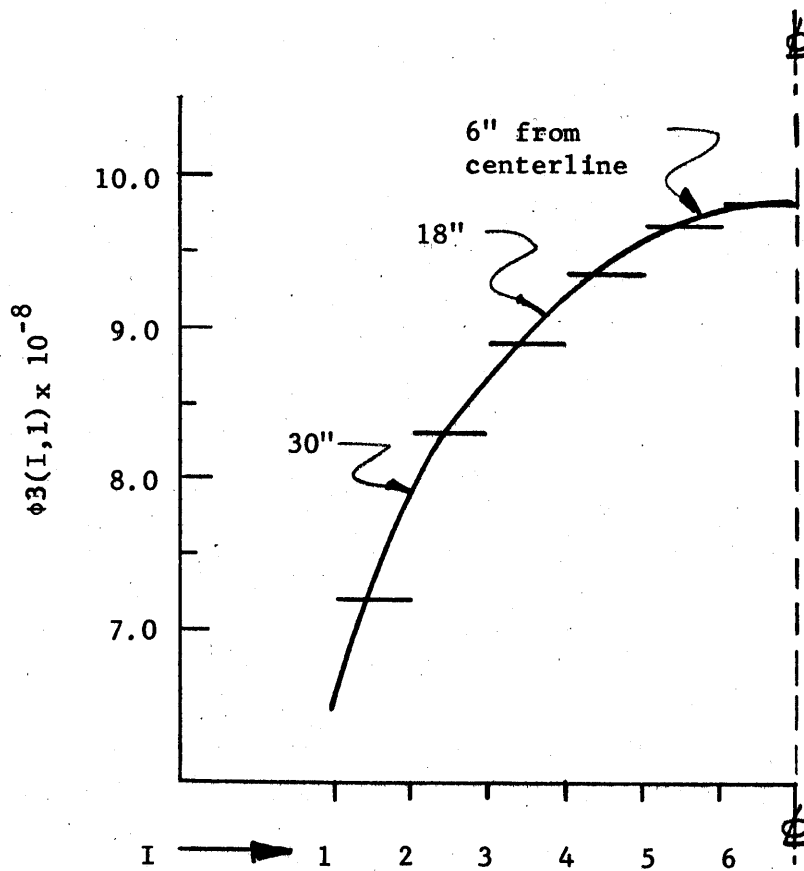


Figure T5.4 The Values of $\phi_3(I,1)$ for Assembly II Plotted from the Centerline to the Edge of the Honeycomb.

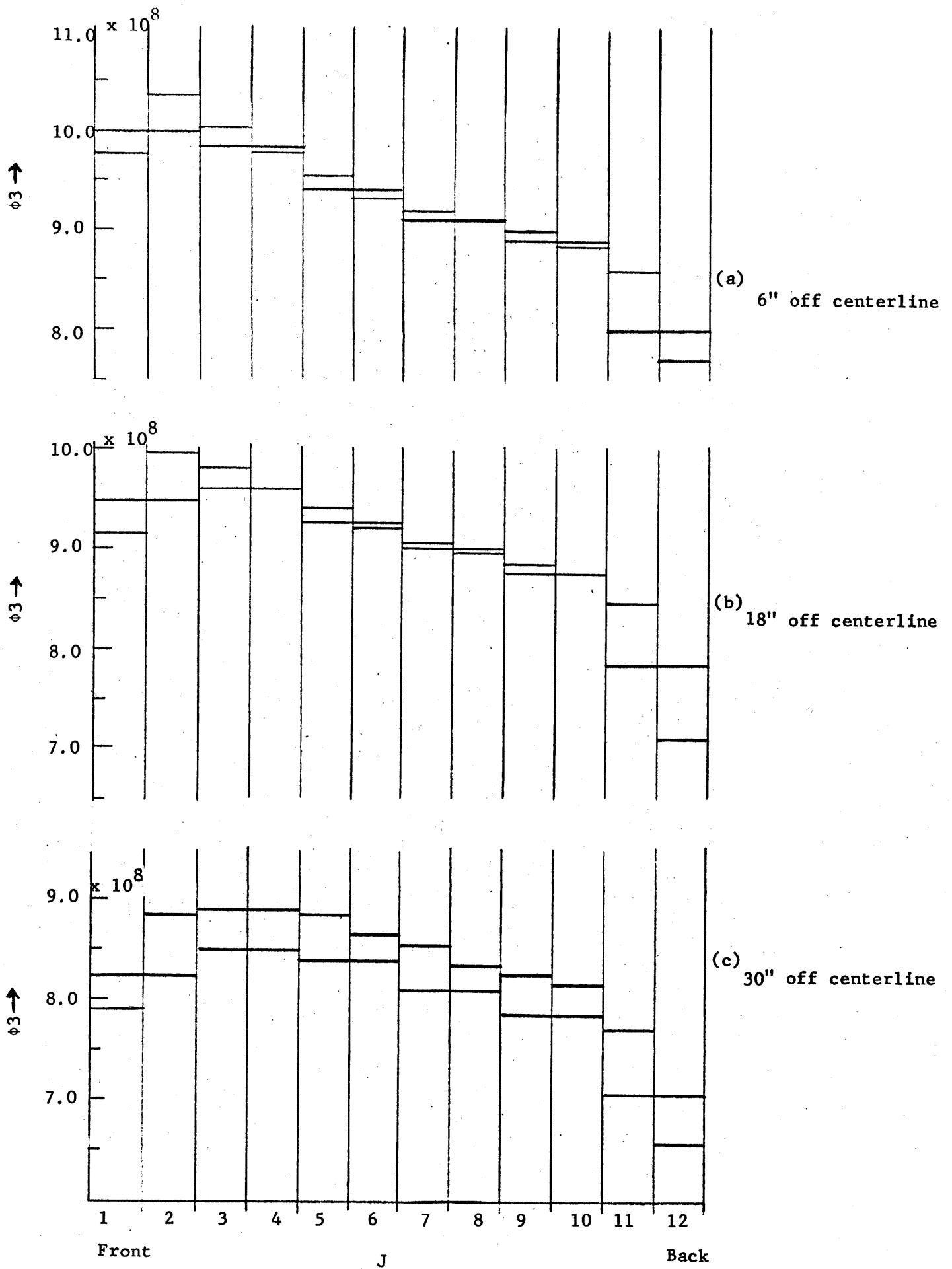


Figure T5.5 Comparison of Theoretical Values of the Flux for 6" and 12" Sub-Areas on Honeycomb of Assembly II.

between the values of flux in the 6" and 12" sub-areas which border the edges of the honeycomb. The discrepancy is clearly seen in Figure T5.5c, where the values of the flux for the 12" sub-areas bordering the side of the honeycomb are about five per cent lower than the values for the 6" sub-areas.

Although calculations based on the use of 6" sub-areas can predict more accurately variations in the flux distribution, calculations for the 12" sub-areas have the advantage of using only one-eighth as much computer time as those for the 6" sub-areas. A large value of the unit length L and a large sub-area are, therefore, useful for a cavity assembly in which the flux distribution has no large variations.

T5.3 Discussion of the Applicability of the Theoretical Model

The approximations made in applying the theoretical model to the five cavity assemblies are discussed next.

In deriving the expressions for the view factors, the neutron current entering the cavity was assumed to be constant over a single sub-area. In Section T2.2 it was shown that if the current varies by ten per cent within a sub-area, the resulting error in the calculated flux for any sub-area is less than one per cent. The two types of currents which enter the cavity are the re-entering current, $T(I,J)$, and the neutron source, $S(I,J)$.

The distribution of the re-entering currents, which was plotted from the calculated values of the $T(I,J)$, shows that almost all of the currents vary by less than ten per cent within either a 6" or a 12" sub-area. The current varies by 10 to 20 per cent only in those sub-areas which border the edge of a wall. This relatively large variation is caused by the large neutron leakage from the edge of a wall. Hence, the variations in the

re-entering currents in both the 6" and 12" sub-areas produce an error of less than one per cent in the flux calculated for those sub-areas which do not border the side or back edges of the honeycomb, and an error of less than two per cent in the flux for those sub-areas which border the side and back edge of the honeycomb.

The magnitude of the neutron source varies by as much as 50 per cent over a 6" sub-area and 100 per cent over a 12" sub-area. As was pointed out in Section T2.2, the variations of the current entering the cavity within a sub-area do not cause any significant error in the flux calculated for sub-areas which are four or five units away. This statement is supported by the fact that the theoretical flux on the honeycomb for the 12" sub-areas agrees with that for the 6" sub-areas, even though the variation of the neutron source within a 12" sub-area is twice as great as the variation within a 6" sub-area.

In the theoretical model it is assumed that the current re-entering the cavity through a given sub-area is proportional to the current incident only on that sub-area. It was shown in Chapter T3 that the magnitude of the current re-entering the cavity through a given sub-area differs only by about one per cent from that calculated with the theoretical model, provided that the current incident on the given sub-area is within ten per cent of the average value of the current incident on adjacent sub-areas. The values of the incident current, as obtained from the calculations, are found to comply with the required condition, except for the sub-areas in the two back corners of the honeycomb. In the latter sub-areas, the incident current is about 15 per cent lower than the average of the currents incident in the adjacent sub-areas.

Only the flux on the honeycomb was corrected for the forward anisotropy of the neutron source; this correction increased the magnitude of the flux on the honeycomb by one to two per cent. The forward anisotropy also affects the flux at the other surfaces of the cavity which, in turn, would have a (secondary) effect on the flux at the honeycomb. Now if the values of the flux on the other surfaces were also corrected for the forward anisotropy of the source neutrons, they would be slightly greater at the back of the cavity and slightly smaller at the front. The effect of these corrections should be small, in view of the small effect of the correction of the neutron source itself, and their effect on the flux at the honeycomb should tend to cancel. Hence, correcting only the flux on the honeycomb for the forward anisotropy of the source neutrons seems to be justified. Since, as will be seen, the flux distributions calculated for the five cavity assemblies agree with experiment, the correction adopted does not seem to introduce any discernible error.

In the representation of the cavity assembly used in the calculations, the thermal column face was assumed to be 3" higher on Surface #1 than it actually is. This discrepancy is small compared to the dimensions of the thermal column face, and is also small compared to the distance between the thermal column face and the honeycomb. It seems probable, therefore, that the discrepancy would introduce, at most, a small error in the distribution of source neutrons, and we would expect intuitively that the effect on the flux at the honeycomb would be small. A similar argument applies to the "frame".

From the above discussion, it is concluded that the theoretical model may be applied to the five assemblies in which the flux was calculated. A maximum error of about two per cent is expected in the calculated flux on

the honeycomb for the sub-areas which do not border the edge of the honeycomb. Although no exact calculations can be made, the error in the flux for the sub-areas which border the back and side edge of the honeycomb should not be very much greater. If an error of one to two per cent is allowed for the convergence of the flux in the computer code (Appendix B2), an estimated maximum error of three or four per cent seems reasonable in the theoretical flux for the sub-areas which do not border the honeycomb.

T5.4 Analysis of the Theoretical Flux Distribution

The effects of the geometrical and material arrangement of the cavity assembly on the magnitude and distribution of the flux at the honeycomb have been discussed in the presentation of the experimental results (see Section E3.6). These effects will now be analyzed in greater detail by considering the computer results.

The direct contribution of the source neutrons to the honeycomb and the neutron leakage from the sides of the pedestal are two major influences on the flux distribution on the honeycomb surface. The flux due to the direct contribution of the neutron source to the honeycomb is obtained with the aid of the computer code, and will be known as the "source" flux. The "reflected" flux due to the neutrons reflected from the walls of the assembly is obtained by subtracting the "source" flux from the total flux on the honeycomb. In Figures T5.6a and T5.6b the distribution from the front to the back of the honeycomb is plotted for the total flux, $\phi_3(3,J)$, the "source" flux, and the "reflected" flux, in Assemblies I and II, respectively, for the case of 12" sub-areas. The "reflected" flux increases considerably with the distance from the front of the honeycomb in Assembly I. The calculations show that few neutrons from the thermal

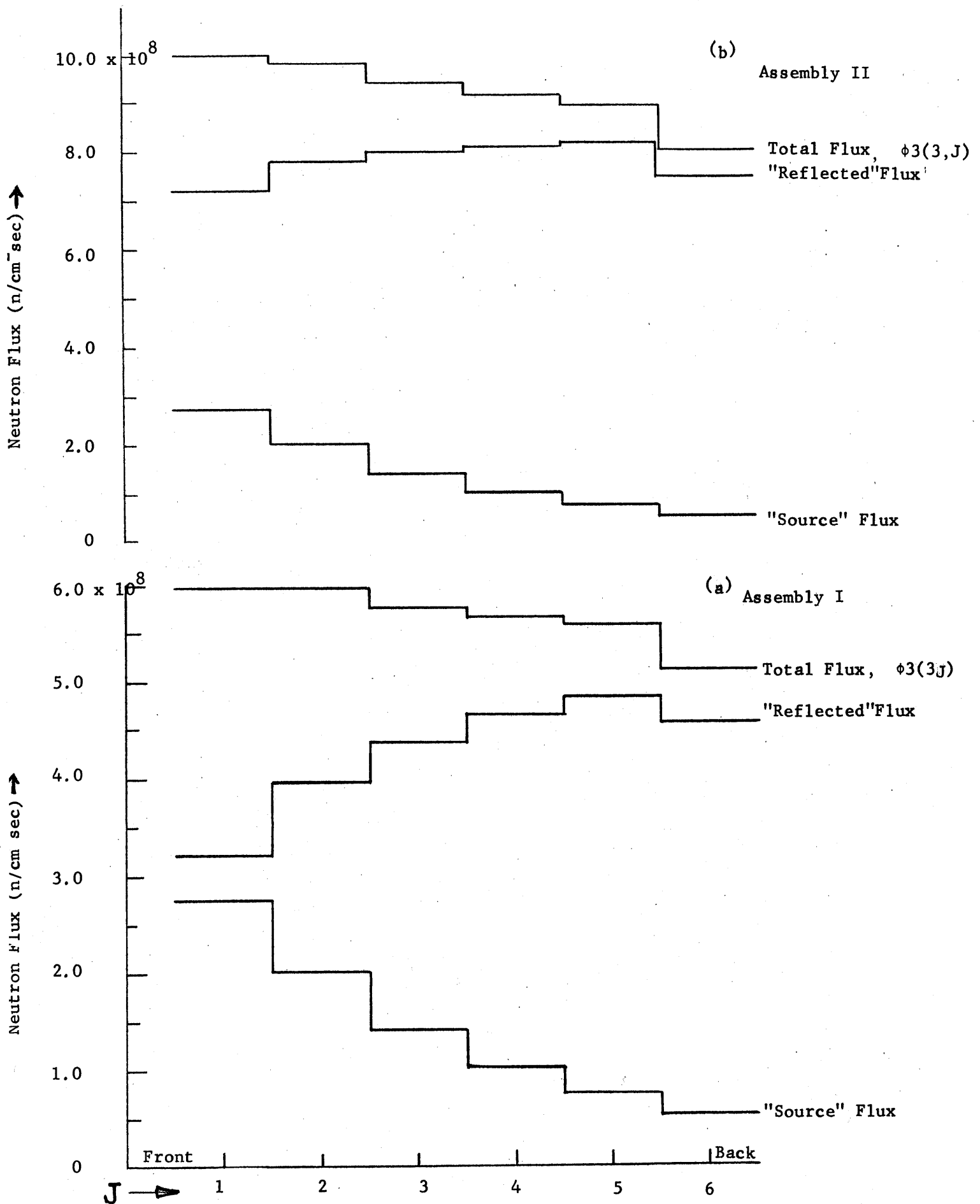


Figure T5.6 The Values of the Total, "Reflected" and "Source" Flux Plotted from Front to Back for Assemblies I and II.

column face of the boral-lined door space contribute to the "reflected" flux on the honeycomb, which is therefore due mainly to the contribution of the flux in the back part of the cavity assembly.

The influence of the "frame" on the "reflected" flux can also be seen in Figure T5.6b. The increase in the "reflected" flux with the distance from the front of the honeycomb is much smaller in Assembly II than in I; neutrons reflected from the frame add to the contribution of the "reflected" neutrons in other parts of the cavity assembly to produce an almost flat "reflected" flux on the honeycomb. Neutron leakage from the front and back edges of the pedestal lowers the values of $\phi_3(3,1)$ and $\phi_3(3,6)$ (see Figure T5.2), so that the distribution is not flat near the edges of the honeycomb.

The distribution of the flux from the north side of the honeycomb to the south side is plotted for Assemblies I and II in Figure T5.7. The distribution of the "reflected" flux is almost uniform for Assembly I, while the distribution of the "reflected" flux for Assembly II is similar to those of the "source" and total flux. The difference in the distribution of the "reflected" flux for Assemblies I and II is due to the reflection of the source neutrons from the frame to the honeycomb.

The effect of neutron leakage was determined by calculating the flux for the case in which there is no neutron leakage from the sides of the cavity walls. This is accomplished by using a constant value of the albedo for all the sub-areas on a surface. The results given by the computer code for the case of a constant albedo is shown for Assembly V in Figure T5.8. The dashed lines represent the flux for a constant albedo, and the solid lines represent the flux for the actual arrangement of Assembly V, with varying albedo. The flux for both cases is plotted from front to back ($J = 1$ to 6) and from side to side ($I = 1$ to 6) in Figures T5.8a and T5.8b,

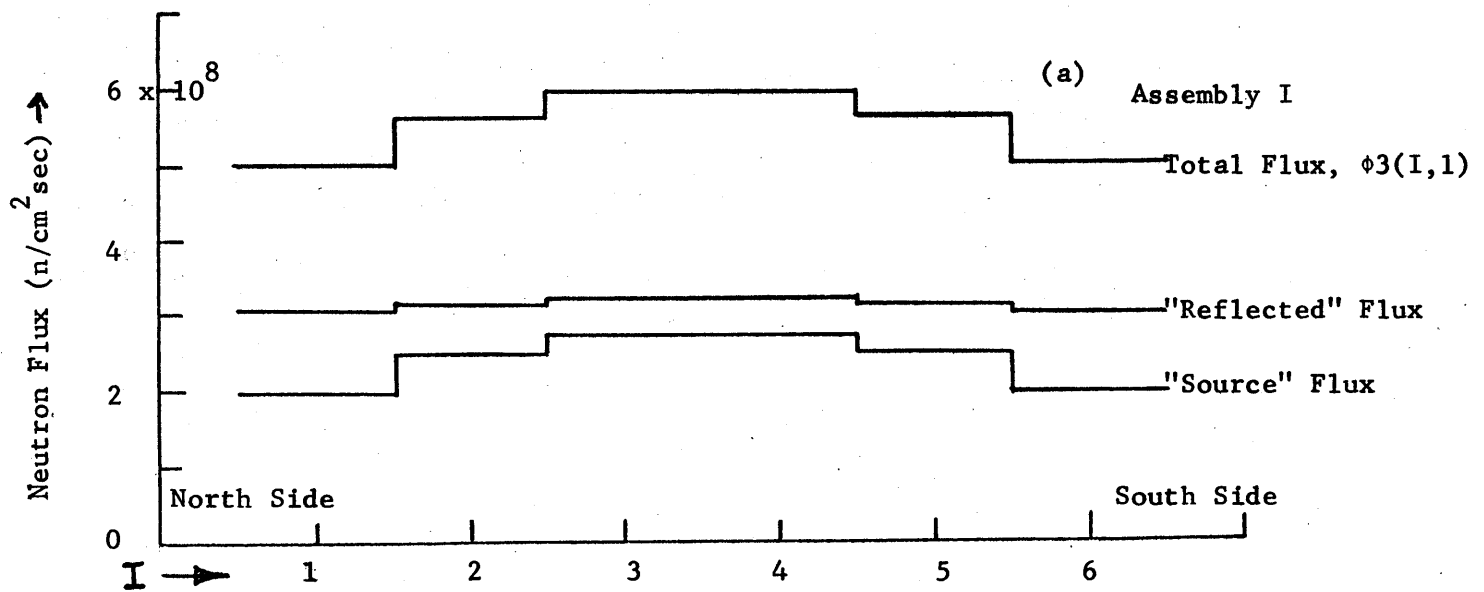
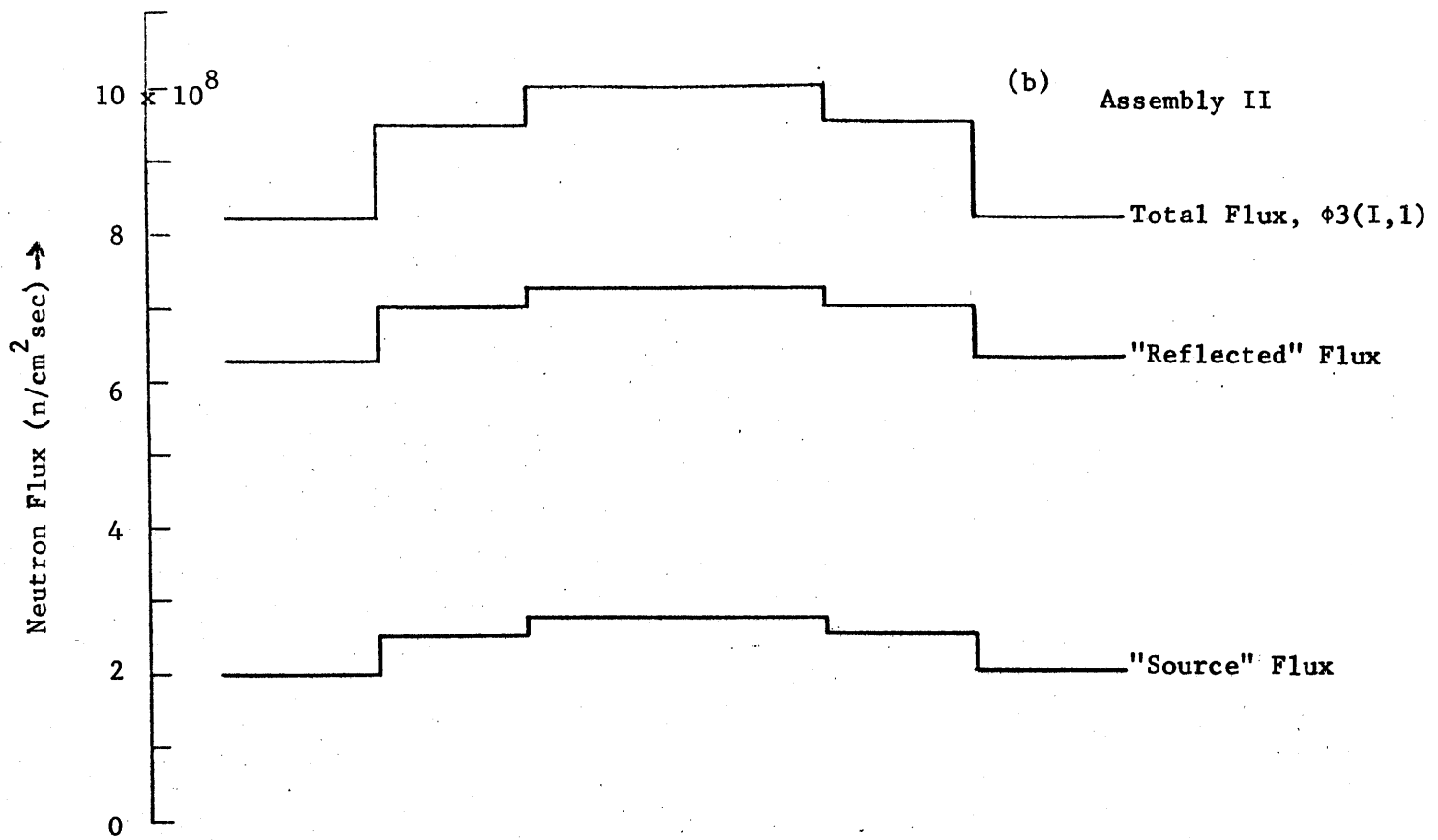


Figure T5.7 The Values of the Total, "Reflected" and "Source" Flux Plotted from Side to Side for Assemblies I and II.

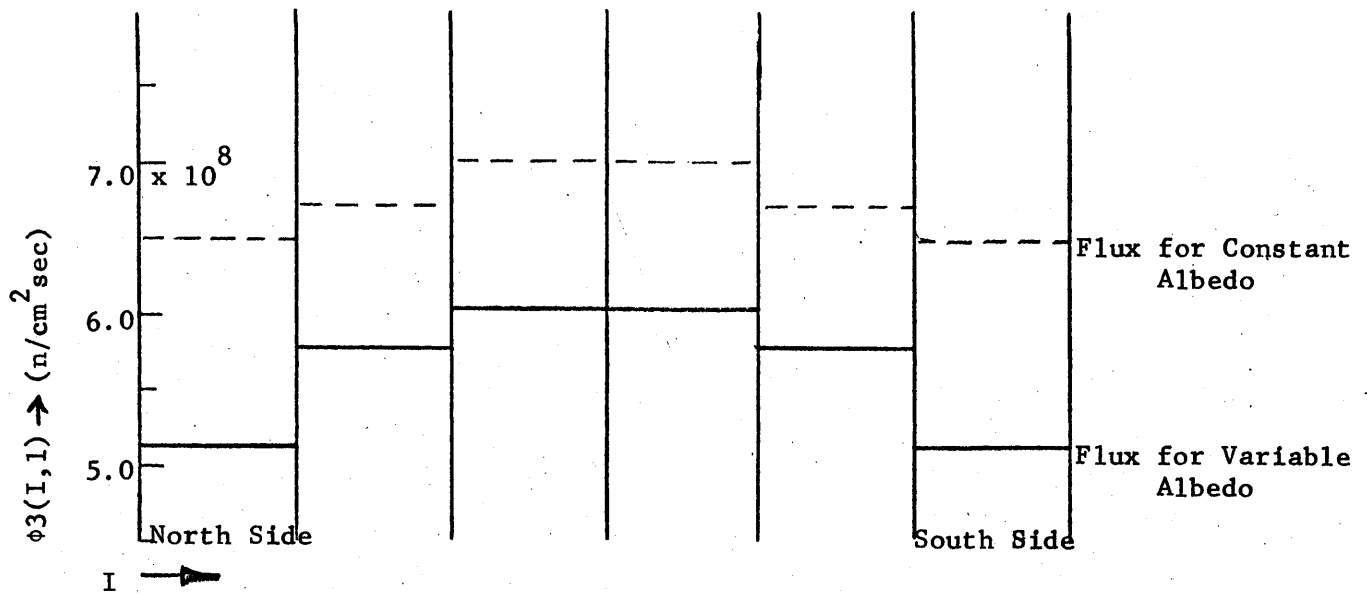


Figure (a)

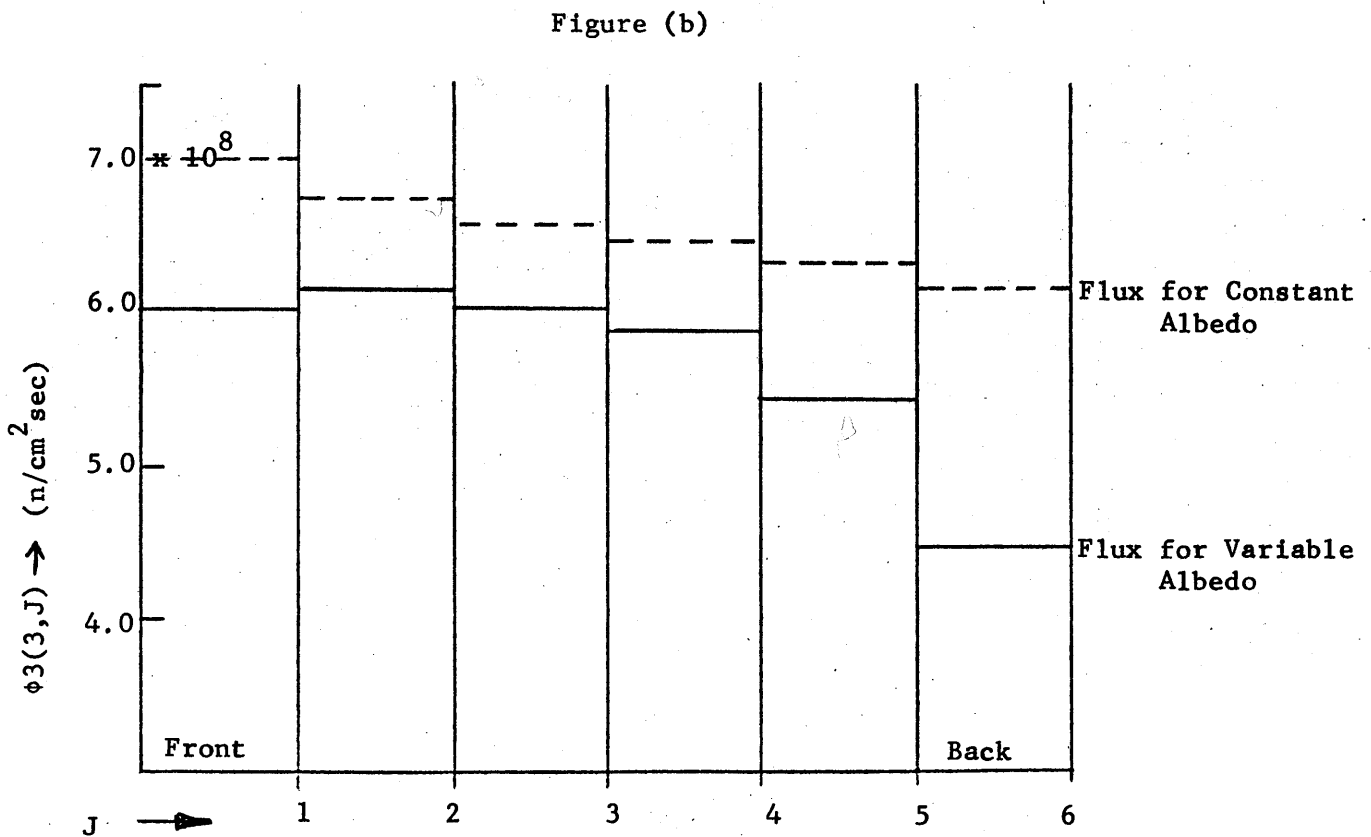


Figure T5.8 The Comparison of the Values of the Flux in Assembly V Obtained by Using a Constant and a Variable Value of the Albedo.

respectively. In both figures, the flux for constant albedo is greater in magnitude and more flat in distribution than is the flux which includes neutron leakage. The effect of the neutron leakage is emphasized by the large difference between the values of the flux near the edges of the honeycomb.

The theoretical results show that neutron leakage from the sides of the wall, and the boral and cadmium lining in the door space reduce the magnitude of the flux on the honeycomb. The flux was calculated for an idealized cavity in which there is no neutron leakage from the sides of the wall, no boral, and cadmium bordering the cavity. Figure T5.9 shows how this assembly would look. An albedo of 0.90 was assigned to all of the sub-areas of the cavity surfaces. Since there is no neutron leakage from the sides of the walls and no neutron absorbers bordering the cavity in this case, the flux on the honeycomb should be the maximum obtainable flux for a wall material having an albedo equal to 0.90. The flux distribution for this idealized cavity, shown in Figure T5.10, is plotted from the front to the back of Surface #3. The magnitude of the flux on the part of Surface #3 corresponding to the honeycomb (48" to 120" in Figure T5.10) is 2.5 to 3.0×10^9 n/cm² sec, which is three times greater than the flux measured in any of the experiments. The distribution in Figure T5.10 is also fairly flat over the surface of the honeycomb; the calculations showed that the source neutrons contribute about five per cent to the total flux on the honeycomb.

The value of 0.90 for the albedo was selected arbitrarily. Since the magnitude of the flux on the honeycomb is approximately proportional to the factor, $1/1-\beta$, (see Appendix B3, equation B3.4) equation (T5.1) may be used to approximate the flux for another value of the albedo.

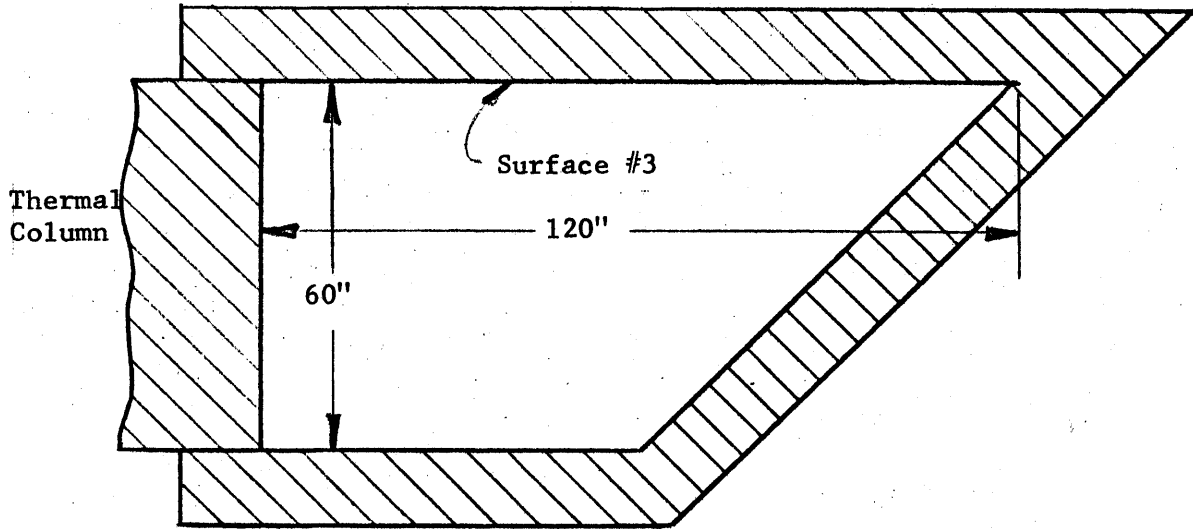


Figure T5.9 Vertical Section of the Idealized 45° Cavity Assembly.

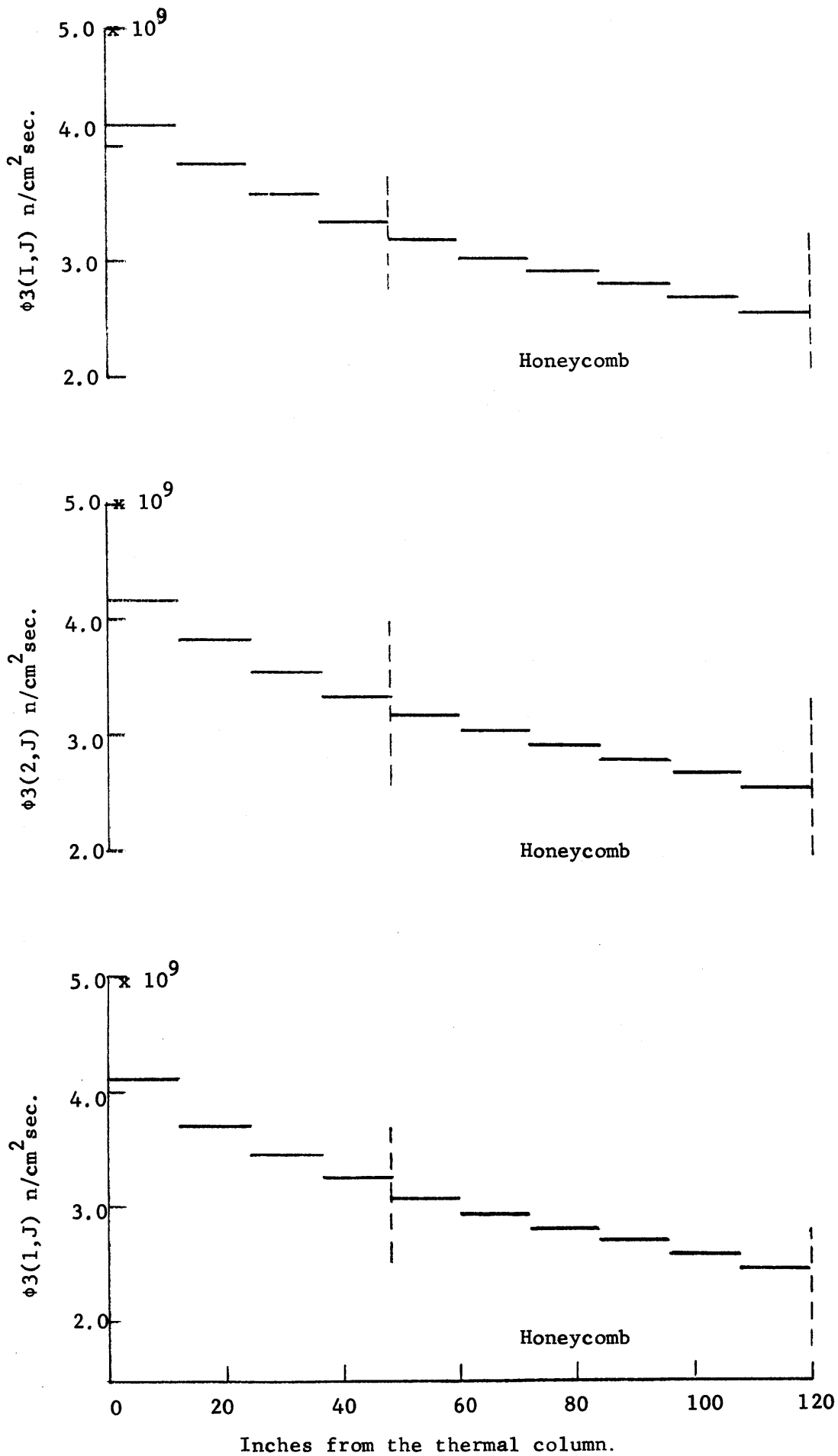


Figure T5.10 The Values of the Flux Calculated for the Idealized 45° Cavity Assembly with $\beta = 0.90$.

$$\phi_1 = \frac{(1-\beta_0)}{(1-\beta_1)} \phi_0 \quad (\text{T5.1})$$

If a value of 0.92 were used for the albedo in calculating the flux in the idealized cavity, the magnitude of the flux would be 25 per cent greater than that calculated by using a value of 0.90. This example illustrates the large influence that neutron leakage and neutron absorbers, such as boral and cadmium, have on the flux in a cavity.

T5.5 Comparison of Theory and Experiment

The theoretical and experimental results are compared by plotting the theoretical and experimental values of the flux from the front to the back of the honeycomb. The foils were located 6", 18", and 30" from the center line of the honeycomb (see Figure T5.3). The corresponding values of the theoretical flux in the 6" sub-areas are obtained by the method described in Section T5.2 of this chapter. The values of the flux, $\phi_3(I,J)$, calculated for 6" sub-areas in Assemblies I and II, are shown together with the flux measured in these assemblies in Figures T5.11 and T5.12, respectively. The circles represent the measured values of the flux and the horizontal lines represent the theoretical values of the flux for each J at a given distance from the center line of the honeycomb. The curve is the flux distribution obtained by connecting the centers of the horizontal lines.

The maximum error in the experimental values of the flux is about one per cent (see Chapter E3.5), while the error in the theoretical results has been estimated as about three to four per cent. All but two of the experimental points are within two per cent of the theoretical flux distribution in the two figures, so that the experimental and theoretical values of the flux are in excellent agreement for these two cases.

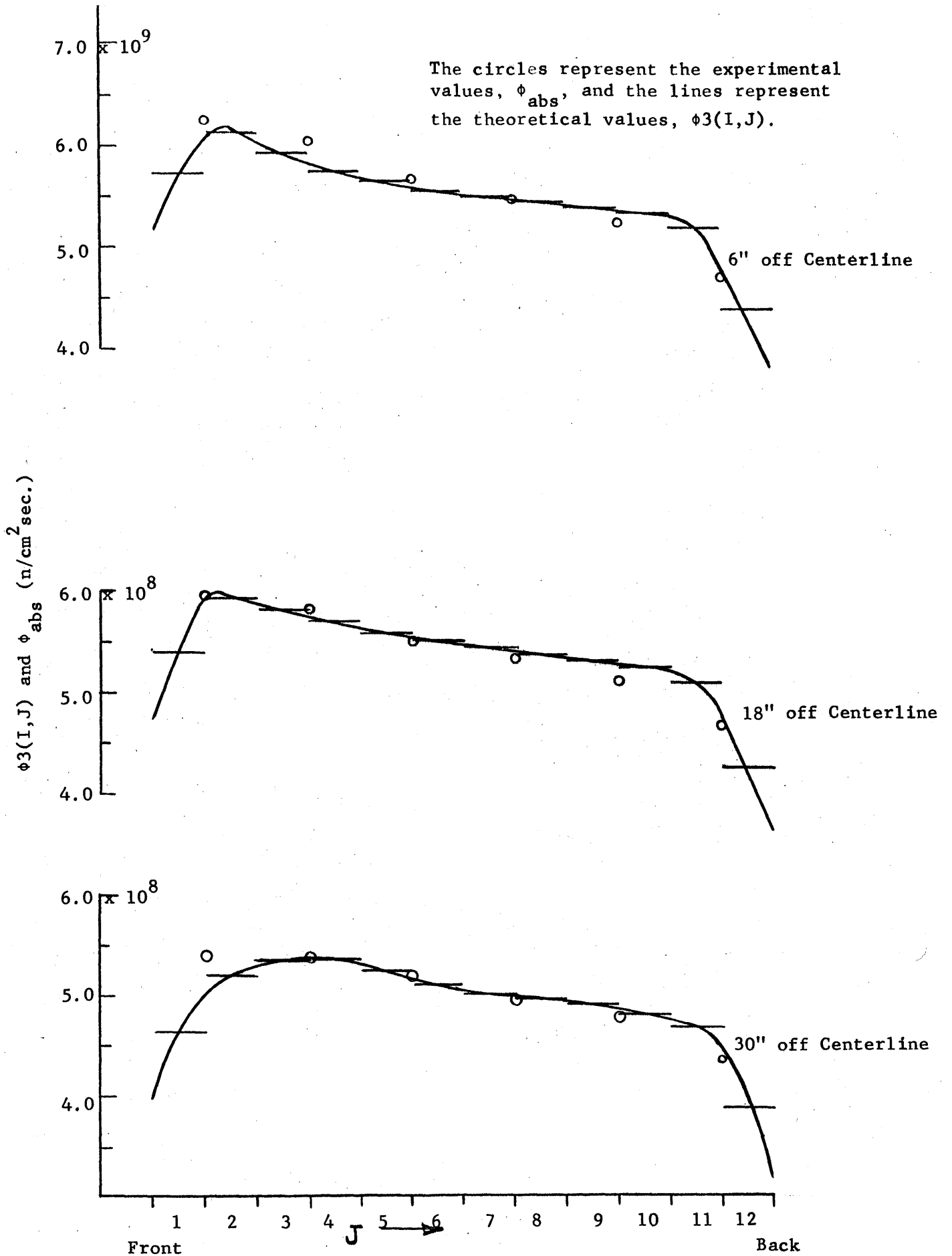


Figure T5.11 Experimental and Theoretical Flux for 6" Sub-Areas on Honeycomb of Assembly I.

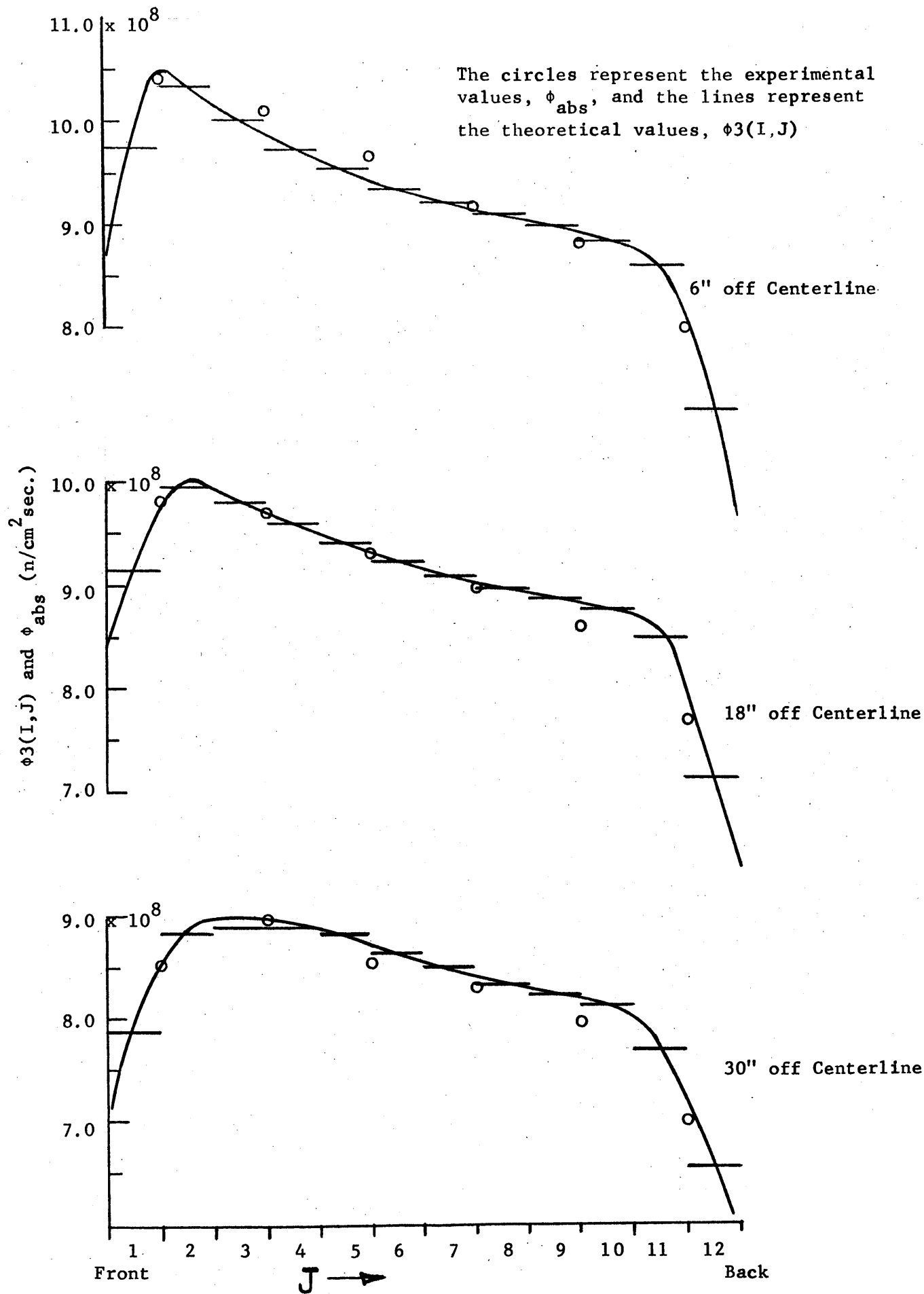


Figure T5.12 Experimental and Theoretical Flux for 6" Sub-Areas on Honeycomb of Assembly II.

The values of the flux for 12" sub-areas were calculated for Assemblies I, II, IV, V, and VI. The flux was measured at the points which correspond to the center of the 12" sub-areas (see Figure T5.3). The experimental and theoretical results are compared by comparing the values of $\phi_3(I,J)$ for the 12" sub-areas with the flux measured at the center of the sub-areas.

The theoretical and experimental results for Assemblies I, II, IV, V, and VI are plotted in Figures T5.13 through T5.17, respectively. The theoretical results are represented by horizontal lines and the experimental results by circles. Since the values of the flux calculated for the 12" sub-areas cannot describe the flux distribution near the front and back edges of the honeycomb (see Section T5.2 of this chapter), continuous curves are not drawn. However, the distribution can easily be visualized for the 12" sub-areas which do not border the front or the back edges.

The agreement between theory and experiment is good. Except for Assemblies I and VI, the values of the flux calculated in the sub-areas which do not border the side and front edges agree with experiment to within two per cent. The close agreement between the theoretical and experimental flux in the sub-areas bordering the back edge is fortuitous, since the theoretical model was shown to be most uncertain in this region. The values of the flux calculated for the sub-areas bordering the side of the honeycomb, $\phi_3(1,J)$, are consistently lower than the corresponding experimental value, as was expected. The values of $\phi_3(1,J)$ are also consistently lower than the corresponding values for the 6" sub-areas, which, in turn, agree with the values of the flux measured in Assemblies I and II. Even though a discrepancy does exist near the edges, the theoretical and experimental values differ by only about five per cent in most cases.

The circles represent the experimental values, ϕ_{abs} , and the lines represent the theoretical values, $\phi_3(I,J)$.

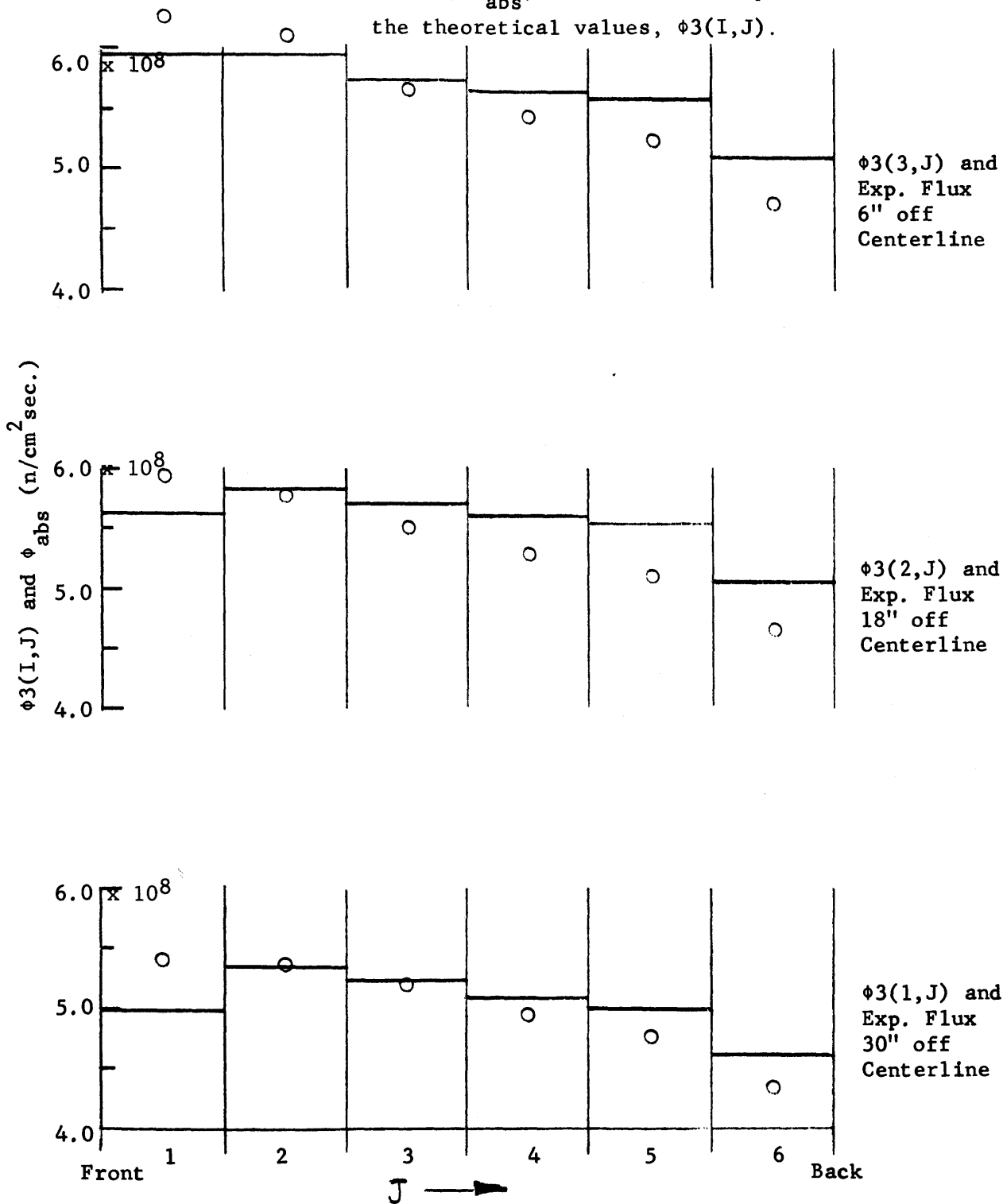
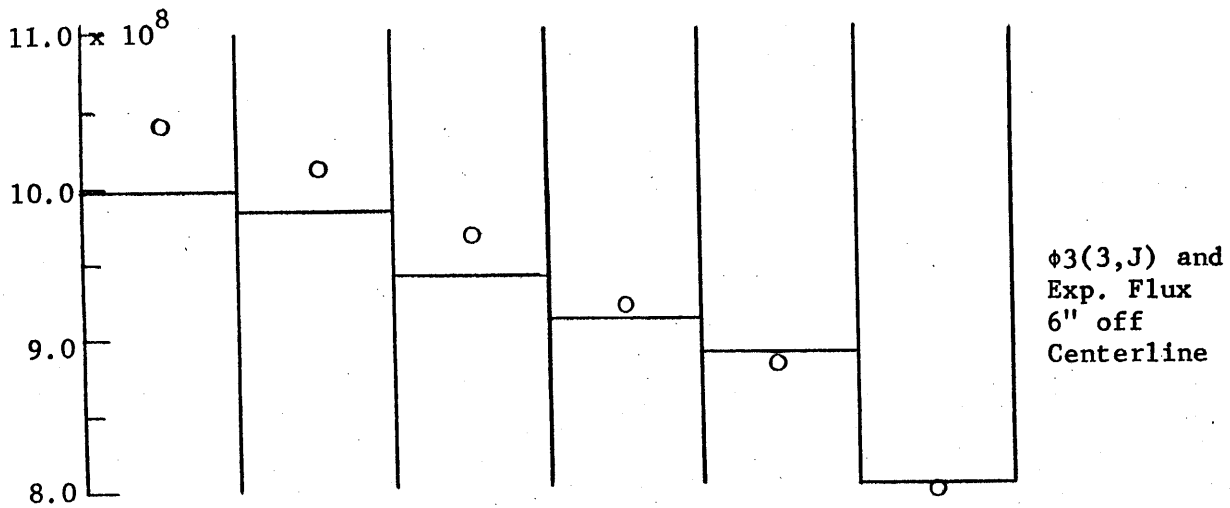


Figure T5.13 Experimental and Theoretical Flux for 12" Sub-Areas on Honeycomb of Assembly I.



The circles represent the experimental values, ϕ_{abs} , and the lines represent the theoretical values, $\phi_3(I,J)$.

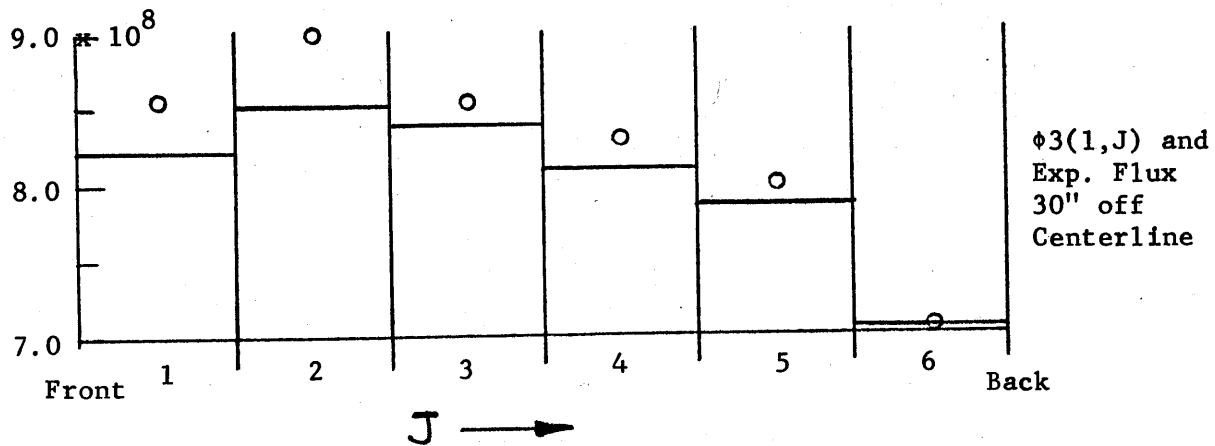
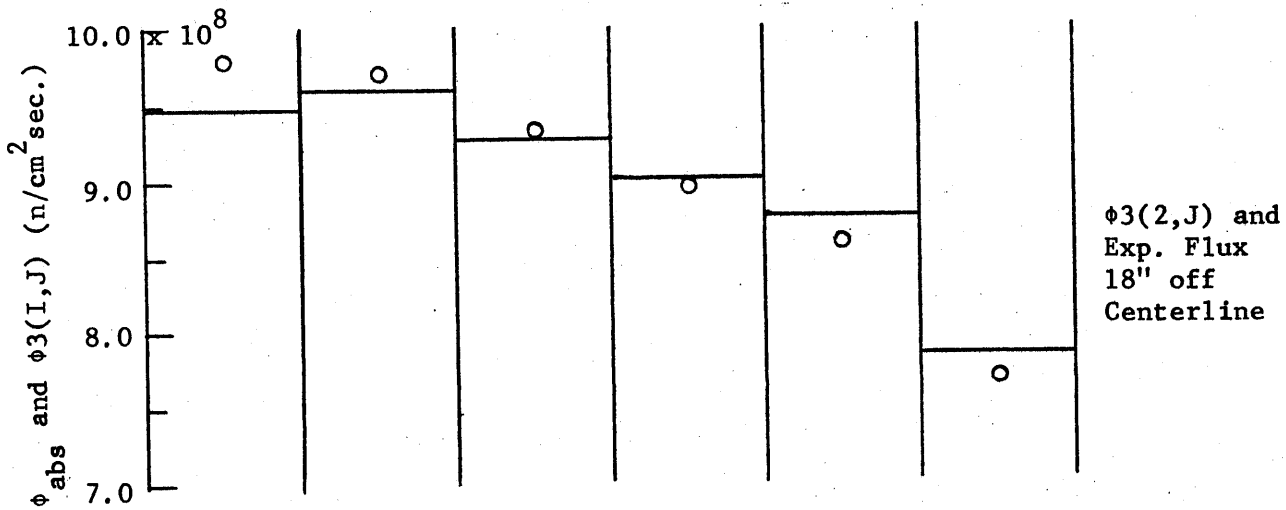
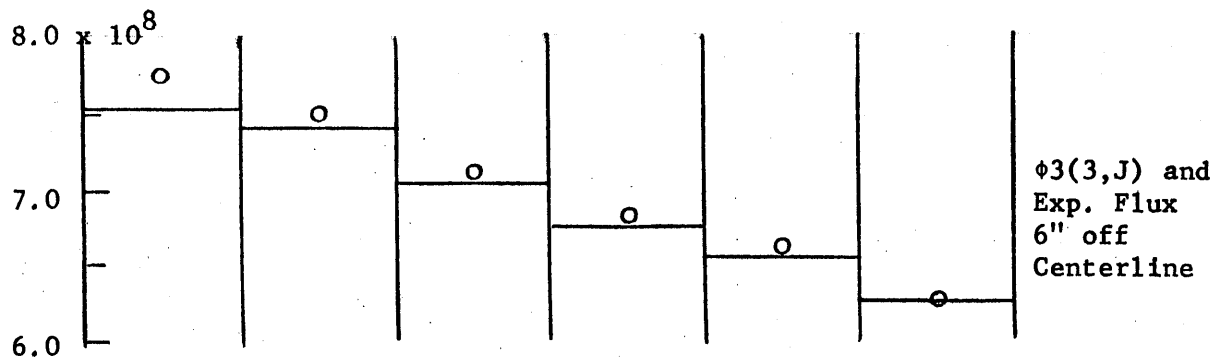


Figure T5.14 Experimental and Theoretical Flux for 12" Sub-Areas on Honeycomb of Assembly II.



The circles represent the experimental values, ϕ_{abs} , and the lines represent the theoretical values, $\phi_3(I,J)$.

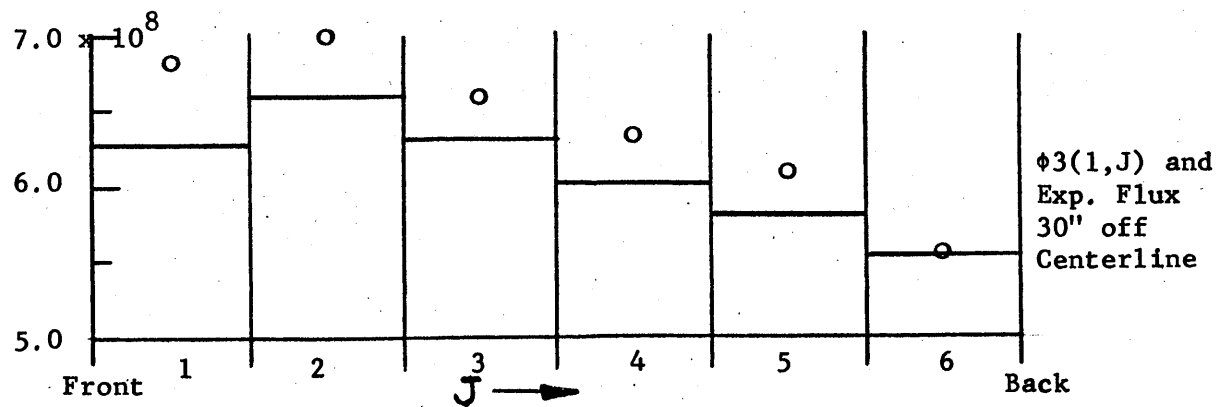
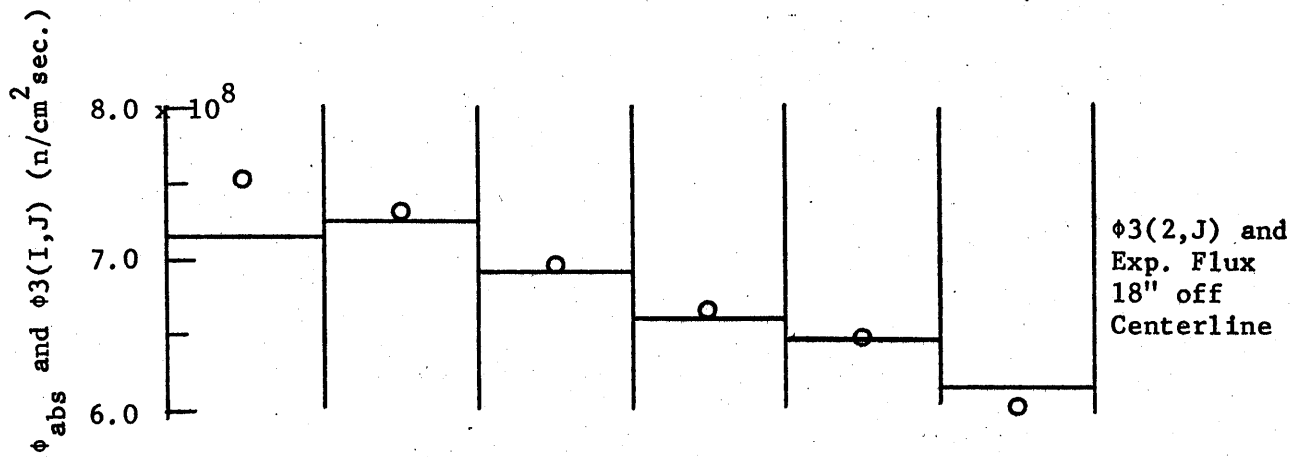
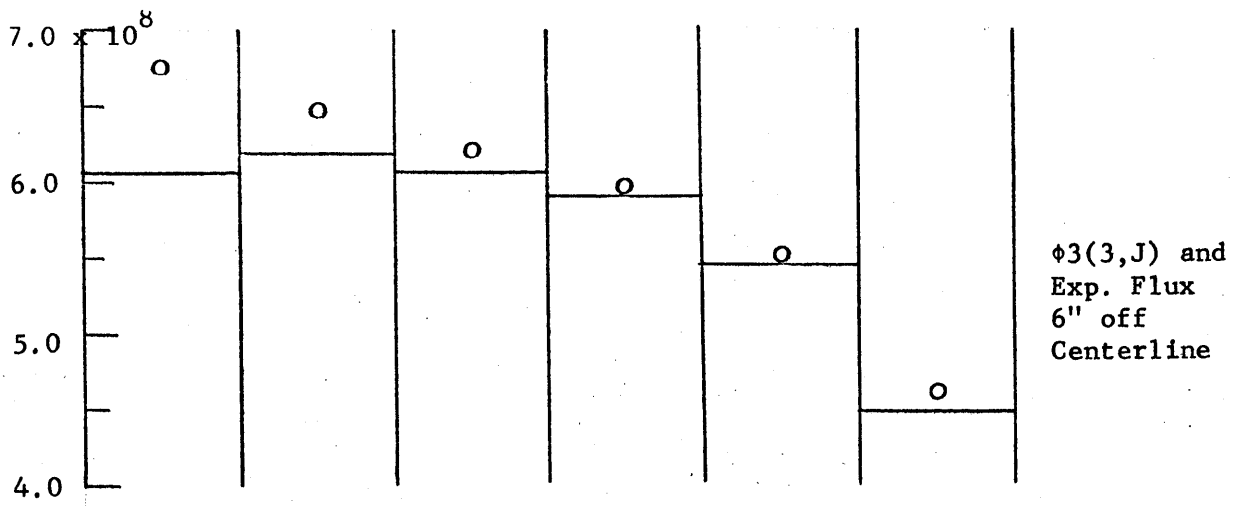
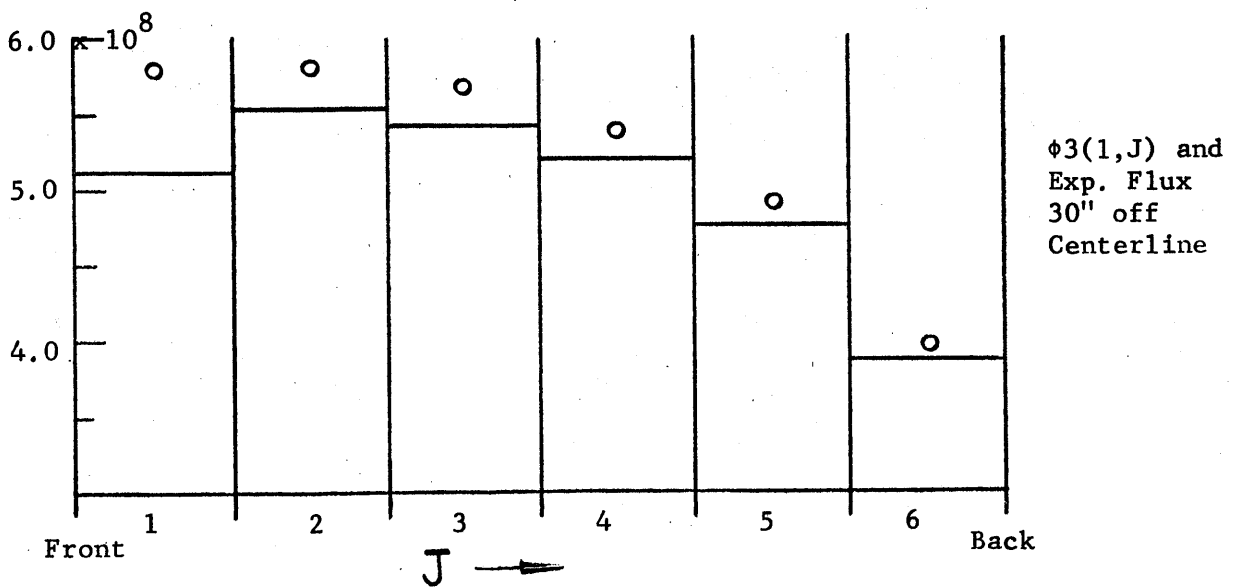
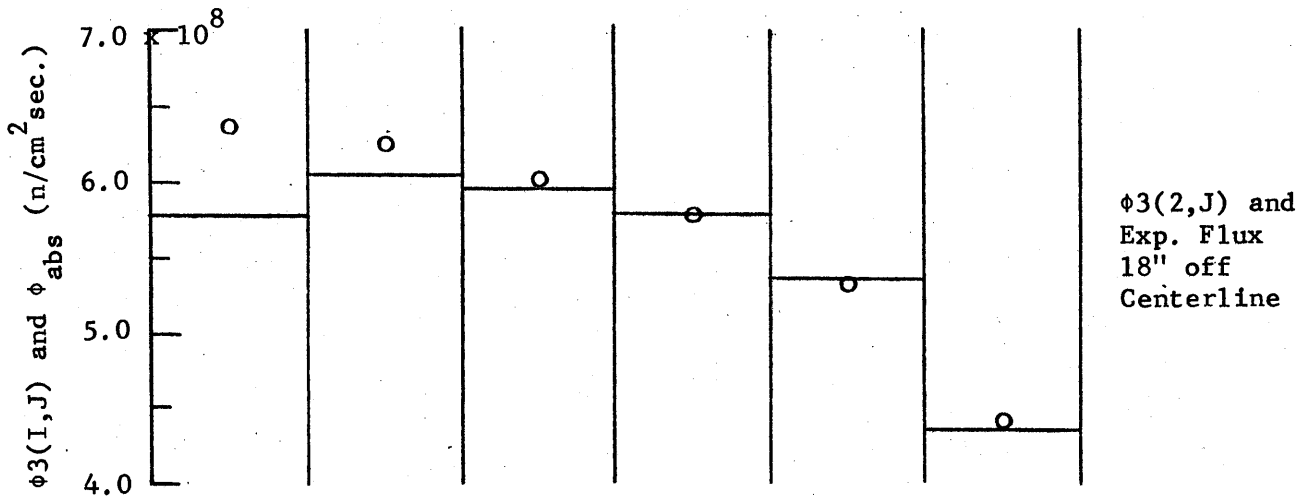


Figure T5.15 Experimental and Theoretical Flux for 12" Sub-Areas on Honeycomb of Assembly IV.



The circles represent the experimental values, ϕ_{abs} , and the lines represent the theoretical values, $\phi_3(I,J)$.



T5.16 Experimental and Theoretical Flux for 12" Sub-Areas on the Honeycomb of Assembly V.

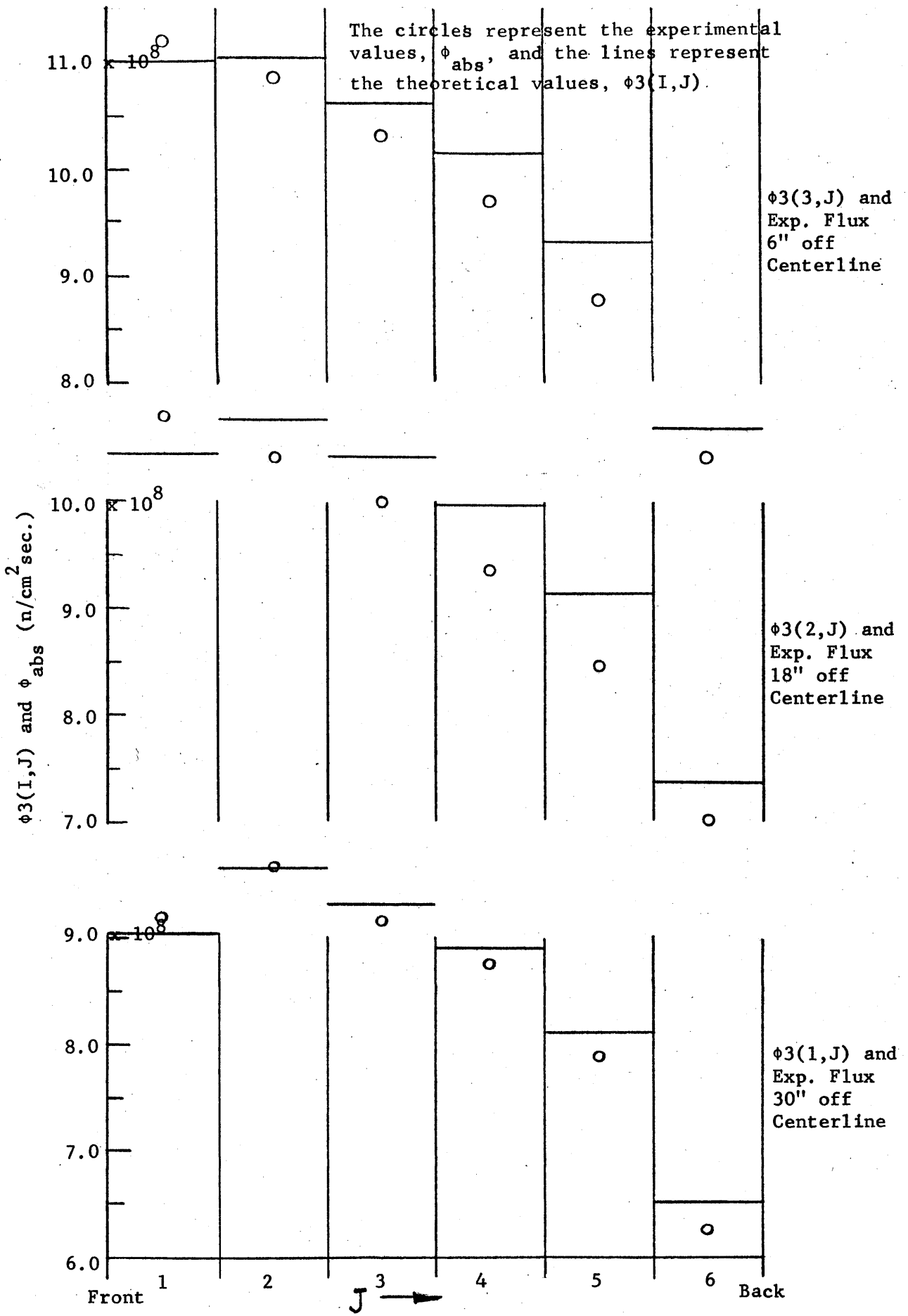


Figure T5.17 Experimental and Theoretical Flux for 12" Sub-Areas on Honeycomb of Assembly VI.

The shape of the flux distribution calculated for the 12" sub-area in Assembly I agrees with experiment, but the magnitude is greater by the factor 1.03 than it should be to achieve a neutron balance (see Appendix B2). Only in this case did the values of $C3(I,J)$ converge before an accurate neutron balance was obtained. The difference appears to be attributable, at least in part, to this effect. The theoretical values of the flux in Assembly VI are consistently greater than the experimental values. The gradient of the flux in Assembly VI is greater than the gradient for any other assembly. The subject of the flux gradients in a sub-area was discussed in Section T5.3 of this chapter. Most of the experimental and theoretical values for Assembly VI agree to within the \pm five per cent which is approximately the total error in the theoretical and experimental results.

The above comparison shows that theoretical and experimental values of the flux agree to within three per cent in most cases. The greatest difference between theory and experiment occurred in the case of Assembly VI, where there was a difference of about five per cent. Since the largest error in the theoretical results may be expected in this case, a discrepancy of five per cent still represents good agreement between the theoretical and experimental values of the flux. The theoretical model also correctly interprets the effects of the inclined plane, the frame, and the edges of the pedestal; these effects were discussed in Section E3.6. The close agreement between theoretical and experimental results supports the statement that the theoretical model can be applied successfully to these five cavity assemblies.

Appendix B1

Derivation of the Expressions for the Thirteen View Factors

B1.1 View Factor for Squares in Perpendicular Planes - VI(I,J,K) (See Figure B1.1)

Let

$$u = A + t + y,$$

$$v = C + s,$$

$$z = B + x.$$

The quantity A is the distance between the two squares along the line of intersection of the perpendicular planes. The quantities B and C are the distances between the intersection of the planes and A₁ and A₂, respectively. From Figure B1.1a, it can be seen that

$$\cos \phi_1 = v/r,$$

$$\cos \phi_2 = z/r,$$

$$r^2 = u^2 + v^2 + z^2,$$

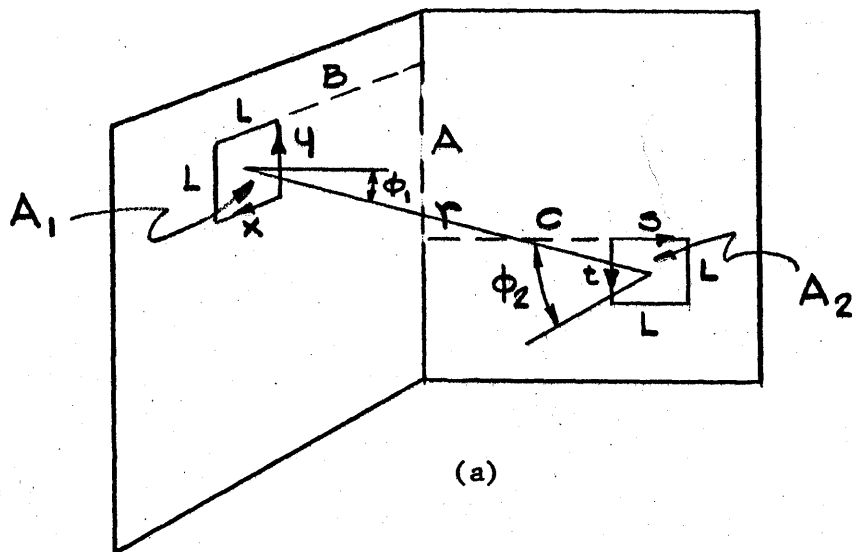
$$dA_2 = ds dt = dv du.$$

Substitution of these values into the equation for the view factor F_{(d1)2} from dA₁ to A₂ equation (T2.6) gives:

$$F_{(d1)2} = \frac{1}{\pi} \int_0^L \int_0^L \frac{u z ds dt}{[u^2 + z^2 + v^2]^2} = \frac{1}{\pi} \int_{y+A}^{y+L+A} dv \int_C^{L+C} \frac{v dv}{[v^2 + u^2 + z^2]^2} \quad (B1.1)$$

The double integration is straight-forward.

$$F_{(d1)2} = \frac{1}{2\pi} \left[\frac{1}{(C^2+z^2)^{\frac{1}{2}}} \tan^{-1} \frac{(y+L+A)}{(C^2+z^2)^{\frac{1}{2}}} - \frac{1}{[(L+C)^2+z^2]^{\frac{1}{2}}} \tan^{-1} \frac{(L+A+y)}{[(L+C)^2+z^2]^{\frac{1}{2}}} \right. \\ \left. - \frac{1}{(C^2+z^2)^{\frac{1}{2}}} \tan^{-1} \frac{(A+y)}{(C^2+z^2)^{\frac{1}{2}}} + \frac{1}{[(L+C)^2+z^2]^{\frac{1}{2}}} \tan^{-1} \frac{(A+y)}{[(L+C)^2+z^2]^{\frac{1}{2}}} \right] \quad (B1.2)$$

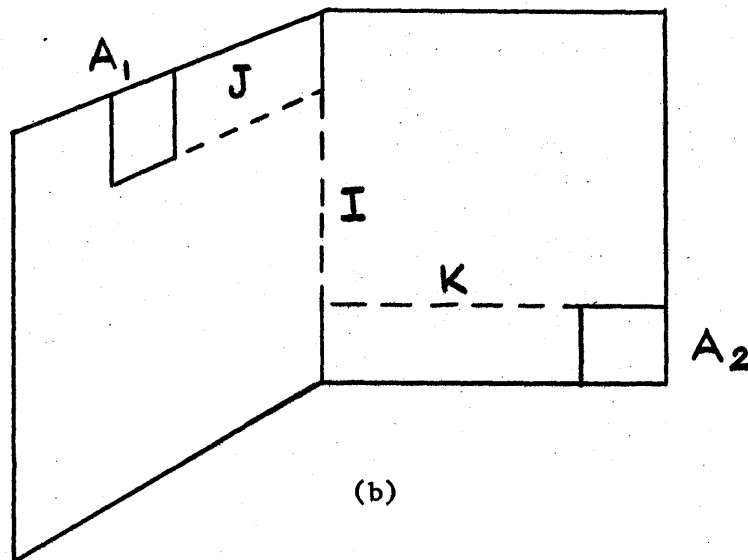


(a)

$I = A/L =$ number of units between A_1 and A_2 along line of intersection of two planes.

$J = B/L =$ number of units between A_1 and intersection of planes.

$K = C/L =$ number of units between A_2 and intersection of planes.



(b)

Figure B1.1 The Geometrical Arrangement of A_1 and A_2 for $V1(I, J, K)$.

Remembering that

$$F_{12} = \frac{1}{A_1} \int_{A_1} F(d_1)_2 dA_1 = \frac{1}{A_1} \int_0^L \int_0^L F(d_1)_2 dx dy, \text{ and letting } I = A/L, J = B/L,$$

and $K = C/L$, we get the final expression for F_{12} :

$$\begin{aligned} 2\pi A_1 \cdot F_{12} = 2\pi V_1(I, J, K) = & (I+2)^2 \left\{ \frac{[(J+1)^2 + K^2]^{\frac{1}{2}}}{(I+2)} \operatorname{ctn}^{-1} \frac{[(J+1)^2 + K^2]^{\frac{1}{2}}}{(I+2)} \right. \\ & - \frac{(J+K)^{\frac{1}{2}}}{(I+2)} \operatorname{ctn}^{-1} \frac{(J+K)^{\frac{1}{2}}}{(I+2)} - \frac{[(J+1)^2 + (K+1)^2]^{\frac{1}{2}}}{(I+2)} \operatorname{ctn}^{-1} \frac{[(J+1)^2 + (K+1)^2]^{\frac{1}{2}}}{(I+2)} \\ & \left. + \frac{[J^2 + (K+1)^2]^{\frac{1}{2}}}{(I+2)} \operatorname{ctn}^{-1} \frac{[J^2 + (K+1)^2]^{\frac{1}{2}}}{(I+2)} \right\} + 2(I+1)^2 \left\{ \frac{(J^2 + K^2)^{\frac{1}{2}}}{(I+1)} \operatorname{ctn}^{-1} \frac{(J^2 + K^2)^{\frac{1}{2}}}{(I+1)} \right. \\ & - \frac{[(J+1)^2 + K^2]^{\frac{1}{2}}}{(I+1)} \operatorname{ctn}^{-1} \frac{[(J+1)^2 + K^2]^{\frac{1}{2}}}{(I+1)} + \frac{[(J+1)^2 + (K+1)^2]^{\frac{1}{2}}}{(I+1)} \operatorname{ctn}^{-1} \frac{[(J+1)^2 + (K+1)^2]^{\frac{1}{2}}}{(I+1)} \\ & \left. - \frac{[J^2 + (K+1)^2]^{\frac{1}{2}}}{(I+1)} \operatorname{ctn}^{-1} \frac{[J^2 + (K+1)^2]^{\frac{1}{2}}}{(I+1)} \right\} + I^2 \left\{ \frac{[J^2 + (K+1)^2]^{\frac{1}{2}}}{I} \operatorname{ctn}^{-1} \frac{[J^2 + (K+1)^2]^{\frac{1}{2}}}{I} \right. \\ & \left. - \frac{[(J+1)^2 + (K+1)^2]^{\frac{1}{2}}}{I} \operatorname{ctn}^{-1} \frac{[(J+1)^2 + (K+1)^2]^{\frac{1}{2}}}{I} - \frac{(J^2 + K^2)^{\frac{1}{2}}}{I} \operatorname{ctn}^{-1} \frac{(J^2 + K^2)^{\frac{1}{2}}}{I} \right. \\ & \left. + \frac{[(J+1)^2 + K^2]^{\frac{1}{2}}}{I} \operatorname{ctn}^{-1} \frac{[(J+1)^2 + K^2]^{\frac{1}{2}}}{I} \right\} + \frac{(I+2)^2}{4} \ln \left\{ \frac{[(I+2)^2 + (J+1)^2 + K^2][I^2 + (I+2)^2 + (K+1)^2]}{[(I+2)^2 + J^2 + K^2][(I+2)^2 + (J+1)^2 + (K+1)^2]} \right\} \\ & + \frac{(I+1)^2}{4} \ln \left\{ \frac{[(I+1)^2 + J^2 + K^2]^2 [(I+1)^2 + (J+1)^2 + (K+1)^2]}{[(I+1)^2 + (J+1)^2 + K^2]^2 [(I+1)^2 + J^2 + (K+1)^2]} \right\} \\ & + \frac{(J+1)^2}{4} \ln \left\{ \frac{[(J+1)^2 + K^2 + (I+1)^2]^2 [(J+1)^2 + (K+1)^2 + (I+2)^2] [(J+1)^2 + (K+1)^2 + I^2]}{[(J+1)^2 + K^2 + (I+2)^2] [(J+1)^2 + (K+1)^2 + (I+1)^2]^2 [(J+1)^2 + K^2 + I^2]} \right\} \\ & + \frac{(K+1)^2}{4} \ln \left\{ \frac{[(J+1)^2 + (K+1)^2 + (I+2)^2] [J^2 + (K+1)^2 + (I+1)^2]^2 [(J+1)^2 + (K+1)^2 + I^2]}{[J^2 + (K+1)^2 + (I+2)^2] [(J+1)^2 + (K+1)^2 + (I+1)^2]^2 [J^2 + (K+1)^2 + I^2]} \right\} \\ & + \frac{I^2}{4} \ln \left\{ \frac{[I^2 + (J+1)^2 + K^2] [I^2 + J^2 + (K+1)^2]}{[I^2 + J^2 + K^2] [I^2 + (J+1)^2 + (K+1)^2]} \right\} \end{aligned}$$

$$\begin{aligned}
& + \frac{J^2}{4} \ln \left\{ \frac{[J^2+K^2+(I+2)^2][J^2+(K+1)^2+(I+1)^2]^2[I^2+J^2+K^2]}{[(I+1)^2+J^2+K^2]^2[(I+2)^2+(K+1)^2+J^2][(K+1)^2+J^2+I^2]} \right\} \\
& + \frac{K^2}{4} \ln \left\{ \frac{[J^2+K^2+(I+2)^2][I^2+J^2+K^2][(J+1)^2+(I+1)^2+K^2]^2}{[(J+1)^2+K^2+(I+2)^2][(J+1)^2+K^2+I^2][J^2+K^2+(I+1)^2]} \right\}
\end{aligned} \tag{B1.3}$$

On examining equation (B1.3), it can be seen that J and K may be interchanged without changing the expression; there is symmetry between the J and K direction. Since I, J, and K define the relative positions of the two squares in the rectangular coordinate system in terms of integral multiples of L, the dimension of the square (see Figure B1.1b), the specification of I, J, and K makes possible the calculation of the view factor.

B1.2 View Factor for Squares in Parallel Planes - $V_2(I, J, K)$

Referring to Figure B1.2a, we let

$$u = y + A + t,$$

$$v = x + B + s,$$

$$C = C,$$

where A and B are the distances between the two squares in the horizontal and vertical directions, respectively, and C is the distance between the two parallel planes. Then:

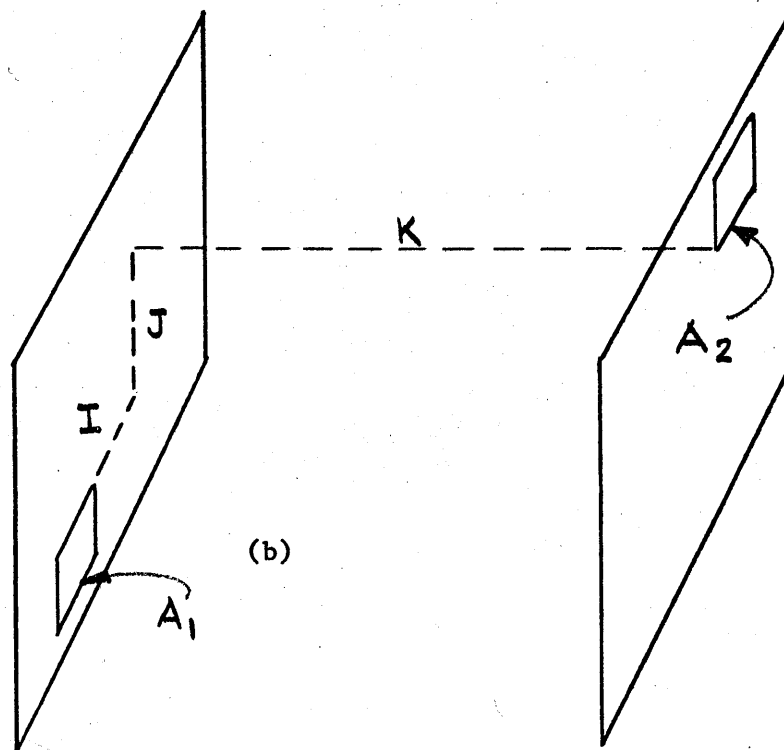
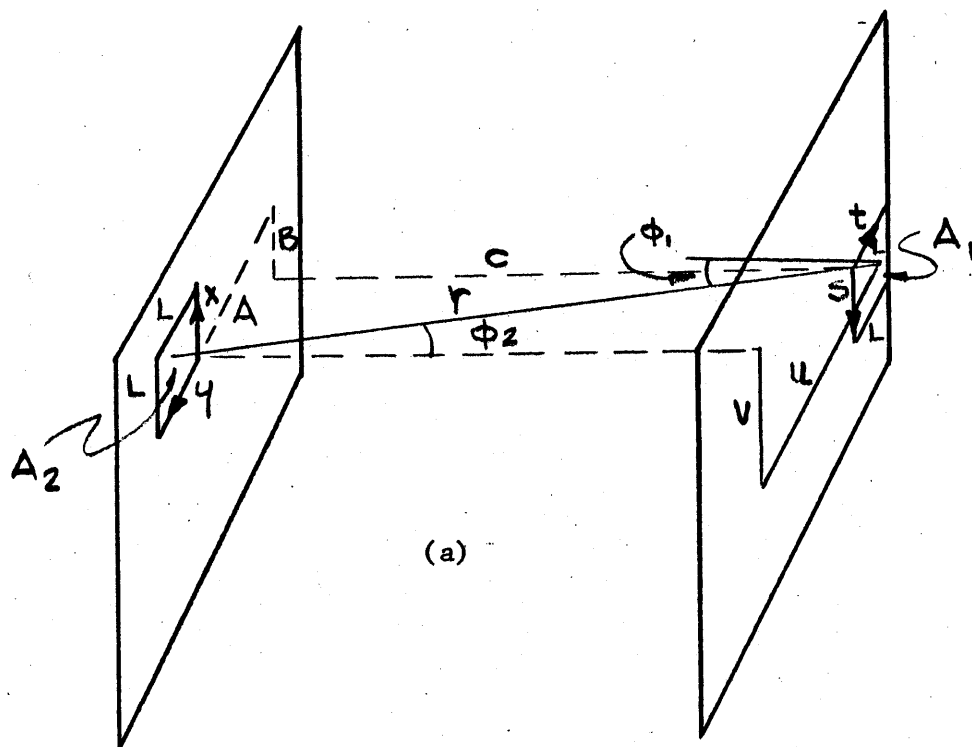
$$r^2 = u^2 + v^2 + C^2,$$

$$\cos \phi_1 = \cos \phi_2 = c/r,$$

and

$$F_{(d1)2} = \frac{1}{\pi} \int_{A_2} \frac{dA_2}{C^4 \left[\frac{u^2}{C^2} + \frac{v^2}{C^2} + 1 \right]^2} = \frac{1}{\pi} \int_a^L \int_a^L \frac{dudv}{C^4 \left[\frac{u^2}{C^2} + \frac{v^2}{C^2} + 1 \right]^2}.$$

The integration could not be done in this form, so the coordinate system is changed to polar; see Figure B1.3. In the new system,



- $I = A/L$ = number of unit lengths between A_1 and A_2 in the horizontal direction.
 $J = B/L$ = number of unit lengths between A_1 and A_2 in the vertical direction.
 $K = C/L$ = number of unit lengths between the two parallel planes.

Figure B1.2 Arrangement of A_1 and A_2 for $V_2(I, J, K)$.

$$\rho^2 = u^2/c^2 + v^2/c^2,$$

and

$$dA_2 = \rho d\rho d\theta.$$

The integration over a square in polar coordinates must be done in three parts:

$$F(d1)_2 = \frac{1}{\pi} \int_{A_2} \frac{d\rho d\theta}{(\rho^2 + 1)^2} = \frac{1}{\pi} \left\{ \int_{\rho_1}^{\rho_2} \int_{\theta_1}^{\theta_2} \frac{d\rho d\theta}{(\rho^2 + 1)^2} + \int_{\rho_3}^{\rho_4} \int_{\theta_3}^{\theta_4} \frac{d\rho d\theta}{(\rho^2 + 1)^2} + \int_{\rho_5}^{\rho_6} \int_{\theta_5}^{\theta_6} \frac{d\rho d\theta}{(\rho^2 + 1)^2} \right\},$$

(B1.4)

where we have introduced the limits of integration,

$$\theta_1 = \tan^{-1} \frac{x+B}{L+A+y}, \quad \rho_1 = \frac{x+B}{C \sin \theta},$$

$$\theta_2 = \tan^{-1} \frac{x+B}{y+A}, \quad \rho_2 = \frac{y+A+L}{C \cos \theta},$$

$$\theta_3 = \tan^{-1} \frac{x+B}{y+A}, \quad \rho_3 = \frac{y+A}{C \cos \theta},$$

$$\theta_4 = \tan^{-1} \frac{x+B+L}{y+A+L}, \quad \rho_4 = \frac{y+A+L}{C \cos \theta},$$

$$\theta_5 = \tan^{-1} \frac{x+B+L}{y+A+L}, \quad \rho_5 = \frac{y+A}{C \cos \theta},$$

$$\theta_6 = \tan^{-1} \frac{x+B+L}{y+A}, \quad \rho_6 = \frac{x+B+L}{C \sin \theta}.$$

The integration yields

$$F(d1)_2 = \frac{1}{2\pi} \left\{ \frac{x+B}{[(x+B)^2 + C^2]^{\frac{1}{2}}} \left[\tan^{-1} \frac{[(x+B)^2 + C^2]^{\frac{1}{2}}}{y+A+L} - \tan^{-1} \frac{[(x+B)^2 + C^2]^{\frac{1}{2}}}{y+A} \right] \right. \\ \left. + \frac{(y+A+L)}{[(y+A+L)^2 + C^2]^{\frac{1}{2}}} \left[\tan^{-1} \frac{(x+B+L)}{[(y+A+L)^2 + C^2]^{\frac{1}{2}}} - \tan^{-1} \frac{x+B}{[(y+A+L)^2 + C^2]^{\frac{1}{2}}} \right] \right\}$$

$$\begin{aligned}
& + \frac{(y+A)}{[(y+A)^2+C^2]^{\frac{1}{2}}} \left[\tan^{-1} \frac{x+B}{[(y+A)^2+C^2]^{\frac{1}{2}}} - \tan^{-1} \frac{(x+B+L)}{[(y+A)^2+C^2]^{\frac{1}{2}}} \right] \\
& + \frac{(x+B+L)}{[(x+B+L)^2+C^2]^{\frac{1}{2}}} \left[\tan^{-1} \frac{[(x+B+L)^2+C^2]^{\frac{1}{2}}}{y+A} - \tan^{-1} \frac{[(x+B+L)^2+C^2]^{\frac{1}{2}}}{y+A+L} \right] \Bigg\} \quad (B1.5)
\end{aligned}$$

To obtain F_{12} , $F(d1)_2$ must be integrated over A_1 :

$$F_{12} = \frac{1}{A_1} \int_{A_1} F(d1)_2 dA_1 = \frac{1}{A_1} \int_0^L \int_0^L F(d1)_2 dx dy.$$

When these integrations are performed and when we set $I = A/L$, $J = B/L$, $K = C/L$, F_{12} takes the form:

$$\begin{aligned}
2\pi A_1 F_{12}(I, J, K) = 2\pi V_2(I, J, K) = (I+2) & \left\{ 2[(J+1)^2+K^2]^{\frac{1}{2}} \tan^{-1} \frac{[(J+1)^2+K^2]^{\frac{1}{2}}}{I+2} \right. \\
& - (J^2+K^2)^{\frac{1}{2}} \tan^{-1} \frac{(J^2+K^2)^{\frac{1}{2}}}{I+2} - [(J+2)^2+K^2]^{\frac{1}{2}} \tan^{-1} \frac{[(J+2)^2+K^2]^{\frac{1}{2}}}{I+2} \Bigg\} + 2(I+1) \cdot \\
& \left\{ (J^2+K^2)^{\frac{1}{2}} \tan^{-1} \frac{(J^2+K^2)^{\frac{1}{2}}}{I+1} + [(J+2)^2+K^2]^{\frac{1}{2}} \tan^{-1} \frac{[(J+2)^2+K^2]^{\frac{1}{2}}}{I+1} \right. \\
& - 2[(J+1)^2+K^2]^{\frac{1}{2}} \tan^{-1} \frac{[(J+1)^2+K^2]^{\frac{1}{2}}}{I+1} \Bigg\} + (J+2) \left\{ (I^2+K^2)^{\frac{1}{2}} \operatorname{ctn}^{-1} \frac{(I^2+K^2)^{\frac{1}{2}}}{J+2} \right. \\
& + [(I+2)^2+K^2]^{\frac{1}{2}} \operatorname{ctn}^{-1} \frac{[(I+2)^2+K^2]^{\frac{1}{2}}}{J+2} - 2[(I+1)^2+K^2]^{\frac{1}{2}} \operatorname{ctn}^{-1} \frac{[(I+1)^2+K^2]^{\frac{1}{2}}}{J+2} \Bigg\} \\
& + 2(J+1) \left\{ 2[(I+1)^2+K^2]^{\frac{1}{2}} \operatorname{ctn}^{-1} \frac{[(I+1)^2+K^2]^{\frac{1}{2}}}{J+1} - (I^2+K^2)^{\frac{1}{2}} \operatorname{ctn}^{-1} \frac{(I^2+K^2)^{\frac{1}{2}}}{J+1} \right. \\
& - [(I+2)^2+K^2]^{\frac{1}{2}} \operatorname{ctn}^{-1} \frac{[(I+2)^2+K^2]^{\frac{1}{2}}}{J+1} \Bigg\} + I \left[2[(J+1)^2+K^2]^{\frac{1}{2}} \tan^{-1} \frac{[(J+1)^2+K^2]^{\frac{1}{2}}}{I} \right. \\
& - (J^2+K^2)^{\frac{1}{2}} \tan^{-1} \frac{(J^2+K^2)^{\frac{1}{2}}}{I} - [(J+2)^2+K^2]^{\frac{1}{2}} \tan^{-1} \frac{[(J+2)^2+K^2]^{\frac{1}{2}}}{I} \Bigg] \\
& + J \left[[(I+2)^2+K^2]^{\frac{1}{2}} \operatorname{ctn}^{-1} \frac{[(I+2)^2+K^2]^{\frac{1}{2}}}{J} + (I^2+K^2)^{\frac{1}{2}} \operatorname{ctn}^{-1} \frac{(I^2+K^2)^{\frac{1}{2}}}{J} \right]
\end{aligned}$$

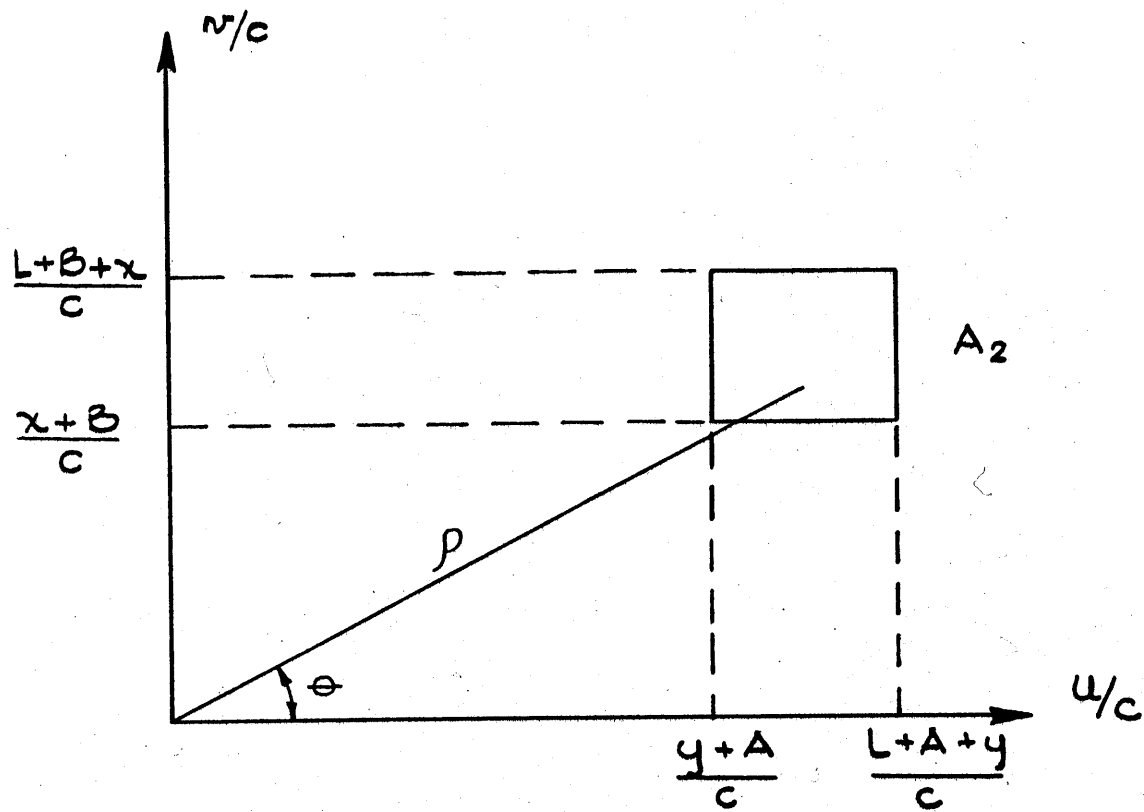


Figure B1.3 Relationship between Rectangular and Polar Coordinates for Area A_2 .

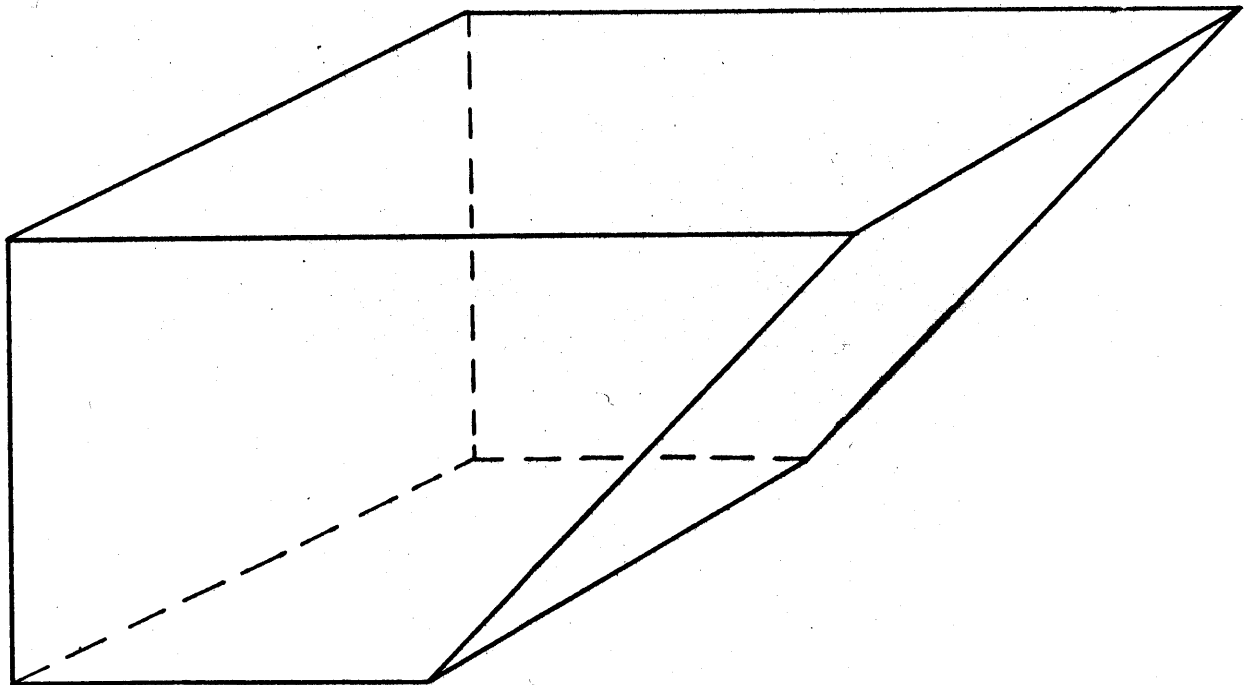


Figure B1.4 Surfaces of the 45° Cavity.

$$\begin{aligned}
& - 2 \left[(I+1)^2 + K^2 \right]^{\frac{1}{2}} \operatorname{ctn}^{-1} \left[\frac{\left[(I+1)^2 + K^2 \right]^{\frac{1}{2}}}{J} \right] - \frac{K^2}{2} \ln \left[K^2 + (I+2)^2 + J^2 \right] + \\
& \frac{K^2}{2} \ln \left(\frac{\left[K^2 + (J+2)^2 + (I+1)^2 \right]^2 \left[K^2 + I^2 + (J+1)^2 \right]^2 \left[K^2 + (I+2)^2 + (J+1)^2 \right]^2 \left[K^2 + (I+1)^2 + J^2 \right]}{\left[K^2 + (I+1)^2 + (J+1)^2 \right]^4 \left[K^2 + (J+2)^2 + I^2 \right] \left[K^2 + (I+2)^2 + (J+2)^2 \right] \left[K^2 + I^2 + J^2 \right]} \right).
\end{aligned}
\tag{B1.6}$$

The quantities I, J, and K again express the relative position of the two squares A₁ and A₂, in parallel planes, in terms of integral multiples of L (see Figure B1.2b). Note that in equation (B1.6), I and J may be interchanged without changing the equation, as would be expected from considering the interchange of I and J in Figure B1.2. The symmetry existing in the expressions for V₁ and V₂ is useful, because it is necessary to calculate only about half of the view factors, resulting in a considerable saving of computation time.

The view factors V₁ and V₂ are the only ones needed to calculate the flux distribution for a cavity in the shape of a parallelepiped, since all sub-areas are either in parallel or perpendicular planes. However, the cavity with an inclined surface required other view factors besides V₁ and V₂. When the surfaces of the cavity shown in Figure B1.4 are divided into sub-areas, the latter are squares, triangles, or rectangles, which do not all lie in parallel or perpendicular planes. The determination of the flux distribution in this type of assembly requires 13 independent view factors, two of which have already been derived, V₁ and V₂. Of the remaining eleven, four can be obtained from equation (T2.5) with the aid of a numerical integration. The last seven are obtained by expressing them in terms of the first six view factors. Considerable difficulty was experienced in obtaining these view factors, an example of the limitations on obtaining accurate

view factors for a cavity with a complicated shape. Approximate methods of obtaining the view factors and the flux distribution would be needed for such a cavity.

B1.3 View Factor between a Square and a Triangle in a Perpendicular Plane with the Triangle at the Same or Higher Elevation than the Square, $V_4(I,J,K)$. (See Figure B1.5.)

The quantity A is the difference in elevation between the square and the triangle where the elevation is defined as the direction parallel to the line of intersection of the perpendicular planes. The quantities B and C are the distances from the line intersection of the planes and the triangle, A_2 , and the square, A_1 , respectively.

Let

$$v = C + s,$$

$$u = t + A - y,$$

$$z = B + x;$$

then

$$\cos \phi_1 = u/v,$$

$$\cos \phi_2 = z/v,$$

$$r^2 = u^2 + v^2 + z^2.$$

Substitution of these expressions into equation (T2.5) results in an integral identical to that in equation (B1.1), so that the result is the same. However, in the integration over A_2 , which is a triangle, a series of terms is obtained for which the integral cannot be found. The view factor for this case is:

$$\begin{aligned}
2\pi A_1 F_{12} &= 2\pi V_4(A, B, C) = \pi \int_{A_2} F(d_2)_1 dA_2 = \int_0^L \int_0^{L-y} F(d_1)_2 dx dy = (B^2 + C^2)^{\frac{1}{2}} \\
&\left\{ 2A \tan^{-1} \frac{A}{(B^2 + C^2)^{\frac{1}{2}}} - (L+A) \tan^{-1} \frac{(L+A)}{(B^2 + C^2)^{\frac{1}{2}}} - (A-L) \tan^{-1} \frac{(A-L)}{(B^2 + C^2)^{\frac{1}{2}}} \right\} + [B + (L+C)^2]^{\frac{1}{2}} \\
&\left\{ (L+A) \tan^{-1} \frac{(L+A)}{B^2 + (L+C)^2} - 2A \tan^{-1} \frac{A}{[B^2 + (L+C)^2]^{\frac{1}{2}}} + (A-L) \tan^{-1} \frac{(A-L)}{[B^2 + (L+C)^2]^{\frac{1}{2}}} \right\} \\
&+ \frac{(L+A)}{4} \ln \left[\frac{(L+A)^2 + B^2 + (L+C)^2}{(L+A)^2 + B^2 + C^2} \right] + \frac{(A-L)^2}{4} \ln \left[\frac{(A-L)^2 + B^2 + (L+C)^2}{(A-L)^2 + B^2 + C^2} \right] + \frac{(L+C)^2}{4} \ln \\
&\left\{ \frac{[A^2 + B^2 + (L+C)^2]^2}{[(L+A)^2 + B^2 + (L+C)^2][(A-L)^2 + B^2 + (L+C)^2]} \right\} \frac{A^2}{4} \ln \left[\frac{A^2 + B^2 + C^2}{A^2 + B^2 + (L+C)^2} \right] + \frac{B^2}{4} \ln \\
&\left\{ \frac{[(L+A)^2 + B^2 + C^2][A^2 + B^2 + (L+C)^2][(A-L)^2 + B^2 + C^2]}{(A^2 + B^2 + C^2)[(L+A)^2 + B^2 + (L+C)^2][(A-L)^2 + B^2 + (L+C)^2]} \right\} \frac{C^2}{4} \ln \\
&\left\{ \frac{[(L+A)^2 + B^2 + C^2][(A-L)^2 + B^2 + C^2]}{(A^2 + B^2 + C^2)^2} \right\} + \int_0^L \left\{ [(L+B-y)^2 + C^2]^{\frac{1}{2}} \operatorname{ctn}^{-1} \frac{[(L+B-y)^2 + C^2]^{\frac{1}{2}}}{L+A-y} \right. \\
&+ \frac{(L+A-y)}{2} \ln [(L+A-y)^2 + (L+B-y)^2 + C^2] - [(L+B-y)^2 + (L+C)^2]^{\frac{1}{2}} \\
&\left. \operatorname{ctn}^{-1} \frac{[(L+B-y)^2 + (L+C)^2]^{\frac{1}{2}}}{L+A-y} - \frac{(L+A-y)}{2} \ln [(L+A-y)^2 + (L+B-y)^2 + (L+C)^2] - [(L+B-y)^2 + C^2]^{\frac{1}{2}} \right. \\
&\left. \operatorname{ctn}^{-1} \frac{[(L+B-y)^2 + C^2]^{\frac{1}{2}}}{A-y} - \frac{(A-y)}{2} \ln [(A-y)^2 + (L+B-y)^2 + C^2] + [(L+B-y)^2 + (L+C)^2]^{\frac{1}{2}} \right. \\
&\left. \operatorname{ctn}^{-1} \frac{[(L+B-y)^2 + (L+C)^2]^{\frac{1}{2}}}{A-y} + \frac{(A-y)}{2} \ln [(A-y)^2 + (L+B-y)^2 + (L+C)^2] \right\} dy. \tag{B1.7}
\end{aligned}$$

The equation for $V_4(I, J, K)$ is obtained by rewriting equation (B1.7)

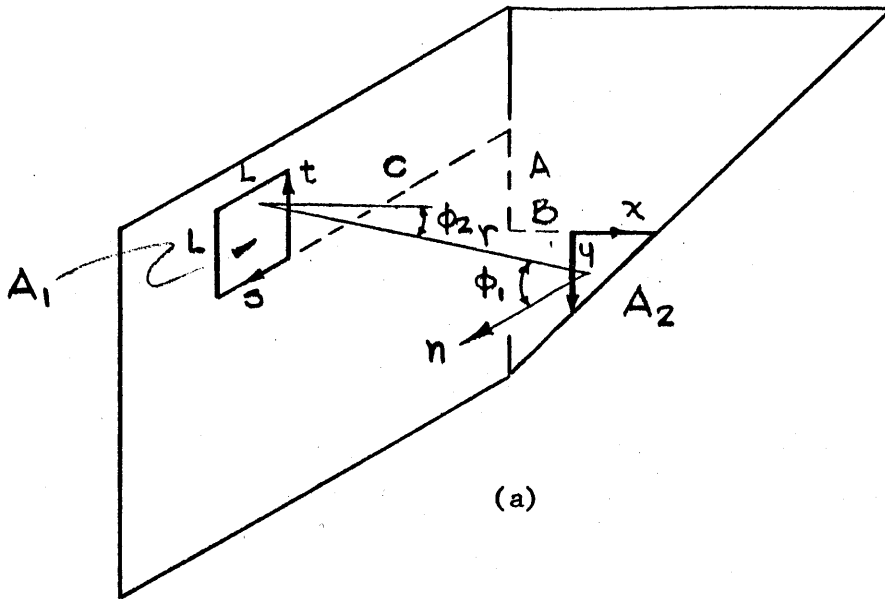
with $I = A/L$, $J = B/L$, and $K = C/L$.

Since the last integration (Bl.7) could not be done analytically, a numerical integration was performed. Examination of the functions involved, and also of the results of the previous two view factors, indicated that the integrand could be expressed by a second order curve, and Simpson's rule was, therefore, used to evaluate the integral.

B1.4 View Factor between a Square and a Triangle in Perpendicular Planes with the Triangle at a Lower Level - V5(I,J,K). (See Figure Bl.6.)

It is of interest to note that V4 and V5 are not the same. The symmetry observed between squares in perpendicular planes is not present here. The view factor is obtained by the procedure used in the last case. The quantities A, B, and C are defined as they were for V4. Simpson's rule was used to perform part of the second integration. The expression obtained for F_{12} is:

$$\begin{aligned}
 2\pi A_1 F_{12} = 2\pi V5(A,B,C) = & (B^2+C^2)^{\frac{1}{2}} \left[2(L+A) \tan^{-1} \frac{L+A}{(B^2+C^2)^{\frac{1}{2}}} - (2L+A) \tan^{-1} \right. \\
 & \left. \frac{(2L+A)}{(B^2+C^2)^{\frac{1}{2}}} - A \tan^{-1} \frac{A}{(B^2+C^2)^{\frac{1}{2}}} \right] + [B^2+(L+C)^2]^{\frac{1}{2}} \left[A \tan^{-1} \frac{A}{[B^2+(L+C)^2]^{\frac{1}{2}}} - 2(L+A) \right. \\
 & \left. \tan^{-1} \frac{(L+A)}{[B^2+(L+C)^2]^{\frac{1}{2}}} + (2L+A) \tan^{-1} \frac{(2L+A)}{[B^2+(L+C)^2]^{\frac{1}{2}}} \right] + \frac{(2L+A)^2}{4} \ln \left[\frac{(2L+A)^2+B^2+(L+C)^2}{(2L+A)^2+B^2+C^2} \right] \\
 & - \frac{(L+A)^2}{2} \ln \left[\frac{(L+A)^2+B^2+C^2}{(L+A)^2+B^2+(L+C)^2} \right] + \frac{A^2}{4} \ln \left[\frac{A^2+B^2+(L+C)^2}{A^2+B^2+C^2} \right] \\
 & + \frac{B^2}{4} \ln \left[\frac{[B^2+(L+A)^2+(L+C)^2]^2 [B^2+(2L+A)^2+C^2] [B^2+A^2+C^2]}{[B^2+(L+A)^2+C^2]^2 [B^2+(2L+A)^2+(L+C)^2] [B^2+A^2+(L+C)^2]} \right] \\
 & + \frac{(L+C)^2}{4} \ln \left[\frac{[(L+A)^2+B^2+(L+C)^2]^2}{[A^2+B^2+(L+C)^2] [(2L+A)^2+B^2+(L+C)^2]} \right] + \frac{C^2}{4} \ln \left[\frac{[(2L+A)^2+B^2+C^2] [A^2+B^2+C^2]}{[(L+A)^2+B^2+C^2]^2} \right]
 \end{aligned}$$

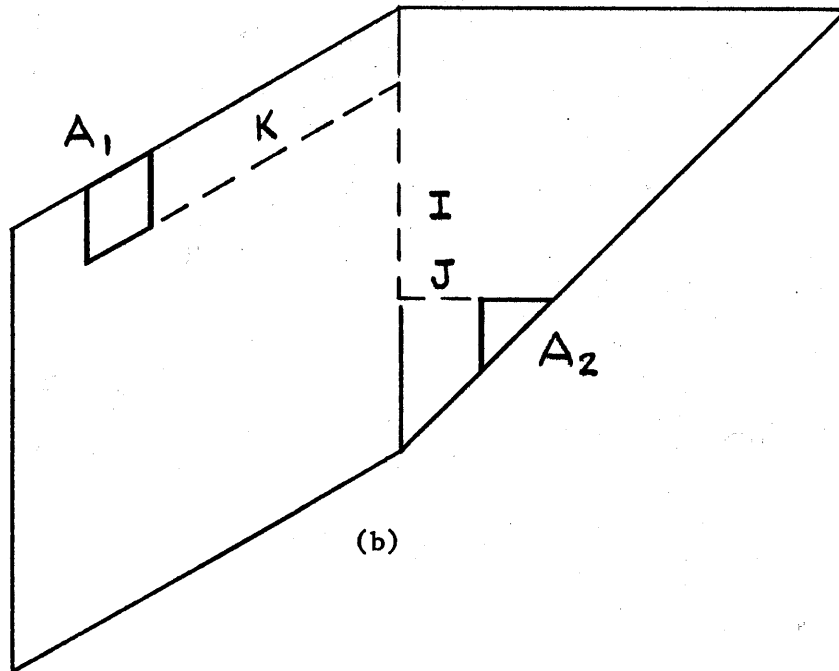


(a)

I = separation of A_1 and A_2 along the line of intersection of the intersection of the two planes in units of L .

J = separation of A_2 and intersection of the planes in units of L .

K = separation of A_1 and intersection of the planes in units of L .



(b)

Figure B1.6 The Arrangement of A_1 and A_2 for $V_5(I, J, K)$.

$$\begin{aligned}
& + \int_0^L \left(\left[(L+B-y)^2 + C^2 \right]^{\frac{1}{2}} \operatorname{ctn}^{-1} \frac{\left[(L+B-y)^2 + C^2 \right]^{\frac{1}{2}}}{L+A+y} + \frac{(L+A+y)}{2} \ln \left(\frac{\left[(L+A+y)^2 + (L+B-y)^2 + C^2 \right]}{\left[(L+A+y)^2 + (L+B-y)^2 + (L+C)^2 \right]} \right) \right. \\
& - \left[(L+B-y)^2 + C^2 \right]^{\frac{1}{2}} \operatorname{ctn}^{-1} \frac{\left[(L+B-y)^2 + C^2 \right]^{\frac{1}{2}}}{A+y} + \left[(L+B-y)^2 + (L+C)^2 \right]^{\frac{1}{2}} \operatorname{ctn}^{-1} \frac{\left[(L+B-y)^2 + (L+C)^2 \right]^{\frac{1}{2}}}{(A+y)} \\
& \left. + \frac{(A+y)}{2} \ln \left(\frac{\left[(A+y)^2 + (L+B-y)^2 + (L+C)^2 \right]}{\left[(A+y)^2 + (L+B-y)^2 + C^2 \right]} \right) - \left[(L+B-y)^2 + (L+C)^2 \right]^{\frac{1}{2}} \operatorname{ctn}^{-1} \frac{\left[(L+B-y)^2 + (L+C)^2 \right]^{\frac{1}{2}}}{L+A+y} \right) dy
\end{aligned} \tag{B1.8}$$

The equation for $V_5(I, J, K)$ is obtained by substituting $I = A/L$, $J = B/L$, and $K = C/L$ into equation (B1.8).

B1.5 View Factor between a Square and a Triangle in Parallel Planes - $V_{12}(I, J, K)$ and $V_{13}(I, J, K)$. (See Figures B1.7 and B1.8.)

For this arrangement, V_{12} and V_{13} are two distinct view factors, as was the case for the square and triangle in perpendicular planes. The view factors are shown in Figures B1.7 and B1.8; V_{12} , shown in Figure B1.7, will be derived first. The quantities A , B , and C , are defined for V_{12} and V_{13} in the same way as for V_2 .

The integration over A_2 , with polar coordinates, yields the same result as the integration for squares see equation (B1.5). Again, a numerical integration must be performed for the evaluation of F_{12} .

$$\begin{aligned}
2\pi A_1 F_{12} = 2\pi A_1 V_{12}(A, B, C) = & (B^2 + C^2)^{\frac{1}{2}} \left[(L+A) \operatorname{ctn}^{-1} \frac{(L+A)}{(B^2 + C^2)^{\frac{1}{2}}} \right. \\
& - 2A \operatorname{ctn}^{-1} \frac{A}{(B^2 + C^2)^{\frac{1}{2}}} + (A-L) \operatorname{ctn}^{-1} \frac{(A-L)}{(B^2 + C^2)^{\frac{1}{2}}} \left. \right] + \left[(L+A)^2 + C^2 \right]^{\frac{1}{2}} \left[(2L+B) \tan^{-1} \frac{(2L+B)}{\left[(L+A)^2 + C^2 \right]^{\frac{1}{2}}} \right. \\
& - 2(L+B) \tan^{-1} \frac{(L+B)}{\left[(L+A)^2 + C^2 \right]^{\frac{1}{2}}} + B \tan^{-1} \frac{B}{\left[(L+A)^2 + C^2 \right]^{\frac{1}{2}}} + (A^2 + C^2)^{\frac{1}{2}} \left[2(L+B) \tan^{-1} \frac{(L+B)}{(A^2 + C^2)^{\frac{1}{2}}} \right.
\end{aligned}$$

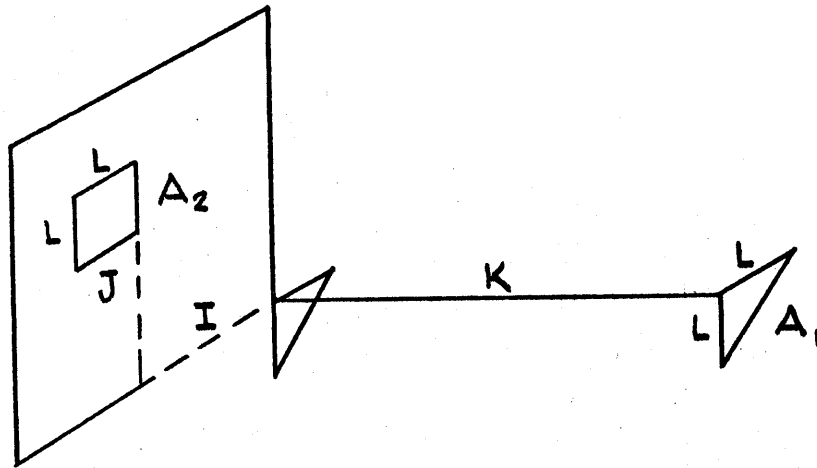
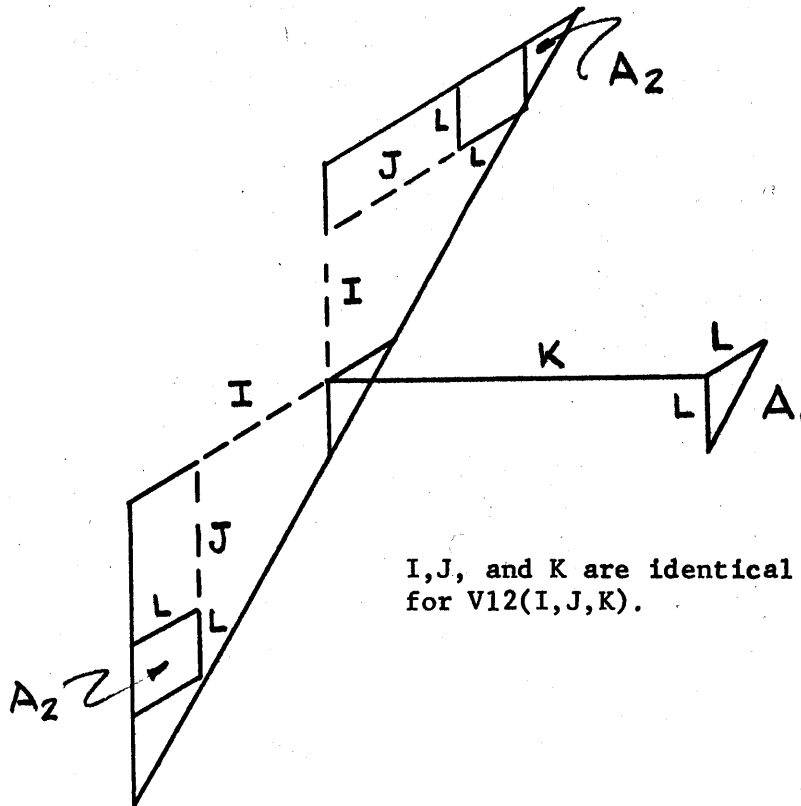


Figure B1.7 The Arrangement of A_1 and A_2 for $V_{12}(I, J, K)$.

I = horizontal separation of A_1 and A_2 in units of L .

J = vertical separation of A_1 and A_2 in units of L .

K = distance separation between the two parallel planes in units of L .



$I, J,$ and K are identical for those for $V_{12}(I, J, K)$.

Figure B1.8 The Arrangement of A_1 and A_2 for $V_{13}(I, J, K)$.

$$\begin{aligned}
& - B \tan^{-1} \frac{B}{(A^2+C^2)^{\frac{1}{2}}} - (2L+B) \tan^{-1} \frac{(2L+B)}{(A^2+C^2)^{\frac{1}{2}}} + [(L+B)^2+C^2]^{\frac{1}{2}} \left[2A \operatorname{ctn}^{-1} \frac{A}{[(L+B)^2+C^2]^{\frac{1}{2}}} \right. \\
& - (A-L) \operatorname{ctn}^{-1} \frac{(A-L)}{[(L+B)^2+C^2]^{\frac{1}{2}}} - (L+A) \operatorname{ctn}^{-1} \frac{(L+A)}{[(L+B)^2+C^2]^{\frac{1}{2}}} \left. + \frac{A^2}{4} \ln \left(\frac{[A^2+C^2+(2L+B)^2]}{[A^2+C^2+B^2]} \right) \right] \\
& - \frac{(L+A)^2}{4} \ln \left(\frac{[(L+A)^2+C^2+(2L+B)^2]}{[(L+A)^2+C^2+(L+B)^2]} \right) - \frac{(A-L)^2}{4} \ln \left(\frac{[(A-L)^2+C^2+(L+B)^2]}{[(A-L)^2+C^2+B^2]} \right) \\
& + \frac{(2L+B)^2}{4} \ln \left(\frac{[(2L+B)^2+C^2+(L+A)^2]}{[(2L+B)^2+C^2+A^2]} \right) - \frac{(L+B)^2}{4} \ln \left(\frac{[(L+B)^2+C^2+(L+A)^2]}{[(L+B)^2+C^2+(A-L)^2]} \right) + \frac{B^2}{4} \ln \left(\frac{[(B^2+C^2+A^2)]}{[B^2+C^2+(A-L)^2]} \right) \\
& + \frac{C^2}{4} \ln \left(\frac{[C^2+B^2+A^2]^3 [C^2+(L+B)^2+(A-L)^2] [C^2+(L+B)^2+(L+A)^2]^3 [C^2+(2L+B)^2+(L+A)^2]}{[C^2+B^2+(L+A)^2]^2 [C^2+B^2+(A-L)^2] [C^2+(L+B)^2+A^2]^4 [C^2+(2L+B)^2+A^2]} \right) \\
& + \int_0^L \left([(2L+A-x)^2+C^2]^{\frac{1}{2}} \left(\operatorname{ctn}^{-1} \frac{[(2L+A-x)^2+C^2]^{\frac{1}{2}}}{x+B+L} - \operatorname{ctn}^{-1} \frac{[(2L+A-x)^2+C^2]^{\frac{1}{2}}}{x+B} \right) \right. \\
& + [(L+A-x)^2+C^2]^{\frac{1}{2}} \left(\operatorname{ctn}^{-1} \frac{[(L+A-x)^2+C^2]^{\frac{1}{2}}}{x+B} - \operatorname{ctn}^{-1} \frac{[(L+A-x)^2+C^2]^{\frac{1}{2}}}{L+B+x} \right) \\
& \left. + \frac{(x+B+L)}{2} \ln \left(\frac{[(x+B+L)^2+(2L+A-x)^2+C^2]}{[(x+B+L)^2+(L+A-x)^2+C^2]} \right) + \frac{(x+B)}{2} \ln \left(\frac{[(x+B)^2+(L+A-x)^2+C^2]}{[(x+B)^2+(2L+A-x)^2+C^2]} \right) \right) dx
\end{aligned}$$

(B1.9)

The equation for $V_{12}(I,J,K)$ is obtained by substituting $I = A/L$, $J = B/L$, and $K = C/L$ into equation (B1.9).

The derivation of the second view factor, $V_{13}(I,J,K)$, is the same as that for the first.

$$\begin{aligned}
2\pi A_1 F_{12} = 2\pi V_{13}(A,B,C) = (B^2+C^2)^{\frac{1}{2}} & \left[2(L+A) \operatorname{ctn}^{-1} \frac{(L+A)}{(B^2+C^2)^{\frac{1}{2}}} - (2L+A) \frac{(2L+A)}{(B^2+C^2)^{\frac{1}{2}}} \right. \\
& \left. - A \operatorname{ctn}^{-1} \frac{A}{(B^2+C^2)^{\frac{1}{2}}} \right] + [(L+B)^2+C^2]^{\frac{1}{2}} \left[A \operatorname{ctn}^{-1} \frac{A}{[(L+B)^2+C^2]^{\frac{1}{2}}} - 2(L+A) \operatorname{ctn}^{-1} \frac{(L+A)}{[(L+B)^2+C^2]^{\frac{1}{2}}} \right]
\end{aligned}$$

$$\begin{aligned}
& + (2L+A) \operatorname{ctn}^{-1} \frac{(2L+A)}{[(L+B)^2+C^2]^{\frac{1}{2}}} + [(L+A)^2+C^2]^{\frac{1}{2}} \left[2(L+B) \tan^{-1} \frac{(L+B)}{[(L+A)^2+C^2]^{\frac{1}{2}}} \right. \\
& \left. - (2L+B) \tan^{-1} \frac{(2L+B)}{[(L+A)^2+C^2]^{\frac{1}{2}}} - B \tan^{-1} \frac{B}{[(L+A)^2+C^2]^{\frac{1}{2}}} \right] \\
& + (A^2+C^2)^{\frac{1}{2}} \left[B \tan^{-1} \frac{B}{(A^2+C^2)^{\frac{1}{2}}} - 2(L+B) \tan^{-1} \frac{(L+B)}{(A^2+C^2)^{\frac{1}{2}}} + (2L+B) \tan^{-1} \frac{(2L+B)}{(A^2+C^2)^{\frac{1}{2}}} \right] \\
& + \frac{(2L+A)^2}{4} \ln \left(\frac{[(2L+A)^2+B^2+C^2]}{[(2L+A)^2+(L+B)^2+C^2]} \right) + \frac{(L+A)^2}{4} \ln \left(\frac{[(L+A)^2+(2L+B)^2+C^2]}{[(L+A)^2+B^2+C^2]} \right) \\
& + \frac{A^2}{4} \ln \left(\frac{[A^2+(L+B)^2+C^2]}{[A^2+(2L+B)^2+C^2]} \right) + \frac{(2L+B)^2}{4} \ln \left(\frac{[A^2+(2L+B)^2+C^2]}{[(L+A)^2+(2L+B)^2+C^2]} \right) \\
& + \frac{(L+B)^2}{4} \ln \left(\frac{[(2L+A)^2+(L+B)^2+C^2]}{[A^2+(L+B)^2+C^2]} \right) + \frac{B^2}{4} \ln \left(\frac{[(L+A)^2+B^2+C^2]}{[(2L+A)^2+B^2+C^2]} \right) \\
& + \frac{C^2}{4} \ln \left(\frac{[(L+A)^2+B^2+C^2]^3 [A^2+(L+B)^2+C^2]^3 [(2L+A)^2+(L+B)^2+C^2] [(L+A)^2+(2L+B)^2+C^2]}{[(2L+A)^2+B^2+C^2] [A^2+B^2+C^2]^2 [(L+A)^2+(L+B)^2+C^2]^4 [A^2+(2L+B)^2+C^2]} \right) \\
& + \int_0^L \left[[(L+B-y)^2+C^2]^{\frac{1}{2}} \tan^{-1} \frac{[(L+B-y)^2+C^2]^{\frac{1}{2}}}{y+A+L} - [(L+B-y)^2+C^2]^{\frac{1}{2}} \tan^{-1} \frac{[(L+B-y)^2+C^2]^{\frac{1}{2}}}{y+A} \right. \\
& \left. + [(2L+B-y)^2+C^2]^{\frac{1}{2}} \tan^{-1} \frac{[(2L+B-y)^2+C^2]^{\frac{1}{2}}}{y+A} - [(2L+B-y)^2+C^2]^{\frac{1}{2}} \tan^{-1} \frac{[(2L+B-y)^2+C^2]^{\frac{1}{2}}}{L+A+y} \right. \\
& \left. + \frac{(L+A+y)}{2} \ln \left(\frac{[(L+A+y)^2+(2L+B-y)^2+C^2]}{[(L+B-y)^2+C^2+(L+A+y)^2]} \right) + \frac{(y+A)}{2} \ln \left(\frac{[(L+B-y)^2+(y+A)^2+C^2]}{[(2L+B-y)^2+C^2+(y+A)^2]} \right) \right] dy \\
& + \int_0^L \left[[(2L+A-x)^2+C^2]^{\frac{1}{2}} \operatorname{ctn}^{-1} \frac{[(2L+A-x)^2+C^2]^{\frac{1}{2}}}{(L+B+x)} - [(2L+A-x)^2+C^2]^{\frac{1}{2}} \operatorname{ctn}^{-1} \frac{[(2L+A-x)^2+C^2]^{\frac{1}{2}}}{x+B} \right. \\
& \left. + [(L+A-x)^2+C^2]^{\frac{1}{2}} \operatorname{ctn}^{-1} \frac{[(L+A-x)^2+C^2]^{\frac{1}{2}}}{x+B} - [(L+A-x)^2+C^2]^{\frac{1}{2}} \operatorname{ctn}^{-1} \frac{[(L+A-x)^2+C^2]^{\frac{1}{2}}}{L+B+x} \right. \\
& \left. + \frac{(L+B+x)^2}{2} \ln \left(\frac{[(2L+A-x)^2+(L+B+x)^2+C^2]}{[(L+A-x)^2+(L+B+x)^2+C^2]} \right) + \frac{(x+B)}{2} \ln \left(\frac{[(x+B)^2+(L+A-x)^2+C^2]}{[(x+B)^2+(2L+A-x)^2+C^2]} \right) \right] dx.
\end{aligned}$$

To determine $V_{13}(I,J,K)$, substitute $I = A/L$, $J = B/L$, and $K = C/L$ into equation (B1.10).

B1.6 View Factor for Two Triangles in Parallel Planes - $V_9(A,B)$.

(See Figure B1.9.)

It will be recalled that the second integration over the area of a triangle for V_4 , V_5 , V_{12} , and V_{13} could not be done analytically. In the case of two triangles, the integration in equation (T2.5) cannot be done over either A_1 or A_2 , so that another method is used. Figure B1.10 shows two triangles whose sides are one unit long, in parallel planes, two units apart. In Figure B1.11 the triangles have been divided into sub-areas, so that the sides are now five units long, and the triangles are ten units apart. The view factor from one sub-area to another can now be approximated because the distance between them is much greater than their own dimensions (ten times greater). It is evident from Figure T2.2 that if r is large compared to the dimensions of A_1 and A_2 , $\cos \phi_1$, $\cos \phi_2$, and r are almost constant over the range of integration. In this case, equation (T2.5) shows that F_{12} is directly proportional to A_2 for constant values of r , $\cos \phi_1$, and $\cos \phi_2$. Hence, the view factor from a square or a triangle to a triangle in a distant parallel plane is very nearly one-half of the view factor from a square or triangle to a square in the same position. Let the sub-scripts t and s denote a triangle and square, respectively. The following relationships hold if the areas are a large distance apart:

$$F_{ts} \cong F_{ss},$$

$$F_{st} \cong \frac{1}{2}F_{ss},$$

$$F_{tt} \cong \frac{1}{2}F_{ss},$$

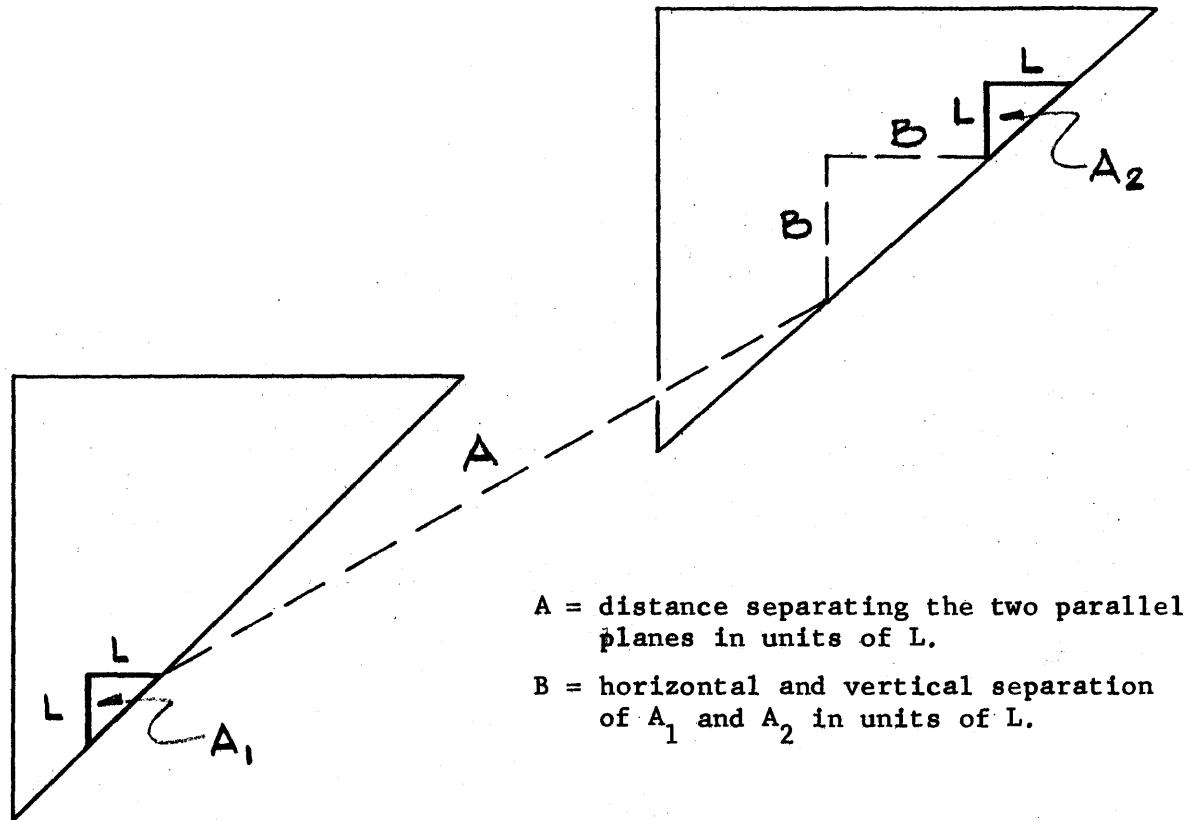


Figure B1.9 Arrangement of A_1 and A_2 for $V9(A,B)$.

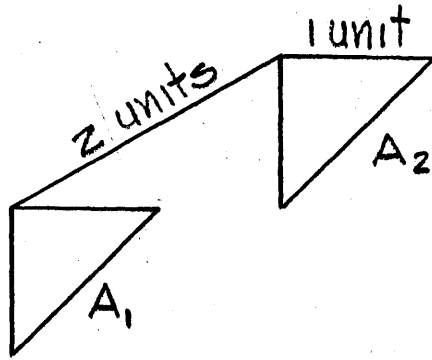


Figure B1.10 Two Triangles, A_1 and A_2 , of Unit Dimension and Two Units Away.

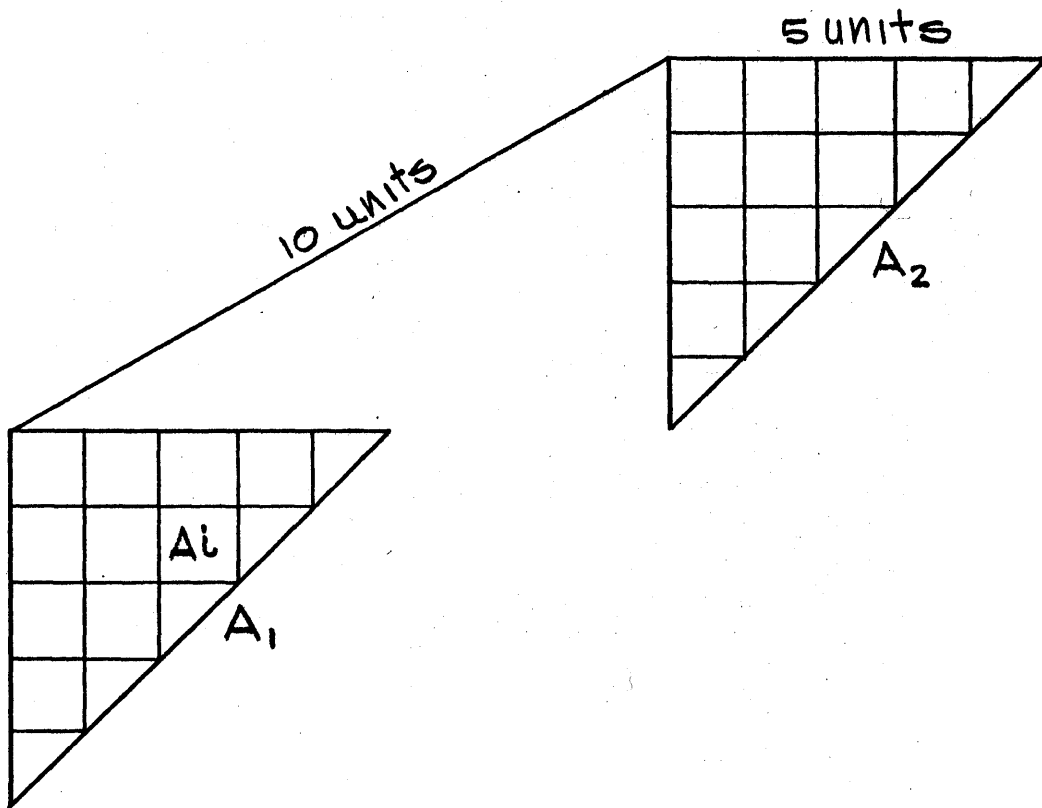


Figure B1.11 The Two Triangles in Figure B1.10 are Divided into Sub-Areas.

where

F_{ts} is the view factor from a triangle to a square,

F_{st} is the view factor from a square to a triangle,

F_{tt} is the view factor from a triangle to a triangle,

F_{ss} is the view factor from a square to a square.

The method used in the calculations will be illustrated for the two triangles shown in Figure B1.11. Let J_1 (a constant) represent the density of the radiation leaving A_1 ; the total amount of radiation reaching A_2 is $J_1 A_1 F_{12}$. The quantity of radiation emitted from sub-area A_i in A_1 and striking all of the sub-areas in A_2 is given by the summation

$$J_1 A_i \sum_j^{A_2} F_{ij}. \quad (\text{B1.11})$$

Summing equation (B1.11) over all of the sub-areas in A_1 and equating the result to $J_1 A_1 F_{12}$ yields

$$J_1 A_1 F_{12} = \sum_j^{A_1} (J_1 A_i \sum_j^{A_2} F_{ij})$$

or

$$A_1 F_{12} = V_9 = \sum_i^{A_1} (A_i \sum_j^{A_2} F_{ij}) \quad (\text{B1.12})$$

The right side of equation (B1.12) can be evaluated by using the approximations given above for the values of F_{ij} . The description of the computer code which carries out this computation is given in Appendix B2.

B1.7 View Factors V_6 , V_7 , V_8 , V_{10} , V_{11} , V_{14} (see Figures B1.12 through B1.17)

The view factors V_6 , V_7 , V_8 , V_{10} , V_{14} , cannot be obtained by integrating equation (T2.5) over A_1 and A_2 , but they can be evaluated from the view factors which have already been calculated. This method will be demonstrated for V_6 , shown as the view factor between the two shaded areas in Figure B1.18. The view factors from A_1 to all of the other areas except A_2 are known. The sum of the view factors from A_1 to all of the areas is equal to unity, because the radiation must strike some area in this closed space. Therefore V_6 can be obtained by subtracting the sum of the other view factors (V_1 's, V_2 's, V_{12} 's) from unity. After the view factor from A_1 to A_2 has been evaluated, the view factor from A_1 to A_3 (see Figure B1.19) can be calculated by the same procedure. This process is carried out until an array of required values of V_6 has been obtained. The view factors V_7 , V_8 , V_{10} , V_{11} , and V_{14} are obtained in the same way.

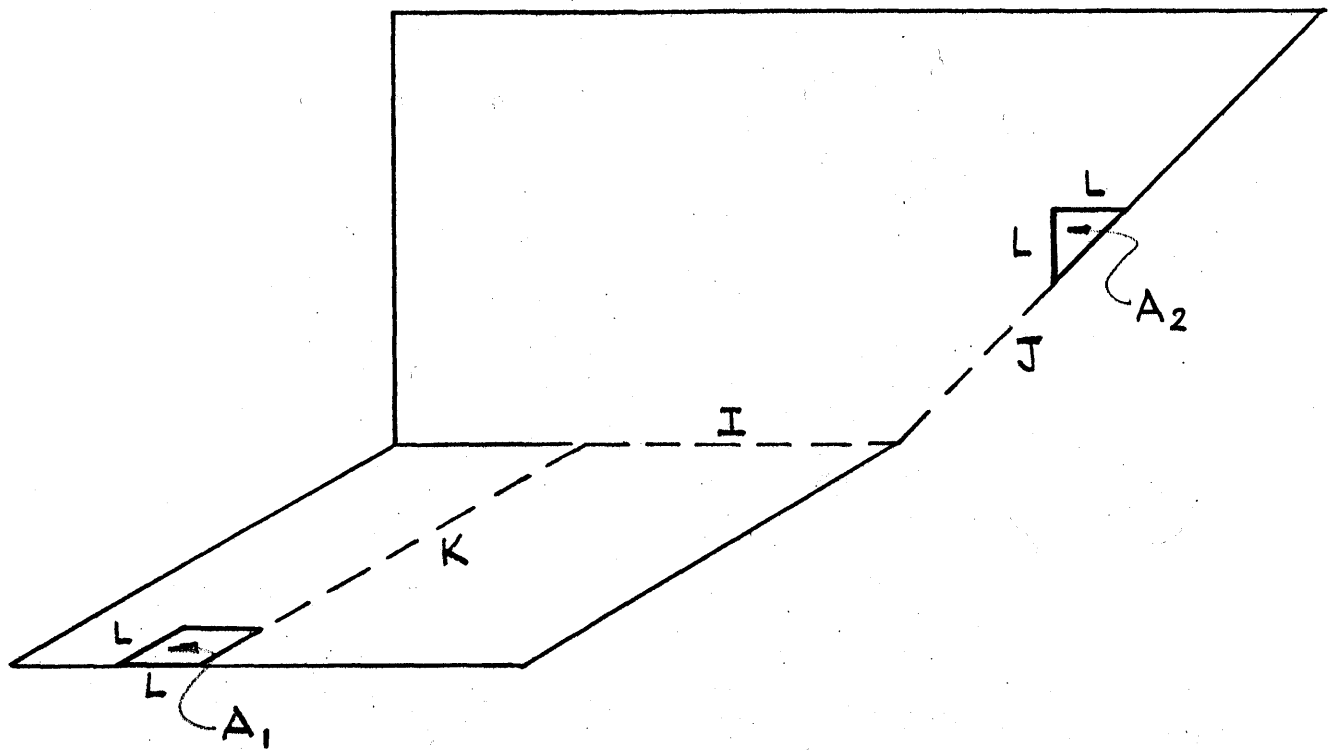


Figure B1.12 Arrangement of A_1 and A_2 for $V_{11}(I,J,K)$.

I = separation of A_1 and A_2 along the line of intersection of the two planes in units of L .

J = separation of A_2 from the intersection of the planes in units of $\sqrt{2} L$.

K = separation of A_1 from the intersection of the two planes.

I = separation of A_1 and A_2 along the line of intersection in units of L .

J = separation of A_1 from the intersection of the planes in units of L .

K = separation of A_2 from the intersection of the planes in units of $\sqrt{2} L$.

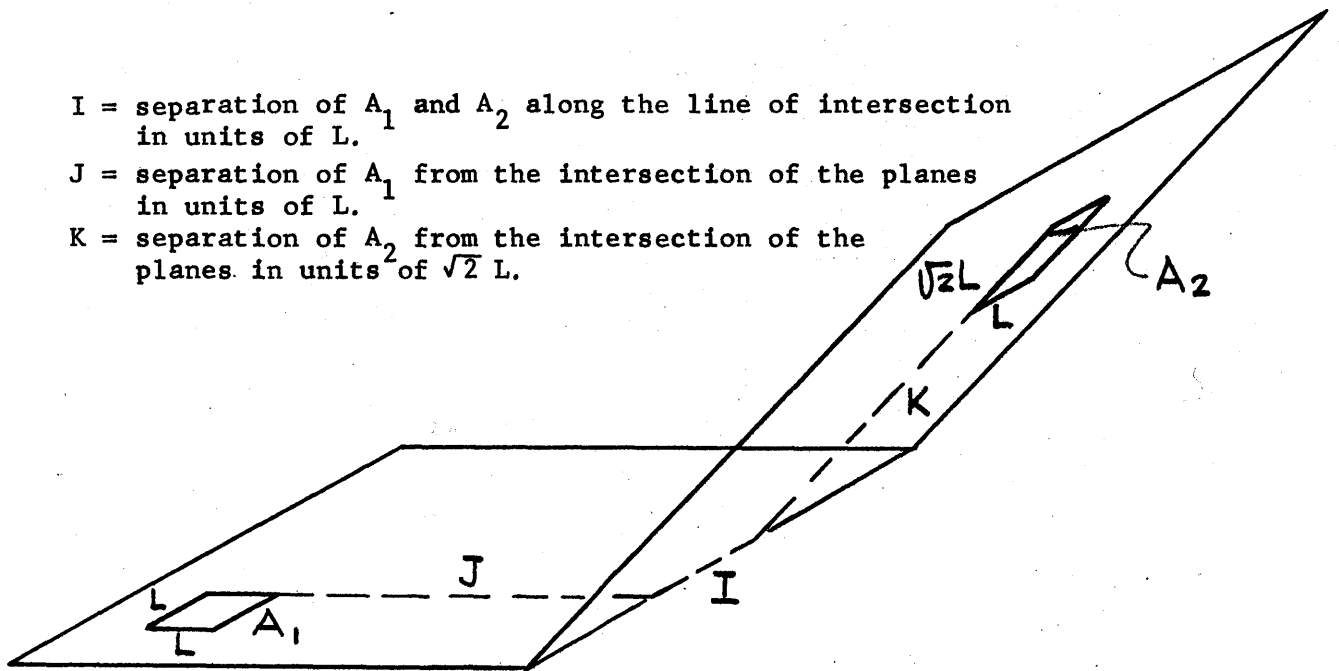


Figure B1.13 Arrangement of A_1 and A_2 for $V_{14}(I,J,K)$.

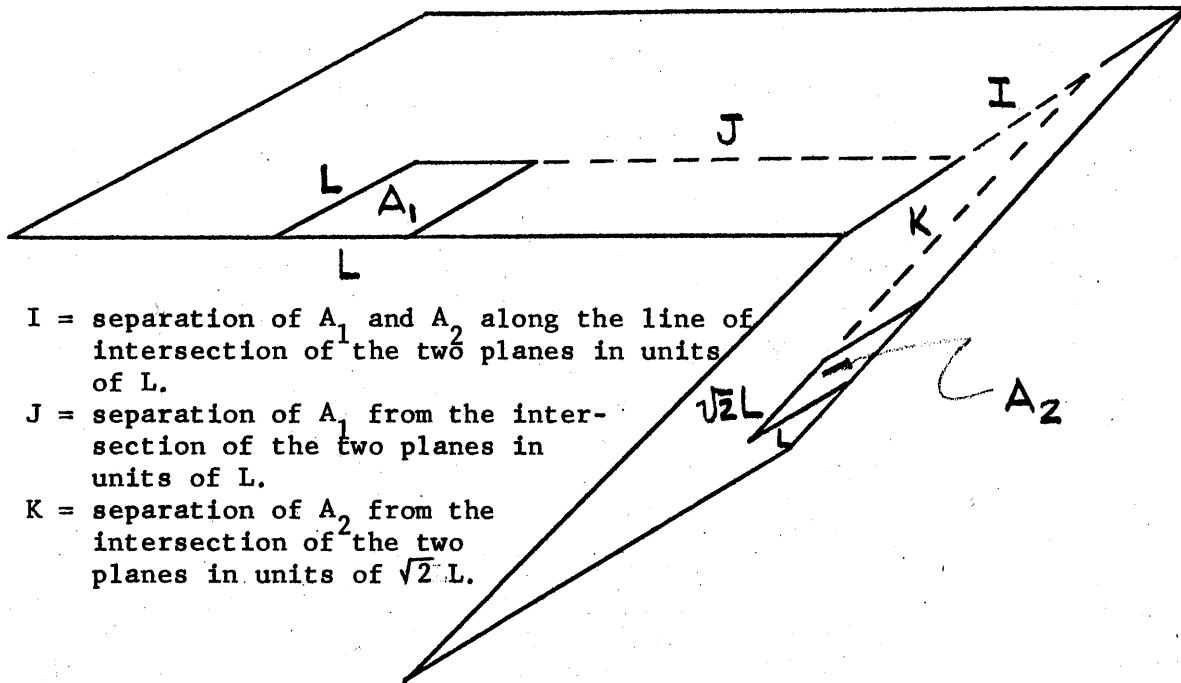


Figure B1.14 Arrangement of A_1 and A_2 for $V8(I,J,K)$.

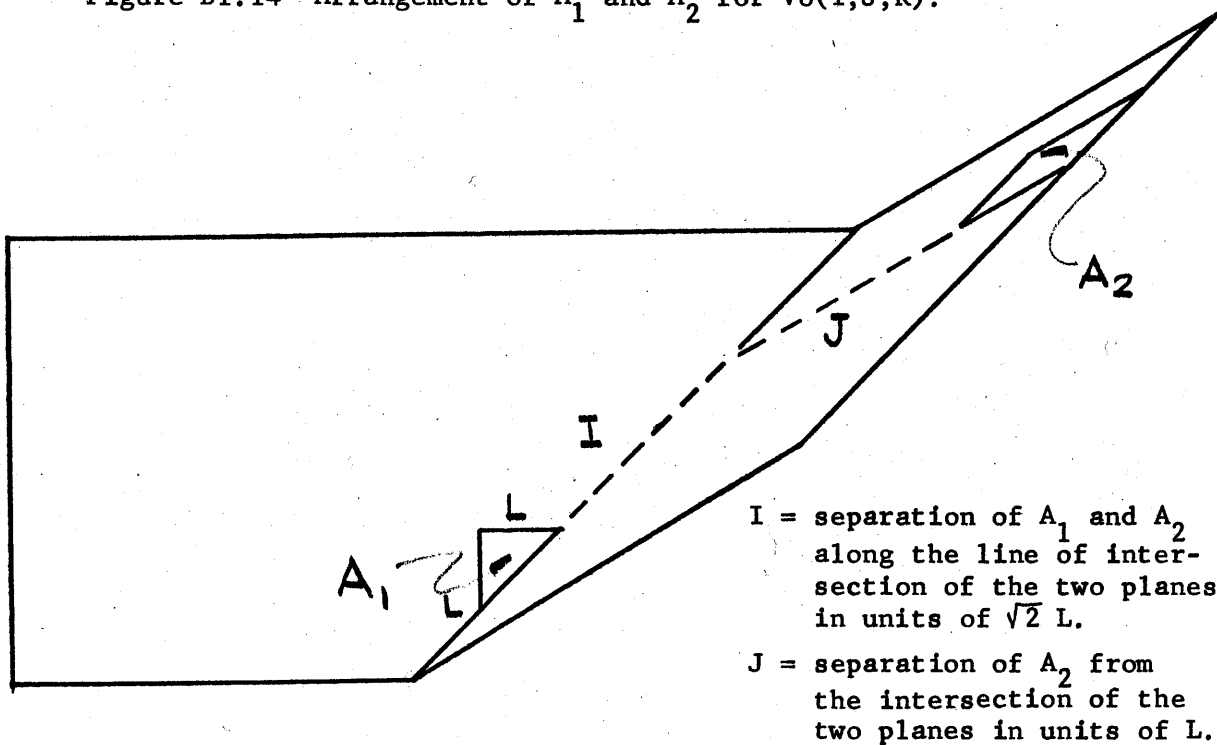


Figure B1.15 Arrangement of A_1 and A_2 for $V10(I,J)$.

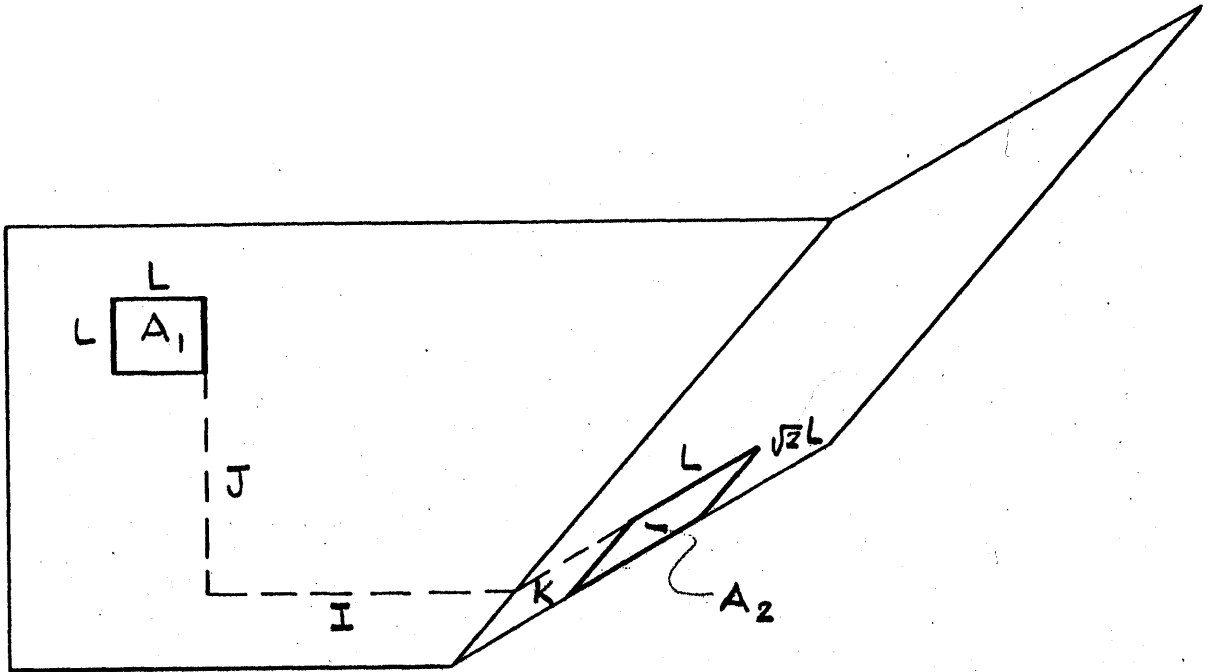
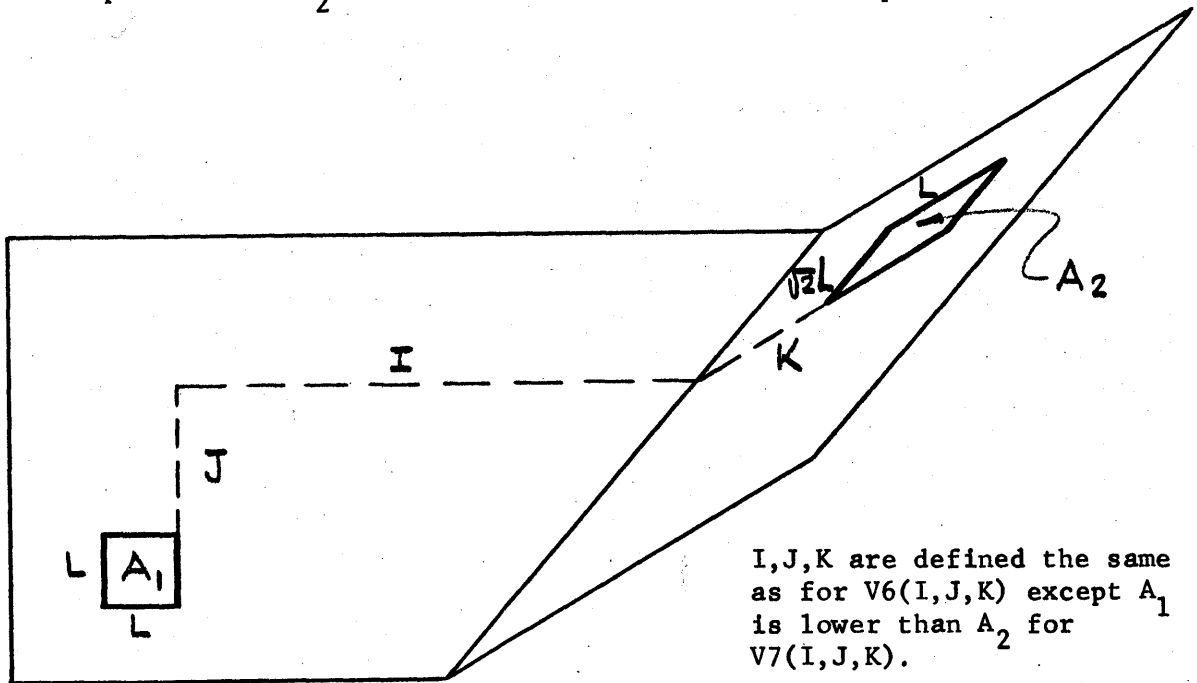


Figure B1.16 Arrangement of A_1 and A_2 for $V6(I,J,K)$.

I = separation of A_1 from the intersection of two planes in units of L .
 J = separation of A_1 and A_2 in the vertical direction in units of L .
 K = separation of A_2 from the intersection of the two planes in units of L .



I, J, K are defined the same as for $V6(I,J,K)$ except A_1 is lower than A_2 for $V7(I,J,K)$.

Figure B1.17 Arrangement of A_1 and A_2 for $V7(I,J,K)$.

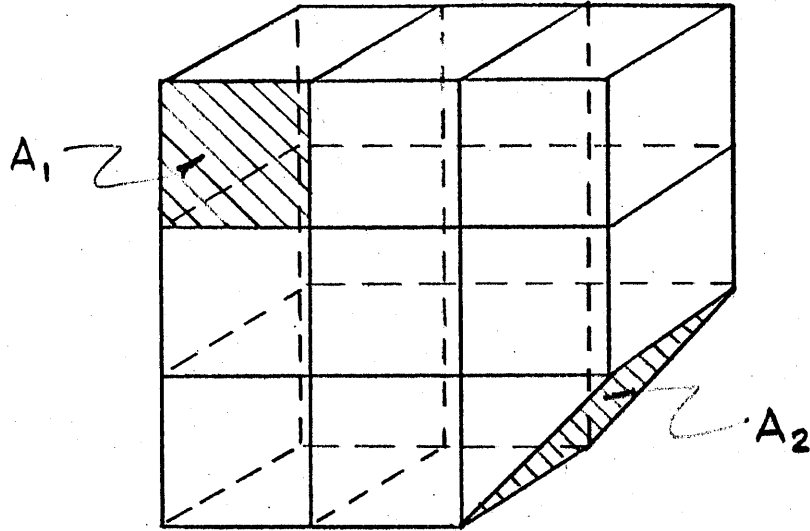


Figure B1.18 Enclosed Space Used to Calculate $V_6(3,3,1)$ between A_1 and A_2 .

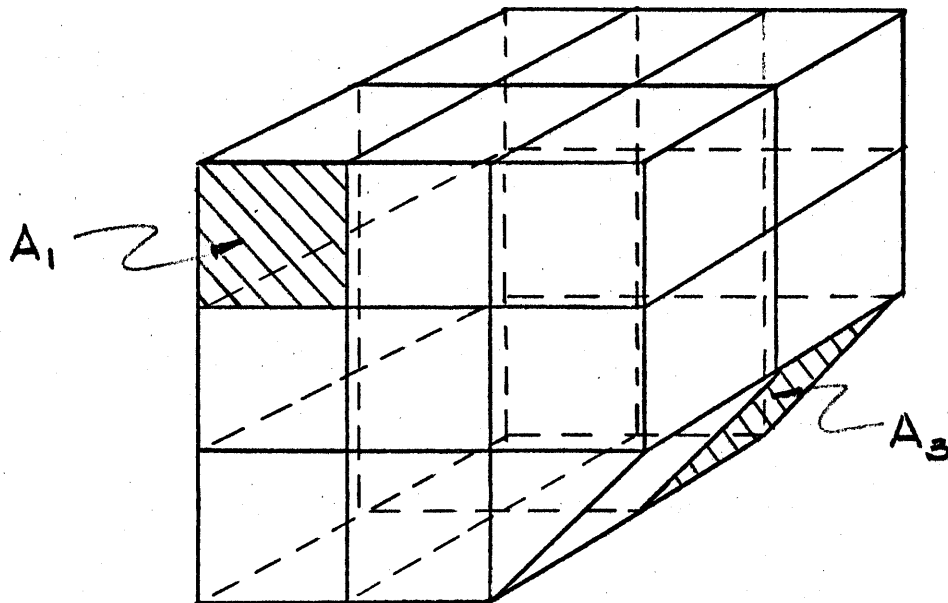


Figure B1.19 Enclosed Space Used to Calculate $V_6(3,3,2)$ between A_1 and A_3 .

Appendix B2

Computation of the View Factors

In Appendix B1, a mathematical expression or a method of evaluation was obtained for each of the view factors. In this appendix, the computer programs used to calculate the required array of these view factors are described. An array, as it is defined in computer terminology, refers to all of the numbers stored in the computer under one symbol. For example, $V_1(I,J,K)$ is evaluated for various values of I , J , and K , and resulting numbers are stored under the symbol V_1 . This group of numbers is referred to as the array of $V_1(I,J,K)$. The results from these programs are written on magnetic tape, or punched on IBM cards and are used as input data in the calculation of the flux distribution.

Each view factor is defined as a function of the relative position of the two areas, e.g., $V_1(I,J,K)$. Before a program can be written, the values of I , J , and K for which the view factor is to be computed must be determined. The quantities I , J , and K are expressed in units of L , just as the dimensions of the surfaces of the cavity are. Once the dimensions of the cavity are set, the values of I , J , and K for all of the view factors are determined. For example, let the dimensions of a cavity in the shape of a parallelepiped be $10 \times 12 \times 20$ in units of L . To calculate the view factor between all of the squares in perpendicular planes, $V_1(I,J,K)$ must be computed for values of I from 1 to 20, J from 1 to 20, and K from 1 to 12. See Figure B1.1 for the coordinate system for $V_1(I,J,K)$.

The flow sheet for the program which evaluates $V_1(I,J,K)$ and $V_2(I,J,K)$ is shown in Figure B2.1. These view factors are calculated by a straightforward evaluation of equations (B1.3) and (B1.6), respectively. The programmer specifies, by means of the input data card, the values of I , J , and

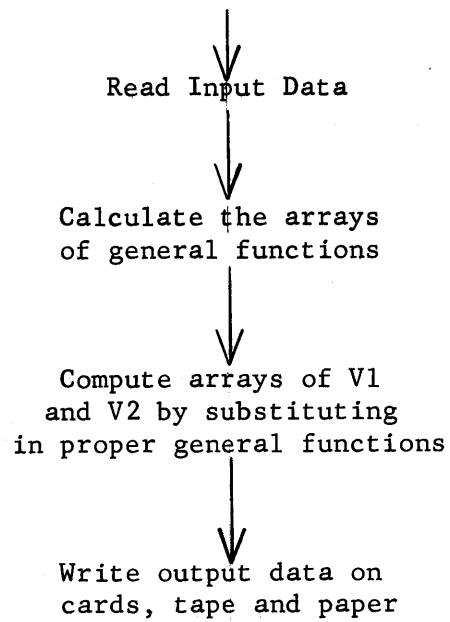


Figure B2.1 Flow Diagram for $V1(I,J,K)$ and $V2(I,J,K)$

K for which equations (B1.3) and (B1.6) are solved. These equations are rewritten in FORTRAN language in terms of four general functions, and an array of each of these general functions is computed DO LOOPS for the specified values of I, J, and K, and is stored in the computer. The array of V1 and V2 is then produced by substituting the correct general functions into the FORTRAN equation and the resulting answers are either punched on IBM cards or written on magnetic tape.

The equations for V4(I,J,K), V5(I,J,K), V12(I,J,K) and V13(I,J,K) are similar to those for V1 and V2, except that some terms have to be evaluated by numerical integration. The equations are rewritten in FORTRAN language in terms of general functions. The terms of the equation, which have been integrated over A₁ and A₂, are written as functions of I, J, and K, and the arrays of the general functions for these terms are calculated and stored in the computer. The variables of the terms under the integral sign are I, J, K, and u, where u is the variable of integration, so that the general functions for these terms must have the same variables. Let f(I,J,K,u) represent such a general function, and let g(I,J,K) represent the integral of f(I,J,K,u). According to Simpson's rule,

$$\int_0^1 f(I,J,K,u) du = \frac{1}{3} \left[f_0 + f_n + 4(f_1 + f_3 \dots + f_{n-1}) + 2(f_2 + \dots + f_4 + f_{n-2}) \right] \Delta u$$

$$= g(I,J,K), \tag{B2.1}$$

where

n = number of spacings,

Δu = width of the spacing.

The function f(I,J,K,u) is integrated numerically by Simpson's rule over the variable u for all of the required values of I, J, and K. To obtain

the number of spacings needed for an accurate numerical integration, a small array of V_4 , V_5 , V_{12} , and V_{13} was calculated for two cases, $n = 10$ and $n = 20$. The effect of changing the spacing, n , from 10 to 20 on the numerical value of a view factor is less than one part in 100,000 and $n = 10$ was therefore used, saving computer time without loss of accuracy. The resulting array of $g(I,J,K)$ is stored in the computer. The view factors are then calculated for the desired values of I , J , and K by substituting the appropriate numbers from the arrays of general functions previously calculated. The flow diagram for the calculation of V_4 , V_5 , V_{12} , and V_{13} is shown in Figure B2.2. The input data tell the computer the values of I , J , and K , for which the general functions and view factors are calculated, the spacing, Δu , and the number of spacings, n , used in the numerical integration. The program first computes the desired arrays of the general functions and, using these numbers, solves the view factor equation for the required values of I , J , and K . The view factors are then punched on IBM cards and also printed on paper.

The view factor $V_9(A,B)$ is evaluated by programming equation (B1.12) which is discussed in some detail because of the logic involved in the program. The flow sheet is shown in Figure B2.3. In equation (B1.12) F_{ij} is approximated from values of V_2 , so that V_2 is part of the input data. The dimensions of A_1 and A_2 , the distance between A_1 and A_2 , and the total area of the triangles, all in units of L , are also read into the program. The pairs of indices, I,J and L,M , designate the sub-areas on A_1 and A_2 , respectively, as shown in Figure B2.4. The summations in equation (B1.12) over A_1 and A_2 are made by letting L and M range through their values for each value of I and J . For each set of (L,M) a check is made to determine

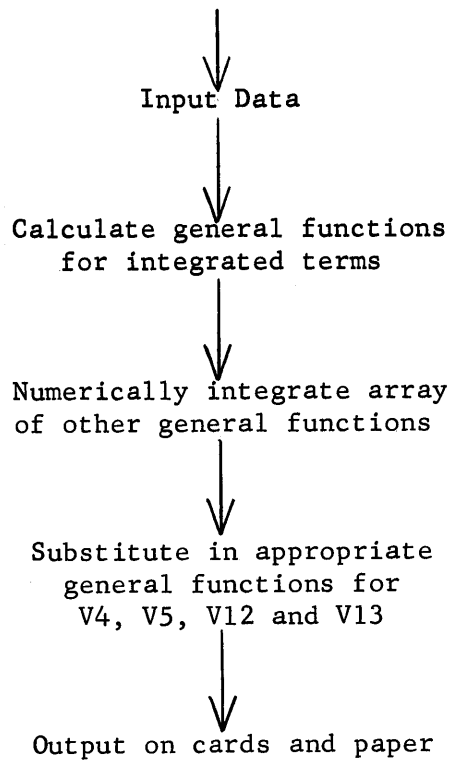


Figure B2.2 Flow Diagram for V4, V5, V12 and V13

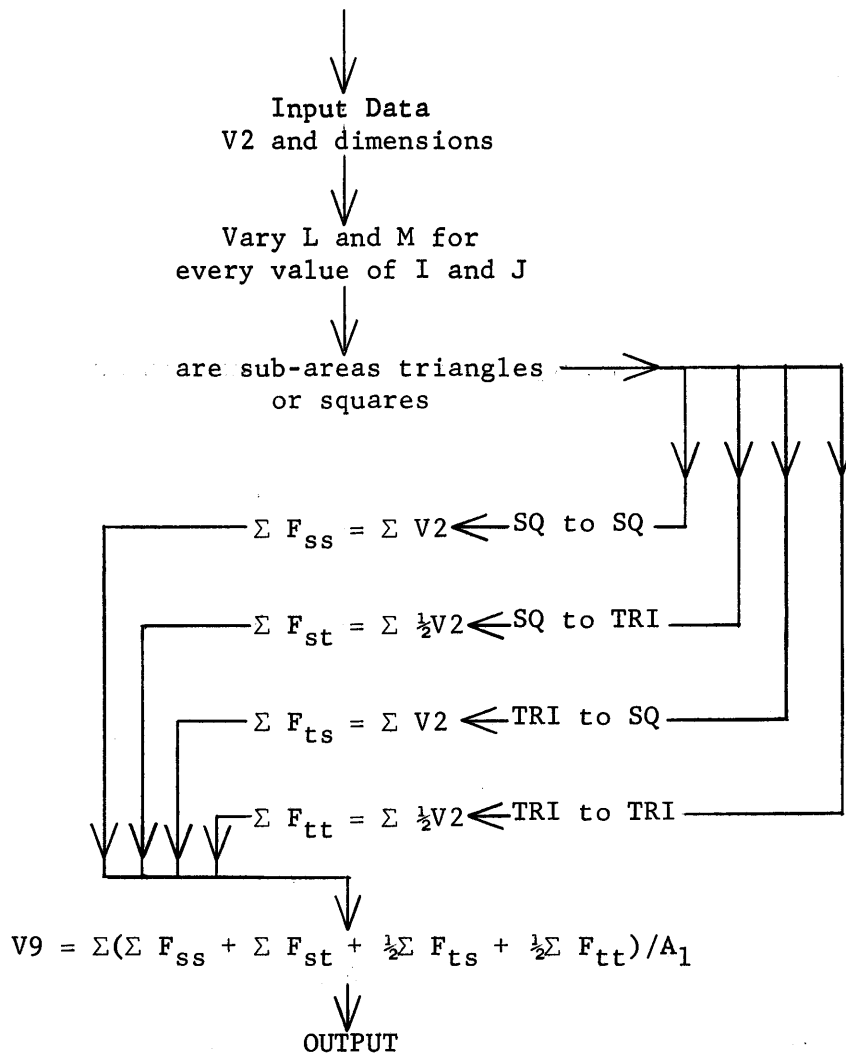


Figure B2.3 Flow Diagram for V9(A,B)

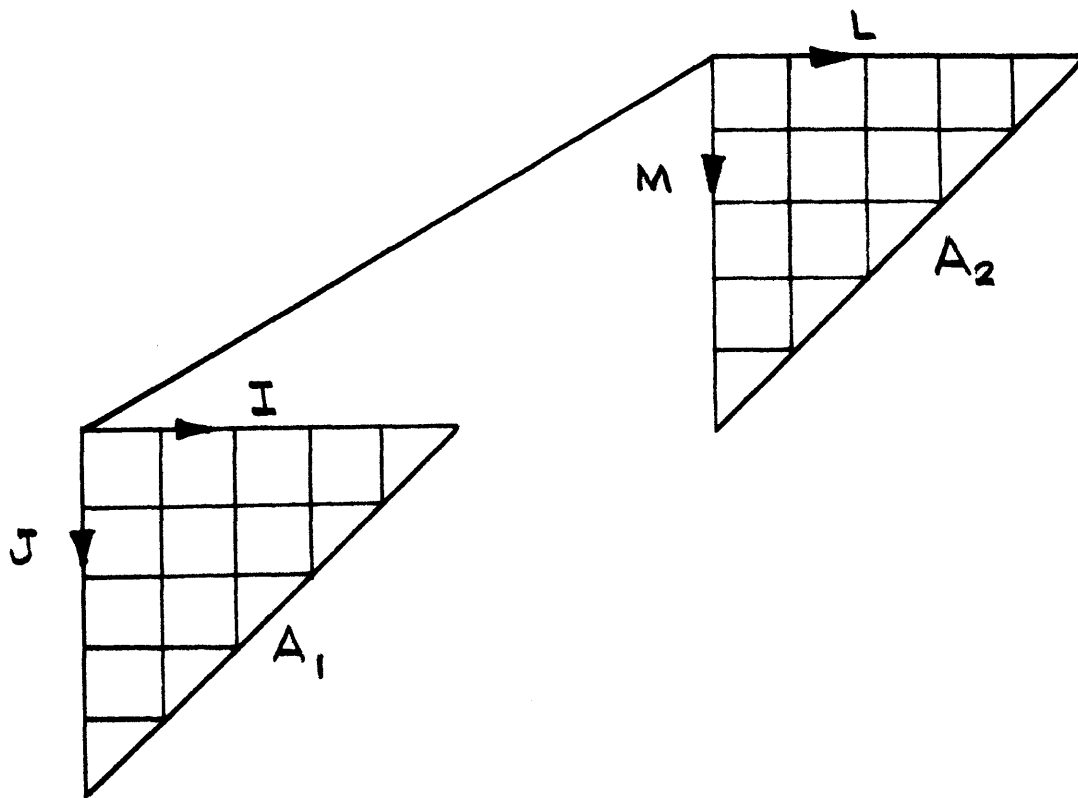
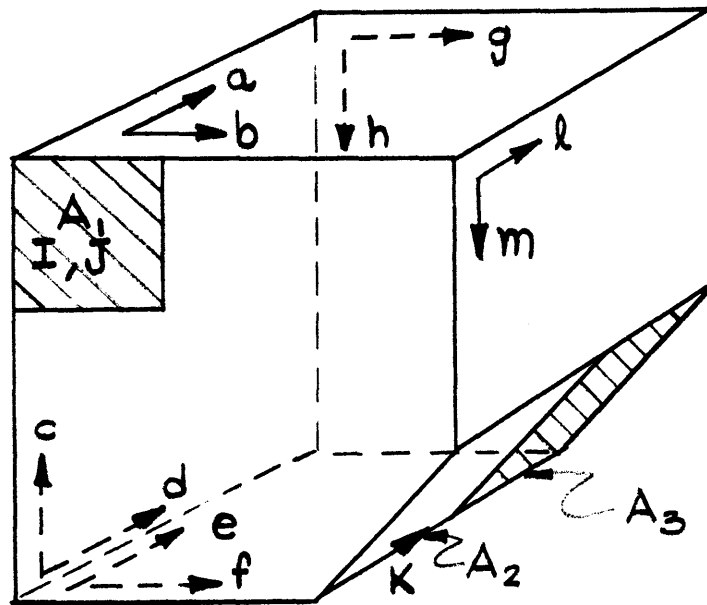


Figure B2.4 Areas A_1 and A_2 with Their Respective Coordinate Systems.



$$V6(I, J, K)$$

Figure B2.5 Enclosed Space used to Calculate $V6(I, J, K)$ is shown with the Coordinate Systems for Each Surface.

if the sub-area is a triangle or a square. A similar check is made for each I,J set to determine if F_{st} , F_{ss} , F_{ts} , or F_{tt} is the proper view factor. Each of the four view factors is summed separately, and when the double summation is completed, these four sums are substituted into equation (B1.12). The array of V9 is punched on IBM cards and also written as output information. The accuracy of this method is demonstrated by considering an example in which the triangles are divided into 55 sub-areas (10 divisions along each side of the triangle). The view factor F_{ss} , (or V2), which is known accurately, makes up 67% of the terms, while F_{st} , F_{ts} , and F_{tt} make up 33% of the terms in the summation. Since F_{st} and F_{tt} equal one-half of F_{ss} , F_{ss} contributes about 75% of the numerical value of V9. The maximum error expected in the approximate values of F_{st} , F_{ts} , and F_{tt} is one per cent. The magnitude of the error is obtained by comparing the values of V2 to V12 or V13 for the same I, J, and K. The maximum error in V9 would then be 0.25 per cent, since F_{ss} contributes a very small error.

The method of calculating V6, V7, V8, V10, V11 and V14 was described by using V6 as an example, and V6 is used again to illustrate the logical steps of the program which computes all of these view factors. The coordinate system for V6, defining the relative position of the two areas, A₁ and A₂, is shown in Figure B1.16. In Figure B2.5 the coordinate systems which define the position of the sub-areas in the enclosed volume are drawn on all surfaces, but the sub-areas are not shown in order to simplify the drawing. (See Figure B1.19 for the drawing which includes the sub-areas.) The flow diagram for the computation of V6(I,J,K) is shown in Figure B1.6. Input data include the values of I, J, and K, for which V6(I,J,K) is computed, and the view factors V1, V2, V4, V5, V9, V12, and V13. In this

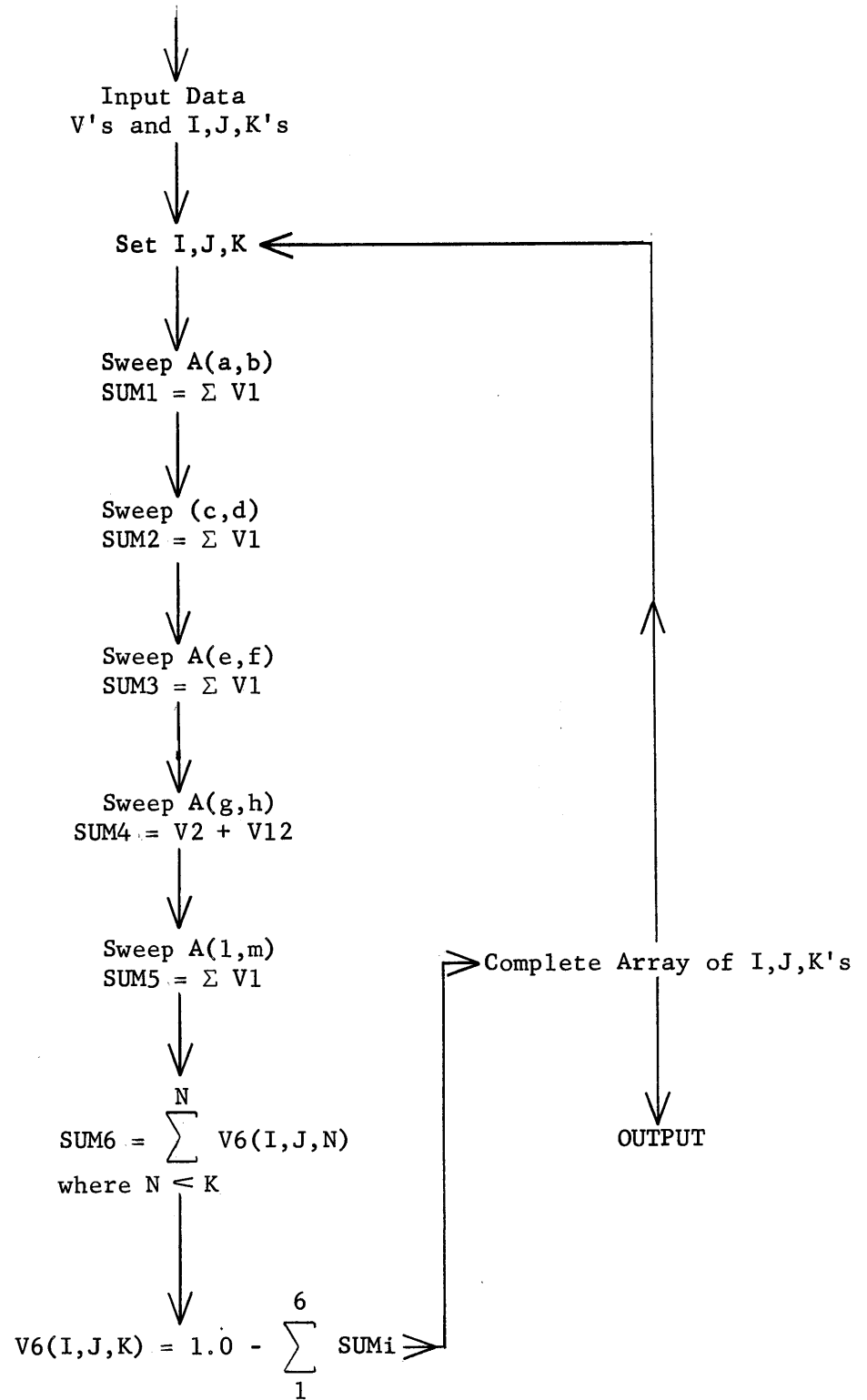


Figure B2.6 Flow Diagram for View Factor $V_6(I,J,K)$

example, $I = 3$, $J = 3$, and $K = 2$, and only V_1 , V_2 and V_{12} are needed. The sum of the view factors from A_1 to all of the other sub-areas except A_2 and A_3 is computed by sweeping the sub-areas in $A(a,b)$, $A(c,d)$, $A(e,f)$, $A(g,h)$ and $A(l,m)$. To this sum is added $V_6(3,3,1)$, which has already been calculated, and the final sum is subtracted from unity, giving the value for $V_6(3,3,2)$, which is then stored in the computer. Another set of values for I , J , and K is selected, and the process is repeated until the complete array of $V_6(I,J,K)$ is obtained. This array is punched on IBM cards and is written as output data.

Appendix B3

Detailed Flow of the Code for the 45° Cavity

To clarify the detailed description of the code, a particular case will be used as an example. It is the 45° cavity with 12" sub-areas, and has essentially the same method of solution as the PARA geometry with 6" and 12" sub-areas. The flow diagrams for the main routine, and the seven sub-routines are given in Figures B3.1 through B3.8, which illustrate the flow for both the 45° and PARA arrangements. A detailed flow diagram for the calculation of the $C(I,J)$ for the 45° and PARA arrangements is given in Figures B3.9 and B3.10, respectively, and this is the only section of the code where the two programs differ significantly. The code is written in as general a way as possible, so that the flux distribution can be obtained for any dimension of the cavity for which view factors are available. The sections of the code for the 45° cavity will be described in the same order as they are used by the computer.

The main routine first calls in SOPNOR (Figure B3.1), which reads the view factors from cards into storage. The value of each view factor is stored according to the indices which, in turn, correspond to the spatial variables I, J, K of the view factor $V(I,J,K)$. Next, the main program stores the following data which have been punched on cards by the programmer.

(1) The dimensions of the cavity surfaces

K_1 = number of unit lengths along the 72" dimension = 6,

K_2 = number of unit lengths along the 60" dimension = 5,

K_3 = number of unit lengths along the 120" dimension = 10,

K_4 = number of unit lengths along the J dimension of surface #4 = 5,

K_5 = $K_2 + K_4 + 1 = 11$,

$$K6 = K1 + 1 = 7,$$

$$K7 = K2 + 1 = 6,$$

$$K8 = K3 + 1 = 11,$$

$$K9 = K4 + 1 = 6,$$

$$K10 = \frac{1}{2}K1 = 3,$$

K11 = distance the graphite frame extends from the thermal column face; if the frame is not present, K11 = 0

(2) Optional transfers ITRAN 1, ITRAN 2, and ITRAN 3

(3) Input constants

ERROR = allowed error in the convergence of the T(I,J)'s,

AL = constant factor for the final value of $\phi(I,J)$,

A = constant value for source neutrons,

CON = initial assumption for the values of the T(I,J),

D = total number of source neutrons being fed into the hohlraum per second on one side of the plane of symmetry.

Next, ITRAN 1 selects a constant feed, A, or a variable one which is read from IBM cards.

ALBEDO (Figure B3.2) is called, and this sub-routine reads in the values of AL and D, according to their indices. The indices I, J refer, for example, to the value of AL 1(I,J) and D1(I,J) for Al(I,J), the sub-area with coordinates I, J on surface #1. Because of symmetry, only the sub-areas on one side of the plane of symmetry need to be assigned a value for AL(I,J) and D(I,J). Sub-routine TEST 1 (Figure B3.3) then sets the T(I,J)'s equal to their initial values, CON or zero. If the material bounding the sub-area is made of graphite, T(I,J) is set equal to CON. If the material is cadmium or boral, T(I,J) is taken to be zero. The

dimensions of the surfaces, denoted by K1 through K11, serve as limits on the DO LOOPS and as control parameters, so that each T(I,J) is assigned the correct dimension and the proper initial value, zero or CON. The first iteration can now begin. The storage locations, which will contain the C(I,J), are cleared by setting them equal to zero. The I and J indices sweep the surfaces for which the values of C(I,J) are calculated, while the L and M indices sweep the surfaces which are contributing to C(I,J). The re-entering current, therefore, is denoted by the L, M indices, such as T1(L,M). The equations for C1(I,J), C2(I,J), C3(I,J), C4(I,J) and C6(I,J) have the same form as equation (T4.3), which was given earlier as an example. The indices I, J, L and M are generated in DO LOOPS whose upper limit is set at the maximum value needed to sweep the largest surface. For 12" sub-areas, the upper limits are I = 5, J = 10, L = 6, and M = 10. Before sweeping any surface, the indices are checked to insure that they do not exceed the dimension of the surface. C6(I,J) is calculated from the values of T5(L,M), T4(L,M), T3(L,M), T2(L,M), T1(L,M), F(L,M) and the proper view factors, as illustrated by equation (T4.3). Sometimes the shape of the sub-area (triangle or square) and its relative position must be determined in order to select the proper view factor. As an example, consider the contribution from A5(L,M) to A6(I,J). If both A5(L,M) and A6(I,J) are squares, V2 is used. If one is a triangle and the other a square, V12 or V13 is used, depending on the relative position of A5 and A6 (see Figures B1.7 and B1.8); if both are triangles, V9 is used. A set of parameters, L1 through L10, which are evaluated for each value of I, J, L, and M, control the flow of the program so that dimensions of surfaces are not exceeded and the proper type of view factor is selected. Another

set (N11 through N22) are the indices of the view factors and are determined from the relative position of A(I,J) and A(L,M), as defined by the view factor's coordinate system. After C6(I,J) is calculated for a particular set of I, J and L, M, C4(I,J), C5(I,J), C2(I,J) and C1(I,J) are calculated by sweeping the surfaces which contribute to their incident current. For each set of I and J the indices L and M sweep all of the surfaces, and the results are printed. This procedure continues until all of C(I,J)'s have been calculated.

One requirement placed on the values of T, C, and F is that a neutron balance must be preserved. In the first two iterations, the assumed values for T(I,J) usually do not preserve this balance, so that a normalization factor, CON 2, is calculated to force a neutron balance; subroutine NORMAL (Figure B3.4) performs this function.

The neutron balance equation is:

$$\begin{aligned}
 \sum_{\text{Surface 1}} \sum_{I,J} A(I,J) \times F(I,J) + \sum_{\text{all surfaces}} \sum_{I,J} A(I,J) \times T(I,J) &= \sum_{\text{all surfaces}} \sum_{I,J} A(I,J) \times J(I,J) \\
 &= \sum_{\text{all surfaces}} \sum_{I,J} C(I,J) \qquad \qquad \qquad (B3.1)
 \end{aligned}$$

This equation states that the number of neutrons entering the cavity (the source neutrons and reflected neutrons) is equal to the total number leaving the cavity.

Since

$$A(I,J) \times T(I,J) = \beta(I,J) \times C(I,J), \qquad \qquad \qquad (B3.2)$$

and since D was defined earlier as the total number of source neutrons per second,

$$D = \sum_{\text{Surface 1}} \sum_{I,J} A1(I,J) \times F(I,J), \quad (\text{B3.3})$$

equation (B3.1) may be rewritten as

$$D = \sum_{\text{all surfaces}} \sum_{I,J} C(I,J) [1 - \beta(I,J)]. \quad (\text{B3.4})$$

Recalling that $D(I,J) = 1 - \beta(I,J)$, we may define the normalization constant CON 2 as:

$$\text{CON 2} = \frac{D}{\sum_{I,J} C(I,J) \times D(I,J)}. \quad (\text{B3.5})$$

Note that D, the total number of source neutrons/sec, is a non-indexed constant, while D(I,J) can be distinguished from D because it is an indexed variable. Sub-routine NORMAL calculates CON 2 by obtaining the product, C(I,J) x D(I,J), for each sub-area on all of the surfaces. D is divided by the sum of these products and the resulting value of CON 2 is printed out. The quantity, CON 2, represents the number by which all of the C(I,J)'s and T(I,J)'s must be multiplied in order to obtain a neutron balance. After the third iteration, the value of CON 2 usually differs from unity by less than 1%. Besides indicating that the magnitude of T(I,J) and C(I,J) is consistent with the neutron balance, a value of CON 2 close to unity is a check on the consistency of the equations for C(I,J) and the data, F(I,J), AL(I,J) and D(I,J). The value of CON 2 for the first

iteration depends upon the value of CON which was used. The second iteration usually produced a value of CON 2 which differs from unity by about 5%. After the second iteration, the magnitude and distribution of the T(I,J) and C(I,J)'s are close to their final values, and therefore, CON 2 is quite close to unity for the following iterations. After CON 2 has been obtained, a test of the degree of convergence is made by CURIN (Figure B3.5); CURIN converts the values of C3(I,J) which have just been calculated to their corresponding values of T3(I,J) by means of the equation:

$$T3'(I,J) = C3(I,J) \times AL3(I,J) \times CON\ 2. \quad (B3.6)$$

T3'(I,J) is compared to the T3(I,J) which was assumed to calculate C3(I,J). If the difference between the two is within a defined range, ERROR, the iteration is completed. If not, another iteration is performed. The test of convergence is made for the T3(I,J)'s on the bottom surface of the honeycomb, that is, for T3(I,J) with I = 1 to 3, and J = 5 to 10 for this example.

Since the flux distribution on the bottom of the honeycomb is the most important result desired from the code, the values of the T3(I,J) on the honeycomb were used as the criteria for convergence. The results of a code which tested for the convergence of all T(I,J)'s showed that all but a few of the T(I,J)'s converge in the same iteration in which the T3(I,J)'s converge, and that the additional iterations, which might be needed to obtain convergence of the last few T(I,J)'s, do not change the values of T3(I,J).

A few T(I,J)'s, which do not significantly effect the value of the flux on the honeycomb surface, might require one or two additional iterations for convergence, which is equivalent to as much as 22 minutes of

computer time. Therefore, the criterion of convergence was based only on the values of $T3(I,J)$ without sacrificing accuracy and with a considerable saving in computer time.

CURIN converts the $C3(I,J)$ to their corresponding $T3(I,J)$ by means of equation (T6.3). It then compares the difference of each $T3'(I,J)$ and $T3(I,J)$ to the quantity, ERROR, for each set of I, J. If any one of the differences exceeds the magnitude of ERROR, this fact is noted by changing the value of KON 3 from zero to one. The quantity, KON 3, is a number introduced in CURIN to control the flow in the program. After KON 3 has been changed, the rest of the $T3'(I,J)$'s are calculated, but the convergence test for these $T3'(I,J)$'s is omitted. After the calculations are completed in CURIN, the main program determines if another iteration is required by checking the value of KON 3. If it is zero (convergence obtained), the results are printed out in FINAL (see Figure B3.7). FINAL converts the values of $T3(I,J)$ on the honeycomb into values of the absolute flux $\phi(I,J)$ by means of the relationship

$$\phi3(I,J) = AL \left[C3(I,J) + T3(I,J) \right] = T3(I,J) \times \left[\frac{1 + AL3(I,J)}{AL3(I,J)} \right] \times AL, \quad (B3.7)$$

where AL converts the relative flux into absolute flux. Recall the $T3(I,J)$ was multiplied by CON 2 in CURIN. FINAL sweeps the honeycomb surface by means of I and J DO LOOPS, and prints out the resulting values of $\phi3(I,J)$. Then the dimensions of the system, initial constants, AL, A, CON, D, and ERROR, and a few values of $AL(I,J)$ and $D(I,J)$ are printed by the main program. These numbers identify the cavity assembly for which the flux was solved.

If KON 3 is equal to unity, the desired convergence has not been reached, and another iteration is performed. The new set of T(I,J) are calculated from the value of C(I,J) resulting from the last iteration in sub-routine RESET (see Figure B3.6). RESET multiplies each C(I,J) by the appropriate AL(I,J) and CON 2, except for the C3(I,J) which have already been changed to T3(I,J) in CURIN, and stores the results in the correct T3(I,J). All of the surfaces are swept by I and J indices, which define the quantities in the equation:

$$T(I,J) = C(I,J) \times AL(I,J) \times CON 2. \quad (B3.8)$$

After this new set of T(I,J) has been obtained, the program transfers the control to the beginning of the iteration where the C(I,J) are set equal to zero.

New values of the C(I,J) are calculated and the procedure continues until all T3(I,J) on the honeycomb converge.

During the testing of the code, several values of ERROR were used to investigate the convergence. After the third iteration, most T3(I,J) agreed within 2% of their values obtained from the second iteration. Most T3(I,J) from the fourth iteration are within ~ 1% of their values from the third iteration. Only the T3(I,J) near the back wall converge slowly. After three iterations, the difference in these T3(I,J)'s is about 3%. The difference is still about 2% after the fourth iteration. A single iteration may take as long as 11 minutes (depending upon the value of L), so that a compromise has been made. The quantity, ERROR, is selected so that the maximum difference of T3(I,J) from successive iterations will be 3%. This value of ERROR usually requires three or four iterations and results in an error of 1 to 2% for most T3(I,J). The T3(I,J)'s which correspond to sub-areas not bordering the back or side edges of the honeycomb surface are within 1% of their exact solution.

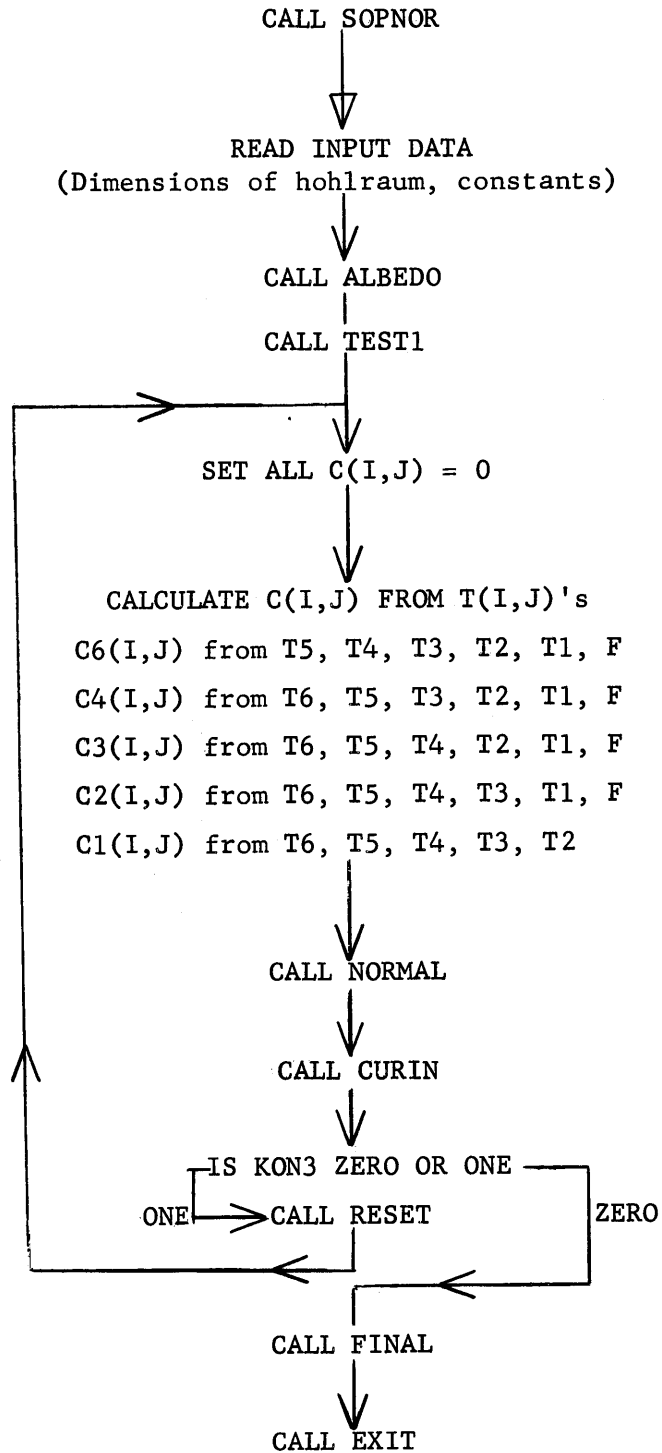


Figure B3.1 Flow Diagram of Main Routine, 45° and PARA Cavities

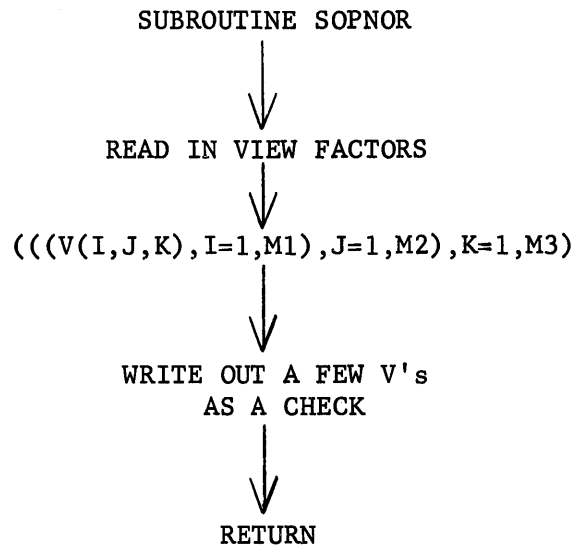


Figure B3.2 Flow Diagram of Subroutine SOPNOR, 45° and PARA Cavities

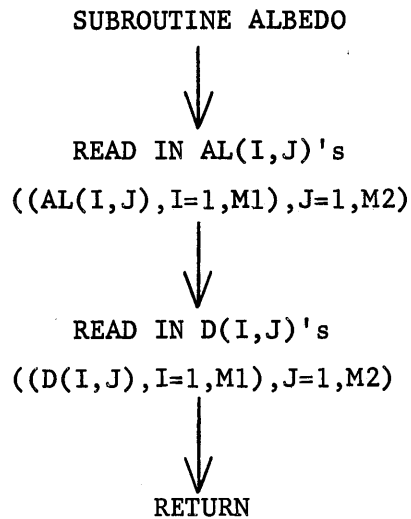


Figure B3.3 Flow Diagram of Subroutine ALBEDO, 45° and PARA Cavities

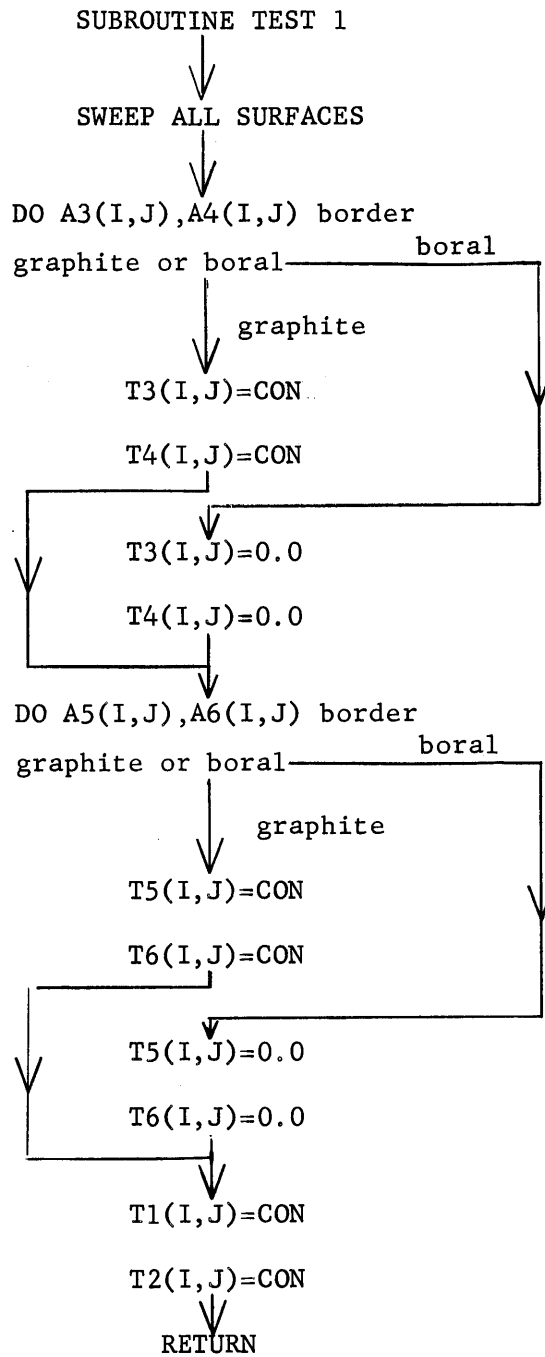


Figure B3.4 Flow Diagram of Subroutine TEST1 for 45° and PARA Cavities

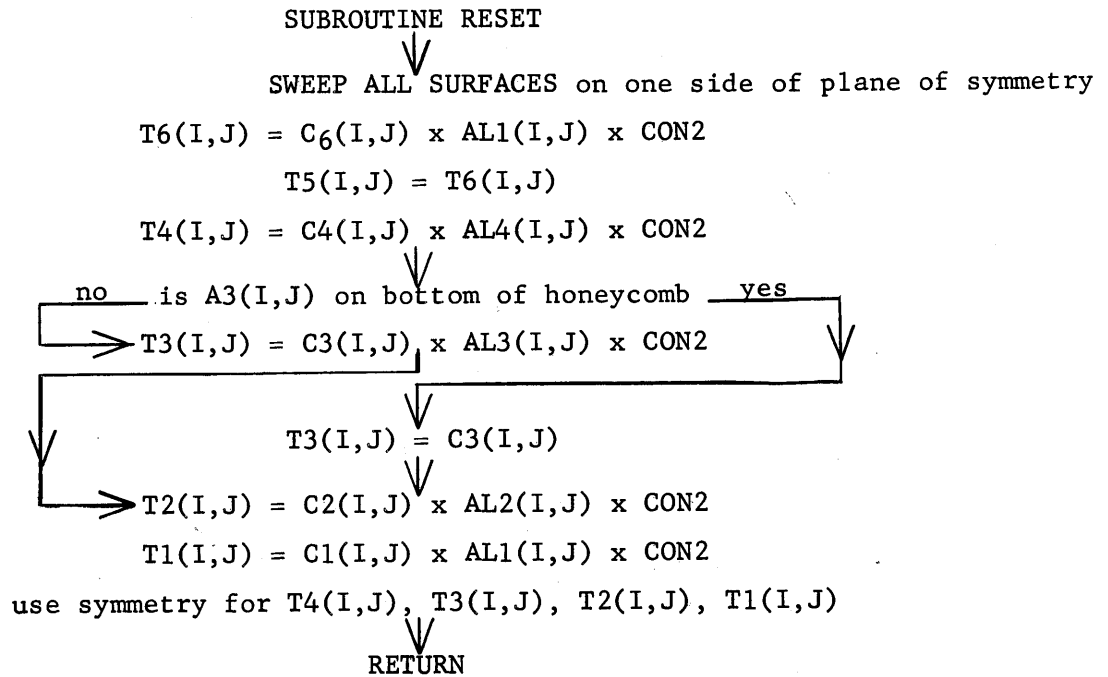


Figure B3.7 Flow Diagram of Subroutine RESET for 45° and PARA Cavities

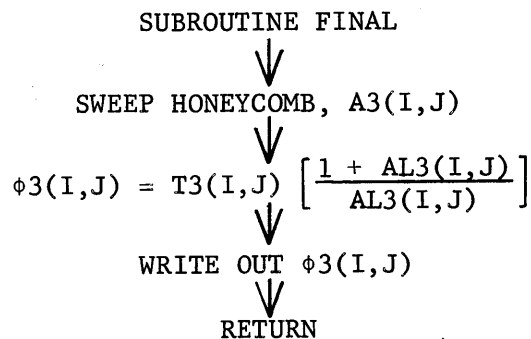


Figure B3.8 Flow Diagram of Subroutine FINAL for 45° and PARA Cavities

Calculation for $C_6(I,J)$, $I=1,5, J=1,10$ when $A_6(I,J)$ is a square

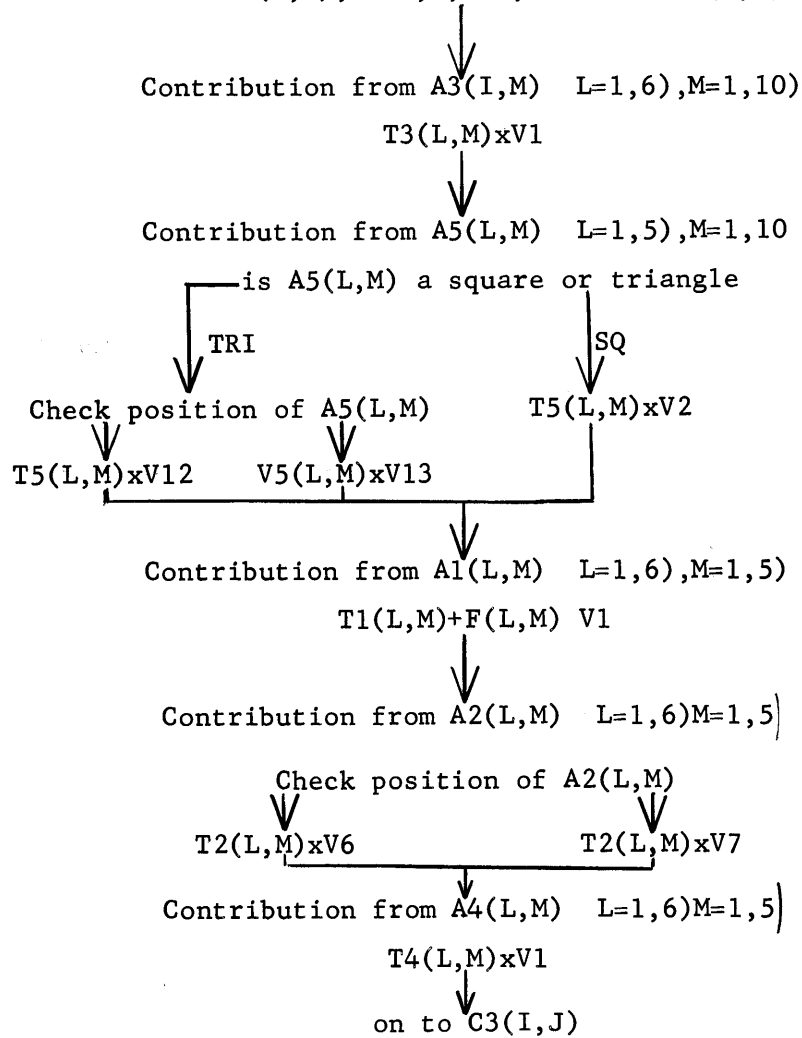


Figure B3.9 Flow Diagram of Code which Calculates $C(I,J)$ for 45° Cavity

Calculation of $C6(I,J)$ $I=1,5),J=1,10)$ when $A6(I,J)$ is a triangle

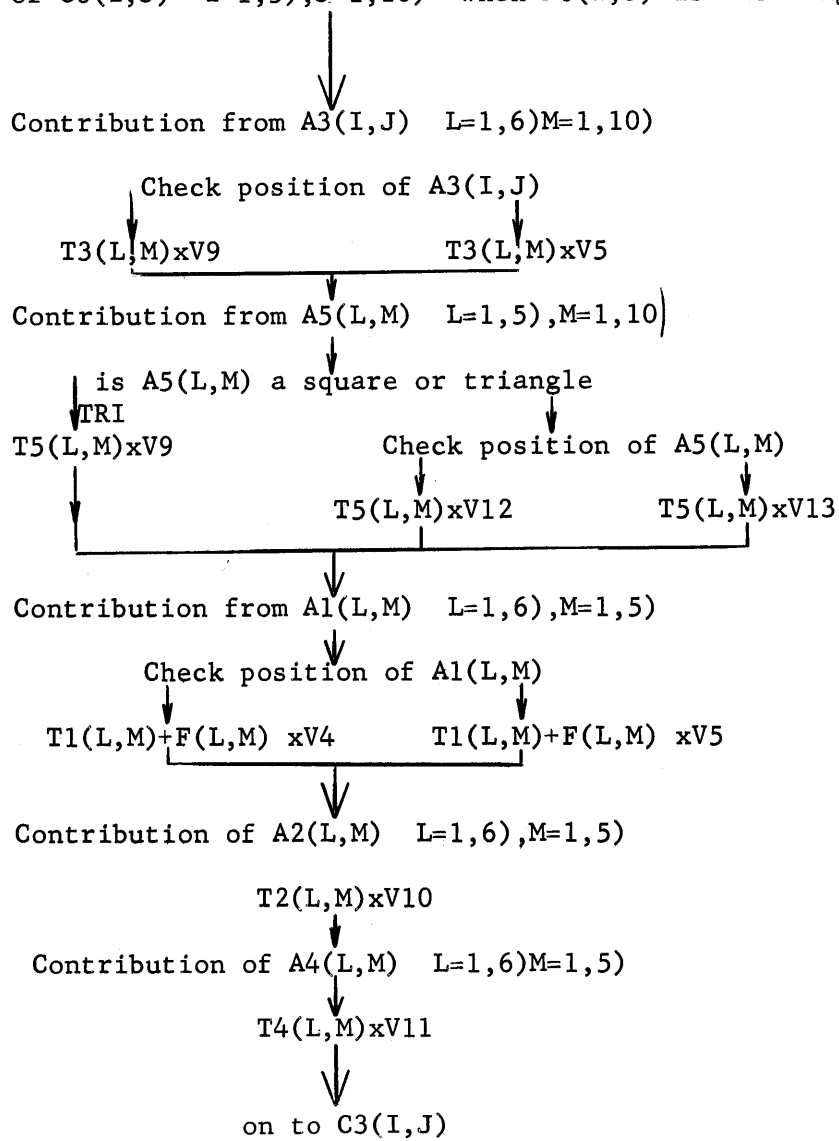


Figure B3.9 (continued)

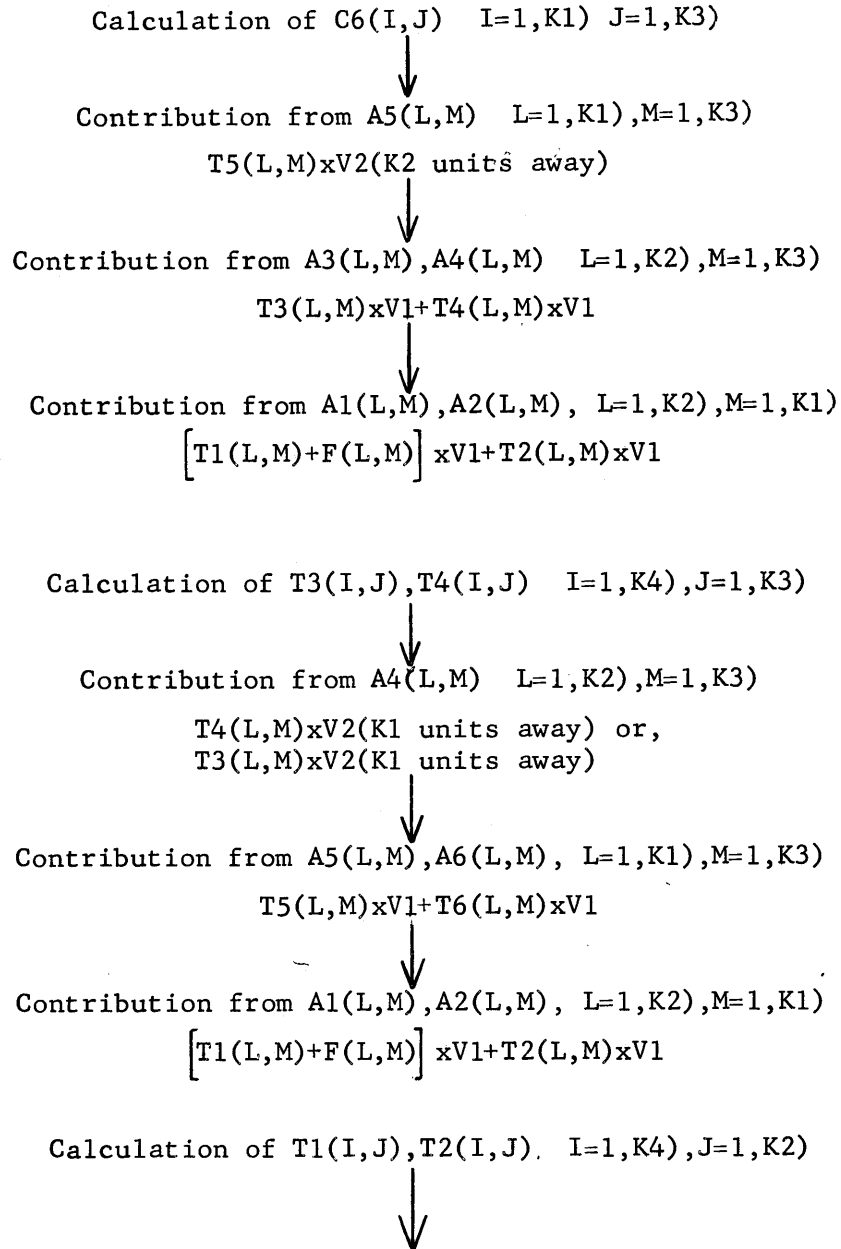


Figure B3.10 Flow Diagram of the Code which Calculated $C(I, J)$ for PARA Cavities

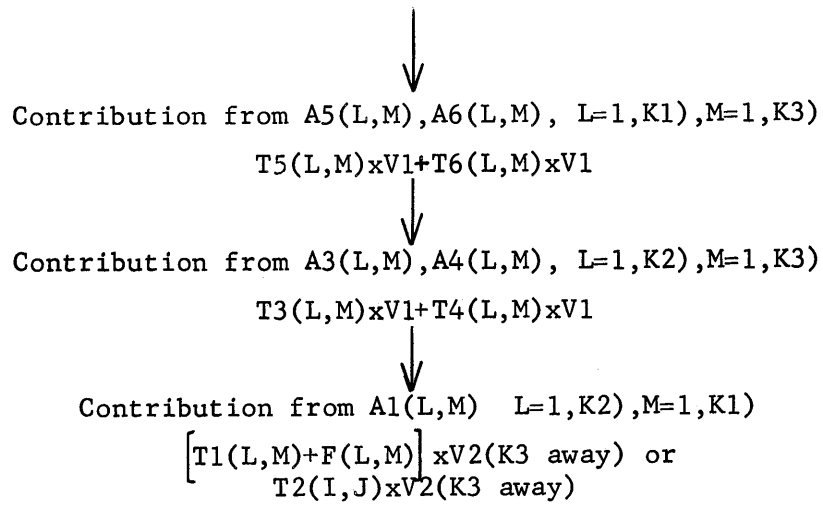


Figure B3.10 (continued)

Appendix A1

A1.1 Selection of the Foil Material

The foil material was selected with due consideration to the following requirements. The material should: (1) form a durable foil, (2) produce only a small perturbation in the neutron flux on the surface of the cavity, (3) have an absorption cross section and a half life which result in a count rate of at least 3000 cpm at the time the foil is counted, (4) be free from impurities which would contribute to the count rate, (5) possess a half life short enough so that the foils may be used for other experiments, (6) be a gamma or beta ray emitter, and (7) be reasonably inexpensive. The irradiation of the foils was limited to about half an hour at a power level of 40 kilowatts, which is equivalent to a flux of 10^6 to 10^7 n/cm sec in the cavity assembly. The time limitation was due to the scheduling of other experiments at the reactor; the power level of 40 kilowatts produced the maximum allowable radiation dose rate in the reactor room since there was no shielding above the cavity when the experiments were done.

A minimum count rate of 3500 cpm at the time of counting was chosen so that all of the foils might be counted within a reasonable time. In most experiments three sets of 36 foils were irradiated simultaneously. Each of the 108 foils was counted three times with a preset count of at least 10,000. If an average of three minutes is allowed for 10,000 counts (about 3500 cpm), the time required to count all 108 foils is 16 hours. Thus, the half life of the foil material must be long enough to produce sufficient activity after 16 hours, and short enough to allow the foils to be used again. The desirability of using a foil several times is emphasized by the fact that 1800 foils were irradiated in the course of the

experiments. Copper meets these requirements more satisfactorily than any other material. Although copper has an absorption cross section of only three barns, the requirement of a 3500 cpm count rate can be met by using a foil 1" in diameter and 26 mils thick.

A1.2 Preparation of the Foils

The foils were punched out of a long, 2" wide strip of high-purity, commercial, rolled sheet copper. Strips of different thicknesses, 23 mil and 26 mil, were used, but the 23 and 26 mil foils were never used in the same irradiation. The thickness of a copper strip was found to be constant within the sensitivity of a micrometer. The foils were punched with a 1" diameter punch and die set, and any burrs resulting from the punching were filed off. The foils were then flattened in a press so that they would lie flat against the surface of the cavity assembly during the irradiation, and would lie flat against the bottom of the counting trays during the counting. An identification number was inscribed on each foil; the 26 mil foils were distinguished by an "A" preceding the number, while the 23 mil foils had a "C" preceding the number. Next, the foils were washed in acetone to remove any foreign material which might have contributed to the foil activity. After the foils were cleaned, they were weighed twice on a Fisher Scientific Gram-atic balance, which gave the weight to 10^{-5} gram, and the two weights were within one part in 10^4 . The average of the two weights was recorded in a ledger with the foil number. Ninety-five per cent of the foils' weights were within a per cent of the average weight, and all were within 2 per cent of the average weight for the "A" and "C" groups of foils. The variation of weight was due to the difference of surface area rather than the thickness of the foil. A two per cent difference

in weight can be accounted for by the difference in the amount of filing required to remove the burrs from the edges of the foils.

An inventory of 400 copper foils was maintained for the flux distribution experiments. Each foil was used several times, and a record was kept of the date on which each foil was irradiated. Before performing an experiment the records were checked to determine if the foils' activity had decayed below a detectable level. A period of 12 days is sufficiently long between irradiations of the same copper foil.

The neutron density in the cavity assembly was obtained from the activity of an array of foils. The density was measured on the thermal column face, on the honeycomb, and in the pedestal for all geometrical arrangements, and on all the surfaces and in the cavity for one geometrical arrangement. The array of foils for measuring the neutron source on the face of the thermal column is shown in Figure A1.1. The arrays for the bottom of the honeycomb, the bottom layer and the second from the bottom layer of the pedestal are shown in Figures A1.2 and A1.3, respectively. The arrays for measuring the neutron density on all of the surfaces appear in Figure A1.4. The arrays of foils in the cavity itself are pictured in Figure A1.5, which shows three arrays of foils, each containing five vertical strings of foils. The arrays were 24" apart, and the strings of an array were 12" apart. The arrays of foils were supported at the top by a length of cord strung between the side walls, and were positioned on the bottom with a piece of mylar tape. Five foils were placed 12" apart and 6" from each end of the strings. Three different orientations of the foils shown in Figure A1.6 were: UP, with the sides of the foil facing the floor and honeycomb; FRONT, with the sides of the foil facing the

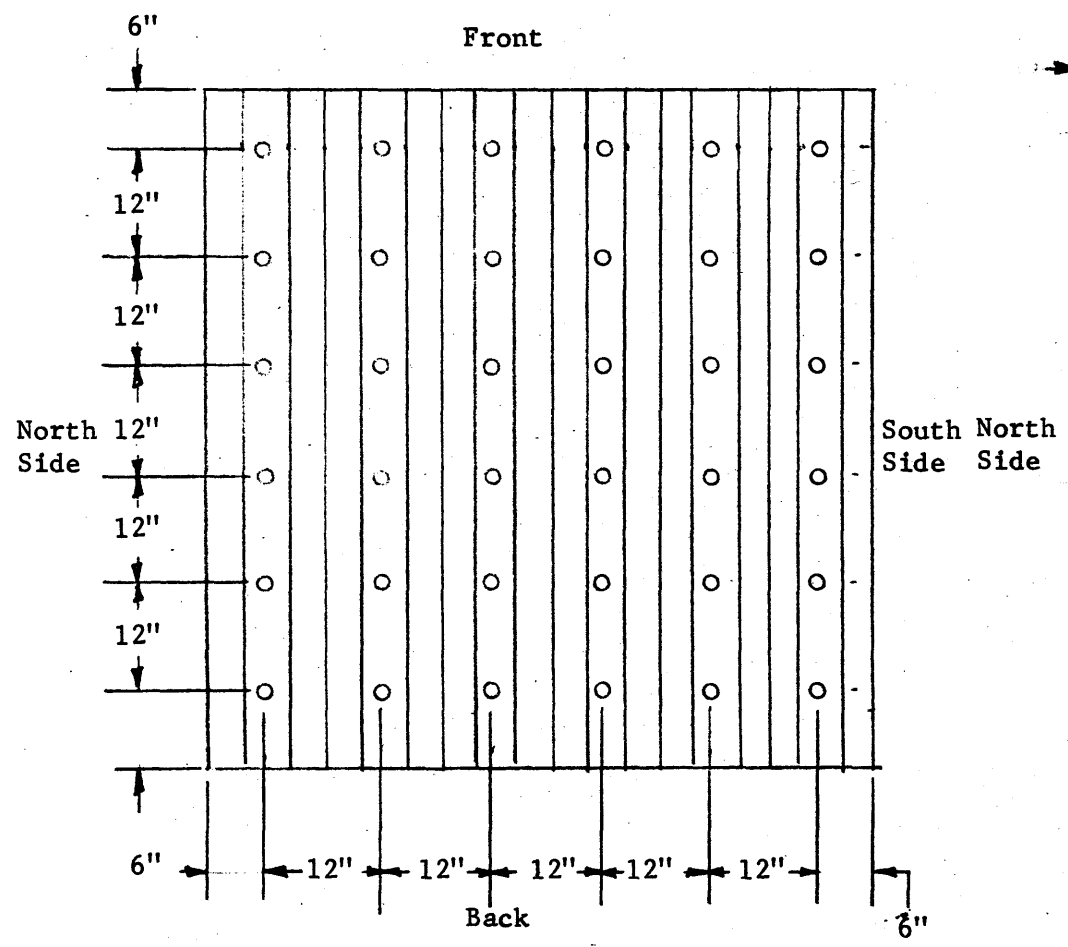


Figure A1.3 Foil Locations on the Bottom and Second from the Bottom Layers of the Graphite Pedestal.

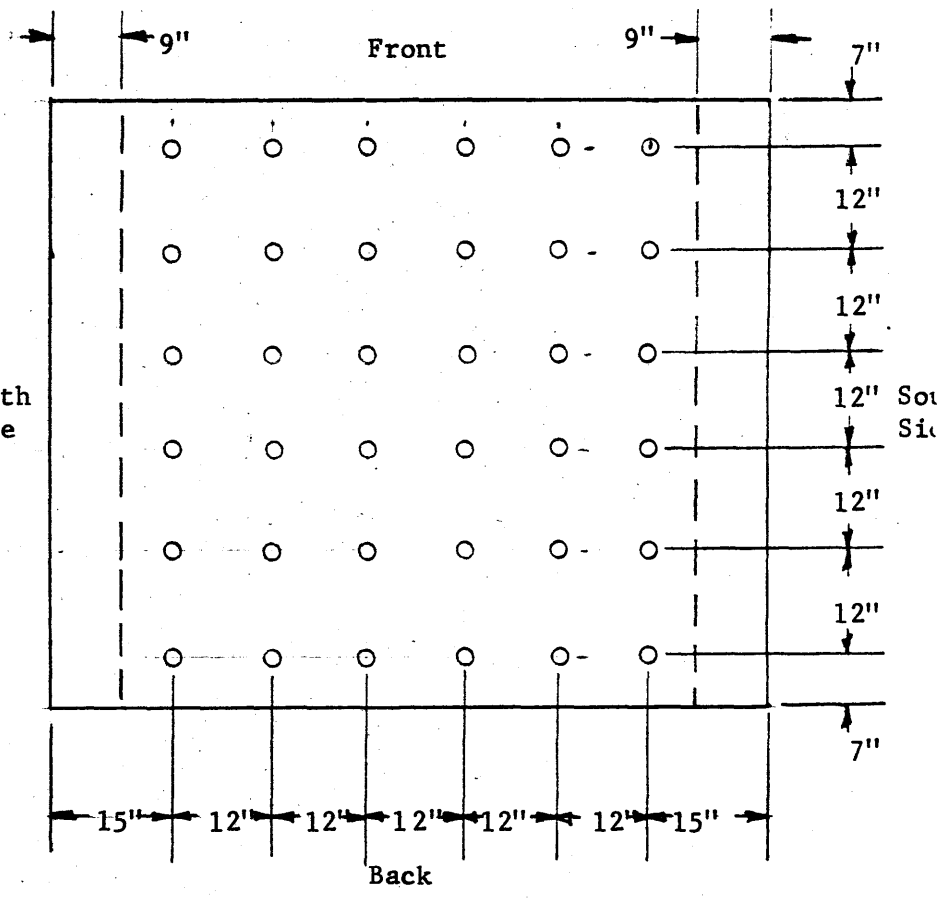
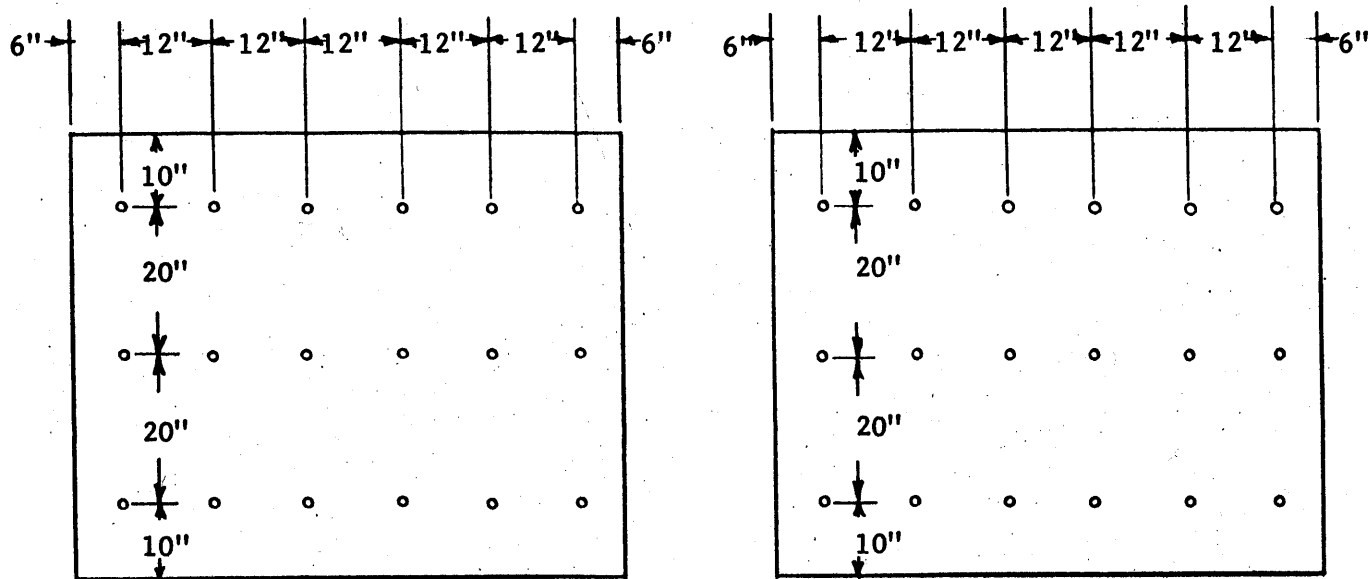
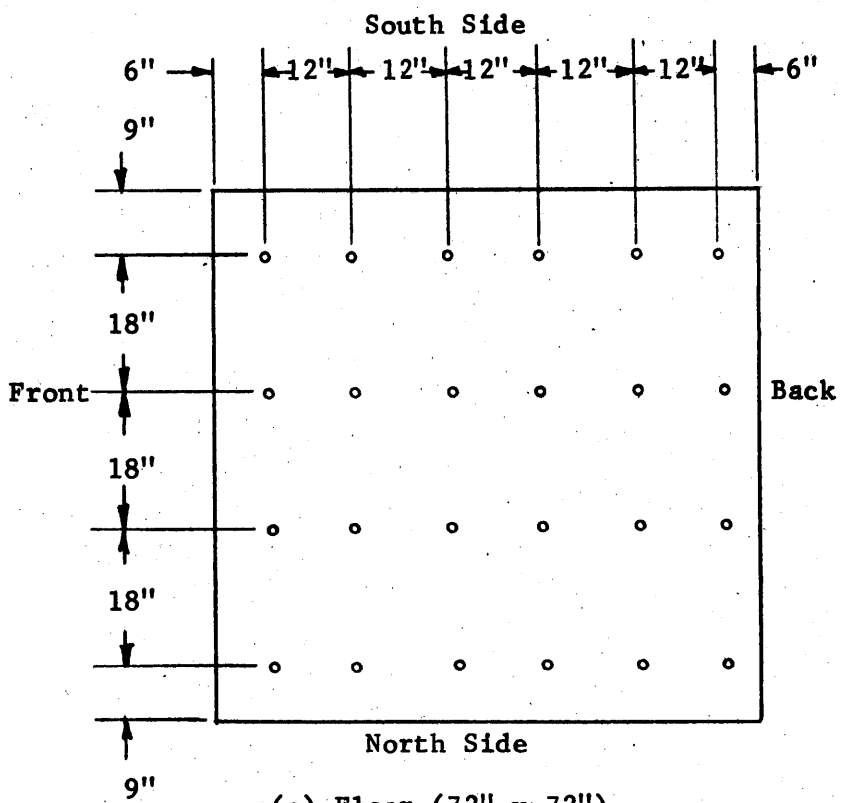


Figure A1.2 Foil Locations on the Bottom of the Honeycomb.



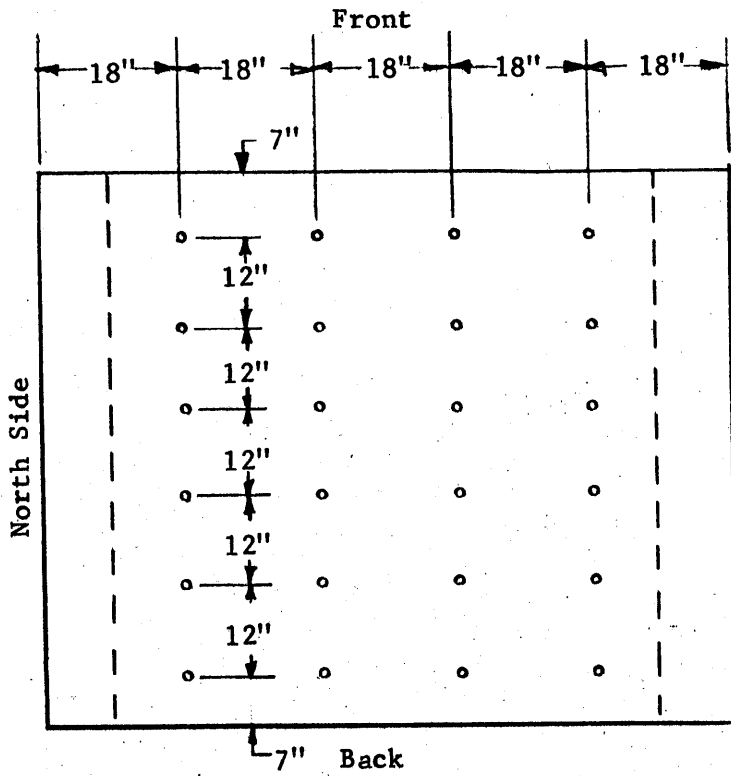
Front (a) Side Wall (72" x 60") Back

(b) Back Wall (72" x 60")

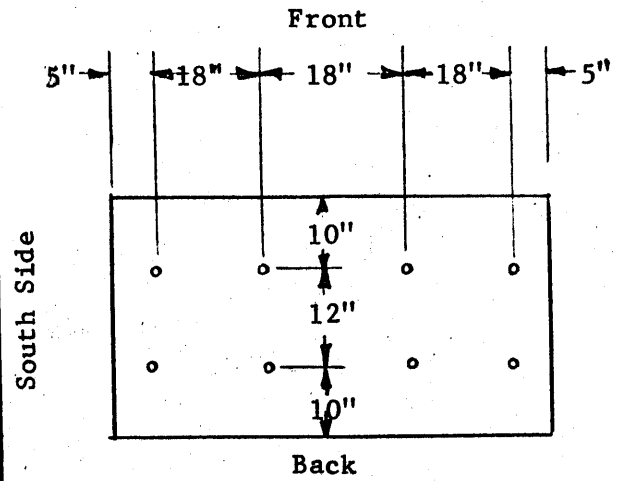


South Side (c) Floor (72" x 72") North Side

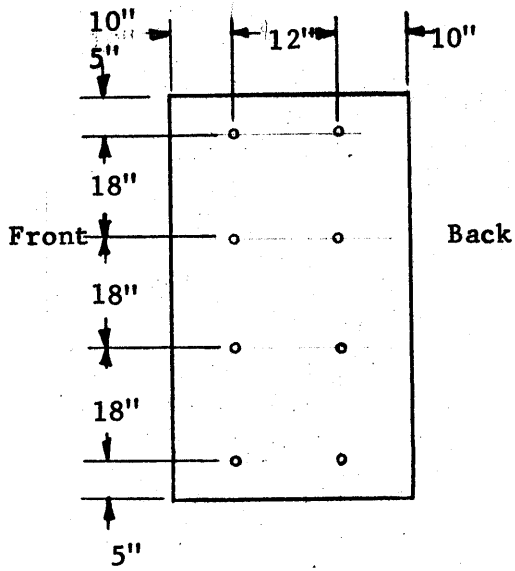
Figure A1.4 Foil Locations on All Surfaces of Assembly II.



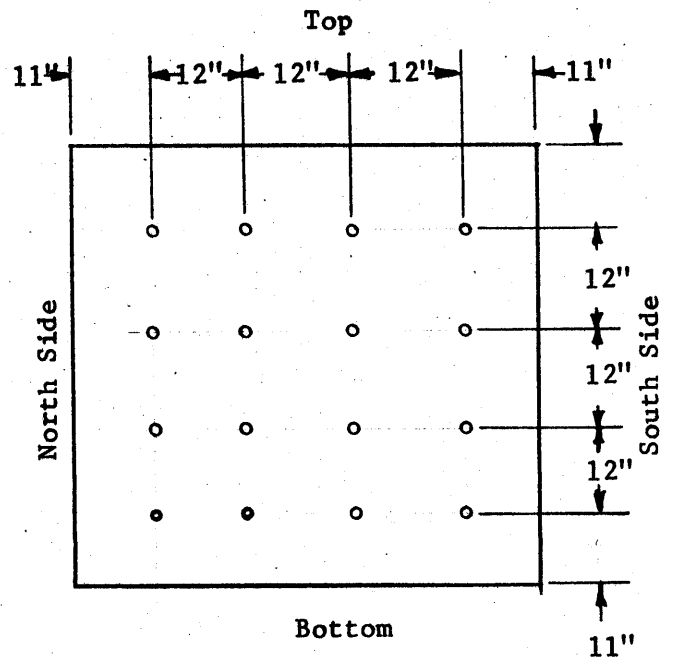
(d) Honeycomb (90" x 74")



(e) Top and Bottom Surfaces of Graphite Frame (58" x 32")



(f) Side Surfaces of Graphite Frame (58" x 32")



(g) Thermal Column Face (58" x 58")

Figure A1.4 (Continued)

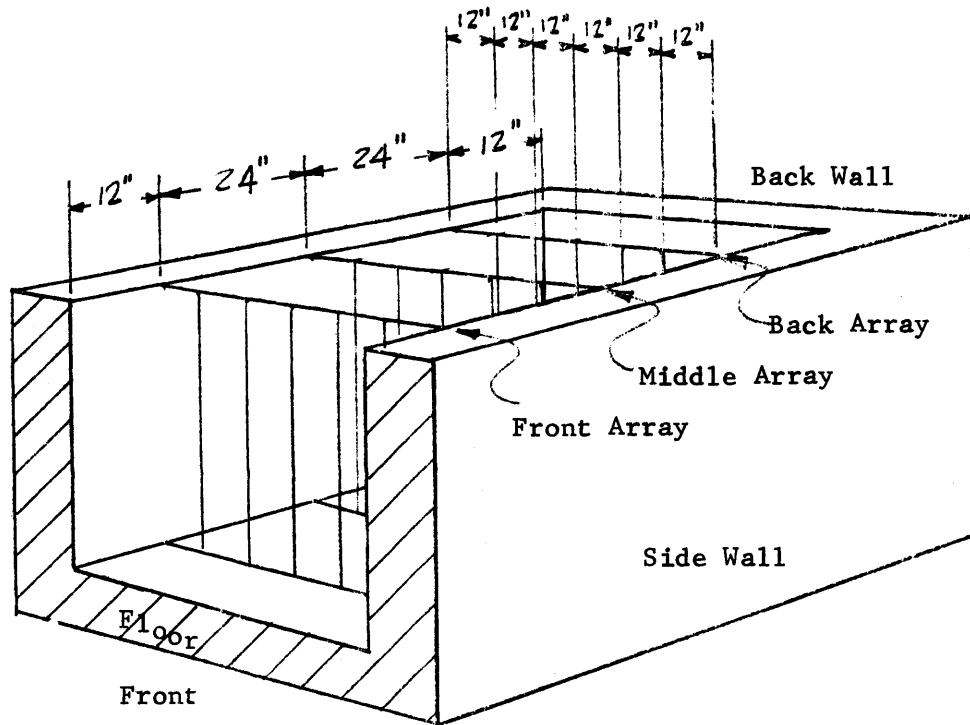


Figure A1.5 Location of the Foils for Experiment #15.

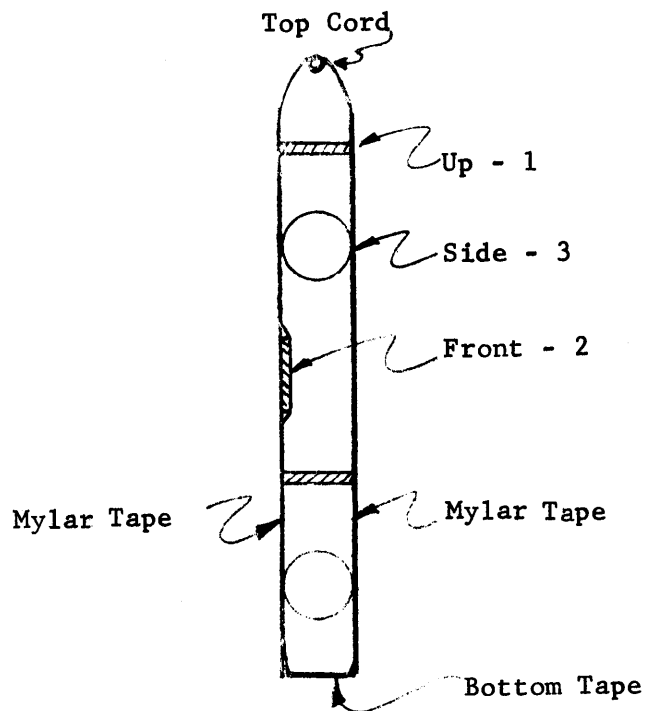


Figure A1.6 Orientation of the Foils on a String in Experiment #15.

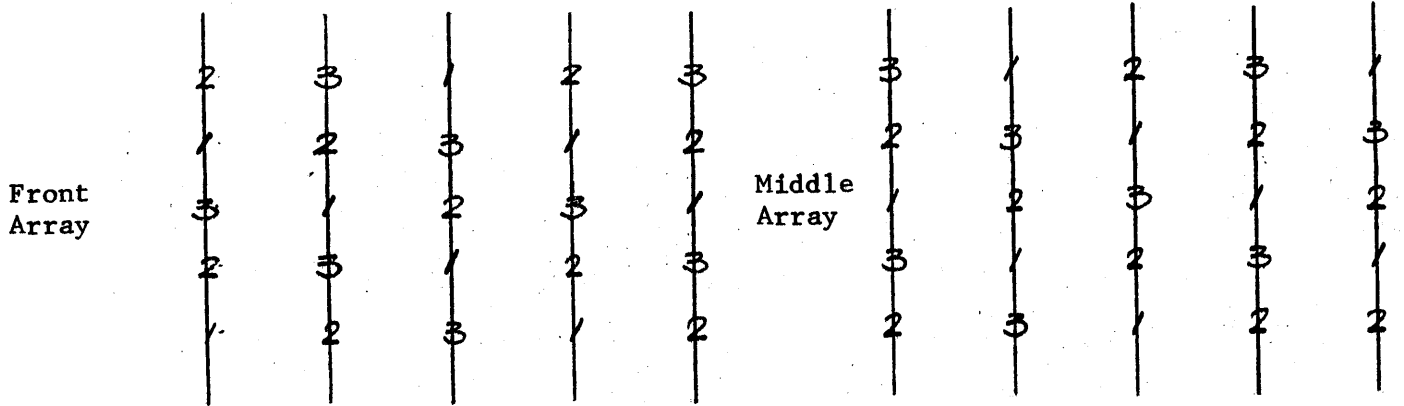
thermal column and back wall; and SIDE, with the sides of the foil facing the side walls. The orientation, denoted by numbers 1, 2, and 3, is shown in Figure A1.7 for each array.

A1.3 Positioning the Foils for Irradiation

The foils for all of the surfaces of the cavity (thermal column face, honeycomb and other surfaces) and for the cavity itself were prepared for the irradiation in the same manner; the foils in the pedestal needed no special preparation.

In describing the pedestal in Chapter E1, the array of notches in the two layers of graphite stringers was shown in Figure E1.7. The clean foils were taken from storage, put in order according to their identification numbers, and the order was recorded in the data book. The foils were always handled with tweezers to prevent contamination. The foils were then placed in the pedestal in the same order in which they had been laid out, with their identification number face up so that the arrangement could be checked. The graphite stringers could easily be slid out from the pedestal so that there was no necessity for unpling the graphite to put the foils in place. After the arrangement of the foils had been checked, the wooden frame and cadmium wrapping were placed around the pedestal.

Positioning the foils on the surfaces of the assembly was slightly more complicated than it was for the pedestal. The clean foils were laid out in the desired arrangement, which was recorded in the data book. Each foil was wrapped with tissue paper and then mylar tape, which kept the tissue in place. The identification number of the wrapped foil was written in ink on the mylar tape. In the wrapping process care was taken to



1 - Up
 2 - Front
 3 - Side

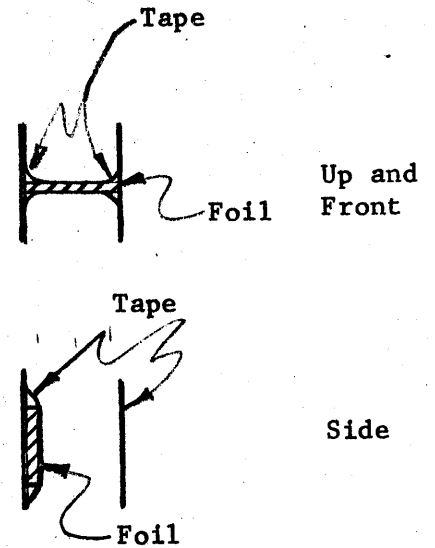
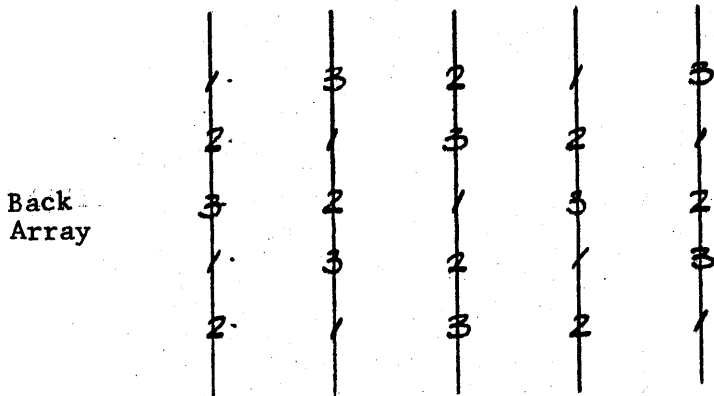


Figure A1.7 Orientation of the Foils for Each Array in Experiment #15.

Figure A1.8 Attachment of the Foils to the Mylar Tape.

remember which side of the foil was inscribed with the identification number, so that the same side would be used for writing the number on the tape. After the foils were wrapped they were placed on a 1" mylar tape. For the array on the honeycomb six 78" long strips of 1" mylar tape were laid out on a table. Six foils were placed, with the identification number face up on each tape, 12 inches apart, starting 9" from each end. A 72" length of mylar tape, adhesive side down, was pressed on top of the 78" strip with foils, leaving three inches on each end of the 78" tape exposed. An ink line was drawn 2" from each end of the string of foils. The distance between the two lines is 74", which corresponds to the 74" length of the honeycomb. Each of the six strings of foils was assembled in this manner to produce an array of 36 foils. A number was written on one end of each of the six strings. The number of the string and the identification number of the foils on the strings were recorded in the data book.

The honeycomb was raised about five feet off the ground and the strings of foils were attached to the bottom surface by means of a 3" piece of exposed mylar tape placed at each end. The six strings were positioned parallel to the 74" dimension of the honeycomb and 12" apart. The outside strings were 15" from the sides of the honeycomb (see Figure A1.2 for the arrangement of the tape and foils on the bottom of the honeycomb).

The strings could be positioned accurately. There were red pencil marks on the bottom surface of the honeycomb, 12" apart, starting 15" from the side, to act as guides for the strings. Each string had two markings 74" apart to position the foils on the honeycomb correctly. The strings were tightly stretched so that the foils did not sag. Three

strips of mylar tape, placed on top of the six strings of foils along the 90" dimension of the honeycomb, kept the strings of foils in place. When the honeycomb was put into place, a 72" square area of the bottom of the honeycomb, indicated by the dotted lines in Figure A1.2, bordered the cavity. The foils were 12" apart, starting 6" from the side and back walls of the hohlraum assembly. A string of foils was identified by the number written on one end of the tape and this number was checked with the data book to insure that the foils were in the correct order on the honeycomb.

By following this procedure and by checking the foil arrangement during these operations, the correct location of the foils on the honeycomb was assured; also, the side of the foil on which the identification number was inscribed was always against the bottom surface of the honeycomb. It should be recalled that the foils were placed in the pedestal with the inscribed side of the foil facing upward, so that both the foils on the honeycomb and in the pedestal had the same orientation during the irradiation.

The foils on the thermal column face were prepared and positioned by the same method as was used for the honeycomb.

The strings of foils for the other surfaces (graphite) were made of only one strip of mylar tape. The strings of foils were attached to the cavity surfaces with the adhesive side of the strip. Except for using one strip of mylar tape instead of two for making a string of foils, the procedure was the same as that used for the honeycomb or thermal column face.

The foils which were placed in the cavity itself were wrapped in tissue paper and mylar tape, and their numbers were written on the tape. The arrangements of the foils, shown in Figure A1.5, were constructed in the

cavity assembly itself. Three cords were stretched across the side walls, 24" apart and 12" from the back wall, and five 10' lengths of mylar tape 12" apart were suspended from each cord. The foils were attached to the 10' length of mylar tape as shown in Figure A1.8. The two ends of the 10' tape were secured to the floor by a strip of mylar tape running between the side walls.

Appendix A2

A2.1 Irradiation Procedure

After the foils were placed in the assembly they were irradiated for a specified time interval at a given power level of the reactor. The results of all of the irradiations were compared on the basis of the same neutron source. Since the source neutrons originated in the reactor core, the magnitude of the neutron source was proportional to the reactor power. The relative magnitude of the neutron source was measured in two ways: with the μ ammeter in the control room of the reactor (which is calibrated in terms of reactor power); with a set of monitor foils which measured the neutron flux in the thermal column. The μ ammeter measures the current from a compensated ion chamber located near the reactor core. The ammeter is calibrated weekly with the thermal power recorder at 1 Mw operation, and each calibration agrees with the earlier ones within two or three per cent.

The two monitor foils were placed in the thermal column through an access hole in the reactor top. The foils were located on the top surface of the thermal column, 28" from the thermal column face and 36" from the core tank. The foils were located far enough away from the reactor core to be insensitive to the small variations in the flux distribution in the

core region from experiment to experiment. The control rod positions varied from experiment to experiment, and caused small variations in the flux distribution within the core. Thus, the activity of the monitor foils gave the relative magnitude of the neutron source without being affected by the variations of the flux in the cavity assembly and reactor core from one irradiation to the next. The readings from the μ ammeter determined the approximate value of the reactor power during the irradiation but were not used in the calculation of the flux distribution.

All of the irradiations of the foils which measured the flux distribution in the cavity assembly followed the same procedure. The foils were put in place, and the honeycomb with the pedestal on top was lowered into position on the top of the side walls. The monitor foils were placed in the thermal column and the shielding doors and lead shutters were opened (except in experiment #1, when the shielding door remained closed). The reactor power was raised to the desired level, indicated by the μ ammeter. The cadmium shutter was closed during all of these operations so that the foils in the thermal column and cavity assembly had not yet become activated. At the specified power, all shim rods were at the same height and the regulating rod was withdrawn 12 to 15 inches. When all these steps had been completed, the cadmium shutter was opened and the time was recorded. When the time for the experiment had expired, the cadmium shutter was closed; the shutter takes approximately 20 seconds to open or close. While the shutters were opening and closing some neutrons were entering the cavity. Since the duration of the experiment was timed from the start of the opening to the start of the closing of the cadmium shutters, no correction was made for the time required to open or close the shutters.

After the cadmium shutter had closed, the lead shutter and shielding doors were closed. The reactor power was decreased to a few watts, and the honeycomb was lifted out of the cavity assembly by means of the overhead crane. The locations of the foils were checked with the recorded positions in the data book as the foils were removed. The two monitor foils were removed from the thermal column and stored in a lead cave on the reactor top. The foils were highly radioactive (about 5 r/hr) and were allowed to cool for three or four days before being counted.

The times at the beginning and the end of the irradiation were recorded in the reactor log book and in the data book. This information was used in reducing the data obtained from counting the foils.

Shortly after the irradiation was completed, the activity of the foils was measured with the gas flow proportional counter described next.

A2.2 Description of the Counting Equipment

The gas flow proportional counting equipment is manufactured by Nuclear Chicago Corporation. It consists of a Model D-47 gas flow counter, Model T3 time delay, Model C01118 printing time, Model C-11018 automatic sample changer, Model D47P preamplifier, and Model 186 decade scaler. The preliminary test of the counting equipment indicated that the line voltage in the counting room was variable. A Sorenson A.C. voltage regulator (Model FRLD 750) was placed in the circuit and stabilized the line voltage. The room temperature in the counting room, which varied between 70° and 80° F, affected the counting efficiency. The small variations in counting efficiency were corrected by means of a standard Ra D + E sample which is discussed in the section describing the counting of the foils. A plateau determination was made by using a radioactive copper foil. The high voltage was set at 2100 volts, the sensitivity at 5 mev, and the preamplifier gain at 5.

A2.3 Background

Before counting, the background was measured with and without the foils in the automatic sample changer. The background count was always between 15 and 20 CPM, regardless of the activity (within the limits of the actual foil activities) of the foils in the sample changer. The variation of 5 CPM in the background rate is negligible compared to the count rate of the foil activity (at least 3500 CPM) and a constant value of 20 CPM was used for the background.

A2.4 Copper Activation

Both natural isotopes of copper, Cu^{63} (69.1%) and Cu^{65} (30.9%), undergo an (n, γ) reaction with thermal neutron absorption cross sections of 4.3 b and 2.1 b, respectively. The half life of Cu^{66} is 5.5 min, and the Cu^{66} was allowed to decay before the foil was counted. Cu^{64} decays by β^- , β^+ and γ emission with a 12.81 hour half life; the positrons give rise to two annihilation gammas. Most of the pulses in the gas flow counter were due to the β^- particles, but a few were caused by the gamma rays interacting with the chamber walls and the gas. Because of its short 12.81 hour half life, the activity of Cu^{64} practically disappears in 12 days, and the foils may be used again. This property is quite advantageous, in view of the fact that 12 experiments with 110 foils each were made in 12 weeks.

A2.5 Procedure for Counting the Foils

The automatic sample changer holds, at most, 38 planchets (foil holders). When more than 37 foils (plus the standard Ra D + E source) were activated in an experiment, the foils were divided into groups; the group having the least active foils was counted first, and then the next active group was counted, and so on.

The foils from experiment #1 were counted in three groups. The monitor foils were counted last, three days after the irradiation. The 36 foils in the thermal column face were divided into two groups because of the large differences in their activities (a factor of 50 between some foils). The foils from experiments #2 through #13 were counted in the following order: (1) the 36 foils from the upper layer of the pedestal, (2) the 36 foils from the lower layer, (3) the 36 foils from the honeycomb surface, and (4) the two monitor foils. The activity of the foils from experiments #14 and #15 was about the same for all foils and the order of counting was arbitrary.

The foils which had been wrapped in tissue paper and mylar tape were removed from their wrappings with scissors and tweezers, and laid out in numerical order. The number on the mylar tape was checked with the identification number of the foil to be sure that they were identical and on the same side of the foils. The foils in the pedestal, which were not wrapped, were washed in acetone and laid out in numerical order. They were then placed in planchets with their identification numbers face up, and the planchets were stacked in the automatic sample changer. The 1" diameter foils fit into the planchets with a 1/32" clearance. The planchets were positioned directly beneath the detector during counting. Since the foils could not move in the planchets, the foils were always located in the same position during counting. The foils were counted in ascending order of their identification numbers. The standard Ra D + E foil was also put in the sample changer with each group of foils.

Before any foils were counted, the counter measured the background activity and the activity of the standard foil for at least an hour. The

background and the standard foil count rates were checked from the output of the printing timer. The counting of the foils followed if the count rates of the background and the standard foil were close to their normal values of 20 CPM and 8000 CPM, respectively. If these count rates did not agree with their normal values, the cause of the discrepancy was found and corrected.

The foils were counted for a specified number of counts instead of for a specified time. The time required to reach this preset number of counts was printed on a paper tape in hundredths of a minute. The settings of the counting equipment (voltage, gain, sensitivity, preset count), the order in which the foils were counted, and the time at the start of counting was written on the paper tape. The preset count was at least 10,000, and sometimes as high as 100,000 if the foils were active enough to be counted in a reasonable length of time (about 3-4 minutes maximum). After all of the foils of one group had been counted three times, they were removed from the automatic sample changer. The order in which they were counted was compared with the order which had been written on the tape as a final check. The same procedure was used in counting the other groups of foils.

A2.6 Reduction of the Data

The activity of a foil is related to the unperturbed flux, ϕ_{abs} , at the surface of the foil by the standard equation for the case of a single radioactive nuclide.

$$\text{Act}(T_r) = \frac{CW\Sigma_a}{\rho} \phi_{\text{abs}}(1 - e^{-\lambda T_r}), \quad (\text{A2.1})$$

where

$Act(T_r)$ is the activity of a foil after T_r minutes of irradiation in disintegration/sec,

C is the correction factor for flux depression, flux hardening, and self-shielding,

W is the weight of the foil (gm),

ρ is the density of the foil material (gm/cm³),

Σ_a is the macroscopic cross section (cm⁻¹) averaged over the energy spectrum of the flux,

λ is the decay constant on the nuclide (minutes⁻¹).

If the time of irradiation is much longer than the half life ($0.693/\lambda$) of the nuclide, the resulting activity is the saturated activity, $Act(sat)$.

$$Act(sat) = \frac{CW\Sigma_a}{\rho} \phi_{abs}. \quad (A2.2)$$

After an irradiation of T_r minutes, and a cooling period of T_d minutes, the activity of the foil, $Act(T_r, T_d)$, is:

$$Act(T_r, T_d) = Act(T_r) e^{-\lambda T_d} = \frac{CW\Sigma_a}{\rho} \phi_{abs} (1 - e^{-\lambda T_r}) e^{-\lambda T_d} \quad (A2.3)$$

After a cooling period of T_d minutes, the foil is counted with a detector, having an efficiency of E . A preset count of PC requires the detector to count for T_c minutes. The average count rate is $\frac{PC - BGD}{T_c}$, and the average foil activity during counting is $\frac{PC - BGD}{ET_c}$, where BGD is the background during counting. A correction for decay during counting, $\frac{\lambda T_c}{1 - e^{-\lambda T_c}}$, relates the average activity to the activity at the start of counting:

$$Act(T_r, T_d) = \frac{(PC - BGD)}{E T_c} \frac{\lambda T_c}{1 - e^{-\lambda T_c}}. \quad (A2.4)$$

Equations (A2.3) and (A2.4) are combined to obtain an expression for ϕ_{abs} .

$$\phi_{\text{abs}} = \frac{1}{\frac{C W \Sigma_a}{\rho} (1 - e^{-\lambda T_r})} \cdot \frac{(PC - BGD)}{E T_c} \cdot \frac{\lambda T_c}{(1 - e^{-\lambda T_c})} \cdot e^{\lambda T_d}. \quad (\text{A2.5})$$

It can be seen from equation (A2.2) that

$$\text{Act}(\text{sat}) = \frac{(PC - BGD)}{E T_c} \cdot \frac{\lambda T_c}{(1 - e^{-\lambda T_c})} \cdot \frac{e^{\lambda T_d}}{(1 - e^{-\lambda T_r})}. \quad (\text{A2.6})$$

CR(sat) is the count rate due to the saturated activity of the foil at the start of counting and is expressed as:

$$\text{CR}(\text{sat}) = E A(\text{sat}) = \frac{(PC - BGD)}{T_c} \cdot \frac{\lambda T_c}{(1 - e^{-\lambda T_c})} \cdot \frac{e^{\lambda T_d}}{(1 - e^{-\lambda T_r})}, \quad (\text{A2.7})$$

so that

$$\phi_{\text{abs}} = \frac{1}{E \frac{\Sigma_a}{\rho} C} \text{CR}(\text{sat})/W. \quad (\text{A2.8})$$

The quantity, CR(sat)/W, is calculated from the known values of T_c , T_r , T_d , PC, BDG, W and ρ . The average value of CR(sat)/W from the three countings is represented by $\overline{\text{CR}(\text{sat})/W}$. The value of ϕ_{abs} for each foil is obtained from the following relationship:

$$\phi_{\text{abs}} = K \cdot N \cdot E(\text{rel}) \cdot \overline{\text{CR}(\text{sat})/W} = K \cdot \text{Act}(\text{rel}), \quad (\text{A2.9})$$

where

K is the conversion constant between Act(rel) and ϕ_{abs} ,

N is the quantity which normalizes $\overline{\text{CR}(\text{sat})/W}$ to a standard value of the neutron source,

E(rel) is the relative counting efficiency of the detector.

The quantity, K , is the same for all of the foils if the terms, Σ_a/ρ and C , in equation (A2.8) are the same for all foils. The activity of a $1/v$ absorber is a function of the density and not the energy distribution of the neutrons. The energy distribution of the flux, ϕ_{abs} , does not affect the value of Σ_a/ρ because copper is a $1/v$ absorber with no low-energy resonances. Hence, the factor Σ_a/ρ is identical for all the foils. The factor C is a correction for flux depression self-shielding and flux hardening. Equations exist in the literature for the flux depression and self-shielding factors (11), but are only applicable to foils surrounded by a diffusing medium. The foils on the honeycomb do not satisfy this condition, since one side of the foil faces the cavity. A method is developed below with which the activity of a copper foil is corrected for flux depression and self-shielding.

Consider the copper foil shown in Figure A2.1. The unperturbed values of the current, J_1 and J_2 , are incident on Surfaces #1 and #2, respectively. The quantity F represents the ratio of the perturbed current to the unperturbed current at the surface of the foil. The neutrons of the perturbed currents are absorbed in the copper foil and the resulting β^- activity is counted.

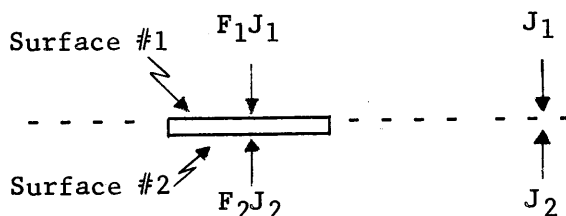


Figure A2.1

A Copper Foil Being Irradiated
by the Perturbed Current, F_1J_1 and F_2J_2 ,
on Surfaces #1 and #2, Respectively

Since the detector is not sensitive to gamma rays, it is assumed that the gamma rays do not contribute to the count rate. The β^- particles have a range of only 3 mils in the 26 mil copper foil, so that, on the average, only those β^- particles emitted within 3 mils of the surface of the foil facing the detector produce pulses in the detector. The quantity M is defined as a quantity proportional to the number of β^- particles leaving Surface #1 of the foil, and thus is also proportional to the count rate due to the foil. Corrections for detector efficiency and the areas of the foil are not included here, since this quantity M is used to investigate only the flux depression and self-shielding.

Equation (A2.10) defines M in terms of the unperturbed currents, J_1 and J_2 , and the effective absorption cross section, Σ .

$$M = (F_1 J_1 \Sigma_1 + f F_2 J_2 \Sigma_2), \quad (\text{A2.10})$$

where f is the fraction of $F_2 J_2$ which passes without absorption from Surface #2 to a plane three mils from Surface #1.

On defining $\beta = J_1/J_2$, equation (A2.10) becomes:

$$(M/J_1) = F_1 \Sigma_1 + f F_2 \Sigma_2/\beta. \quad (\text{A2.11})$$

If the value of (M/J_1) is identical for all of the foils in the cavity assemblies, the corrections for flux depression and self-shielding are identical for all foils. The values of (M/J_1) were calculated for the foils in the pedestal and on the front and back edge of the honeycomb. In the flux distribution experiments, care was taken to insure that the side of a foil facing upward in the assembly was the same side of the foil which faced the detector during the counting. In these calculations, Surface #1 refers to the surface of the foil facing upwards during the irradiations.

The quantity F for this 26 mil copper foil in the graphite pedestal is 0.996. (11) The depression of the flux in the cavity, due to foils on the surface of the cavity, is approximated by using equation (B3.4) in Appendix B3, according to which the flux in the cavity is proportional to the factor, $\frac{1}{\sum_{\text{all surfaces}} A_i(1 - \beta_i)}$. The ratio of the perturbed to unperturbed flux in the cavity is then,

$$F = \frac{\sum_{\text{all surfaces}} A_i(1 - \beta_i)}{\sum_{\text{all surfaces}} A_i(1 - \bar{\beta}_i)}, \quad (\text{A2.12})$$

where $\bar{\beta}_i$ = the albedo of area A, on which the foils are located.

The value of β_i is approximated by equation (A2.13).

$$\bar{\beta}_i = (A_n \beta_n + A_c \beta_c) / A_i,$$

where the subscript n refers to the area not covered by foils, and the subscript c refers to the area covered by a foil.

The value of the albedo, β_c , is obtained by assuming that:

$$\beta_c = t^2 \beta_n,$$

where t is the fraction of the J_1 or J_2 which passes through the foil without absorption.

In experiments #2 through #13, 36, 1" diameter, copper foils were placed on the 72" x 72" honeycomb surface. The value of F for these experiments was calculated by using the values,

$$\beta_i = 0.90 \quad A_n = 1.96 \text{ square feet}$$

$$\beta_n = 0.90 \quad A_c = 278 \text{ square feet}$$

$$t = 0.90$$

in the above equations; the result is $F = 0.9882$.

The effective absorption cross section, Σ , is a function of the absorption cross section, Σ_a , and the angular distribution of the current striking the foil. If the current is isotropic, $\Sigma = 2\Sigma_a$. If the current is that of a unidirectional beam of neutrons, $\Sigma = \Sigma_a/\cos \phi$, where ϕ is the angle of incidence of the beam with the foil. The factor f is defined as:

$$f = e^{-\Sigma L}, \quad (\text{A2.14})$$

where $L = 23$ mils for the 26 mil thick foil.

The quantity M/J_1 is calculated first for the foils in the graphite pedestal. The currents, J_1 and J_2 , are assumed to be isotropic. On using

$$F_1 = F_2 = 0.996,$$

$$\beta = 0.90,$$

$$\Sigma_2 = \Sigma_1 = 2\Sigma_a,$$

$$f = 0.89,$$

the result is:

$$\frac{M}{J_1} = 3.962 \Sigma_a.$$

Next the quantity (M/J_1) was calculated for the foils on the bottom of the honeycomb for Assembly II. Surface #1, the side of the foil facing the detector, is also the side of the foil facing the honeycomb during the irradiation. The current J_1 is assumed to be isotropic, so $\Sigma_1 = 2\Sigma_a$. The current J_2 is due to two groups of neutrons, those arriving directly from the neutron source and those reflected by the walls. By letting n_s and n_r equal the fractions of source and reflected neutrons, respectively, equation (A2.11) may be rewritten as:

$$\frac{M}{J_1} = F_1 \Sigma_1 + \frac{F_2}{\beta} \left[n_s (f \Sigma_2)_s + n_r (f \Sigma_2)_r \right]. \quad (\text{A2.15})$$

The fractions, n_s and n_r , are obtained from the results of an appropriate computer program (see Section T5.4). The reflected neutrons, $n_r J_2$, are assumed to be incident isotropically on the foil, while the cosine of the angle of incidence, $\cos \phi$, for $n_s J_2$ is calculated by assuming that all of the source neutrons are emitted at one point on the thermal column face.

The quantity (M/J_1) is calculated for the foil on the front of the honeycomb in Assembly I by inserting the values,

$$\begin{aligned} F_1 &= 0.996, & n_s &= 0.51, & f_s &= 0.885, \\ F_2 &= 0.998, & n_r &= 0.49, & f_r &= 0.890, \\ \beta &= 0.91, & \cos \phi^{-1} &= 2.06, & \Sigma_{2r} &= 2\Sigma_a, \\ & & & & \Sigma_{2s} &= 2.06 \Sigma_a, \end{aligned}$$

into equation (A2.15), which then yields:

$$(M/J_1)_{\text{front}} = 3.97 \Sigma_a.$$

For the foils on the back of the honeycomb in Assembly I the results were:

$$\begin{aligned} F_1 &= 0.996, & \cos \phi^{-1} &= 3.00, & f_r &= 0.890, & f_s &= 0.840, \\ F_2 &= 0.998, & n_s &= 0.12, & \Sigma_{2r} &= 2\Sigma_a, & (M/J_1)_{\text{back}} &= 4.04 \Sigma_a. \\ \beta &= 0.91 & n_r &= 0.88, & \Sigma_{2s} &= 3\Sigma_a, \end{aligned}$$

The values of (M/J_1) for the foils between the front and back edges of the honeycomb lie between $3.97 \Sigma_a$ and $4.04 \Sigma_a$ for Assembly I. The values of (M/J_1) for the foils in frame and tooth assemblies also lie between 3.97 and 4.04. Thus, the values of (M/J_1) for the foils on the honeycomb in all of the assemblies differ by only \pm one per cent from an average value of $4\Sigma_a$. The correction factors for flux depression and self-shielding, therefore, are practically identical for all of the foils.

The detector efficiency may vary slightly due to the variation of the room temperature, and this change in detector efficiency is corrected by

using the count rate of the Ra D + E sample. The average value of CR(sat) for the three countings of a foil, $\overline{CR(sat)}$, is normalized by the average value of the count rate of the Ra D + E sample for the same three countings. A count rate of 8000 CPM is used as a normalization constant for the Ra D + E foil, so the relative counting efficiency, E(rel), is then:

$$E(\text{rel}) = \frac{8000}{\text{STD}} , \quad (\text{A2.16})$$

where STD is the average count rate of the Ra D + E foil during the three countings of each group of foils.

The activities of the foils must be compared on the basis of the same neutron source. The activity of the two monitor foils from each experiment is proportional to the strength of the source. In each experiment the activities of the foils in the cavity assembly are compared on the basis of a standard activity for the monitor foils. The latter activity is obtained by multiplying the average activity of the monitor foils from experiment #1 by a factor of 25. Since experiment #1 was run at 40 kw, the standard activity is the activity which the monitor foils in experiment #1 could have at one Mw power. The activity, MAct, of a monitor foil from an experiment is defined by relation:

$$\text{MAct} = E(\text{rel}) \cdot \overline{CR(sat)}/W, \quad (\text{A2.17})$$

where $\overline{CR(sat)}$ is the average value of CR(sat) from the three countings of the monitor foils. The standard activity, SMAct, is therefore:

$$\text{SMAct} = 25 \text{ MAct from experiment \#1.} \quad (\text{A2.18})$$

The quantity, $E(\text{rel}) \cdot \overline{CR(sat)}/W$, for each foil in the assembly is normalized to the same neutron source by means of the normalization constant, N, defined as

$$N = \frac{SMAct}{MAct}. \quad (A2.19)$$

The quantity, Act(rel), for a foil represents the relative value of the foil's activity due to the unperturbed neutron flux that strikes the foil at one Mw operation of the MITR.

The conversion factor, K, between the relative activity, Act(rel) and absolute value of the flux, ϕ_{abs} , is obtained in Chapter E4.

No correction for the dead time of the counter is necessary in reducing these data. The highest count rate that was measured was about 20,000 CPM. The equipment has a dead time of 1×10^{-7} minutes, so that the dead time correction is at most 0.002.

REFERENCES

- (1) Thompson, T. J., personal communication, M.I.T., 1961. The cavity principle was suggested for the conceptual design of a facility for a heavy water reactor prepared for the Bell Telephone Laboratory in 1956.
- (2) Völcker, H., "Investigation on the Possible Deflection of a Neutron Flux", Atomkern-Energie, 3, 389-94, (1958).
- (3) Sleeper, Jr., H. P., "Experimental Evaluation of a Thermal Neutron "Hohlraum" Source in a Graphite Thermal Column", GAMD-481, Aug. 20, 1958.
- (4) Clark, D.D., and Jurgoven, R.J., "An Investigation of a Neutron Hohlraum", Trans. of the A.N.S., Dec. 1958, pg.11.
- (5) Saha, M.H., and Srivastava, H.N., "A Treatise on Heat", The Indian Press Private Ltd., Allahabad and Calcutta, 1958.
- (6) Thompson, T.J., "M.I.T. Research Reactor", p/417, Peaceful Uses of Atomic Energy, 1958.
- (7) Profio, A.E., Madell, J.T., Thompson, T.J., and Kaplan, I., "Flux Distribution in the Hohlraum Assembly", Trans. of the A.N.S., Dec. 1960, pg.420.
- (8) Madell, J.T., "Spatial Neutron Flux Distribution on the Surfaces of a Graphite-lined Cavity", Sc. D. Thesis, MIT, 1961
- (9) Hughes, D.J., et.al., "Neutron Cross Sections", second edition, 1958, BNL 325.
- (10) Sullivan, W.H., "Trilinear Chart of Nuclides", second edition, 1960.
- (11) Reactor Physics Constants, ANL 5800, Sections 8 and 9, 1958.
- (12) Weitzberg, A., personal communication, M.I.T., 1960.
- (13) Rockwell, III, T., (Ed.), "Reactor Shielding Design Manuel", March 1956, TID - 7004.
- (14) Simon, A., and Clifford, C.E., "The Attenuation of Neutrons by Air Ducts in Shields", ORNL 1217 (Rev.), March 8, 1954.
- (15) McAdams, W.H., "Heat Transmission", second edition, McGraw Hill, New York, 1942.
- (16) Perry, J.H., Editor-in-chief, "Chemical Engineers' Handbook", McGraw Hill, New York, 1933, pg. 483-98.
- (17) Jacob, M., "Heat Transfer" , John Wiley & Sons, New York, Vol. I, 1949, pg. 27-41.

- (18) Pigford, T.H., Jones, A.C., Martinez, J.S., and Kirschbaum, A.J., "Angular Distribution of Neutrons from a Graphite Surface", Trans. of A.N.S. , Dec. 1960, pg. 466.
- (19) Placzek, G., "The Angular Distribution of Neutrons Emerging from a Plane Surface", Phys. Rev., 72, 556, 1947.
- (20) Clark, M., class notes on Advanced Reactor Physics, M.I.T., 1958
- (21) M.I.T. Computation Center, memo on FMS Subprograms, Nov. 1960.